Doctoral Dissertation

Fast localization of coalescing binaries with gravitational wave detectors and low frequency vibration isolation for KAGRA

A Dissertation Submitted for the Degree of Doctor of Philosophy

December 2019

Department of Astronomy, Graduate School of Science,
The University of Tokyo

Yoshinori Fujii

Abstract

Gravitational waves (GWs) are ripple of spacetime. They are generated by accelerated objects and propagate at the speed of light by stretching/shrinking the space. The direct detection of a GW signal has been achieved for the first time in 2015. This event was due to the merger of two block holes at a distance of the order of 1 billion light years. This detection opened the field of GW astronomy. Two years later, in 2017, the detection of a GW signal from a binary neutron star merger event in coincidence with an electromangetic (EM) transient has been also achieved. This event opened a new era of multi-messenger astronomy.

In this era, in order to expand the multi-messenger astronomy, GW and EM transient observation plays an important role. To this purpose it is demanded to effectively conduct the EM follow up as rapidly as possible after the event is detected. As a consequence from the point of view of EM follow up observation, a fast and precise source localization by GW detectors is primordial importance. Currently a network made by several GW detectors is being built around the world, with the detectors in the US (LIGO), in Europe (Virgo), in Japan (KAGRA) and in India (LIGO-India). This network will drastically improve the sky coverage, the sky localization performance and the identification of the source parameters.

In the real life, however, we are now facing a heterogeneous configuration with GW detectors at different level of development having different sensitivities. Likely, this will continue to be the case with more detectors coming on line in the future. At present, there are two higher sensitivity detectors (Advanced LIGO), a middle sensity one (Advanced Virgo), and KAGRA which is currently being commissioned. This implies that we have to consider a scheme which enables to make effective use of the less sensitive detector information. In this thesis, we have considered an analysis approach to deal with the heterogeneous network and estimate the fast localization performance by that approach.

In addition to the fast localization aspect, having higher network duty cycle is also important for the EM follow up observation. For this purpose, operating a fourth robust interferometer KAGRA is of paramount importance also to minimize the chances to miss detectable events. In all the ground-based GW detectors, the mirrors are suspended in order to realize a situation where the test masses are in free-fall condition. This is necessary also to attenuate the transmission of vibrations from the ground to the mirror. These suspensions have internal resonances, that if not properly damped, can produce large mirror

motion at very low frequencies. Thus, it is important to damp the mechanical resonances of the suspensions and freeze the mirrors in order to start GW observation. Consequently, for more robust interferometer operation, we need a system that enables to damp the mechanical resonances rapidly and to reduce the mirror motion amplitude. Such a system is realized by active controls using sensors and actuators implemented on the suspension system. Based on this fact, the second part of this thesis is focused on the control system for the suspension system in the fourth detector KAGRA. The system has been built and it has allowed to proceed with the KAGRA interferometer alignment and locking. In the following, a more detailed explanation of these works is given.

In the first part of this thesis, we investigate the expected performance regarding fast sky localization of coalescing binaries with a network of three or four GW detectors having heterogeneous sensitivities, such as the LIGO-Virgo, LIGO-KAGRA and LIGO-Virgo-KAGRA network. This work was done in collaboration with members of the LIGO-Virgo collaboration. A hierarchical approach can be used in order to make an effective use of information from the least sensitive detector. In this approach, the presence of an event seen in coincidence in the two more sensitive detectors triggers a focused search in the data of the third (and fourth), less sensitive, detector(s) with a lower SNR threshold.

We show the expected fast localization performance when a hierarchical search is implemented into a GW-EM follow-up pipeline. The study was done using MBTA, a coalescing binary search algorithm based on matched filtering, and Bayestar, a software able to reconstruct sky maps from the outputs of the search algorithms. We confirm that the hierarchical search improves both the localization accuracy and precision compared to those achieved by a double coincidence search with the two LIGO detectors alone. The hierarchical network effectively improves the localization accuracy and precision when threshold SNR for the lower sensitivity detector is set to around 3.5 provided that the BNS range of that the detector is greater than 20% of the more sensitive detectors in the case where the detector network is composed of the two LIGO detectors and the Virgo detector. In the case where the detector network is composed of the two LIGO detectors and KAGRA detector, we found a clear sky localization improvement when the relative sensitivity of KAGRA becomes greater than 28% of the more sensitive detectors. In addition, the hierarchical network by four detectors will improve the localization accuracy and precision when threshold SNR for the lowest sensitivity detector is set to around 3.5 provided that the BNS range of that the detector is greater than 28% of most sensitive detectors. This result assumes that the sensitivity of the middle sensitivity detector (Virgo) is half of the LIGO one.

Consequently, we conclude that once the sensitivity of the third or fourth detector reaches the required one, the search with this hierarchical approach will be most useful when adding new, less sensitive detectors to the network, as they are undergoing commissioning.

In the second part of this thesis, a suspension control system for KAGRA detector has been constructed. KAGRA is now being commissioned and is planned to join to the network in second half of O3 as the fourth detector.

We construct active control system for the low-frequency vibration isolation system for KAGRA, especially for the suspension system which holds the arm cavity mirrors, and which is called Type-A suspension. The target is to achieve the performances required for acquiring the interferometer lock.

The Type-A suspension is 13.5 m in height and consists of a nine stages pendulum. The lower four stages of the Type-A suspension are located inside a cryostat and are operated at cryogenic temperature in order to reduce thermal noise. For cooling, the stages of the lower four stages are connected each other with high purity aluminum cables, called heat links. The absorbed heat on the mirror flows to upper stages and is then extracted to the cryostat structure through the heat links and their specific vibration isolation systems. After implementing the local control system for the Type-A suspension, we then conduct the following tests for the evaluation of the KAGRA Type-A suspension and of its control system:

1. suspension mechanical response,

2. active control performance for the suspension mechanical resonances damping,

3. active control performance for the mirror motion suppression required to help the interferometer lock acquisition.

Based on the first test, we concluded that the assembled Type-A suspension has the characteristics of the pendulum, although some unexpected resonances relate to the heat link system are observed. From this issue, we find that we have to include the heat link system in the model of the suspension mechanics to have a more precise modeling of the system. From the second test, we confirm that the installed damping control system satisfies its requirement for the lock-recovery mode. The third test demonstrates the effectiveness of a feed-forward system using seismometer on the ground to suppress the mirror residual motion. Thie system satisfies the requirement on the mirror residual motion on the time scale of 1 min. Overall, the local control systems realized for Type-A suspensions within thesis work allows the interferometer locking.

In conclusion, the work described in this thesis shows the importance of adding KAGRA to the present GW detector network, even in the context of a heterogeneous network of detectors with different sensitivities, and provides a contribution to the commissioning of KAGRA towards the joining of the network.

Acknowledgements

I sincerely thank all of you who have shared the time with me in these five and a half years.

I deeply appreciate Raffaele Flaminio, who have supervised me for more than five years. He always gave me a good direction and opportunities to work on various field in the gravitational wave detection. I cannot thank him more about communication in English: he always guessed precisely what I meant and he tried to hear my poor English continuously. I was able to pursue the two topics in these years thanks to his continuous help. Indeed he gave me a lot of chances to go abroad for research. Especially the experience in Annecy, France (in 2016 and 2017 summer) has enriched my life indeed. I thank his family as well. They warmly welcomed me in Annecy, it was impressive.

I sincerely thank Frédérique Marion, who have supervised my research about the localization part. She always and kindly directed me with her great insight whenever I asked her unsophisticated questions, and whenever I found troubles in my research. Actually the life in Annecy became bright thanks to her.

I appreciate Leo P. Singer and the MBTA team at LAPP and Università degli Studi di Urbino for providing help with Bayestar and MBTA.

I appreciate Thomas Adams, he instructed me how to use Bayester. He kindly corrected my English so many times, even after leaving from his job in research there. I also thank all the people met in Annecy for making my life there bright.

Ryutaro Takahashi and Yoichi Aso warmly welcomed me to the vibration isolation system (VIS) group in KAGRA two times; 2014 October for the first and 2018 March for the second. They indeed gave me a lot of chances to touch/develop the actual KAGRA suspensions including the Type-A, Type-B, Type-Bp and Type-C. I learnt that the suspensions (not only the interferometer) were actually *perishable*; sometimes the suspensions changed the behavior abruptly and made me in trouble. Thanks to them (the two persons and all the suspensions) I was able to get precious experiences in the mine. I am 100 % sure that I could not have such experience elsewhere. In addition, the team, Ryutaro and Naohisa Satou, conducted the mechanical installation of the Type-A suspensions. Without their effort I could not start my measurement with ETMX suspension.

I sincerely appreciate Koki Okutomi, his comments always helped me to un-

derstand facing issues more correctly and deeply. In addition, he sometimes went to a picnic to the end stations instead of me, even in mid-night in weekend. I cannot forget this and cannot thank him enough.

I appreciate Lucia Trozzo, she gave me a good knowledge about IP-stage controls based on her experience, especially for the Type-A suspension. Actually I desired to work with her for the controls using inertial sensors, more slowly, without thinking about the project schedule and the sensitivities of the sensors.

Tomohiro Yamada also kindly helped my work at the mine especially about the mechanics/hardware maintenance of the cryogenic payload. Kindly he sometimes calmed down my positively fed-back brain. I cannot appreciate him more.

I deeply thank the Type-B team, Mark A. Barton, Fabián Erasmo Peña Arellano, Enzo Nicolás Tapia San Martin and Naoatsu Hirata, their positive minds helped me so many times.

I also appreciate Takayuki Tomaru and the team. Without their mechanical installation work of the cryogenic payloads, I could not start to work on the payload.

I thank Yutaro Enomoto, he provided me the stably locked X-arm cavity (in 2018 winter). In addition, his comments always helped me to solve a lot of issues happened on the KAGRA suspensions.

I appreciate Koseki Miyo, oftenly the discussion with him helped with the progress on my experiment. Actually without his effort on the installation/maintenance of the seismometers in the mine, I could not finish the measurement.

Indeed the backs of Yutaro and Koseki, who had started working at the site mostly at the same time (from the Master's period), helped me a lot to pursue/finish the work at the site.

I thank Kunihiko Hasegawa, Koji Nagano and Tomofumi Shimoda, sometimes having a chat with them kicked away my extra anxieties for my life.

I thank Takanori Sekiguchi, without his kind guidance for the KAGRA suspensions and the KAGRA project, I could not obtain this research results. It was done more than five years ago and was for about a half year, however, the experience of the work with him helped my thesis work a lot.

I thank Ayaka Shoda and her family. I learnt how the KAGRA SASs work mechanically through the PR suspension maintenance during her presence/absence at the mine. (I cannot forget at all about playing with you, PR2, PR3 and PRM.) She sometimes brought me away form the desk and in front of a wall for climbing when I was in Mitaka. Bright smile of her son also gave me a spirit to tackle to the issues in my research.

I thank Tomotada Akutsu, I learnt from him how a experimentalist (and a supervisor) should be.

I also thank Satoshi Tanioka, he always come to my office and told me about his daily events even in weekend. I could enjoy all the days in Mitaka thanks to him.

I also deeply appreciate Masayuki Nakano, Takahiro Yamamoto and Takaaki Yokozawa, who led the main commissioning work at KAGRA mine. They indeed

continuously worked on the commissioning, in terms of the interferometer locking, maintenance of all the digital system infrastructures, and the noise hunting and its debugging. They provide me finely aligned interferometer, and also gave me many chances to break the alignment for my experiment at the upper stages such as the IP-stage of the Type-A. Actually at the site I could smoothly forget that one day consisted of 24 hours, thanks to them.

The team TAMA/NAOJ, Matteo Leonardi, Eleonora Capocasa, Yuhang Zhao, Naoki Aritomi, Manuel Marchiò and Simon Zeidler, always made me relaxed and put me away from the highly pressured mind.

The administrative office members in NAOJ, Mihoko Kondo, Mizuho Yoshizumi, Mikiko Harada, Megumi Ohyama and Eri Sakamoto indeed helped/supported my life a lot. With their kind help, I could make schedule change going to/coming back to Mitaka/Kamioka KAGRA site so easily.

I thank Kyouichi Takayama, Mihoko Okinaka, Yukari Maeda, Yayoi Hara and Miho Iwamatsu, who are the administrative office members in Kamioka KAGRA site. Without their continuous help, I could not spend my life at the site.

Indeed I have countless people who have helped me to have bright lives in these five and a half years. I cannot appreciate all of them more. Thanks to all such people, I could enjoy the life and the experience in these years.

This work was supported by MEXT, JSPS Leading-edge Research Infrastructure Program, JSPS Grant-in-Aid for Specially Promoted Research 26000005, JSPS Grant-in-Aid for Scientific Research on Innovative Areas 2905: JP17H06358, JP17H06361 and JP17H06364, JSPS Core-to-Core Program A. Advanced Research Networks, JSPS Grant-in-Aid for Scientific Research (S) 17H06133, the joint research program of the Institute for Cosmic Ray Research, University of Tokyo, National Research Foundation (NRF) and Computing Infrastructure Project of KISTI-GSDC in Korea, the LIGO project, and the Virgo project.

This work was also supported by JSPS Grant-in-Aid for JSPS Fellow 17J03639.

Finally, I sincerely appreciate my family; my father, my mother, my sister and her family. They allowed me to concentrate on the work in the field of research as whatever I like. Sometimes her son kicked away all my worries literally. I truly thank all of them for the thoughtful support at home.

Table of Contents

Abbreviations

Astrophysics

EM	Electro-Magnetic (wave)
BNS	Binary Neutron Star
BBH	Binary Black Hole
BH	Black Hole
CBC	Compact Binary Coalescence
GR	General Relativity
GW	Gravitational Wave
NS	Neutron Star
SNe	Supernovae

Detectors

LIGO	Laser Interferometric Gravitational wave Observatory
Virgo	Virgo detector
KAGRA	KAGRA detector
H, H1	LIGO Hanford detector
L, L1	LIGO Livingston detector
V, V1	Virgo detector
K, K1	KAGRA detector

Pipelines

GstLAL low-latency CBC search pipeline [1]

pyCBC Live low-latency CBC search pipeline [2]

MBTA low-latency CBC search pipeline [3]

Bayestar Bayesian rapid localization algorithm [4]

Interferoemter

IMC Input Mode Cleaner

PRM Power Recycling Mirror

PR2 Power Recycling Mirror 2

PR3 Power Recycling Mirror 3

SRM Signal Recycling Mirror

SR2 Signal Recycling Mirror 2

SR3 Signal Recycling Mirror 3

BS Beam Splitter

TM Test Mass

ITMX Input Test Mass X

ITMY Input Test Mass Y

ETMX End Test Mass X

ETMY End Test Mass Y

FPMI Fabry-Perot Michelson Interferometer

DARM Differential Arm

PDH Pound-Drever-Hall (technique)

KAGRA suspensions

SAS Seismic Attenuation System

VIS Vibration Isolation System

IP Inverted Pendulum

GAS Geometric Anti-Spring

F0 Top GAS filter

F1, F2, F3, F4, SF Standard GAS filter

BF Bottom GAS filter

Payload The lower suspension part

PF Platform

MN Marionette

RMN Recoil Marionette

IM Intermediate Mass

IRM Intermediate Recoil Mass

RM Recoil Mass

HLVIS Heat Link Vibration Isolation System

L Longitudinal

T Transverse

V Vertical

R Roll

P Pitch

Y Yaw

DoF, dof Degree of Freedom

Sensors and actuators for KAGRA suspensions

LVDT	Linear Variable Differential Transducer
GEO	Geophone L-4C
ACC	Accelerometer
Oplev	Optical lever
Length-oplev	Length sensing optical lever
PD	Photo Diode
QPD	Quadrant Photo Diode
SLD	Super Luminescent Diode
PS	(Reflective) Photo Sensor

Others

SNR	Signal-to-Noise ratio
ASD	Amplitude Spectral Density
PSD	Power Spectral Density
RMS	Root Mean Square
Q	Quality factor
ADC	Analogue-to-Digital Converter
DAC	Digital-to-Analogue Converter
IPsc	Sensor correction system at IP-stage

Chapter 1

Introduction

The existence of gravitational waves (GWs) was predicted by A. Einstein in 1916 according to his theory of general relativity [5]. 100 years after the prediction, a GW signal from the coalescence of two black holes was detected for the first time in 2015 by the Laser Interferometric Gravitational-wave Observatory (LIGO) in the U.S. [6]. In 2017, the first detection of a GW signal from the coalescence of two neutron stars by LIGO-Virgo network in coincidence with an electro-magnetic transient was achieved and this opened the era of multi-messenger astronomy [7].

This chapter describes the background of detection of GWs and that of the current GW detectors. Section 1.1 summarizes the theoretical aspect of GWs. Section 1.2 introduces GW sources expected to be detected. Section 1.3 describes the interferometric detection method, which is used for the current GW detectors. Section 1.4 introduces current GW detector and its property using the KAGRA, the fourth detector joining to the network. Section 1.5 describes the currently working GW detectors. These are also referred to as second generation detectors. Section 1.6 summarizes this chapter.

1.1 General relativity and Gravitational waves

1.1.1 Gravity in general relativity

In general relativity (GR), the Einstein field equation describes the relationship between the metric of spacetime and the mass distribution as:

$$G_{\mu\nu} \equiv R_{\mu\nu} - \frac{1}{2} g_{\mu\nu} R = \frac{8\pi G}{c^4} T_{\mu\nu}. \tag{1.1}$$

The variables in eq (1.1) are summarized as follows:

- $g_{\mu\nu}$: Metric tensor, which characterizes the geometry of spacetime. $g_{\mu\nu}$ is a dimensionless quantity and is defined as the inner product of basis vectors: $g_{\mu\nu} \equiv \boldsymbol{e}_\mu \cdot \boldsymbol{e}_\nu$.
- $T_{\mu\nu}$: Energy-momentum tensor, which characterizes mass distribution. The elements of $T_{\mu\nu}$ include the following quantities:

T_{00}: Energy density, T_{i0}: ith element of momentum density,
T_{0j}: jth element of energy flux,
T_{ij}: Stress tensor in non-relativistic fluid dynamics ($i, j = 1, 2, 3$).

- $G_{\mu\nu}$: Einstein tensor
- $R_{\mu\nu} \equiv R^{\alpha}{}_{\mu\alpha\nu}$: Ricci tensor, which is defined by
  $R^{\mu}{}_{\alpha\beta\gamma} \equiv \frac{\partial \Gamma^{\mu}_{\alpha\beta}}{\partial x^{\gamma}} - \frac{\partial \Gamma^{\mu}_{\alpha\gamma}}{\partial x^{\beta}} + \Gamma^{\mu}_{\lambda\gamma}\Gamma^{\lambda}_{\alpha\beta} - \Gamma^{\mu}_{\lambda\beta}\Gamma^{\lambda}_{\alpha\gamma}$,
  where $\Gamma^{\mu}_{\alpha\beta} \equiv g^{\mu\nu}\left(\frac{\partial g_{\beta\nu}}{\partial x^{\alpha}} + \frac{\partial g_{\alpha\nu}}{\partial x^{\beta}} - \frac{\partial g_{\alpha\beta}}{\partial x^{\nu}}\right)$.
- $R \equiv g^{\mu\nu}R_{\mu\nu}$: Scalar curvature (or Ricci scalar).
- G : Gravitational constant.
- c : Speed of light.

In the eq (1.1), the line element ds between two points x^{μ} and $x^{\mu}+dx^{\mu}$, which are infinitesimally separated from each other, is $ds^2 = (dx^{\mu}\boldsymbol{e}_{\mu})\cdot(dx^{\nu}\boldsymbol{e}_{\nu}) = g_{\mu\nu}dx^{\mu}dx^{\nu}$, where $\boldsymbol{e}_{\mu}, \boldsymbol{e}_{\nu}$ denote the basis vectors of the coordinates. In spacetime which is described by the metric $g_{\mu\nu}$ as defined above, the motion of a free particle is explained by its geodesic equation:

$$\frac{\mathrm{d}^2 x^{\alpha}}{\mathrm{d}\tau^2} = \Gamma^{\alpha}_{\mu\nu}\left(\frac{\mathrm{d}x^{\mu}}{\mathrm{d}\tau}\right)\left(\frac{\mathrm{d}x^{\nu}}{\mathrm{d}\tau}\right), \tag{1.2}$$

where τ is an arbitrary parameter. By using these equations, GR concludes that what we observe as gravity is a curvature of spacetime. The characteristics of gravity are described by the metric in GR. The more details in this chapter are described in [8].

1.1.2 Theoretical expression of gravitational waves

The equation which describes the GWs are derived from the Einstein equation; first, we derive eq (1.1) in a weak gravitational field. Since spacetime is flat if there is no gravity, we assume that the spacetime is mostly flat in the weak gravitational field. In the weak field, the metric $g_{\mu\nu}$ is explained by the superposition of a metric of flat spacetime, that is, Minkowski metric $\eta_{\mu\nu}$ and that of a small perturbation $h_{\mu\nu}$:

$$g_{\mu\nu} = \eta_{\mu\nu} + h_{\mu\nu} + \mathcal{O}(h^2), \qquad (\ |h_{\mu\nu}| \ll 1\ ). \tag{1.3}$$

In above equation, $h_{\mu\nu}$ describes actual spacetime as a perturbation from Minkowski spacetime. The quantities in eq (1.3) are defined for following calculation:

$$h^{\mu}{}_{\nu} \equiv \eta^{\mu\lambda}h_{\lambda\nu}, \qquad h^{\mu\nu} \equiv \eta^{\mu\alpha}\eta^{\nu\beta}h_{\alpha\beta}, \qquad h \equiv \eta^{\mu\nu}h_{\mu\nu}. \tag{1.4}$$

By rearranging eq (1.1) using a formula $g^{\mu\nu} = \eta^{\mu\nu} - h^{\mu\nu} + \mathcal{O}(h^2)$, we obtain eq (1.5). I note that $g_{\mu\nu}$ denotes the inverse matrix of $g^{\mu\nu}$, and that terms in h^2 and higher are neglected in this calculation.

$$
\begin{aligned}
G_{\mu\nu} &= \frac{8\pi G}{c^4} T_{\mu\nu} \\
&\simeq R_{\mu\nu} - \frac{1}{2}\eta_{\mu\nu} R \\
&= \frac{1}{2}\left(-\Box h_{\mu\nu} + \partial_\nu \partial^\alpha h_{\mu\alpha} + \partial_\mu \partial^\alpha h_{\nu\alpha} - \partial_\mu \partial_\nu h - \eta_{\mu\nu}\partial^\alpha \partial^\beta h_{\alpha\beta} + \eta_{\mu\nu}\Box h\right), \quad (1.5)
\end{aligned}
$$

where $\partial_\mu \equiv \frac{\partial}{\partial x^\mu}$, $\partial^\alpha = \eta^{\alpha\nu}\partial_\mu$ and $\Box \equiv \partial^\alpha \partial_\alpha = \eta^{\alpha\beta}\partial_\alpha \partial_\beta = -\frac{1}{c^2}{\partial_t}^2 + \nabla^2 = -\frac{1}{c^2}\frac{\partial^2}{\partial t^2} + \frac{\partial^2}{\partial x^2} + \frac{\partial^2}{\partial y^2} + \frac{\partial^2}{\partial z^2}$. Here, by applying a gauge transformation which satisfies the following condition:

$$
\partial^\alpha h_{\mu\alpha} - \frac{1}{2}\partial_\mu h = 0, \quad (1.6)
$$

we obtain the below equation:

$$
\Box\left(h_{\mu\nu} - \frac{1}{2}\eta_{\mu\nu} h\right) = -\frac{16\pi G}{c^4} T_{\mu\nu}. \quad (1.7)
$$

This equation is called the linearized Einstein equation. In most cases, eq (1.7) is expressed as follows by using another tensor $\bar{h}_{\mu\nu} \equiv h_{\mu\nu} - \frac{1}{2}\eta_{\mu\nu} h$:

$$
\Box \bar{h}_{\mu\nu} = -\frac{16\pi G}{c^4} T_{\mu\nu}. \quad (1.8)
$$

This $\bar{h}_{\mu\nu}$ is called trace-reversed tensor, and has the relationship below:

$$
\bar{h} \equiv \bar{h}^\mu{}_\mu = -h^\mu{}_\mu = -h. \quad (1.9)
$$

Note that $\bar{h}_{\mu\nu}$ satisfies $\partial_\mu \bar{h}^\mu{}_\nu = 0$, under the condition of eq (1.6). Eq (1.8) explains the wave equation of the $\bar{h}_{\mu\nu}$ which describes the small perturbation $h_{\mu\nu}$ from the Minkowski metric. Eq (1.8) also implies that $\bar{h}_{\mu\nu}$ propagates away from the source of the energy-momentum tensor $T_{\mu\nu}$ with the speed of light c. Here, If a vacuum condition $T_{\mu\nu} = 0$ $(= R_{\mu\nu} = R)$, i.e., a spacetime without masses is considered, eq (1.8) becomes

$$
\Box \bar{h}_{\mu\nu} = 0. \quad (1.10)
$$

Consequently, the expression becomes similar to the wave equation for electromagnetic waves which propagate in vacuum. This ripple of the spacetime $\bar{h}_{\mu\nu}$, which propagates with speed of light c, describes a GW.

1.1.3 Properties of gravitational wave

Here we briefly explore the properties of GWs which propagate in vacuum, by considering a monochromatic plane wave:

$$
\bar{h}_{\mu\nu} \equiv a_{\mu\nu} e^{ik_\alpha x^\alpha} = a_{\mu\nu} \exp[i(\boldsymbol{k}\cdot\boldsymbol{r} - \omega t)], \quad (1.11)
$$

where k^α denotes the wave vector $k^\alpha = (\omega/c, k^1, k^2, k^3)$, $a_{\mu\nu}$ describes its amplitude via a 4×4 matrix of constant numbers. Here, we can choose the following gauge conditions so that $a_{\mu\nu}$ (or $\bar{h}_{\mu\nu}$) holds only information about the GWs []:

$$\bar{h}_{0\nu} = 0, \tag{1.12}$$
$$\bar{h}^i{}_i = 0, \tag{1.13}$$
$$\partial_j \bar{h}^{ij} = 0. \tag{1.14}$$

The set of conditions eq (1.12) to (1.14) is called the transverse traceless (TT) gauge. In most cases, GWs are discussed under this gauge. Under this gauge, we obtain the following properties of GWs:

- Eq (1.12) says that GWs have only space element.
- Eq (1.13) says that GWs are traceless and thus the difference between $\bar{h}_{\mu\nu}$ and $h_{\mu\nu}$ vanishes due to this equation ($\bar{h}^{\rm TT}_{\mu\nu} = h^{\rm TT}_{\mu\nu}$).
- Eq (1.14) says that GWs are transverse waves.

Here, by inserting eq (1.11) into eq (1.14), we obtain the following equation:

$$k^j a_{ij} = k^j \bar{h}_{ij} = 0. \tag{1.15}$$

This equation describes that the wave vector is orthogonal with $\bar{h}_{ij}$. In addition, if we consider a plane GW which propagates along the z axis, we get the below $a_{\mu\nu}$ by using the equations $k^\mu = (k^0, k^1, k^2, k^3) = (\omega/c, 0, 0, \omega/c)$, $a_{12} = a_{21}$ and $a_{11} + a_{22} = 0$:

$$a^{\rm TT}_{\mu\nu} = \begin{pmatrix} 0 & 0 & 0 & 0 \\ 0 & a_+ & a_\times & 0 \\ 0 & a_\times & -a_+ & 0 \\ 0 & 0 & 0 & 0 \end{pmatrix}. \tag{1.16}$$

This expression implies that GW have two degrees of freedom.

Polarization

The remaining two degrees of freedom appear as polarizations. These two polarizations are called *plus* and *cross* mode according to the distortion shapes. If we suppose that some free point masses are put in a circle around a point (0,0,0) whose radius is given by L. First, the line element ds^2 between the origin and one of the masses is

$$\begin{aligned} ds^2 &= -(cdt)^2 + dl^2 \\ &= -(cdt)^2 + (1+h_+)dx^2 + 2h_\times dxdy + (1-h_+)dy^2 + dz^2. \end{aligned} \tag{1.17}$$

If a two dimensional plane is considered, dl^2 becomes:

$$dl^2 = (1+h_+)dx^2 + 2h_\times dxdy + (1-h_+)dy^2. \tag{1.18}$$

In this condition, if a GW is injected along the z axis, the infinitesimal distances between the origin and one of the masses, $dx,\ dy$ vary as

$$dl^2 \simeq dx'^2 + dy'^2 \tag{1.19}$$

$$\begin{pmatrix} dx' \\ dy' \end{pmatrix} = \begin{pmatrix} 1+\frac{1}{2}h_+ & \frac{1}{2}h_\times \\ \frac{1}{2}h_\times & 1-\frac{1}{2}h_+ \end{pmatrix} \begin{pmatrix} dx \\ dy \end{pmatrix}. \tag{1.20}$$

Finally, if we use $(dx,\ dy) \equiv (L\cos\theta,\ L\sin\theta)$, the proper distance l is

- if $h_+ \neq 0, h_\times = 0$;
  according to $dl^2 = (1+h_+)dx^2 + (1-h_+)dy^2 \simeq L^2(1+h_+\cos 2\theta)$,

$$l \simeq L \times \left(1+\frac{1}{2}h_+\cos 2\theta\right) \quad : \ + \text{ mode}, \tag{1.21}$$

- if $h_+ = 0, h_\times \neq 0$;
  according to $dl^2 = dx^2 + dy^2 + 2h_\times dxdy \simeq L^2(1+h_\times \sin 2\theta)$,

$$l \simeq L \times \left(1+\frac{1}{2}h_\times\sin 2\theta\right) \quad : \ \times \text{ mode}. \tag{1.22}$$

By inserting $h_+ = a_+\exp[i(kz-\omega t)]$, or $h_\times = a_\times\exp[i(kz-\omega t)]$ into these equations, the location of the masses become as shown in Figure 1.1.

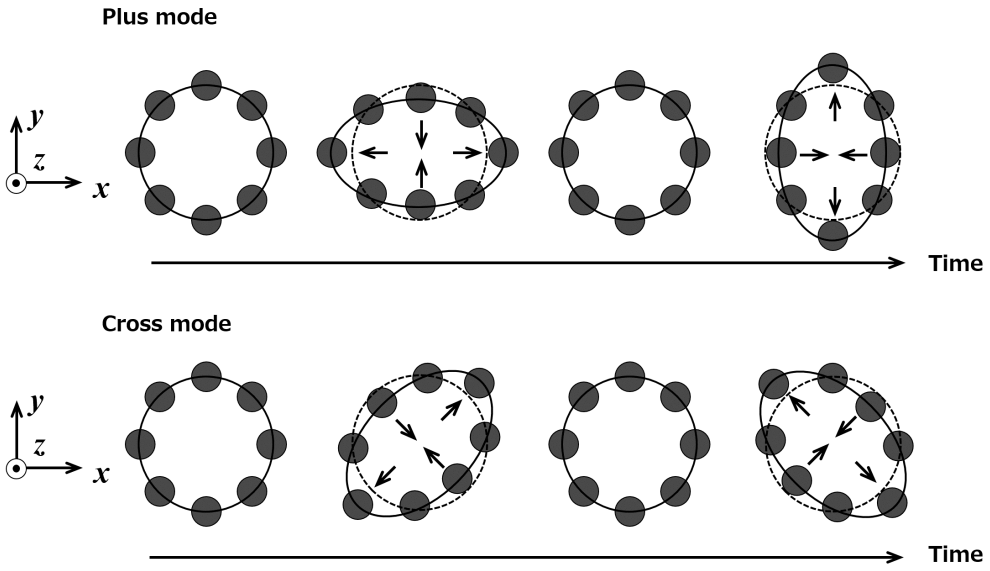

Figure 1.1: Polarizations of a GW. Black points denote free particles. If a GW incidents into $+z$ axis, the positions of free particles arrayed in circle are changed as shown in this figure.

Effect on free point mass

We consider how a GW affects free point masses here. If we suppose that a free point mass is at rest at a coordinate and is then exposed to a GW (in the TT gauge), the geodesic equation of the free point mass is expressed by

$$\frac{dU^\alpha}{d\tau} + \Gamma^\alpha{}_{\mu\nu} U^\mu U^\nu = 0, \tag{1.23}$$

where U^α denotes the coordinate velocity of the mass. Then due to $h^{TT}_{\beta 0} = 0$, the initial acceleration of the mass is always 0:

$$\left(\frac{dU^\alpha}{d\tau}\right)_{\text{initial}} = -\Gamma^\alpha{}_{00} = \frac{1}{2}\eta^{\alpha\beta}(\partial_0 h_{\beta 0} + \partial_0 h_{0\beta} + \partial_\beta h_{00}) = 0. \tag{1.24}$$

This implies that if we choose the TT gauge, the basis changes so that the each mass stays at the original coordinate position.

Here we examine the behavior of the proper distance between two free point masses. If we set the masses at origin (0,0,0) and (L,0,0), the proper distance l is

$$\begin{aligned} l &= \int |ds^2|^{1/2} = \int |g_{\alpha\beta} dx^\alpha dx^\beta|^{1/2} \\ &= \int_0^L |g_{xx}|^{1/2} dx \simeq |g_{xx}(x=0)|^{1/2} \times L \\ &\simeq \{1 + \frac{1}{2} h^{\text{TT}}_{xx}(x=0)\} \times L, \end{aligned} \tag{1.25}$$

where $h^{\text{TT}}_{xx}(x=0)$ is a non-zero term. Thus the eq(1.24) and eq(1.25) implies that neither of the two masses move but the proper distance l is changed if a GW is injected. Consequently, we can sense the GWs by observing the proper distance(s) between two (or more) masses. In addition, according to eq(1.25), the length shift due to the GW injection ΔL is described by

$$\frac{\Delta L}{L} = \frac{1}{2} h, \tag{1.26}$$

where h is the spatial distortion in the measurement direction.

1.1.4 Emission of gravitational wave

Here we take a look at the GW emissions according to the linearized Einstein equation. First, we transform eq (1.8) using a Green's function for the d'Alembert operator $G(x^\sigma - y^\sigma)$:

$$G(x^\sigma - y^\sigma) = -\frac{1}{4\pi|\boldsymbol{x} - \boldsymbol{y}|} \delta\left(|\boldsymbol{x} - \boldsymbol{y}| - (x^0 - y^0)\right) \theta(x^0 - y^0), \tag{1.27}$$

$$\Box G(x^\sigma - y^\sigma) = \delta^{(4)}(x^\sigma - y^\sigma) \tag{1.28}$$

where $\sigma = 0, 1, 2, 3$, $\delta(x)$ and $\theta(x)$ denote Dirac's δ function and a step function respectively. We also assume that $\boldsymbol{x}$ and $\boldsymbol{y}$ are the observing location and the source position respectively. Hence the distance between $\boldsymbol{x}$ and $\boldsymbol{y}$ is $|\boldsymbol{x} - \boldsymbol{y}| = \{\delta_{ij}(x^i - y^i)(x^j - y^j)\}^{1/2}$. Note that $\theta(x^0 - y^0)$ is equal to 1 where $x^0 > y^0$ is satisfied, otherwise it equals to 0. With this setting, $\bar{h}_{\mu\nu}$ is expressed as below by using eq (1.8), eq (1.27) and eq (1.28), if we assume that the observation point is far enough away compared to the size of the source, that is, $r \equiv |\boldsymbol{x}| \gg |\boldsymbol{y}|$:

$$\begin{aligned} \bar{h}_{\mu\nu}(t, \boldsymbol{x}) &= -\frac{16\pi G}{c^4} \int G(x^\sigma - y^\sigma) T_{\mu\nu}(y^\sigma) d^4y \\ &= \frac{4G}{c^4} \int \frac{T_{\mu\nu}(ct - |\boldsymbol{x} - \boldsymbol{y}|, \boldsymbol{y})}{|\boldsymbol{x} - \boldsymbol{y}|} d^3y, \\ &\simeq \frac{4G}{rc^4} \int T_{\mu\nu}(ct - r, \boldsymbol{y}) d^3y. \end{aligned} \tag{1.29}$$

For the next step, here we consider the local energy-momentum conservation, i.e., $\partial_\nu T^{\mu\nu} = 0$. Under this condition, we obtain the relationship $\partial_\alpha \partial_\beta (T^{\alpha\beta} x^\mu x^\nu) = 2T^{\mu\nu}$ and the integration below:

$$\int T^{ij} d^3y = \frac{1}{2c^2} \frac{d^2}{dt^2} \int T^{00} y^i y^j d^3y = \frac{1}{2} \frac{d^2}{dt^2} \int \rho y^i y^j d^3y. \tag{1.30}$$

Then if we define a quadrupole mass distribution I_{ij} as:

$$I_{ij} \equiv \int \rho y^i y^j d^3y, \tag{1.31}$$

$\bar{h}_{ij}$ is given by eq (1.32), From eq (1.29):

$$\bar{h}_{ij}(t, \boldsymbol{x}) = \frac{2G}{rc^4} \ddot{I}_{ij}(ct - r). \tag{1.32}$$

In this expression, we find that the amplitude of a GW is proportional to the second derivative of the quadrupole with respect to time. Here, if we consider the TT gauge, eq (1.32) becomes

$$\begin{aligned} &\bar{h}^{\mathrm{TT}}_{ij}(t, \boldsymbol{x}) = \frac{2G}{rc^4} \ddot{\mathit{I}}_{ij}(ct - r), \\ &\text{where } \bar{h}^{\mathrm{TT}}_{ij} = \left(P_i{}^k P_j{}^l - \frac{1}{2} P_{ij} P^{kl} \right) \bar{h}_{kl}, \quad P_j{}^i \equiv \delta_j{}^i - n^i n_j \ , \ n^i \equiv x^i / r, \\ &\mathit{I}_{ij} \equiv \int \rho \left(x^i x^j - \frac{1}{3} \delta_{ij} r^2 \right) d^3x. \end{aligned} \tag{1.33}$$

In summary, GWs are generated when the quadrupole moment changes with time.

A typical luminosity of a GW is approximately summarized here using a formula is given by:

$$\frac{dE_{\rm GW}}{dt} = \frac{G}{5c^5} \langle \dddot{I}^{ij} \dddot{I}_{ij} \rangle. \tag{1.34}$$

If the source is characterized by mass M, size R, emitting time duration T and the velocity $v = R/T$, eq (1.34) becomes

$$\begin{aligned} \frac{dE_{\rm GW}}{dt} &\sim \frac{G}{c^5}\left(\frac{MR^2}{T^3}\right)^2 \sim \frac{c^5}{G}\left(\frac{GM}{Rc^2}\right)^2\left(\frac{v}{c}\right)^6 \\ &\sim 3.6\times 10^{59}[\mathrm{erg/s}]\left(\frac{GM}{Rc^2}\right)^2\left(\frac{v}{c}\right)^6 \\ &\sim 1.0\times 10^{26}\times L_\odot\left(\frac{r_s}{2R}\right)^2\left(\frac{v}{c}\right)^6, \end{aligned} \tag{1.35}$$

where r_s denotes the Schwarzschild radius $2GM/c^2$. Moreover, if the virial theorem ($Mv^2 \sim GM^2/R$) is available in this system, eq (1.35) becomes

$$\frac{dE_{\rm GW}}{dt} \sim 1.0\times 10^{58}[\mathrm{erg/s}]\left(\frac{r_s}{R}\right)^5 \sim 2.6\times 10^{25}\times L_\odot\left(\frac{r_s}{R}\right)^5. \tag{1.36}$$

More particularly, if we consider two equal-mass objects which follow Kepler's law, the luminosity is expressed as the following assuming that $2GM \sim (2\pi/T)^2R^3$ is available,

$$\frac{dE_{\rm GW}}{dt} \sim 1.2\times 10^5\times L_\odot\left(\frac{1\mathrm{s}}{T}\right)^{10/3}\left(\frac{M}{M_\odot}\right)^{10/3}. \tag{1.37}$$

We then have the luminosity about 1.2 $L_\odot$ when these parameters are to set $T = 1$ s, $M = M_\odot$. This implies that detectable GWs come not from events on the earth but from violent celestial events.

Approximate estimation: GW from coalescing binary

Based on the above, we briefly check the typical properties of GWs such as amplitude and frequency. We consider a system composed by two point-particles in a plane in uniform circular motion with the newton's gravitational force as shown in Figure 1.2. The masses are m_1 and m_2 respectively, and Ω is the angular frequency of the uniform circular motion. In this estimation, we assume that we can neglect the tidal force compared to the gravitational force in the system. In this setting, we obtain the positions of the two particles in the center-of-mass system as:

$$\boldsymbol{r}_1 = \left(\frac{m_2}{M}\, a\, \cos(\Omega t+\Phi)\ ,\ \frac{m_2}{M}\, a\, \sin(\Omega t+\Phi)\right), \tag{1.38}$$

$$\boldsymbol{r}_2 = \left(-\frac{m_1}{M}\, a\, \cos(\Omega t+\Phi)\ ,\ -\frac{m_1}{M}\, a\, \sin(\Omega t+\Phi)\right). \tag{1.39}$$

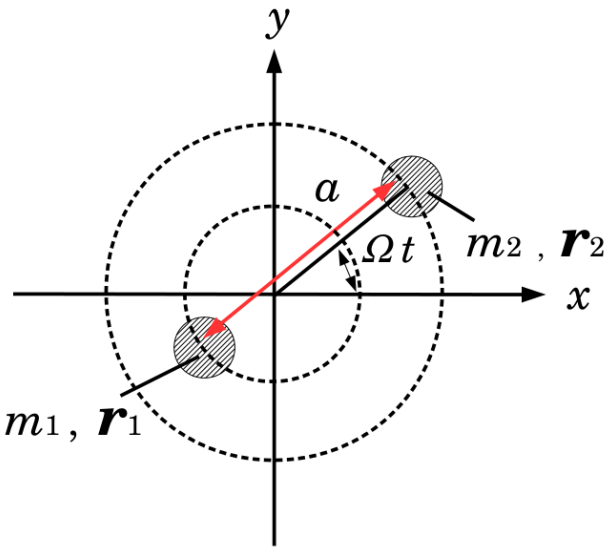

Figure 1.2: A binary system composed by two point-particles in a plane in uniform circular motion with the newton's gravitational force.

In the above, the quantities are defined as follows: gravitational constant G, the distance between the two particles a and total mass $M(= m_1 + m_2)$, respectively.

In this system, by following eq (1.32), the amplitudes of GW of the *plus*- and *cross*-mode h_+, $h_\times$ are described by:

$$h_+ = -\frac{2}{ra}\frac{Gm_1}{c^2}\frac{Gm_2}{c^2}\cos\left(2\Omega t_{ret} - 2\phi + 2\Phi\right)\left(\cos^2\theta + 1\right), \tag{1.40}$$

$$h_\times = -\frac{2}{ra}\frac{Gm_1}{c^2}\frac{Gm_2}{c^2}\sin\left(2\Omega t_{ret} - 2\phi + 2\Phi\right)\,2\cos\theta, \tag{1.41}$$

where t_{ret} is defined by $t_{ret} = t - r/c$. For this calculation, we assume that the the observation point is at the origin of the coordinate, and the binary system is at (r, θ, ϕ). Since we assume that the tidal force is negligible compare to the gravitational force, the frequency of the GWs $f_{\rm GW}$ from this system is given by:

$$f_{\rm GW} = 2\Omega = \frac{1}{\pi}\sqrt{\frac{GM}{a^3}} = \frac{1}{\pi}\sqrt{\frac{G(m_1+m_2)}{(R_1+R_2)^3}}. \tag{1.42}$$

We then think the time evolution. Since the energy of the system is decreased by the emission of GW, their orbital distances decrease, and this causes the frequency of the GWs to increase until the moment of coalescence. By assuming that GW takes away the energy of the system, we obtain the following about the orbital radius a:

$$\dot{a} = -\frac{64}{5}\frac{G^3 m_1 m_2 M}{c^5}\frac{1}{a^3} \equiv -K\frac{1}{a^3}. \tag{1.43}$$

By choosing the initial condition as $a(t_{ret} = t_0) = 0$, the time evolution of a is written as $a = [4K(t_0 - t_{ret})]^{1/4}$. From eq (1.42) and eq (1.43), the derivative of the frequency of GW is also written as:

$$\dot{f}_{\rm GW} = \frac{96}{5}\pi^{8/3}\left(\frac{GM_c}{c^3}\right)^{5/3} f_{\rm GW}^{11/3}, \tag{1.44}$$

where $M_c = (m_1 m_2)^{3/5}/M^{1/5}$, which is so-called chirp mass. We then obtain the followings as the time evolution of the frequency $f_{\rm GW}$ and the strain amplitude $h_+,\ h_\times$:

$$f_{\rm GW}(\tau) \sim 135\ {\rm Hz}\left(\frac{M_c}{1.2M_\odot}\right)^{5/8}\left(\frac{\tau}{1{\rm s}}\right)^{-3/8} \tag{1.45}$$

$$h(\tau) \sim 2.1\times 10^{-23}\left(\frac{M_{\rm chirp}}{1.2M_\odot}\right)^{5/3}\left(\frac{r}{200{\rm Mpc}}\right)^{-1}\left(\frac{\tau}{1{\rm s}}\right)^{-1/4}, \tag{1.46}$$

where τ is $t_0 - t_{ret}$, the time to coalescence. Figure 1.3 and 1.4 summarizes the time evolution of h_+, a and $f_{\rm GW}$, assuming a binary system composed by two point masses at 100 Mpc away whose masses are $1.4M_\odot$. A condition $\theta = \pi/2$, $\phi = 0$ is also assumed. For this example case, in order to get a GW amplitude larger than 10^{-21} in stain, we have to wait until about 20 sec before the collision. At that time the separation of the two objects is about 250 km based on eq (1.44). As in later section, with current sensitivities of the GW detectors, we would oftenly see the final scene of the coalescence.

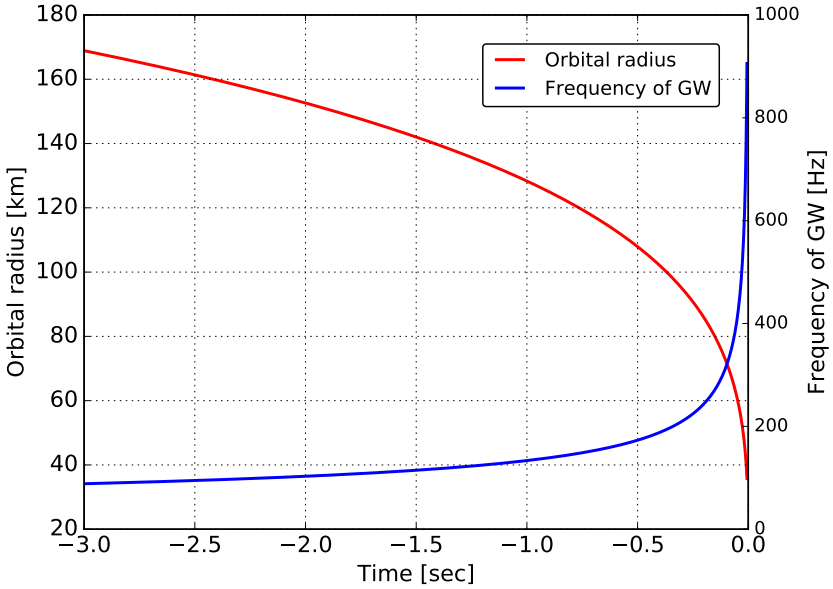

Figure 1.3: Final 3 sec time evolution of the orbital radius a and the frequency of GW $f_{\rm GW}$, assuming a binary system composed by two neutron stars at 100 Mpc away whose masses are $1.4M_{\odot}$.

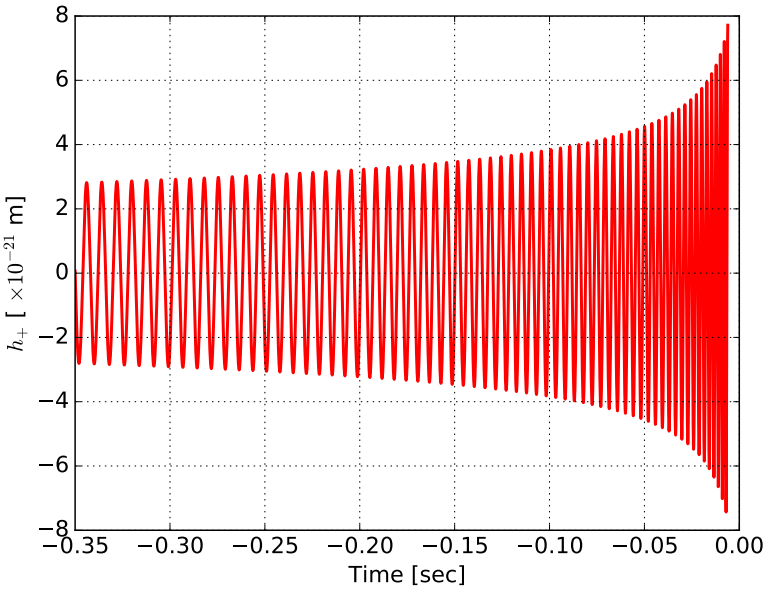

Figure 1.4: Final 0.35 sec time evolution of the strain amplitude of GW h_+, assuming a binary system composed by two neutron stars at 100 Mpc away whose masses are $1.4M_{\odot}$. The final 0.35 sec is drawn.

1.2 Expected astrophysical sources

As examined in section 1.1.4, the expected amplitude of GWs are quite small. On the other hand, compact binary coalescence (CBC) is the most interesting sources of GWs, and indeed the detected GW signals were from the merger of compact objects such as BNS, BBH and NS-BH [6, 9, 10]. In this subsection, the interesting/promising sources of GWs and the astrophysical motivations are briefly described.

1.2.1 Compact binary coalescence

As described in section 1.1.4, merger of compact objects such as BNS, BBH and NS-BH generates GWs and are one of the target sources for the current GW detectors.

By using the GW signals from CBC, we can test GR under strong gravity condition, for example by using polarization of GW [11]. In addition, we can measure Hubble constant [12] independently from the ordinal methods based on type Ia supernovae observation [13] and the method using cosmic microwave background observation [14].

In addition, using the GW signals from BNS merger events, we can investigate the mechanism of the kilonovae and its nucleosynthesis [15] more precisely. The equation of state inside NSs can be also investigated with the signals from BNS merger [16, 17].

1.2.2 Supernovae

Core-collapse supernovae (SNe) are considered as a promising source. The explosion will accelerates an huge amount of mass dramatically in a short period asymmetrically, and it will generate GWs. The prediction of the actual wave forms emitted from supernovae is challenging, however, based on progress in the field of numerical relativity, the estimation of GWs from core-collapse SNe are being progressed [18, 19]. If we achieve the detection of the GW signal from such SNe events, we can test the mechanism of the explosion mechanism.

1.2.3 Stochastic background

A stochastic background of GWs is expected from numerous unresolved astrophysical sources such as white dwarf binaries, cosmological origins such as inflation, phase transition in the early universe and cosmic strings [20]. The amplitude and the frequency of the GWs with cosmological origins depends on the theory considered. Detection of stochastic backgrounds is generally conducted by investigating cross-correlation between observations by several detectors.

1.3 Detection with interferometer

This section describes how to detect the GWs with laser interferometric technique.

1.3.1 Basic principle

according to the polarization mentioned in section 1.1.3, We need to monitor the differential displacements of two masses in orthogonal directions. For detection of GWs, the simplest interferometric configuration would be a Michelson interferometer built with suspended mirrors as shown in Figure 1.5. As the result of interference, a fraction of the beam goes to the photodiode and the remainder goes back to the laser source. The output beam intensity at the photodiode P_{out} is then given by

$$P_{\text{out}} = \frac{1}{2} P_0 \left(1 - \cos \delta\phi\right), \tag{1.47}$$

where P_0, λ, and $\delta\phi = 2\pi(L_x - L_y)/\lambda$ represent the incident laser power, the wavelength of the laser beam, and the phase difference between the two optical paths, respectively. Consequently, We can obtain information about the phase shift by monitoring the beam intensity on the photodiode.

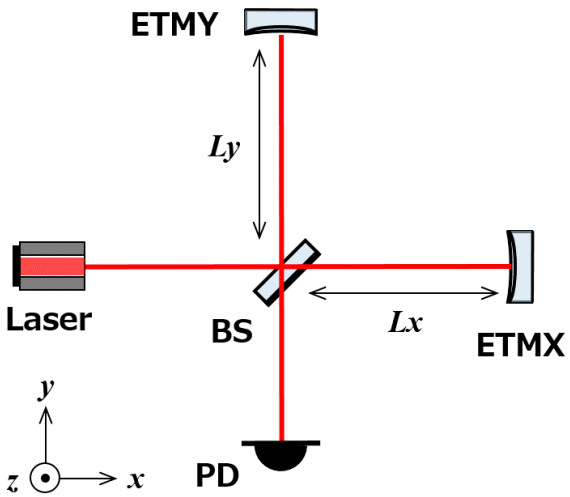

Figure 1.5: An optical configuration of a Michelson interferometer. ETMX(Y), BS, PD denote the end mirrors at X(Y) end, the beam splitter, and photodetector, respectively.

We then calculate how the GW affects to the phase difference between the two optical paths $\delta\phi$. we suppose that a GW which has plus polarization and amplitude $h(t)$ is injected along the $+z$ direction. If we consider that one of the

photons comprised by the laser beam in the x direction, from eq (1.17) and this configuration, the line element ds^2 of the photon is given by

$$\frac{dx}{dt} = \frac{c}{\sqrt{1+h_+(t)}}, \tag{1.48}$$

by using $dy = dz = ds^2 = 0$. The round trip time Δt_1 of a photon between the beam splitter and one end mirror is given by:

$$\int_t^{t+\Delta t_1} \frac{dt'}{\sqrt{1+h_+(t')}} = \frac{2l_1}{c}. \tag{1.49}$$

If we use $(1+h)^{-1/2} \sim (1-h/2)$ by assuming $|h_+| \ll 1$, the above equation becomes

$$\Delta t_1 = \frac{2l_1}{c} + \frac{1}{2}\int_t^{t+\Delta t_1} h_+(t')\, dt'. \tag{1.50}$$

Since the first term is larger compared to the second term due to $|h_+| \ll 1$ on the right hand side, we can set the integral upper limit at $t + 2l_1/c$. Consequently, the phase shift ϕ_1 due to Δt_1 is written by

$$\phi_1 = \frac{2\pi c}{\lambda}\left(\frac{2L_x}{c} + \frac{1}{2}\int_t^{t+2L_x/c} h_+(t')\, dt'\right), \tag{1.51}$$

where λ is the wavelength of the laser. In the same way, the phase shift ϕ_2 for the other axis is given by:

$$\phi_2 = \frac{2\pi c}{\lambda}\left(\frac{2L_y}{c} - \frac{1}{2}\int_t^{t+2L_y/c} h_+(t')\, dt'\right). \tag{1.52}$$

By using ϕ_1 and ϕ_2, the phase difference $\Delta\phi = \phi_1 - \phi_2$ of the two optical paths is

$$\begin{aligned}\Delta\phi &= \frac{4\pi}{\lambda}(L_x - L_y) \\ &+ \frac{2\pi c}{\lambda}\left(\frac{1}{2}\int_t^{t+2L_x/c} h_+(t')\, dt' + \frac{1}{2}\int_t^{t+2L_y/c} h_+(t')\, dt'\right).\end{aligned} \tag{1.53}$$

The first term is the phase shift due to the arm length shift, while the second term is the shift due to the GW transient. By assuming that $L_x \sim L_y = L$ for simplicity, the phase shift due to the GW (the second term) $\delta\phi_{\rm GW}$ is written by

$$\delta\phi_{\rm GW}(t) = \frac{2\pi c}{\lambda}\left(\int_t^{t+2L/c} h_+(t')\, dt'\right). \tag{1.54}$$

In a case where the change of $h_+(t)$ is slow enough, $\delta\phi_{\rm GW}(t) = 4\pi h_+ L/\lambda$. The frequency response of the Michelson interferometer to GWs, $H_{\rm MI}(\omega)$, is given by following equation by using the Fourier transform:

$$H_{\rm MI}(\omega) = \frac{\tilde{\phi}_{\rm GW}(\omega)}{\tilde{h}_{\rm GW}(\omega)} = \frac{4\pi c}{\lambda} \exp\left(-i\omega L/c\right) \frac{\sin(\omega L/c)}{\omega l/c}. \tag{1.55}$$

where ω is an angular frequency of a GW. This equation implies that the response $|H_{\rm MI}|$ is maximized at

$$L = \frac{\pi c}{2\omega} = \frac{c}{4f_{\rm GW}}. \tag{1.56}$$

By following (1.55), ideally the optimal arm length for a GW of 250 Hz becomes 300 km, for example. Even though to construct a Michelson interferometer with large arm is one solution to increase a phase shift caused by GW transient, we cannot construct such a large-scale interferometer on the Earth. Thus some techniques to expand effective arm lengths are necessary for further sensitivity improvement.

1.3.2 Fabry-Perot cavity

One option to expand the effective optical path lengths is to Fabry-Perot cavities, in which the light is reflected multiple times while keeping the optical paths aligned. The light incident into the cavity is reflected many times between the mirrors. The optical configurations is illustrated in Figure 1.6. The frequency response of a Fabry-Perot Michelson interferometer (FPMI) to gravitational waves is given by

$$H_{\rm FPMI}(\omega) \;=\; \frac{4\pi L\alpha}{\lambda} \frac{\exp\left(-i\omega L/c\right)}{1 - r_F r_E \exp(-2i\omega L/c)} \frac{\sin(\omega L/c)}{\omega L/c}, \tag{1.57}$$

when the two Fabry-Perot cavities are in resonance condition [21]. α is given by

$$\alpha = \frac{t_F^2 r_E}{1 - r_F r_E}, \tag{1.58}$$

where r_F and r_E denote the amplitude reflectivity of the front and end mirrors, and t_F represents the transmissivity of the front mirror. The bounce number in a Fabry-Perot cavity N is given by

$$N = \frac{2\sqrt{r_F r_E}}{1 - r_F r_E} = \frac{2\mathcal{F}}{\pi}. \tag{1.59}$$

Here $\mathcal{F}$ denotes the sharpness of the resonance of the Fabry-Perot cavity and is called the finesse.

The amplitudes of the frequency responses $H_{\rm MI}$ and $H_{\rm FPMI}$ are shown in Figure 1.7 assuming that the arm lengths are set to 3 km in all cases, and that The finesse $\mathcal{F}$ is set at 80 for FPMI.

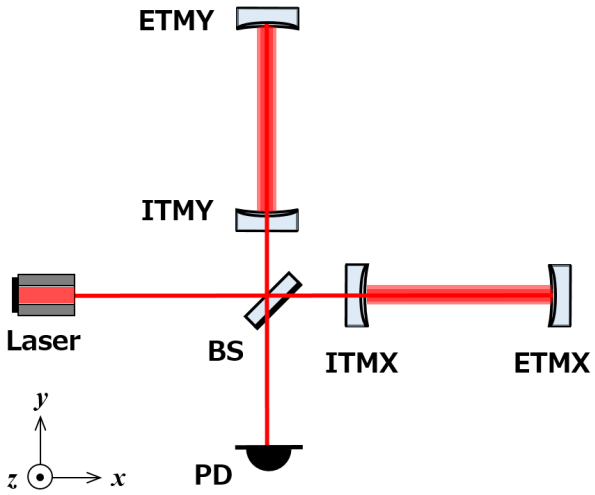

Figure 1.6: An optical configuration of a Fabry-Perot Michelson interferometer (FPMI). The input mirrors labeled ITMX(Y) are added to the configuration in Figure 1.5.

1.3.3 Fundamental noise sources

In a laser interferometric ground-based GW detectors, we have the following noise sources which fundamentally or possibly limit its sensitivity. The sensitivity of the detector is fundamentally limited by the seismic noise, thermal noise and shot noise. The other noise sources are the candidates possibly limit the sensitivity.

Seismic noise

At the low frequency, the sensitivity of a ground-based detector critically depends on vibrations of the optics induced by the seismic vibration. This is called seismic noise. In order to detect GWs with the ground-based detectors, the seismic motion have to be suppressed typically by 10^{-8} to 10^{-10} at 10 Hz. The seismic noise at higher than about 0.1 Hz is attenuated by using vibration isolation systems based on pendulum systems and springs. The seismic noise at lower frequency than about 0.1 Hz, which is related to the tidal morion of the ground for example, is compensated by using the strain signal sensed by the interferometer or geophysical interferometer developed in [22].

Thermal noise

Since the mirror and the suspension system are in thermal baths and receive energy from their surroundings, a random energy flow to and from the thermal baths can happen, and this causes a fluctuation of the optical paths of the interferometer. This noise is called thermal noise. In the field of GW detection,

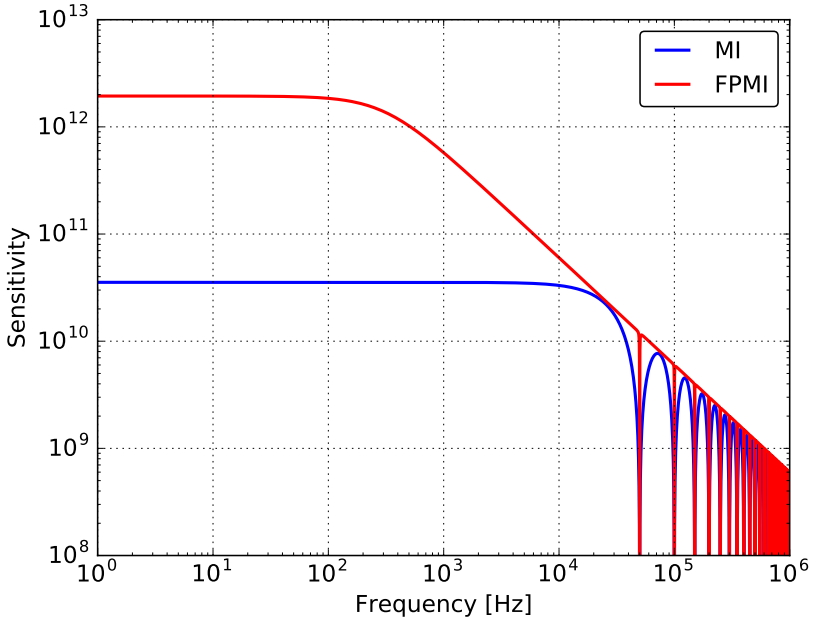

Figure 1.7: Amplitudes of the frequency responses H_{MI} and H_{FPMI} with 3 km arm length. MI and FPMI denotes Michelson interferometer and Fabry-Perot Michelson interferometer, respectively. The finesse $\mathcal{F}$ is set at 80 for FPMI. The wavelength of the laser is assumed the following: $\lambda = 1064$ nm.

thermal noise induced in mirror substrates is called mirror thermal noise, while the noise caused in the suspension systems is called suspension thermal noise. In order to suppress the impact from the thermal noise, fused silica is typically used for room-temperature mirror substrates [23], while sapphire is a good candidate for cryogenic temperature mirror substrates [24],[25].

Shot noise

A photodetector counts the number of photons and converts it into photocurrent. In the process, the number of photons counted, or the electrons composing the photocurrent, has a probability distribution, which results in fluctuations of the measured rate. The noise induced by this fluctuation is called shot noise. The shot noise is a fundamental noise in optical power sensing, associated with the quantum nature of light. This noise in length sensing caused by the probability distribution is proportional to $\sqrt{P_{\mathrm{in}}}$, where P_{in} is the incident power on the mirrors. While the signal amplitude of the gravitational wave is proportional to P_{in}, the signal to noise ratio is proportional to $1/\sqrt{P_{\mathrm{in}}}$. Consequently the shot noise can be reduced by increasing the power of the laser.

Newtonian noise

It is expected that we would find the direct coupling between the moving ground and the optics due to Newtonian gravitational attraction. This is called Newtonian noise. Since the vibration isolation system attenuates mainly its mechanical motion, this noise cannot be reduced by the suspension system. One option to reduce this noise is to place the interferometer underground where the optics are less affected by the gravity gradient field of surrounding rocks. Another option is to subtract the noise by calculating the gravity gradient from measurements of the ground motion surrounding the optics [26].

Laser noise

since an interferometric GW detector monitors the length between the mirrors using the wavelength of the laser as a reference, noise of a laser such as frequency and intensity fluctuation, can degrades the detector sensitivity. In order to minimize the impact of the intensity fluctuation, the interferometer is operated at a dark fringe, where the photo-detector receives no light in the absence of GW signals.

Residual gas noise

Random motions of molecules can cause fluctuation of the refraction index in the optical paths of an interferometer and this causes fluctuations of the effective arm lengths. This noise is called the residual gas noise. In order to suppress the impact of this noise, the GW detectors are operated in an ultrahigh vacuum condition.

1.3.4 Power recycling and resonant side-band extraction

For further improvement of the detector sensitivity, additional mirrors are added.

Power recycling

In order to reduce the shot noise, we want to increase the laser power. This is realised by putting a mirror at the incident-laser side. By reflecting the light which comes back from the Michelson interferometer to it again, the laser power at BS becomes increased. This technique is called power recycling, the added mirror is called power recycling mirror (PRM). The cavity composed of PRM and the Michelson interferometer with ITMX(Y) and BS is called power recycling (PR) cavity.

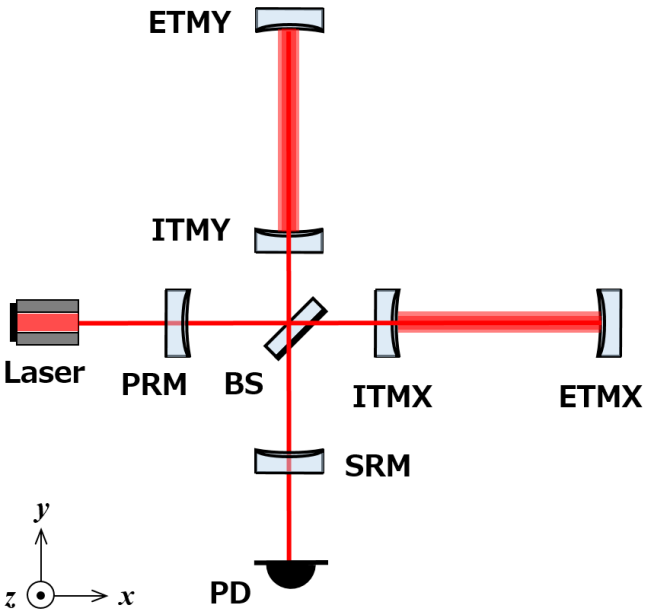

Figure 1.8: On optical configuration of Fabry-Perot Michelson interferometer with the power and signal recycling mirrors. The cavity composed of PRM and the Michelson interferometer with ITMX(Y) and BS is called power recycling (PR) cavity. On the other hand, the cavity composed of SRM and the Michelson interferometer with ITMX(Y) and BS is called signal recycling (SR) cavity.

Resonant side-band extraction

If the interferometer controls is done so that the Anti-Symmetric (AS) port[1], the common signal of the arm length signal would be found in the incident-laser side, while the differential signal is appeared in AS port. If a mirror is put at the AS port, and if a cavity composed of the newly added mirror, ITMX(Y) and BS, is kept in resonance, the finesse of the arm-cavities for the differential signal is decreased. By doing this, although the shot noise level at the lower frequency region is increased, at the higher frequency region, the shot noise level would be decreased. The added mirror is called signal recycling mirror (SRM) and the cavity composed of SRM and the Michelson interferometer with ITMX(Y) and BS is called signal recycling (SR) cavity.

These above techniques are used in the current ground-based GW detectors, and called dual recycling Fabry-Perot Michelson interferometer (DRFPMI). The schematic view of the optical configuration is shown in Figure 1.8.

[1]The port which is not incident-laser side of a Michelson interferometer.

1.3.5 Interferometer length sensing and lock acquisition

In order to detect GW signals, it is necessary to control cavity length variation to keep a condition where the cavities are resonated. For this purpose, it is required to sense the cavity length displacement. For length sensing of Fabry-Perot cavity, Pound-Drever-Hall (PDH) technique is adopted [27]. In PDH technique, the incident laser frequency (or amplitude) is modulated before entering a cavity, and then de-modulate the laser which is reflected by the cavity. From this process, we can obtain an error signal which has the information of the cavity length displacement. The error signal becomes proportional to the cavity length displacement only around the resonant point of the cavity. Thus it is necessary to trap and keep the mirror position at resonant point for the interferometer operation.

Conventionally the state where the mirrors are kept at positions where the cavity resonates is called *locked* state. The effective width of the linear range ΔL_{lin} for a cavity is obtained by

$$\Delta L_{\rm lin} = \frac{\lambda}{2\mathcal{F}}, \tag{1.60}$$

where $\mathcal{F}$ is the finesse of the cavity, and λ represents the wavelength of the laser. Typically the effective width is about order of nm, and the mirror displacement has to be kept within that range.

We acquire/keep the cavity lock by using an active control system with sensors and actuators. We actuate the mirrors based on a feedback control system. In order to start the observation, we need to lock all the cavities consists of DRFPMI. In the process to lock the cavities for the DRFPMI, we have to lock the X-arm and Y-arm cavities.

For the lock-acquisition of the X- and Y-arm cavities, KAGRA detector uses the green-lock scheme [28] for the guide as its first step. This method uses an auxiliary green laser which is the half wavelength of the main laser. This auxiliary laser has a resonance in the arm cavities with finesse of about 50. In this scheme, voltage controlled oscillators (VCOs), which are free from mechanical resonances of the suspensions, are adopted for the cavity length control. Using the VCOs, the control bandwidth can be set up to 10 kHz.

By using this technique, the linear regime of the cavity length is expanded. After the lock is acquired with the green laser, we lock the arm cavities with the main laser. This lock acquisition system with green laser enables more stable lock acquisition of the arm cavities with the main laser. In addition, we can obtain a looser requirement on the velocity for the arm cavity mirrors.

1.3.6 Calibration

GW signals can be found in mirror displacement signals, especially in the differential arm length variation signal, which is called DARM signal. DARM signal is calculated from interferometer control signal which is used for the mirror actuation to keep the interferometer locked. More concretely, the mirror displacement δx, which will have GW signals, is obtained by:

$$\delta x = \frac{G_{\rm act}}{G_{\rm inf}}\ \delta V_{\rm inf}, \tag{1.61}$$

where $\delta V_{\rm inf}$ is the interferometer control signal (in voltage). In this equation, $G_{\rm act}$ represents the transfer function from the actuator to the mirror displacement, while $G_{\rm inf}$ denotes the transfer function from the actuator to the interferometer control signal.

1.4 KAGRA detector

This subsection describes a GW detector and its property, using KAGRA detector as an example.

KAGRA is the fourth GW detector build in Japan [29], and it is being commissioned from 2019. KAGRA detector has been constructed in underground, and the main four mirrors are to be cooled down to about 20K. By using the underground environment and the cryogenic mirrors, it is planed to suppress the seismic noise contribution and the thermal noise contribution to the detector sensitivity.

Section 1.4.1 describes the optical design of KAGRA detector. Section 1.4.2 briefly summarizes the required mirror displacement for KAGRA detector in order to get GW signals. Section 1.4.3 shows the seismic motion at KAGRA site. This subsection briefly describes how much the seismic noise has to be attenuated. Section 1.4.4 briefly introduces the seismic attenuation systems in KAGRA detector.

1.4.1 Optical design

The optical layout is shown in Figure 1.9.The laser beam from the pre-stabilized laser source goes into the main interferometer part by passing through the input mode cleaner (IMC). The main interferometer consists of 3 km-length arm cavities, and is operated by using power recycling technique and the resonant side-band extraction. The arm-cavity mirrors are called TMs. In order to improve the spacial mode stability of the power- and the signal- recycling cavities, those recycling cavities are Z-shaped by inserting other two mirrors for each cavity. The PR cavity is composed by PRM, PR2, PR3 and the input test masses, called ITMs. On the other hand, the SR cavity consists of SRM, SR2, SR3 and ITMs. The output from the signal recycling cavity passes through the output mode cleaner (OMC) and is detected by a photo diode.

KAGRA has two observation modes called BRSE (broadband resonant side-band extraction) and DRSE (detuned resonant side-band extraction) [30]. These two modes can be switched by changing interferometer condition, depending on the target GW frequency.

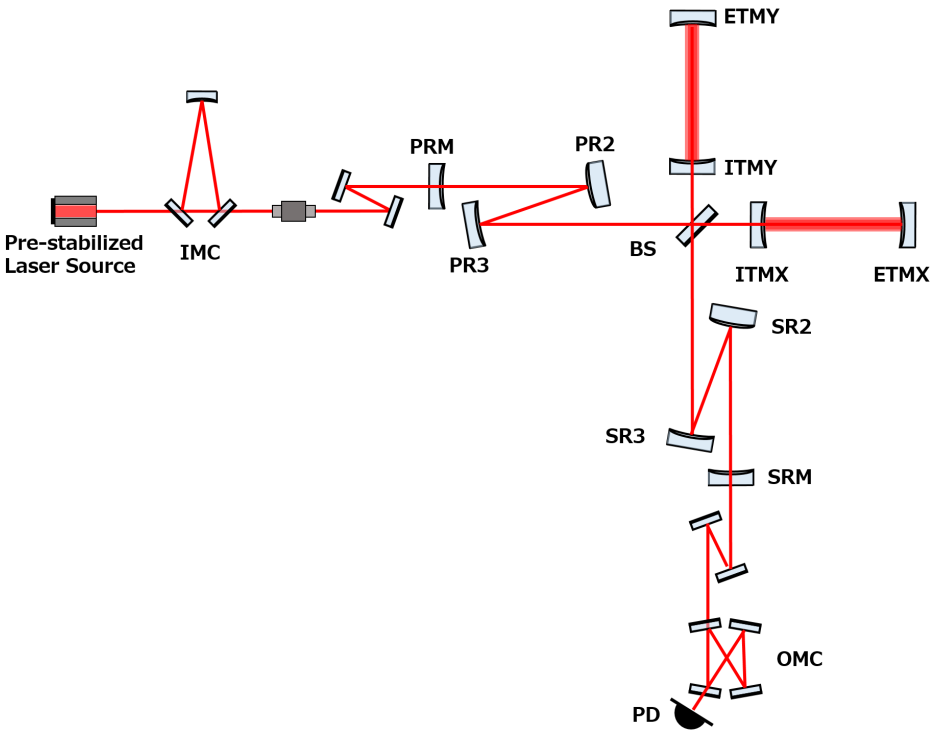

Figure 1.9: The Optical layout of KAGRA detector. IMC denotes input mode cleaner. PRM, PR2 and PR3 are power recycling mirrors, and SRM, SR2 and SR3 are the signal recycling mirrors. Test masses are located at ITMX, ITMY, ETMX and ETMY (Input/End Test Mass X/Y). BS is beam splitter. OMC and PD represent the output mode cleaner and photo diode respectively.

1.4.2 Displacement noise requirement

GW signal can be found in DARM signal, and thus the displacement of the four TMs have to be sufficiently suppressed. Indeed, not only the TM displacement, but also the displacement of the BS, PR mirrors and SR mirrors have to be suppressed since the displacements induced by those optics can couples to the detector sensitivity[31]. Figure 1.10 shows the required displacement level of the main interferometer mirrors in KAGRA. This plot includes a safety factor of 10. Table 1.1 summarizes the required displacement in spectral density at 10 Hz. The requirement for PR2 and PR3 (SR2 and SR3) are more strict compared to PRM (SRM) case by a factor of 2. This is due to a fact that those mirror displacement can change the optical path of the recycling cavities two times larger than PRM (SRM).

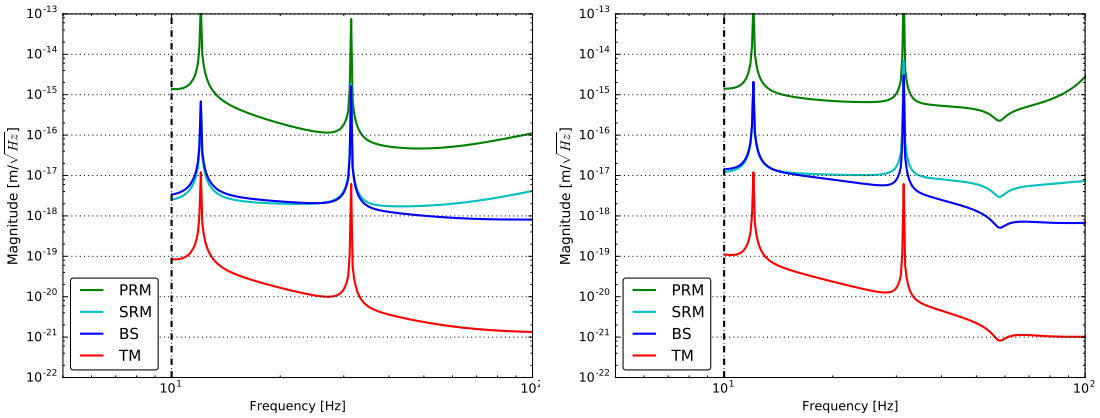

Figure 1.10: Requirement for displacement noise in BRSE detection mode ($left$) and DRSE detection mode ($right$).

Table 1.1: Requirements on longitudinal displacement noise of the core optics for the KAGRA detector.

Optic	Spectrum density at 10 Hz
PRM	1.5×10^{-15} m/$\sqrt{\text{Hz}}$
PR2,3	7.5×10^{-16} m/$\sqrt{\text{Hz}}$
SRM	2.5×10^{-18} m/$\sqrt{\text{Hz}}$
SR2,3	1.3×10^{-18} m/$\sqrt{\text{Hz}}$
BS	3.4×10^{-18} m/$\sqrt{\text{Hz}}$
TM	8.0×10^{-20} m/$\sqrt{\text{Hz}}$

1.4.3 Seismic motion at KAGRA

The ground vibrates continuously and randomly due to oceanic, atmospheric and human activities. The amplitude of the seismic vibration changes by a few orders of magnitude depending on the site and time, as well as on surrounding environment influences such as weather, industrial activities. The worldwide seismic background noise was investigated by J. Peterson [32]. He estimated typical seismic vibration based on data from a worldwide network of seismometers and constructed the high/low noise model, according to the upper and lower bounds of the measured power spectral densities. Figure 1.11 shows the spectra of ground motion of the high/low noise model, and that of KAGRA underground. The spectrum of seismic motion at the KAGRA site in the figure shows that from 1 year of measured seismic noise data [33]. The seismic noise was measured by Trillium120QA [34] at the 2nd floor in the X-end station in KAGRA underground (shown in Figure 1.9). The general key features of the seismic-motion spectrum are:

1. At low frequencies below 1 mHz, the amplitude increases due to the tidal deformation of the ground caused by the gravitational attraction from the sun and moon.

2. The peak measured at $0.1 \sim 0.5$ Hz is known as the microseismic peak and is mainly caused by oceanic wave activities. Thus the peak has a large magnitude along the coast while it is smaller in the middle of the continents [35].

3. At frequencies higher than ~ 1 Hz, the typical displacement amplitude spectra of the seismic motions is given by

$$\tilde{x}_{\mathrm{seismic}}(f) \;=\; A \times \left(\frac{f}{1\ \mathrm{Hz}}\right)^{-2} \ \mathrm{m}/\sqrt{\mathrm{Hz}}, \tag{1.62}$$

   The factor A is a constant which depends on sites and is typically about $10^{-9} \sim 10^{-6}$.

Based on the above, in GW detectors, the seismic vibration at frequencies of microseismic peak has an impact on stable interferometer operation by inducing optic vibration which is not coherent among the optics. To reduce this microseismic peak impact is one of the main purposes of the vibration isolation system for GW detectors. In addition, at frequencies lower than about 1 mHz, such low-frequency seismic motion have to be compensated for the GW observation (in order to keep the locked situation) since the test masses of ground-based detectors move differentially following to the ground [22]. However, this compensation cannot be done with vibration isolation system since the lowest resonant frequency of the system is typically about a few ten mHz. For this treatment, we need to have the interferometer signal or the strain meter signal.

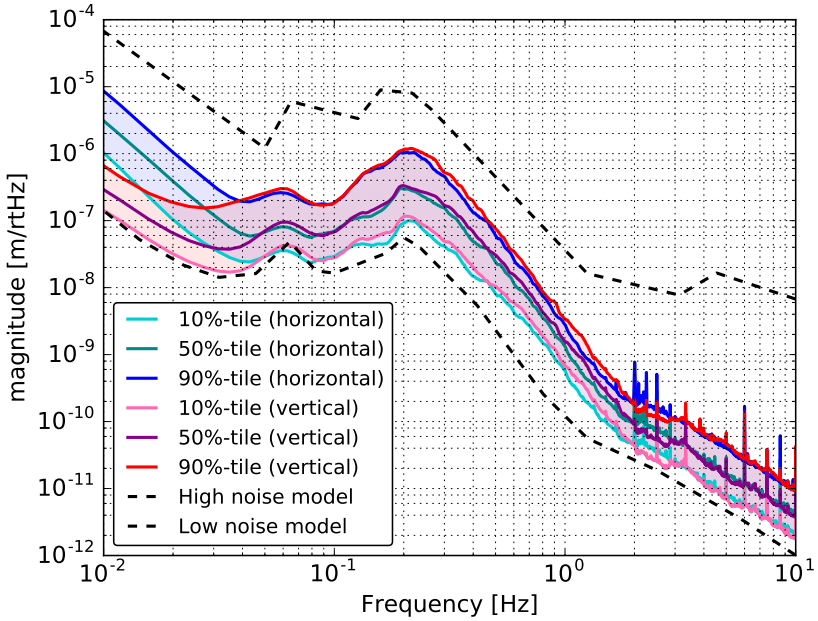

Figure 1.11: Spectrum of measured seismic motion at the KAGRA site in the stational state [33] (solid curves) and the worldwide seismic noise from J. Peterson's study [32] (dashed curves). The colored bands of the spectra of the KAGRA seismic motion denote the range between the 10 percentile to 90 percentile.

As other interests, it is known that, in the underground environment, the seismic vibration is reduced compared with that on the surface of the ground since the surrounding rocks tend to isolate the vibration from atmospheric and human activities on the surface [36]. This vibration mitigation due to the underground environment is effective above 1 Hz, where the atmospheric and human activities dominate. However the microseismic peak is not reduced much, since the origin of the microseismic peak is the motion which propagates through the continents.

Consequently, at around 10 Hz, the typical amplitude of the seismic vibration is larger than about 10^{-12} m$/\sqrt{\text{Hz}}$. On the other hand, the required arm-length fluctuation of the GW detectors is on the order of 10^{-20} m$/\sqrt{\text{Hz}}$. Based on that the displacement of the mirror caused by seismic vibration has to be attenuated by a factor of $10^{-10} \sim 10^{-8}$, for detection of GWs.

1.4.4 Seismic attenuation systems in KAGRA

In KAGRA detector, three types of SAS are installed depending on the required displacement noise level above 10 Hz as detailed in section 1.4.2. We called them Type-A, Type-B and Type-Bp suspension, and they are used for the following optics.

- Type-A: for four arm-cavity mirrors,
- Type-B: for three SR cavity mirrors and BS,
- Type-Bp: for three PR cavity mirrors.

The location of each suspension system and an overview of the three suspensions are shown in Figure 1.12 and Figure 1.13. This subsection briefly summarizes the mechanics of the assembled KAGRA SAS and their expected mirror displacement. More details about the KAGRA suspension systems is described in chapter 4.

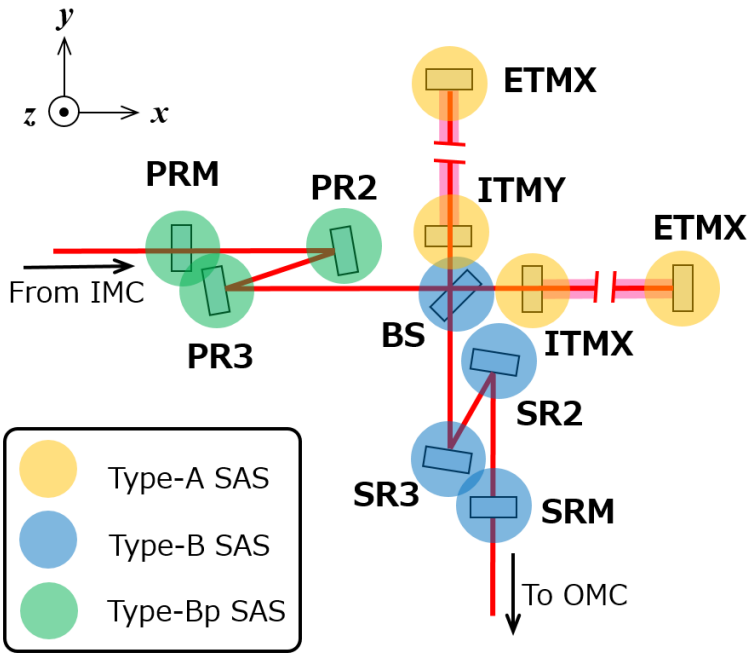

Figure 1.12: The Location and the type of suspensions in the KAGRA interferometer. PRM, PR2 and PR3 (the power recycling mirrors) are suspended by Type-Bp system, while SRM, SR2 and SR3 (the signal recycling mirrors) are suspended by Type-B system. The four TMs are suspended by Type-A system.

Figure 1.13: Overview of the suspension system for KAGRA detector. Type-A system is used for TMs, Type-B is for BS and SR mirrors, and Type-Bp system is used for PR mirrors. More details are described in chapter 4.

1.5 Second generation GW detectors

A network of GW detectors composed of km-scale laser interferometers, has been built over the world starting from the 90's. Present ground-based GW detectors are called second generation detectors since they follow a main upgade of initial laser interferometer GW detectors in years 2000's. In the coming years, it is expected that the sensitivities of these detectors will be progressively improved to achieve and then go beyond their design sensitivities.

In the U.S., two detectors called advanced LIGO[2] were built and their operation was started from 2015. The two detectors are located at Hanford, Washington and Livingston, Louisiana, and they have 4 km-length arm. In Europe, Advanced Virgo, which has 3 km-length arms, started the operation from 2017. These detectors have been operated for long periods interrupted by breaks to allow for upgrades and detector sensitivity improvements. The observation periods are called $O1$, $O2$ and $O3$. The first observation period $O1$ was done from September 12, 2015 to January 19 to 2016 with only the two LIGO detectors. The second observation $O2$ was started from November 30, 2016 and terminated to August 25 to 2017. At first, two LIGO detectors had been operating alone. Then Advanced Virgo joined the network in the final one month of the data taking. The third observation $O3$ has been started from April 1, 2019, and is planned to be finished on April 30, 2020.

Starting from 2012, the construction of the KAGRA detector started underground in the Kamioka mine in Japan. KAGRA is planned to join the detector network in the second half of the $O3$.

[2]Laser Interferometric Gravitational wave Observatory

1.6 Summary

This chapter briefly describes the general background of detection of GWs, especially about:

1. theoretical aspect of GWs and how they are generated (section 1.1),
2. expected astrophysical GW sources (section 1.2),
3. detection of GWs using interferometer (section 1.3),
4. a current GW detector using KAGRA as an example (section 1.4),
5. current GW detector network (section 1.5).

As introduced in the beginning of this chapter, the first detection of GW signal has been achieved in 2015. A natural step for the next is to start GW and multi-messenger astronomy. For this purpose GW observation in coincidence with electromagnetic (EM) signals is crucially demanded. This implies that an effective EM follow up observation plays an important role to start those new astronomy.

The next chapter start to focus on more details about the following topics, which are the key points of this thesis work:

1. EM follow up observation and current GW detectors,
2. EM follow up observation and the fourth detector KAGRA.

Chapter 2

Localization of coalescing binaries and vibration isolation

In order to conduct an effective EM follow up observation, it is important:

1. to localize the source position by GW detectors precisely and rapidly,
2. to have higher network duty cycle.

About the first point, it is demanded to localize the GW sources within a small region rapidly in order to observe EM transients more in detail.

For the second point, making the detector available time as long as possible allows us to have more chances to detect astrophysical phenomena. Since the mirrors of ground-based GW detectors are suspended by multi-stage pendulum systems, we have to damp the mechanical resonance of the suspensions as rapidly as possible, and also have to freeze the mirror position and its orientation in order to start GW observation. Due to this fact, realizing a system to deal with those issues for the suspension system truly plays an important role for a robust GW detector operation.

This thesis focuses on dealing with these listed two topics in the above (Especially I focus on KAGRA detector for the second part in following chapter). This chapter introduces the background of the two topics addressed in this thesis, namely:

1. localization of coalescing binaries with GW detectors,
2. low frequency vibration isolation system for GW detector.

After these introduction, this chapter summarizes the the target and outline of this thesis specifically.

Section 2.1 briefly summarize the principles at the basis of the sky localization of a compact coalescing binary by means of a network of GW detectors. Section 2.2 describes the basis of low frequency vibration isolation system adopted in GW detectors. This section explains the principle of the seismic attenuation

and that of suspension mechanical resonance damping and keeping mirror position/orientation. Section 2.3 summarizes the target and outline of this thesis work.

2.1 Localization of coalescing binaries

This subsection briefly describes the background of the localization of coalescing binaries by GW detectors. More details can be found in [8].

Section 2.1.1 explains the essence of the data analysis of the GWs from compact binary coalescence (CBC) which is based on the so-called matched filtering. Section 2.1.2 describes the antenna pattern of GW detectors. Section 2.1.3 describes the principle of source localization by means of triangulation. Section 2.1.4 summarizes the localization performance by the current GW detector network. This subsection includes the demanded area by the localization with GW detectors. Section 2.1.5 describes what is practically demanded on the fourth detector KAGRA in order to realize more effective EM follow up observation.

2.1.1 Matched filtering

Matched filtering is the analysis method commonly used in searching GW signals from CBCs. The matched filter compares the measured signal to the theoretical signal by taking into account the detector noise and it outputs the signal-to-noise ratio (SNR), $\rho(t)$ as a function of time t. For this purpose, the matched filtering needs theoretical wave forms corresponding to all the possible masses and the spins of the two compact objects. These wave forms are called templates.

We assume that the detector outputs as the function of time t are given as:

$$x(t) \;=\; s(t) \;+\; n(t), \tag{2.1}$$

where $s(t)$ is a GW signal and $n(t)$ is the detector noise. The SNR $\rho(t)$ is given by[1]:

$$\rho^2(t) \;=\; 4Re\left[\int_0^\infty \frac{\tilde{x}(f)\;\tilde{u}^*(f)}{S_n(f)}\;df\right], \tag{2.2}$$

where $S_n(f)$ is the one-sided noise power spectral sensitivity, $\tilde{x}(f)$ and $\tilde{u}(f)$ are the spectra of $x(t)$ and $u(t)$ respectively, and $u(t)$ is the wave form called template. As supplemental note, in this calculation, we assume that $S_n(f)$ meets the followings:

$$\langle \tilde{n}(f)\tilde{n^*}(f')\rangle \;=\; \frac{1}{2}\delta(f-f')S(f), \tag{2.3}$$

where angle $\langle ...\rangle$ denotes an ensemble average. $S(f)$ has dimension of Hz^{-1}, and satisfies $S(-f) = S(f)$. The factor of $1/2$ is inserted in the definition so that the

[1] technically we have other steps to reach $\rho(t)$. For more details, see [37]

total noise power is calculated by integrating over the range $0 \leq f < \infty$:

$$\langle n^2(t) \rangle \;=\; \int_0^\infty df S(f). \tag{2.4}$$

Consequently, the data sets which give higher SNR $\rho(t)$ than a SNR threshold, are to be searched. The maximum SNR above the threshold is called a trigger, and the corresponding event is considered as a candidate event. The generated triggers are then used to make the detection network by several detectors.

2.1.2 Antenna Patterns

As a starting point, we have to consider the angular dependence of the interferometer response to GWs. Let's assume that the source is located at the position (θ, ϕ), and that the source is rotated by ψ (usually called polarization angle). In this configuration, the amplitude of the GW signal $h(t)$ that the interferometer would detect becomes:

$$h(t) = F_+(\theta, \phi, \psi) h_+(t) + F_\times(\theta, \phi, \psi) h_\times(t), \tag{2.5}$$

where $h_+(t)$ and $h_\times(t)$ denote the amplitudes of the GW signal in the two polarizations. The terms F_+ and $F_\times$, in eq (2.5), are called antenna pattern functions, and describe how the two GW polarizations are combined by the detector angular response. In the coordinate system described above, the antenna pattern functions are given by

$$F_+(\theta, \phi, \psi) = \frac{1}{2}(1 + \cos^2\theta)\cos 2\phi \cos 2\psi - \cos\theta \sin 2\phi \sin 2\psi, \tag{2.6}$$

$$F_\times(\theta, \phi, \psi) = \frac{1}{2}(1 + \cos^2\theta)\cos 2\phi \sin 2\psi + \cos\theta \sin 2\phi \cos 2\psi. \tag{2.7}$$

The quadrature sums of the F_+ and $F_\times$ where $\psi = 0$, for each of the GW detectors introduced previously, are shown in Figure 2.1 and 2.2.

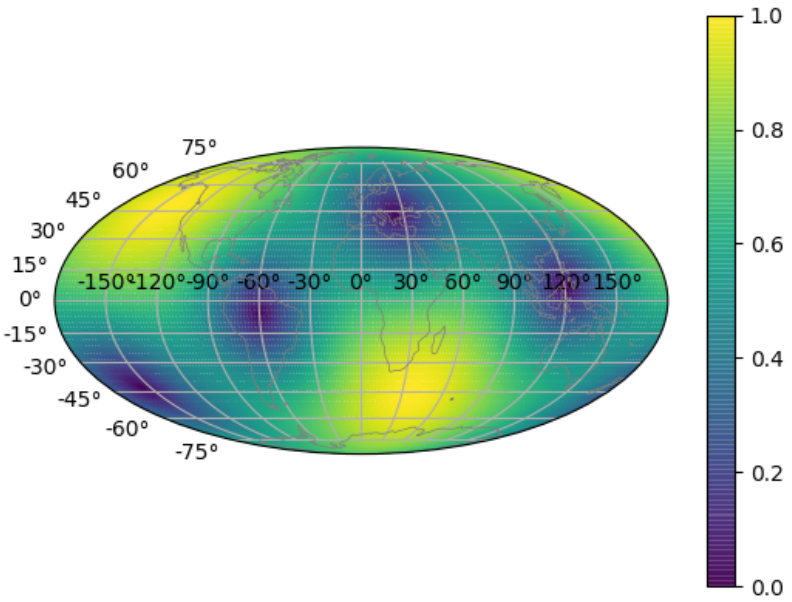

(a) Antenna pattern of LIGO Hanford detector

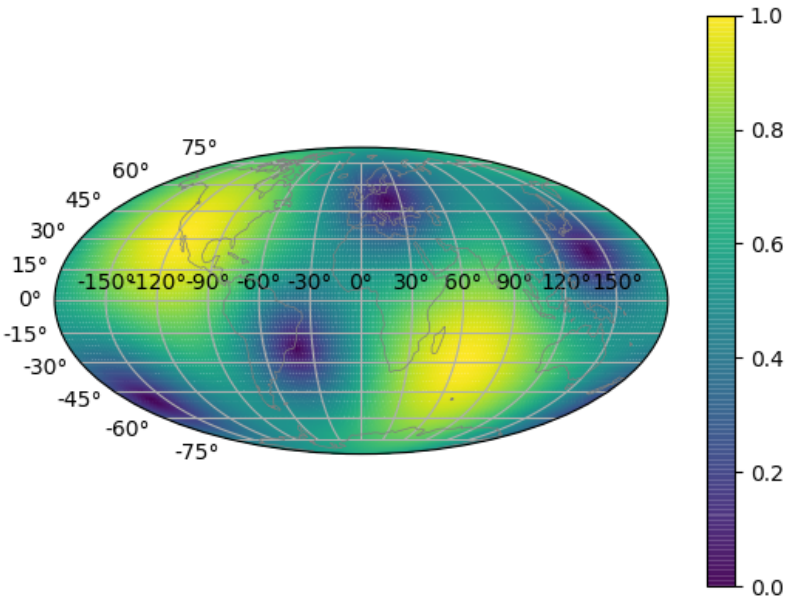

(b) Antenna pattern of LIGO Livingston detector

Figure 2.1: Projection of the antenna patterns of second generation detectors. The quadrature sums of the F_+ and $F_\times$ where $\psi = 0$, i.e, $\sqrt{F_+^2(\theta, \phi, \psi = 0) + F_\times^2(\theta, \phi, \psi = 0)}$ is projected.

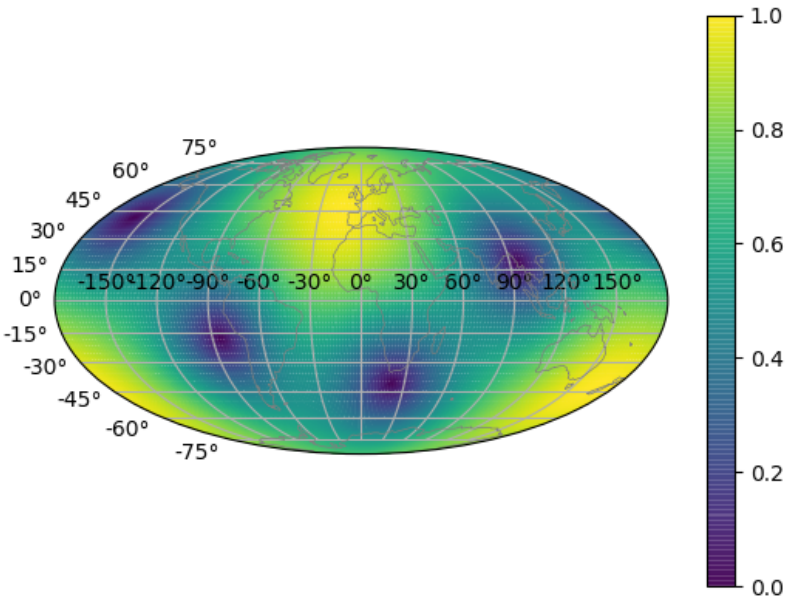

(a) Antenna pattern of Virgo detector

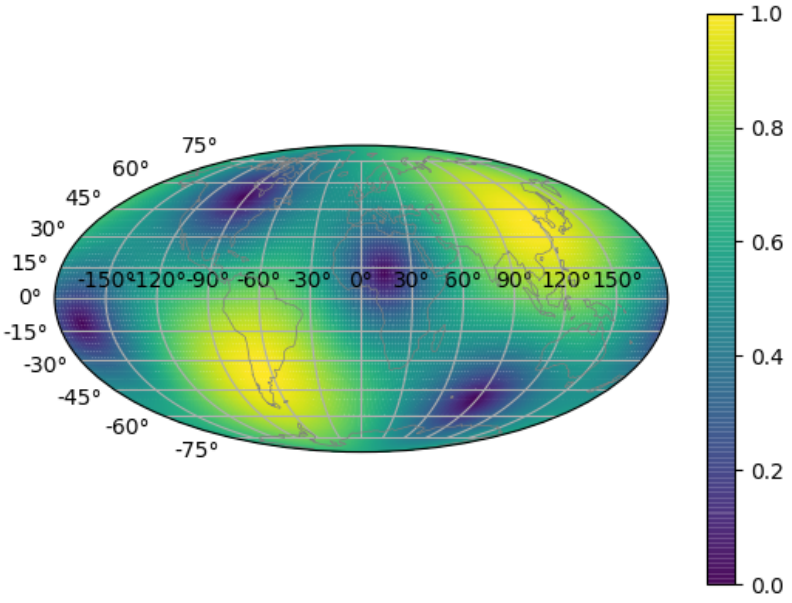

(b) Antenna pattern of KAGRA detector

Figure 2.2: Projection of the antenna patterns of second generation detectors. The quadrature sums of the F_+ and $F_\times$ where $\psi = 0$, i.e, $\sqrt{F_+^2(\theta, \phi, \psi = 0) + F_\times^2(\theta, \phi, \psi = 0)}$ is projected.

2.1.3 Source localization

The position of the source in the sky is localized by means of a triangulation based on the detection time delay at each detector. This is not only of astrophysical interest, but also essential for EM follow-up observation.

Following [38], a two-detector network will give the following distribution. Supposing that the source is located at position $\boldsymbol{R}$ on the unit sphere, and consider two detectors separated by a distance (expressed in light seconds) of $\boldsymbol{D}$, the difference in the time of arrival of the signal at the two sites is given by $(T_1 - T_2) = \boldsymbol{D} \cdot \boldsymbol{R}$. Then assuming that the two detectors have timing accuracies σ_1 and σ_2, and the observed times t_1 and t_2, the distribution of the reconstructed location $\boldsymbol{r}$ would be given by

$$p(\boldsymbol{r}|\boldsymbol{R}) \;\propto\; p(\boldsymbol{r}) \exp\left[-\frac{(\boldsymbol{D}\cdot(\boldsymbol{r}-\boldsymbol{R}))^2}{2(\sigma_1^2+\sigma_2^2)}\right]. \tag{2.8}$$

In the above,it is assumed that the measured time delay $(t_1 - t_2)$ is given by $\boldsymbol{D}\cdot\boldsymbol{r}$, and the timing accuracy of one detector is expressed as $\sigma \sim (2\pi\rho\sigma_f)^{-1}$, where ρ is observed SNR, and σ_f is the effective bandwidth of the signal in the detector which is calculated by $\sigma_f^2 = \overline{f^2} - \overline{f}^2$ with

$$\overline{f^n} \;=\; 4\int_0^\infty \mathrm{d}f \frac{|\tilde{h}(f)|^2}{S(f)} f^n. \tag{2.9}$$

The distribution by three-detector network can be given in a similar way by:

$$p(\boldsymbol{r}|\boldsymbol{R}) \;\propto\; p(\boldsymbol{r}) \exp\left[-\frac{1}{2}(\boldsymbol{r}-\boldsymbol{R})^T \boldsymbol{M} (\boldsymbol{r}-\boldsymbol{R})\right], \tag{2.10}$$

where the matrix $\boldsymbol{M}$ which describes the localization accuracy, is given by

$$\boldsymbol{M} = \frac{\boldsymbol{D}_{12}\boldsymbol{D}_{12}^T}{\sigma_{12}^2} + \frac{\boldsymbol{D}_{23}\boldsymbol{D}_{23}^T}{\sigma_{23}^2} + \frac{\boldsymbol{D}_{31}\boldsymbol{D}_{31}^T}{\sigma_{31}^2}. \tag{2.11}$$

In the above, the pairwise timing accuracy is given by $\sigma_{ij}^2 = \sigma_i^2 + \sigma_j^2 + \sigma_i^2\sigma_j^2/\sigma_k^2$, where $k \neq i, j$.

Two-detector network will give a ring-shape reconstructed region since it is only possible to restrict the location of the source in the direction parallel to the separation $\boldsymbol{D}$ between the detectors. In order to have a smaller reconstructed region, we need to have at least three detectors.

2.1.4 Multi-messenger observation

If a precise source position localization by GW detectors is achieved, we can start to observe astrophysical phenomena, such as supernova and BNS mergers with available EM telescopes more effectively. GW detection in coincidence with EM and neutrino detections will play an important role in the discovery and subsequent study of astrophysical phenomena.

Current localization performance and target

In the real life, however, the sky localization provided by GW detectors will be poor by optical telescope standards. With the advanced detectors in the coming years this localization is expected to be in the range of 100 deg^2. The actual size of the area in the sky corresponding to the alerts produced by the LIGO-Virgo network during the first half of $O3$[2] are summarized in Figure 2.3. The median values are about 1600 deg^2 for two LIGO detector network and about 950 deg^2 for LIGO-Virgo three detector network. During this period the detector sensitivities of advanced LIGO Hanford, LIGO Livingston and Advanced Virgo in terms of BNS range (defined as the maximum distance at which a BNS can be detected) were about 120 Mpc, 140Mpc and 45 Mpc respectively [39].

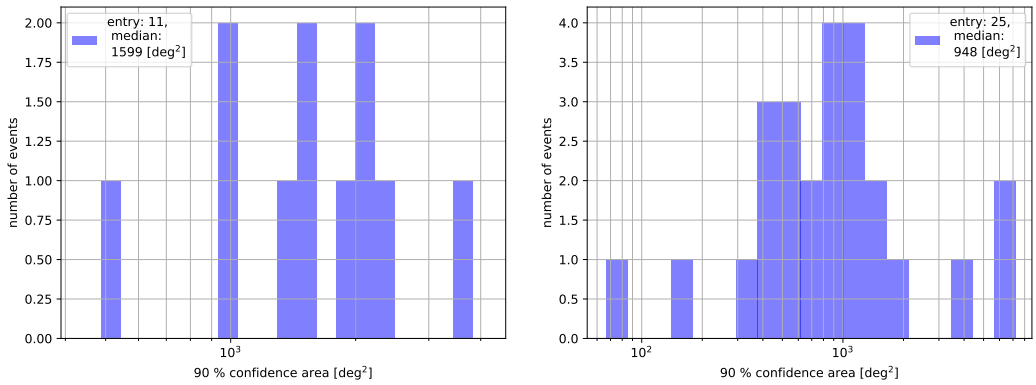

Figure 2.3: The size of 90 % confidence area which are alerted in the first half of $O3$, which is called $O3a$. The events detected by the two LIGO detector network ($left$) and the events by LIGO-Virgo three detector network ($right$) are included.

As an example, if we assume that we search for kilonovae [40] with BlackGEM telescope array, it will take 5 minutes to observe the area of 2.7 deg^2 [41]. while the luminosity of a kilonova decays in the time scale of days to weeks, it is very important to identify it as soon as possible so as to be able to observe its EM emmission rapidly after the merger. In order to e.g. complete the scan of the sky region given by GW detectors within one night (about 9 hours), it will be necessary that this region is smaller than about 300 deg^2. In order to achieve this localization area, it is indeed important to detect GW signals with several detectors at the same time. In addition, especially for the coming years, we also need EM telescopes that are able to quickly scan this relatively large area of the sky.

[2]The information is available from [10].

2.1.5 Fourth GW detector

As described in the above, in order to achieve a small localization area, it is demanded to detect GW signals with several detectors at the same time. More specifically, at least we need three detectors for the localization, otherwise we will have much large area which is totally not suitable for EM follow up observation.

Currently the GW network is composed of the three detectors by LIGO and Virgo detectors. However, sometimes these GW detectors are not operational due to interferomenter lock loss and/or maintenance operation. For example, assuming that all the detectors have an equal duty cycle of 80%, the duty cycle by three detectors in the three detector network would be about 51%. On the other hand, for a network made by four detectors, the duty cycle by three or four detectors becomes about 82%. Indeed the probability to have at least three detectors up and running increases considerably when a fourth detector is added to the network. This is a benefit of adding detectors to the network and reduces the chances to miss detectable events.

Based on this fact it is demanded that operating a fourth robust interferometer is of paramount importance to achieve high network duty cycle, namely, to conduct EM follow up observation more effectively.

For the purpose of robust interferometer operation, practically we need to take care the suspension system adopted in the forth detector KAGRA. More specifically it is necessary:

1. to damp the mechanical resonance of the suspensions as rapidly as possible,

2. to freeze the mirror position and its orientation.

2.2 Low frequency vibration isolation

This subsection introduces the background of vibration isolation system for GW detectors realized by pendulum-based suspension system.

As in section 1.3.3, the seismic noise is the one of the fundamental noises for the ground-based GW detectors. In addition, in order to detect GWs, we have to realize a situation where the test masses are in free-fall condition. To meet these constraints, we suspend the main optics with pendulum system called seismic attenuation system (SAS). This implies that it is necessary to take care of the mechanical resonances in order not to drastically decrease the duty cycle.

More specifically, seismic motion limits the detector sensitivity at low frequency by inducing mirror vibration. In order to detect GWs and to achieve the target sensitivity for KAGRA detectors, the seismic motion have to be suppressed typically by 10^{-8} to 10^{-10} at 10 Hz. This attenuation performance is realized by adopting multi-stage pendulum system. However, due to the use of such pendulum system, we need a system which damps mechanical resonances as soon as possible, and which enables to freeze the mirror motion, for the stable interferometer operation. This system is basically realized by using active control system in the GW detectors.

Section 2.2.1 describes the background of the passive vibration isolation. The passive vibration isolation is the most basic idea to realize the required seismic attenuation at above 10 Hz. Section 2.2.2 summarizes the physics and the basic technique used for the actual vibration isolation system for GW detectors. Section 2.2.3 describes the background of the active vibration isolation, which is used for the mechanical resonance damping, and for alignment of the suspended mirrors.

2.2.1 Passive vibration isolation

As described in the above, the seismic noise have to be attenuated by factor of 10^{-8} to 10^{-10} at 10 Hz. This attenuation is realized by using multi-stage pendulum in GW detectors. This subsection describes the physics of the pendulum system.

Harmonic oscillator

Isolating optics from ground motion is realized by using mechanical filters based on multi-stage pendulum system. For the simplest case, we here consider a single-pendulum system consisting of a mass m, and which is suspended by massless wire from a ceiling as in Figure 2.4. Its equation of motion is given by

$$m\ddot{x} = -\frac{mg}{l}\,(x - X), \tag{2.12}$$

where g denotes local gravitational acceleration, l is the length of the wire and x, X are the displacements of the payload and the suspension point respectively. Taking the Fourier transformation, the displacement transfer function from the ground to the mass becomes:

$$H(\omega) = \frac{\tilde{x}}{\tilde{X}} = \frac{{\omega_0}^2}{{\omega_0}^2 - \omega^2}, \tag{2.13}$$

where $\omega_0 = 2\pi f_0 = \sqrt{g/l}$ represents the resonant angular frequency of the suspension system. The transfer function of this system where the suspension wire length is set to 0.25 m and 1 m are shown in Figure 2.4 (*right*). This figure shows:

1. At low frequencies where $f \ll f_0$,
   The suspended mass follows the motion of the suspension point.

2. Near the resonant frequency, where $f \simeq f_0$,
   the amplitude of the transfer function increases substantially and goes to infinity at the resonant frequency.

3. At higher frequencies where $f \gg f_0$,
   The amplitude of the transfer function decreases in proportional to f^{-2}.

4. The lower the resonant frequency is, the more improved the attenuation performance at high frequencies is.

In a real life, however, the amplitude of a transfer function of an oscillator has finite amplitude at the resonant frequency affected by dissipation due to a residual gas damping and so on.

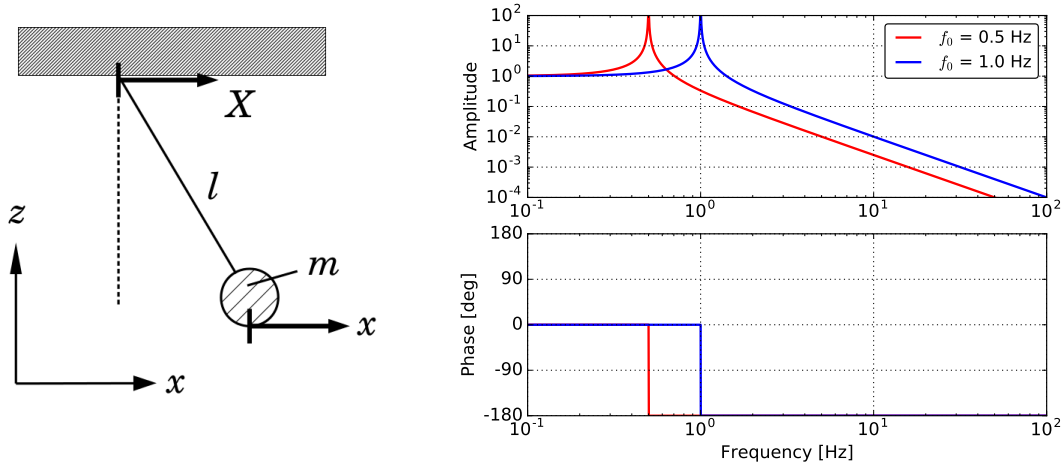

Figure 2.4: A single pendulum system (*left*) and its displacement transfer function (*right*) for the case where the length of the suspension wire is set to 1 m and 0.25 m (corresponding resonant frequencies are $f_0 = 0.5$ Hz, $f_0 = 1.0$ Hz respectively). The lower the resonant frequency is, the more improved the attenuation performance at high frequencies is.

In addition, the response of the mass when a external force is applied is obtained with eq (2.14) as eq (2.15).

$$m\ddot{x} = -\frac{mg}{l}\ (x - X)\ + F, \tag{2.14}$$

$$H_{\text{force}}(\omega) = \frac{\tilde{x}}{\tilde{F}} = \frac{1/m}{{\omega_0}^2 - \omega^2}. \tag{2.15}$$

This is called force transfer function in this work. The force transfer function is a useful tool to make a active control filter as in chapter 5.

As a figure of merit to estimate the effective amplitude of a oscillation, we use the root-mean square (RMS) amplitude. By using the oscillation in time domain $x(t)$, the RMS amplitude x_{RMS} is calculated:

$$x_{\text{RMS}}\ = \sqrt{\int_a^b d\omega\ S_x(\omega)}, \tag{2.16}$$

where $S_x(\omega)$ is the power spectrum density of $x(t)$. The frequency band of the integration is selected based on a frequency region of interest.

Multi-stage suspension

In a multi-stage pendulum system, the vibration isolation ratio of the N-th stage is proportional to f^{-2N} at a frequency higher than the resonant frequencies of the system, as shown in Figure 2.5. The dissipation effect is not assumed in

this figure. By implementing a sufficient number of isolation stages and also by using components whose resonant frequency is low enough, we acieve the required seismic attenuation performance at frequency at above 10 Hz.

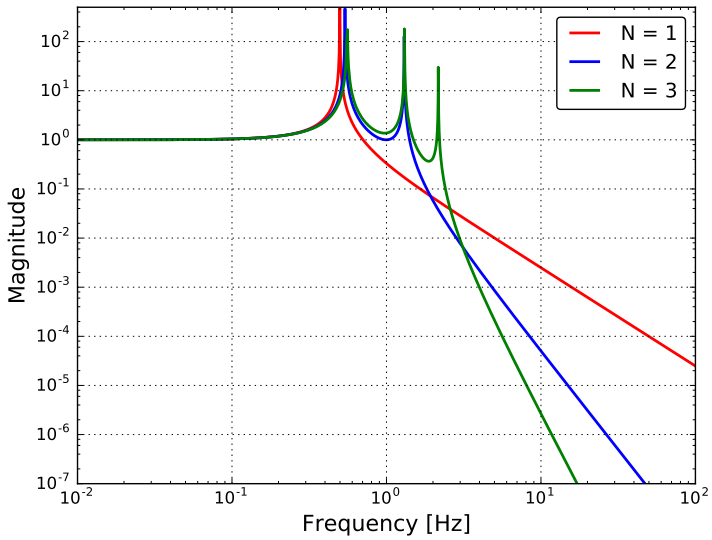

Figure 2.5: The amplitudes of the transfer functions from the suspension point displacement to an N-th stage mass displacement with N =1 to 3. The total length of the suspension is set at 1 m in all cases.

Axis definition of suspension motion

For more realistic system, we assume that the pendulum is described by 3D-rigid body model. In such system the motion of each component has 6 degrees of freedoms (dofs) in total. The axis definition is shown in Figure 2.6. We call the three translational axes as longitudinal, transverse and vertical respectively. The three rotational axes are called as roll, pitch, and yaw.

Especially we use the 3D-rigid body model when we build active control system for suspension system by ignoring the resonances of internal dynamics of a component. We use this assumption since the target control band width is lower than the frequency band where the internal motion becomes dominant, and is in the band where the rigid-body dynamics can be available.

Couplings from vertical and rotational vibration

In an actual system, not only the horizontal ground vibration but also the vertical ground vibration contributes to the mirror displacement. This vertical-to-horizontal coupling can be caused by mechanical imperfections in each attenuation stage and also by the non-parallelism of the verticality at locations kilometers

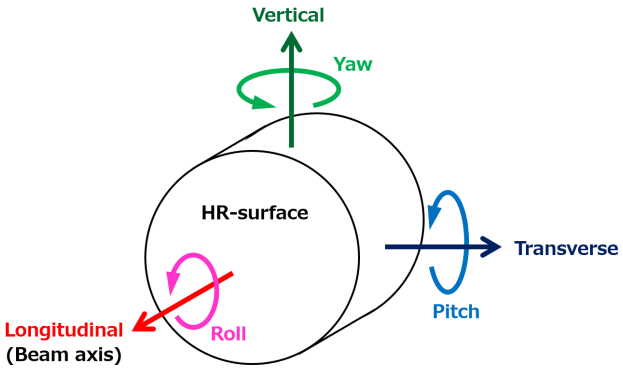

Figure 2.6: Definition of axes used in this thesis. HR-surface indicates the side of the surface of the mirror with high-reflectivity coating.

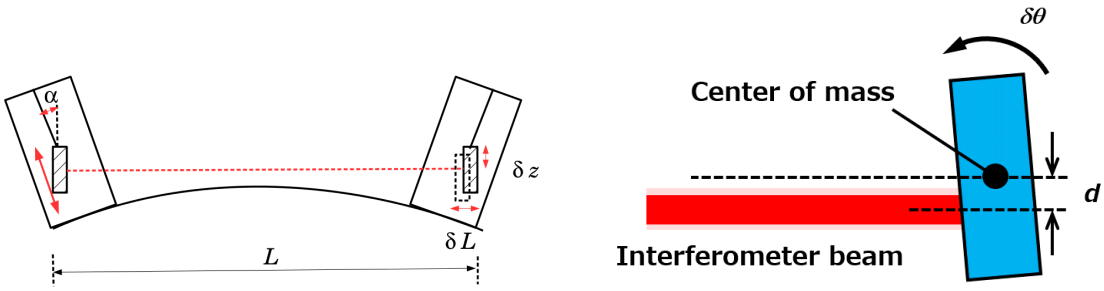

Figure 2.7: Couplings from vertical vibration due to the Earth curvature ($left$) and that from rotational motion due to beam shit ($right$).

apart in the detector. Due to the curvature of the ground, the front and end mirrors of the Fabry-Perot cavities make an angle of $\alpha = L/2R_{\oplus}$ with the vertical direction for the interferometer, as shown in figure 2.7 ($left$), considering that L is the cavity length and $R_{\oplus}$ is the radius of the earth. If the optic shifts vertically by δz, it couples to a variation $\alpha\delta z$ of the cavity length. Hence assuming a 3-km interferometer, the minimum coupling caused by earth curvature is $\alpha \sim 2 \times 10^{-4}$.

The rotational motions of the optic can also change the optical path length, as shown in figure 2.7 ($right$). If the laser beam locates at the center of the optic, the rotational motion of a mirror does not couple to the motion in the beam direction. However, the beam spot can be off-center to some extent practically, and then an angular motion causes a change of the optical path length. Assuming that the beam spot is off-centered by a distance d and the angle of the other test mass does not shift, the angular shift of the optic $\delta\theta$ couples to the length variation along the beam axis by $d\delta\theta$.

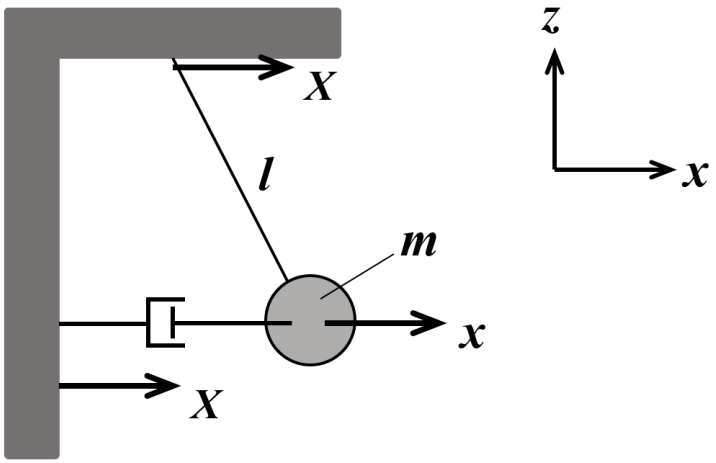

Figure 2.8: An example of a passively damped suspension system.

Passive damping system

As another aspect, we have to consider that a pendulum system can excite a large-amplitude motion due to the mechanical resonances and this makes huge impact to the interferometric operation. We have to damp them in order not to disturb the operation. One option to treat this fact is to use a passive damping system.

A passive damping system can be modeled by adding a viscous damper which makes a force proportional to the relative velocity between the damper and the suspended mass. In that system the equation of motion is given by:

$$m\ddot{x} \;=\; -k\,(x-X) - \gamma(\dot{x}-\dot{X}), \tag{2.17}$$

where k denotes the spring constant, γ is the damping coefficient of the damper, and X represents the ground motion. The schematic view is shown in Figure 2.8. Taking the Fourier transform, the transfer function from the ground motion to the suspended mass is given by

$$H(\omega) \;=\; \frac{\tilde{x}}{\tilde{X}} \;=\; \frac{{\omega_0}^2 + 2i\eta\omega\omega_0}{{\omega_0}^2 + 2i\eta\omega\omega_0 - \omega^2} \;=\; \frac{{\omega_0}^2 + i\omega\omega_0/Q}{{\omega_0}^2 + i\omega\omega_0/Q - \omega^2}, \tag{2.18}$$

where the damping ratio $\eta = \gamma/2m\omega_0$ and Q $(= 1/2\eta)$ is the quality factor of the resonance.

The displacement transfer function with some quality factors are plotted in $left$ of Figure 2.9. The $right$ of Figure 2.9 shows the impulse response of a mechanical oscillator with a viscous damper, with some Q factors. The $left$ panel in Figure 2.9 indicates that:

1. the amplitude of the peak at the resonant frequency gets smaller as the damping force becomes stronger,

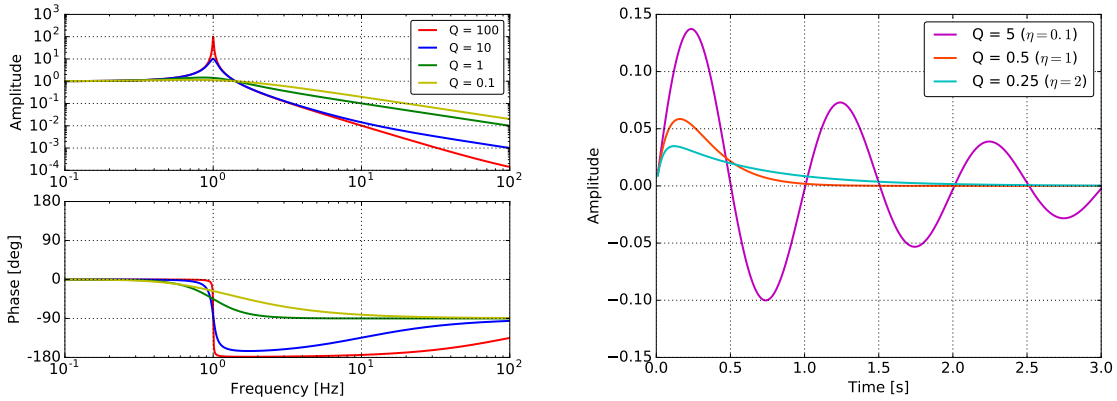

Figure 2.9: The transfer function eq (2.18) (*left*) and the response of a mechanical oscillator with a damper to an impulsive force injected to the suspended mass (*right*), with various Q factors (viscous damping factors).

2. the amplitude of the transfer function becomes proportional to f^{-1} instead of f^{-2}, where frequency is above Qf_0 enough.

Thus, if a damper is attached on the ground, the performance of the mechanical filter is degraded. This attenuation performance with a viscous-damper system can be improved by suspending the damper from the ground with a mechanical filter. This damping method is called flexible damping. By using the flexible damping, the vibration isolation curve will have one additional resonant peak due to the suspended damper, however, the response at higher frequency becomes proportional to f^{-2}, which is same case as a system without viscous damping system. Based on this fact, the passive damping system in a GW detector is basically suspended.

The *right* panel in Figure 2.9 shows an impulse response of this system to a driving force on the suspended mass with some Q factors. In the system with a damper, if the damping strength is not too strong, the suspended mass moves oscillation decays in the time scale of τ, which is $1/e$ decay time, i.e, the decay time in which the oscillation amplitude decreases by a factor of $1/e$. τ can be also described by $\tau = Q/\pi f_0$. The oscillation amplitude decays faster if the damping factor is increased. In the critical damping condition, i.e, $(Q = 0.5)$, the displacement of the suspended mass decays with the fastest decay time $\tau = 1/\omega_0$ without oscillation. In the over-damped condition where $Q < 0.5$, the excited displacement amplitude is decreased but the decay time gets longer compared to the case where the mass is critically damped.

Implementation of viscous damping system

An eddy-current damper [42] is a viscous damping system oftenly used in an actual GW detector. An eddy-current damping system consists of permanent magnets on one component acting on conductive plate mounted on the component

to be damped. A time-varying magnetic field on a conductive material surfaces generates eddy currents in the conductor. Then a magnetic field with opposite polarity of the applied field is induced by the eddy currents, and this makes a delay due to the induced field decay. Consequently a resistive force is generated. Figure 2.10 shows the working mechanism of an eddy current damper with a toy model. The damping coefficient which indicates the damping strength of an eddy current damper is given by

$$\gamma_x = A\sigma B\frac{\partial B}{\partial x}, \tag{2.19}$$

where B is the magnetic field from the permanent magnet, σ denotes the electrical conductivity of the conductor and A represents a factor determined from the geometry of the conductor. Generally, implementing a permanent magnet with strong magnetic field and a conductive object with large electric conductivity are demanded in order to get a large damping strength for the actual implementation.

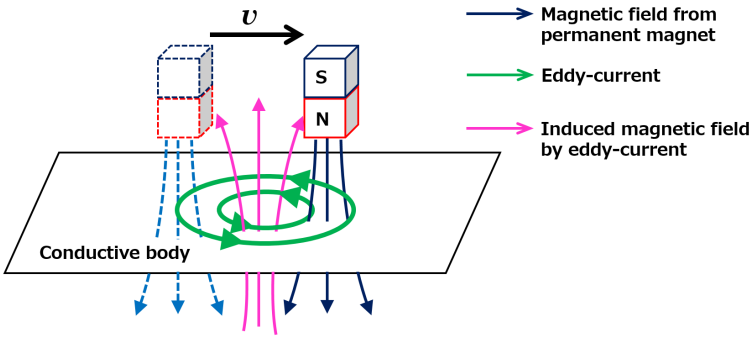

Figure 2.10: Working mechanism of an eddy-current damping system with a toy model.

Effect of suspension thermal noise

One demerit of using the passive damping system is that the system can introduce thermal fluctuation of the suspended optics in the detection band of GW detector. According to the fluctuation dissipation theorem, the power spectral density of the spontaneous fluctuations $S_{\rm thermal}(\omega)$ can be described by using external perturbation forces ($H_{\rm force}(\omega)$) as:

$$S_{\rm thermal}(\omega) \;=\; -\frac{4k_BT}{\omega}Im[H_{\rm force}(\omega)], \tag{2.20}$$

where k_b denotes the Boltzmann constant and T is the temperature.

Based on this fact, in an actual multi-stage suspension, we locate the passive dampers well apart from the optics so that thermal fluctuations due to their dissipation can be filtered out by mechanical filters, and do not affect the detector sensitivity.

2.2.2 Physics of passive filters for GW detectors

We can improve the attenuation performance at higher frequency by using lower resonant-frequency mechanical filters. In order to obtain sufficiently low resonant frequency with a compact mechanics, we use the anti-spring techniques in the passive filters in GW detectors.

The key components of such passive filters are inverted pendulum (IP) and co-called geometric anti-spring (GAS) filter. They provide horizontal and vertical vibration attenuation respectively. Since the resonant frequency of IP can be lowered to about 30 mHz, it can passively attenuate the ground vibration at the microseismic peak (at about 0.1-0.5 Hz). IP also mitigate the microseismic impact to RMS amplitude of the suspended optic motion. The resonant frequency of the GAS filter can be tuned to about 0.3 Hz, and GAS filter can have comparable vibration attenuation performance to the horizontal. The physics for IP and GAS filter is described in this subsection.

Inverted pendulum (IP)

An toy model of IP is shown in $left$ of figure 2.11. We consider a system which consists of a flexure fixed to the ground, a cylindrical object connected to the flexure, called IP leg. A mass is mounted on the top of the IP leg. If the top mass displaces horizontally from the vertical point, a restoring force acts on the mass, and the equation of motion can be obtained by

$$M\ddot{x} \;=\; -\,\frac{k_\theta}{L^2}(x-x_0) \;+\; \left(\frac{m}{2}+M\right)\frac{g}{L}(x-x_0), \tag{2.21}$$

where k_θ denotes the bending spring constant of the flexure, M and m are the mass of the top mass and that of IP leg respectively, and L represents the length of the IP leg. Based on this, the effective spring constant is given by

$$k_{\text{eff}} \;=\; \frac{k_\theta}{L^2} - \left(\frac{m}{2}+M\right)\frac{g}{L}. \tag{2.22}$$

The second term in eq (2.22) represents a repulsive force due to gravitational anti-spring effect, and this describes that k_{eff} decreases as the mass of the payload increases. Especially it goes to 0 when the mass reaches the critical mass $M_c = (k_\theta/gL - m/2)$. The resonant frequency of the IP whose mass is lighter than M_c is given by

$$f_{\text{IP}} \;=\; \frac{1}{2\pi}\sqrt{\frac{g}{L}\left(\frac{M_c-M}{M}\right)}. \tag{2.23}$$

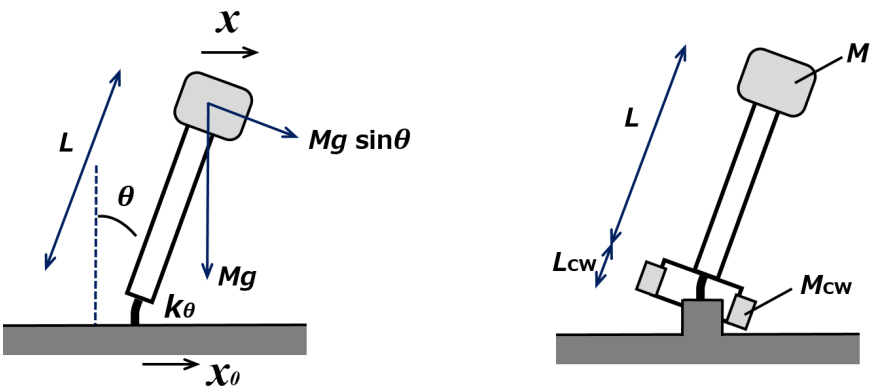

Figure 2.11: Analytic model of an inverted pendulum (*left*) and a schematic view of the inverted pendulum with the counter wight for the compensation of the center of percussion effect (*right*).

Concerning the vibration isolation performance in frequency domain, the displacement transfer function from the ground to the mass on the IP, H_{IP}, is calculated by [43]

$$H_{\mathrm{IP}} = \frac{A + B\omega^2}{A - \omega^2}, \tag{2.24}$$

$$\text{where } A = \frac{k_{\mathrm{eff}}}{M + \frac{m}{4} + \frac{I}{L^2}}, \quad B = \frac{\frac{m}{4} - \frac{I}{L^2}}{M + \frac{m}{4} + \frac{I}{L^2}}. \tag{2.25}$$

In eq (2.25), I denotes the moment of inertia of IP leg. the amplitude of H_{IP} saturates at high frequencies due to so-called the center of percussion (CoP) effect [43, 44]. This can be seen from the coefficient B in eq (2.25). The saturation can be mitigated by adjusting the mass distribution of the leg, and this is realized by implementing a counter weight at the bottom of the IP leg, as shown in *right* of figure 2.11.

Geometric Anti-Spring (GAS)

The GAS filter consists of a set of symmetrically arranged cantilever blades (for the actual structure, see section 4.1.2). The one end of the blades is clamped on the base frame and the other end is fixed to the central small disk, which is called the keystone. We then compress the blades in horizontally at the installation process, and obtain the anti-spring force. The typical behavior of the GAS filter can be described by a simple analytical model [45] as shown in Figure 2.12, i.e, a combination of vertical and horizontal springs can describe a cantilever spring. The equation of motion and the effective stiffness are obtained as the following procedure.

If we consider a situation where the suspended payload, whose mass is m, shifts vertically by z, as shown in figure 2.12 (*right*). The equation of motion of the suspended mass is described by

$$m\ddot{z} = -k_z(z - z_{eq} - l_{0z}) - 2k_x(l - l_{0x})\sin\theta - mg, \tag{2.26}$$

where k_x, l_{0x} are the stiffness and the natural length of the horizontal spring respectively, θ represents the angle between the horizontal axis and the horizontal spring at the clamp point, and l is the length of the horizontal spring when the payload shifts vertically by z. In addition, it is assumed a situation where the working point, which is the height where the forces of the horizontal springs cancel each other is called the working point z_{eq}, is given by $z_{eq} = (m_0 g/k_z + l_{0z})$, where g denotes the gravity acceleration, m_0 is the mass of the payload, k_z and l_{0z} are the stiffness and the natural length of the vertical spring respectively. It is also assumed that the force of the vertical spring balances the gravitational force on the suspended mass.

Then assuming x_0 is the horizontal distance between keystone and the clamping point of the spring, eq (2.26) becomes eq (2.28), by using $l = \sqrt{{x_0}^2 + z^2}$, z_{eq} and ${k_x}' = 2k_x$.

$$\begin{aligned} m\ddot{z} &= -k_z(z - \frac{m_0 g}{k_z}) - {k_x}'\left(1 - \frac{l_{0x}}{\sqrt{{x_0}^2 + z^2}}\right) z - mg & (2.27)\\ &= -(k_z + {k_x}')z + {k_x}' l_{0x}\frac{z}{\sqrt{{x_0}^2 + z^2}} - (m - m_0)g. & (2.28) \end{aligned}$$

Consequently, the effective stiffness k_{eff} of the modeled GAS filter is obtained as

$$\begin{aligned} k_{\text{eff}} &= -\frac{\partial f}{\partial z} = (k_z + {k_x}') - \frac{{k_x}' l_{0x} {x_0}^2}{({x_0}^2 + z^2)^{\frac{3}{2}}}, & (2.29)\\ &\sim \left[k_z - \left(\frac{l_{0x}}{x_0} - 1\right){k_x}'\right], \quad (\text{if} \quad x_0 \gg z). & (2.30) \end{aligned}$$

Eq (2.30) implies that when the horizontal spring is compressed ($x_0 < l_{0x}$), it makes a repulsive force in the vertical direction and the k_{eff} is reduced from that of the vertical spring ($k_{\text{eff}} < k_z$) due to the anti-spring effect.

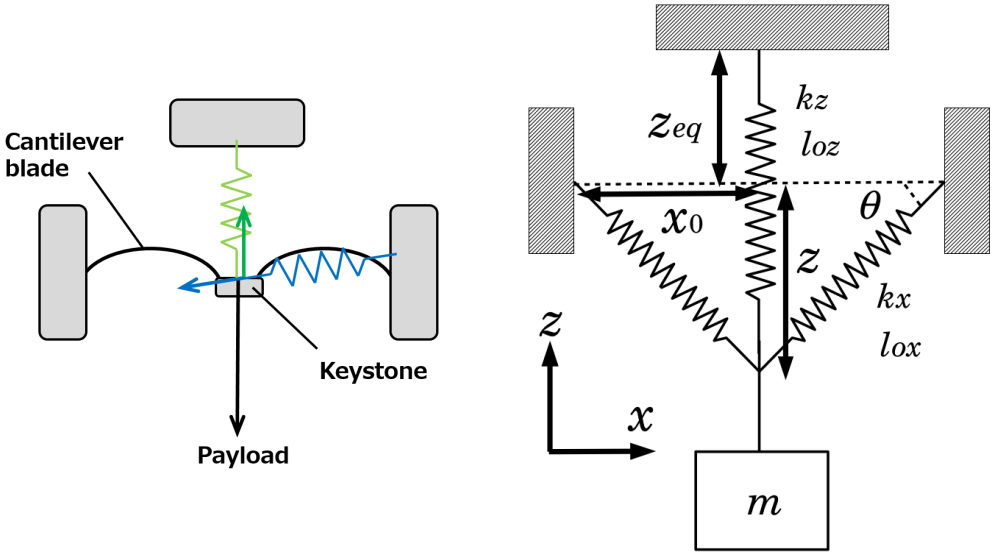

Figure 2.12: A schematic view of an analytical model of the GAS filter ($left$) and the definition of the parameters used in the calculation of the effective stiffness of the GAS filter ($right$).

About the vibration isolation performance in frequency domain, the displacement transfer function from the frame to the keystone is given by the same form as in eq (2.24). The saturation level at high frequencies due to the CoP effect is typically about 10^{-3}. This saturation can be improved by adding a counter weight, which is called magic-wand [46].

2.2.3 Active vibration isolation

By using the mechanical filters, we can attenuate the seismic noise at higher frequency i.e. above the resonant frequencies of the multi-stage vibration isolation system. However, in order to reduce the amplitude of the mirror motion at low frequency, we have to damp the mechanical resonances. Passive damping is one option to deal with this issue. Another option is to implement an active vibration isolation system. This option is introduced in this subsection.

Such an active control system can be used not only to damp the resonance but also to steer and maintain the position and orientation of the vibration isolation stage under control in a pre-defined reference position. The main risk associated with the operation of such an active control system is that the noise of the sensors and/or actuators used for the control might affect the attenuation performances of the vibration isolation system.

Feedback control is the most basic system used for this purpose. We realize the desired active control system by implementing appropriate feedback filters for required Cartesian dofs and stages. This subsection introduces the basic idea of feedback control and how the noise couplings are estimated assuming some control system used in the low frequency vibration isolation.

Feedback control with inertial sensor

A simple example is shown in Figure 2.13. We consider a case where we want to control a suspended stage with an actuator that applies a force from the ground.

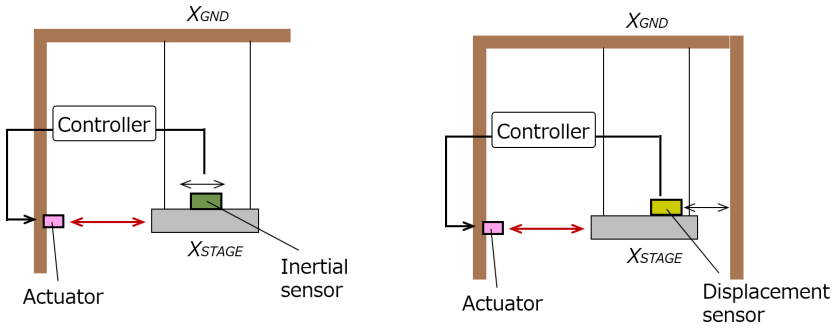

Figure 2.13: A simple model of feedback control with an inertial sensor $(left)$ and with displacement sensor $(right)$.

In the case where we have an inertial sensor which senses the suspended mass acceleration as shown in Figure 2.13 $(left)$, the corresponding block diagram is shown in Figure 2.14. In that diagram, we assume that the displacement transfer function P_s from the ground to the suspended mass motion, and the force transfer function P_a from force on the suspended stage to the suspended

stage displacement. The response of the inertial sensor is described by $S_{\rm inert}$ in this system, and $S_{\rm inert}$ calibrates the sensor signal such as in voltage to displacement motion of the suspended stage. F_{fb} denotes the feedback filter for active control. $N_{\rm act}$ and $N_{\rm inert}$ represent the actuator noise and the inertial sensor noise.

In this configuration, the actuator noise $N_{\rm act}$, the sensor noise $N_{\rm inert}$ and the seismic noise couple to the motion of suspended stage by $X_{\rm stage}/N_{\rm act}$, $X_{\rm stage}/N_{\rm inert}$ and $X_{\rm stage}/X_{\rm GND}$ respectively. These transfer functions are calculated from the diagram respectively as

$$\frac{X_{\rm stage}}{N_{\rm act}} = \frac{P_a}{1+G}, \tag{2.31}$$

$$\frac{X_{\rm stage}}{N_{\rm inert}} = \frac{-G}{1+G}, \tag{2.32}$$

$$\frac{X_{\rm stage}}{X_{\rm GND}} = \frac{P_s}{1+G}, \tag{2.33}$$

where G denote the open loop gain which is given by $P_a F_{\rm fb} S_{\rm inert}$. Then an external disturbance and the seismic noise coupling are to be suppressed by $1/(1+G)$. On the other hand, the sensor noise can induce the vibration depended on the feedback filter shape F_{fb} where $|G| \ll 1$, since eq (2.32) becomes close to $P_a F_{fb} S_{\rm inert}$ there. In this single-stage pendulum configuration, P_a and P_s becomes smaller with f^{-2} at higher frequencies. However, the filter shape can have an impact to the residual motion of the mass at $|G| \ll 1$ (typically at higher frequency region).

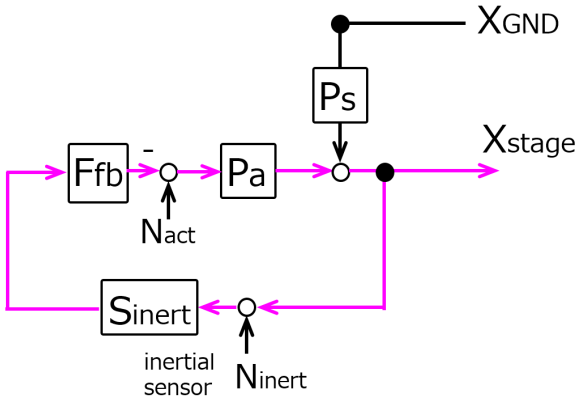

Figure 2.14: Corresponding block diagram of the system shown in Figure 2.13 (*left*).

The stability of a feedback control loop can be obtained by having enough phase margin of open loop gain G at its unity gain frequency (UGF).

Feedback control with displacement sensor

On the other case where we have an displacement sensor which sense the suspended mass motion with respect to ground, the corresponding block diagram

becomes as shown in Figure 2.15. In that diagram, we also assume that the displacement transfer function P_s from the ground to the suspended mass motion, and the force transfer function P_a from force on the suspended stage to the suspended stage displacement. The response of the displacement sensor is described by $S_{\rm L}$, and it calibrates the sensor signal such as in voltage to displacement motion of the suspended stage with respect to ground. F_{fb} denotes the feedback filter for active control. $N_{\rm act}$ and $N_{\rm L}$ represent the actuator noise and the inertial sensor noise.

In this configuration, the actuator noise $N_{\rm act}$, the sensor noise $N_{\rm L}$ and the seismic noise couple to the motion of suspended stage by $X_{\rm stage}/N_{\rm act}$, $X_{\rm stage}/N_{\rm L}$ and $X_{\rm stage}/X_{\rm GND}$ respectively. These transfer functions are calculated from the diagram respectively as

$$\frac{X_{\rm stage}}{N_{\rm act}} = \frac{P_a}{1+G}, \tag{2.34}$$

$$\frac{X_{\rm stage}}{N_{\rm L}} = \frac{-G}{1+G}, \tag{2.35}$$

$$\frac{X_{\rm stage}}{X_{\rm GND}} = \frac{G+P_s}{1+G}, \tag{2.36}$$

where G denote the open loop gain which is given by $P_a F_{\rm fb} S_{\rm L}$. In this case (comparing to the inertial sensor control), the response from the actuator noise and from the sensor noise to the suspended stage are same as those in the feedback system with an inertial sensor. However, the seismic noise coupling has a contribution from the controller as shown in eq (2.36). At $G \ll 1$, typically at high frequency, the seismic noise coupling becomes equal to $(G+P_s)$. For a pendulum, P_s become small at high frequency and the coupling through the feedback control ends up dominating.

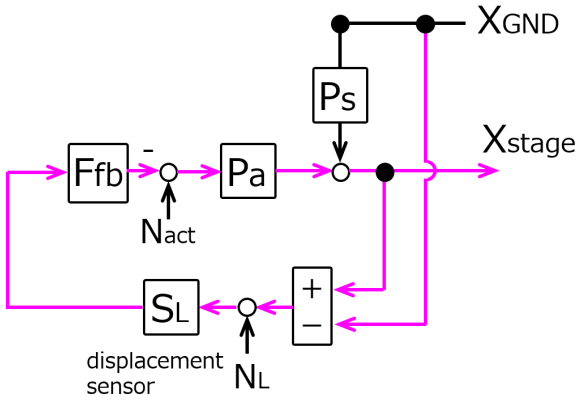

Figure 2.15: Corresponding block diagram of the system shown in Figure 2.13 (*right*).

Feedback control with blended sensor

Since displacement sensors are more robust in lower frequency region, we mainly use displacement sensors for the purpose of robust mechanical damping. However, since displacement sensors couple to seismic noise at higher frequency, it is required to use the inertial sensors after the system becomes calmed down enough, in order to get more suppression of the seismic noise coupling. On the other hand, at lower frequency, inertial sensors becomes less useful since their output signals become dominated by sensitivity to tilt motions and also by their self-noise.

The solution to circumvent these issues consists in combining the signals of an inertial sensor and a displacement sensor using high-pass and low-pass filters. This is called sensor blending technique [47, 48]. Here we assume that the position of the suspended mass to be controlled in Figure 2.13 is monitored by both an inertial sensor and a displacement sensor. The block diagram of the feedback control with blended sensors are shown in Figure 2.16. We blend the sensor signals by applying a low-pass filter $F_{\mathrm{LP}}(s)$ to the displacement sensor signal, and a complimentary high-pass filter $F_{\mathrm{HP}}(s) = 1 - F_{\mathrm{LP}}(s)$ to the inertial sensor signal. By doing this we can avoid phase distortion around the blending frequency. As an example, we can select the following blending filters based on seventh order polynomial function of the Laplace variable (s) as

$$F_{LP}(s) = \frac{35\omega_b^4 s^3 + 21\omega_b^5 s^2 + 7\omega_b^6 s + \omega_b^7}{(s+\omega_b)^7}, \tag{2.37}$$

$$F_{HP}(s) = \frac{s^7 + 75\omega_b s^6 + 215\omega_b^2 s^5 + 355\omega_b^3 s4}{(s+\omega_b)^7}, \tag{2.38}$$

where ω_b denotes the crossover frequency of $F_{\mathrm{LP}}(s)$ and $F_{\mathrm{HP}}(s)$, which is called blending frequency. Since the displacement sensor in this configuration measures the relative displacement between the suspended stage and the ground, the control system will introduce the ground vibration to the stage via the displacement sensor. For the purpose of seismic noise attenuation, especially due to the micro-seismic peak, it is necessary to set the blending frequency below 0.1 Hz. This is required in order to avoid that the large seismic noise due to the micro-seismic peak couples to the suspended test mass motion via the active control. On the other hand, the self-noise of the inertial sensor becomes larger at below 0.1 Hz making its use detrimental to the performances of the active control at the lowest frequencies. Based on this fact, the blending frequency and the order of the polynomial function in $F_{\mathrm{LP}}(s)$ and $F_{\mathrm{HP}}(s)$ are tuned depending on the sensitivity of the inertial sensor at the low frequency.

Using the above blending filters F_{LP} and F_{HP}, the actuator noise coupling $X_{\mathrm{stage}}/N_{\mathrm{act}}$, the sensor noise coupling $X_{\mathrm{stage}}/N_{\mathrm{inert}}$ and the seismic noise coupling $X_{\mathrm{stage}}/X_{\mathrm{GND}}$ of this system are obtained respectively as the followings, assuming

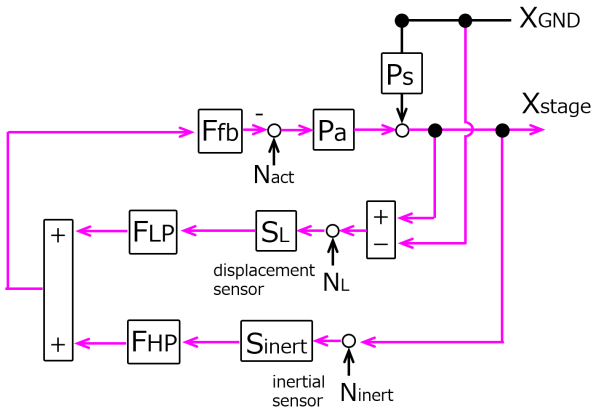

Figure 2.16: Block diagram of the feedback system with blended sensor. It assumes that the position of the suspended mass to be controlled in Figure 2.13 is monitored by both an inertial sensor and a displacement sensor.

an ideal case where the sensor responses $S_{\rm inert} = S_{\rm L} = 1$ and using $F_{\rm HP} + F_{\rm LP} = 1$:

$$\frac{X_{\rm stage}}{N_{\rm act}} = \frac{P_a}{1+G}, \tag{2.39}$$

$$\frac{X_{\rm stage}}{N_{\rm inert}} = \frac{-GF_{\rm HP}}{1+G}, \tag{2.40}$$

$$\frac{X_{\rm stage}}{N_{\rm L}} = \frac{-GF_{\rm LP}}{1+G}, \tag{2.41}$$

$$\frac{X_{\rm stage}}{X_{\rm GND}} = \frac{GF_{\rm LP} + P_s}{1+G}, \tag{2.42}$$

where G is given by $P_a F_{\rm fb}$. By using a low-pass filter whose crossover frequency is below about 0.1 Hz, coupling of the ground seismic noise due to the control system is suppressed compared to eq (2.36). The sensor blending technique is commonly used system in the GW detectors. However, in order to make use of this effectively, it is important to have inertial sensors that have good enough sensitivities at frequencies lower than 0.1 Hz.

Feedback control with feed-forwarding

Another option to suppress the coupling of seismic noise is the so-called feed-forwarding technique. This consists in adding an independent inertial sensor placed on the ground in the proximity of base of the vibration isolation system. The seismic noise measured by this sensor is then used to subtract the seismic noise coupling from the suspension displacement sensor. Figure 2.16 shows the block diagram of the Feedback control system using a displacement sensor with a feed-forwarding.

In this system, the ground vibration sensed by a seismometer on the ground is sent to the displacement sensor signal before applying the control filter with a

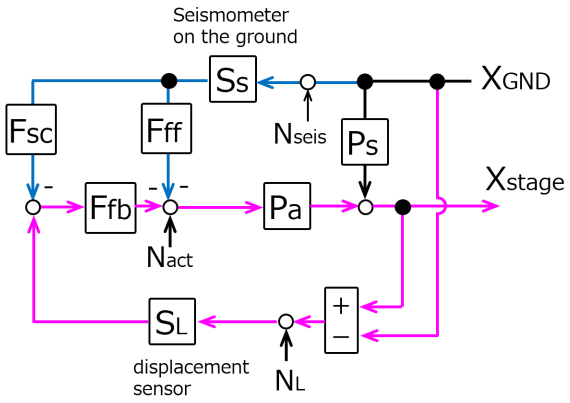

Figure 2.17: Block diagram of the feedback system using a displacement sensor with a feed forward system.

filter $F_{\rm sc}$, and also sent to the actuation port with a filter $F_{\rm ff}$, in order to subtract the seismic noise coupling. The actuator noise coupling $X_{\rm stage}/N_{\rm act}$, the sensor noise coupling $X_{\rm stage}/N_{\rm inert}$ and the seismic noise coupling $X_{\rm stage}/X_{\rm GND}$ of this system are obtained respectively as

$$\frac{X_{\rm stage}}{N_{\rm act}} = \frac{P_a}{1+G}, \tag{2.43}$$

$$\frac{X_{\rm stage}}{N_{\rm L}} = \frac{-G}{1+G}, \tag{2.44}$$

$$\frac{X_{\rm stage}}{N_{\rm seis}} = \frac{S_s P_a}{1+G}\left(F_{\rm sc}F_{\rm fb} - P_a F_{\rm ff}\right), \tag{2.45}$$

$$\frac{X_{\rm stage}}{X_{\rm GND}} = \frac{1}{1+G}\left[G\left(1+\frac{S_s}{S_L}F_{\rm sc}\right) + \left(P_s - P_a S_s F_{\rm ff}\right)\right], \tag{2.46}$$

where G is given by $P_a F_{\rm fb} S_{\rm L}$. By selecting the condition for the $F_{\rm sc}$ and $F_{\rm ff}$ described by eq (2.47) and eq (2.48), the seismic noise coupling becomes zero in an ideal case. This is a case where the $F_{\rm sc}$ subtracts the ground motion from the displacement sensor, and $F_{\rm ff}$ compensates the mechanical seismic noise coupling P_s. $F_{\rm sc}$ and $F_{\rm ff}$ are called the sensor-correction filter and feed-forwarding filter respectively.

$$F_{\rm sc} = -\frac{S_{\rm L}}{S_{\rm s}}, \tag{2.47}$$

$$F_{\rm ff} = \frac{P_{\rm s}}{P_a S_{\rm s}}, \tag{2.48}$$

In this condition, the sensor noise coupling from the ground motion sensor becomes

$$\frac{X_{\rm stage}}{N_{\rm seis}} = \frac{-P_a}{1+G}\left(S_{\rm L}F_{\rm fb} + P_{\rm s}\right). \tag{2.49}$$

Feedback control with blended sensor with feed-forwarding

As one of other options, a feedback control system using a blended sensor with a feed-forwarding is also used for further seismic noise suppression in the GW detectors as discussed in [49].

2.3 Targets and Outline

This thesis aims to consider/realize systems to help more effective EM follow up observation. More specifically:

1. I consider an on-line analysis approach to deal with a network composed of GW detectors with different sensitivities. I show the fast localization performance of such an approach when applied to the localization of a compact binary merger.

2. I have realized active control system for the KAGRA Type-A SAS, which allows to acquire the interferometer locking.

More details are described in this subsection.

2.3.1 Fast localization by hierarchical approach

The goal of first part of this thesis is to obtain the expected performance regarding sky localization of coalescing binaries in low-latency mode with a network of three or four GW detectors having heterogeneous sensitivities, such as the LIGO-Virgo, LIGO-KAGRA and LIGO-Virgo-KAGRA network. A hierarchical approach can be used in order to make an effective use of information from the least sensitive detector. In this approach, the presence of an event seen in coincidence in the two more sensitive detectors, triggers a focused search in the data of the third (and fourth), less sensitive, detector(s) with a lower SNR threshold. The first part shows the expected fast localization performance when a hierarchical search is implemented into a GW-EM follow-up pipeline composed of MBTA, a coalescing binary search algorithm based on matched filtering, and Bayestar, a software able to reconstruct sky maps from the outputs of the search algorithms. It is confirmed that the hierarchical search improves both the localization accuracy and precision in low-latency mode, compared to those achieved by a double coincidence search with the two LIGO detectors alone. This work has been done in collaboration with members of the LIGO-Virgo collaboration.

This thesis work is unique by means of the hierarchical approach with three- and four- detector network. I have worked on the calculation to estimate the rapid localization performance by MBTA and Bayestar.

Prior works have focused on:

1. LIGO- and LIGO-Virgo-network with a few specific detector-sensitivity cases without considering the hierarchical search [50],

2. LIGO-network using MBTA and Bayestar without considering the hierarchical search [3].

It should be noted that this thesis work does not include the development of the MBTA and Bayestar themselves.

2.3.2 Active control of KAGRA Type-A SAS

The second goal of this thesis work has been to construct a local control system for the KAGRA suspensions, especially for the arm-cavity mirrors, that is the so-called Type-A suspensions. The target is to achieve the required performance in terms of mechanical resonance damping time and of mirror residual motion for acquiring the interferometer lock.

As it is shown in section 1.3.3, the sensitivity of the ground-based GW detector is limited by the seismic noise at lower frequencies. We then adopt vibration isolation systems based on multi-stage pendulum system in order to realize the designed detector sensitivity. We additionally take care of the suspension mechanical resonances of the suspension system in order to lock the interferometer, i.e. in order to start the observation. For this purpose, we need to construct a system to control the suspensions that is able to:

1. rapidly damp all the mechanical resonances disturbing interferometer lock,
2. reduce the residual motion of the mirror and keep its orientation.

In the second part, I have realized the local control system for the Type-A suspension that deals with the suspensions resonance damping and the residual mirror motion suppression. More concretely, I have worked on the followings:

1. measuring/estimating the typical sensor noises, for the sensors implemented in the Type-A SAS (section 4.2),
2. integration of the KAGRA suspensions by means of installation, maintenance and repairing (section 4.4),
3. developing/implementing the control system for the Type-A SAS (chapter 5/chapter 6).

I note that the work in this thesis does not include the following tasks. They have been achieved by the KAGRA project:

1. basic design of the mechanical systems for all the KAGRA suspensions,
2. installation of data-acquisition system and real-time digital system infrastructure.

Chapter 3 addresses the fast localization with the hierarchical approach and summarizes the expected improvement. Chapter 4 describes the KAGRA seismic attenuation system called KAGRA-SAS. The measured/estimated sensor noise floors are also summarized in this chapter. Chapter 5 sets the requirements and develops the desired control system for KAGRA-SAS. Chapter 6 summarizes the implementation/performance of the designed and installed controls system (discussed in chapter 5). Finally, the conclusion and perspectives are given in chapter 7.

Chapter 3

Hierarchical search in heterogeneous network

This chapter describes the benefit of adding new detectors to the network in terms of the fast sky localization performance of the coalescing binaries. We estimate the impact on the fast source localization with GW detectors when the detectors have heterogeneous sensitivities.

Adding GW detectors to the network benefits both the detection confidence and the sky localization of the source. Finding a GW signal in coincidence at a number of distantly separated locations, increases the confidence that the signals are coming from astrophysical sources, rather than from technical glitches in the detector outputs, which are expected to be uncorrelated. In addition, as mentioned in section 2.1.3, as the number of GW detectors increases, the sky localization becomes more precise, since triangulation techniques are used based on the arrival times at the various detectors for the localization of the source in the sky. The precise prediction of the source position provided by GW detectors plays a crucial role for the EM follow-up observation.

This work focuses on the sky localization performances, especially in the low-latency mode considering situations where the detector sensitivities are heterogenous in the network detectors. This setting is motivated since we are already facing this configuration, and, likely, this will continue to be the case with more detectors coming on line in the future. In the US, the Advanced LIGO detectors started operation in 2015 following a decade of commissioning and operation of initial LIGO whose construction started in the 1990's. Advanced Virgo started operation two years later in 2017, after a period of commissioning and upgrade of initial Virgo whose construction had also started in the middle of 1990's. Then KAGRA detector whose construction started much later in 2012, is now being commissioned and is planned to join to the network in second half of O3. As a result, currently there are two higher sensitivity, one middle sensitive and one less sensitive detectors.

This chapter addresses the benefit of adding new detectors to the network made of the two higher sensitive detectors in terms of fast localization performance. The total number of detectors in the network in this work is set to three or four, and the calculation is done assuming 100% duty cycle for each detector. The following sections describe the details of this study. The discussion for the case of the LIGO-Virgo network with the hierarchical approach is reproduced from [51].

3.1 Fast localization with heterogeneous network

In the upcoming years, it is expected that the detectors in the network will have heterogeneous sensitivities, with detectors still at an early configuration and commissioning stage being less sensitive than the more advanced detectors. As written in the above, in this section, we investigate how to make an effective use of such a network in order to localize coalescing binaries at best.

Compact coalescing binaries are sources of particular interest for ground-based GW detectors. When detecting the signals from these events, we perform sky localization in a low-latency mode in order to trigger follow-up observations, especially in the electromagnetic spectrum. In a nutshell, low-latency search pipelines that specifically target CBC sources operate in the following way:

1. they process the data with matched filtering, based on a discrete set of templates covering a broad source parameters space, and they record triggers when the SNR of the filtered data exceeds some threshold [37].

2. Triggers coincident in several detectors are identified and used to reconstruct the sky location of the source.

3. Events with sufficient significance are then communicated to the astronomy community for follow-up observations.

The LIGO-Virgo Collaboration has been performing low-latency CBC searches with several pipelines: multi-band template analysis (MBTA) [3], GstLAL [1] and pyCBC Live [2]. Candidate events are uploaded to the GraceDb [10] and processed through the Bayesian rapid localization algorithm (Bayestar) [4] for fast position reconstruction, which generates probability sky maps.

With three or four detectors of heterogeneous sensitivities in terms of typical detection range for CBC sources, a hierarchical approach can be adopted in order to make an effective use of data from the less sensitive detectors. In this approach, the presence of an event seen in coincidence in the two more sensitive detectors triggers a focused search in the data of the third (and fourth), less sensitive, detector(s) with a lower SNR threshold. In this process we look for a signal in a small time window around the time of the identified coincidence and having

the same source parameters.

The following subsections explores the benefit that can be expected from such a hierarchical approach. Particularly this study was conducted in the framework of the MBTA pipeline, coupled to Bayestar for source localization, but the approach and results are quite general and could apply beyond the case of a specific pipeline. Section 3.2 describes the settings of the simulation and the figures of merit of the localization performance. Section 3.3 to 3.5 shows the simulated results.

3.2 Calculation set up

This study is based on simulated data previously generated in the context of [50] and analyzed in order to derive the sky localization performance obtained when post-processing MBTA triggers reported in [3] are used. The data set features 248 simulated signals from binary neutron star (BNS) sources, injected into simulated detector noise designed to match the expected initial performance of the Advanced LIGO detectors [50]. Although the corresponding detector sensitivity, which translated into a BNS detection range of 54 Mpc, does not match the more recent performance of the LIGO detectors, this is not an issue for this study, which depends primarily on the relative sensitivities of the detectors in the network and hardly on the absolute value of the BNS range. Therefore our results are relevant for the current and future LIGO-Virgo-KAGRA network.

In order to build a sky map for the location of a source, Bayestar processes information about the signal as it was measured in each detector (SNR, time and phase of arrival) and also takes as input the sensitivity curve of each detector, represented by the noise power spectral density (PSD). This study investigates the localization performance for the set of injections introduced above with the following network composed by LIGO, Virgo and KAGRA detectors:

- three-detector network made by LIGO-Virgo network,
- three-detector network made by LIGO-KAGRA network,
- four-detector network made by LIGO-Virgo-KAGRA network.

While for the LIGO detectors, the trigger information (SNR, time, and phase) is extracted from running the MBTA pipeline on the data, as was done in [3], for Virgo and KAGRA we use a different procedure. Since we want to explore several relative sensitivities of Virgo and KAGRA compared to LIGO, and several possibilities for the SNR threshold used in the Virgo analysis, but we want to avoid running the analysis multiple times, the Virgo and KAGRA triggers are artificially generated in a way that emulates the result of running the MBTA pipeline and is described below. The overview of main calculation flow is summarized in Figure 3.1. In this work, SNR threshold for the two LIGO detectors are set to 5.

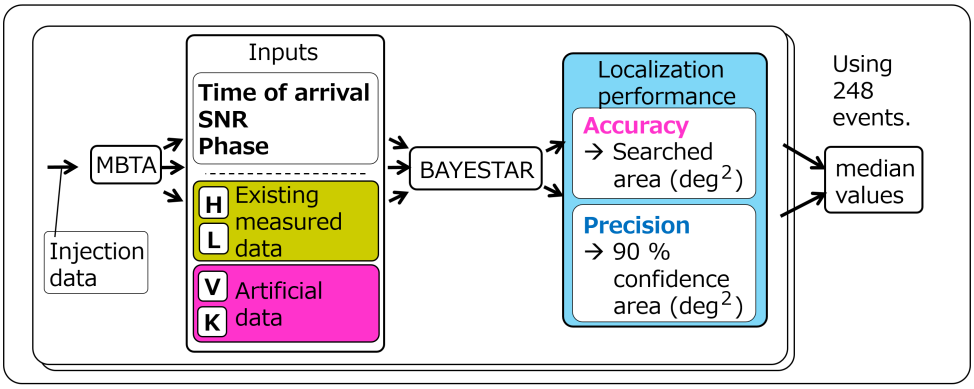

Figure 3.1: Overview of calculation flow. Using sky maps generated for 248 events processed by MBTA and Bayestar, we investigate the accuracy and precision of the localization, quantified by the median values of the searched area and 90% confidence area respectively. We repeat this calculation with different sensitivities and SNR threshold values for the least sensitive Virgo detector (or, less sensitive Virgo and KAGRA detectors).

3.2.1 Simulated data set and injections

The simulated data set used in this study was generated assuming noise curves based on early expectations of the 2015 performance of the detectors [50]. Since we want to explore various cases for the sensitivity of Virgo and KAGRA, the Virgo and KAGRA PSDs were rescaled to correspond to various relative values of the BNS range with respect to LIGO. The noise curves of the network detectors are drawn in Figure 3.2.

As described in the beginning of this subsection, 248 simulated signals from BNS sources are used for this calculation which is generated in [50] and once analyzed in [3] using LIGO network. We use this injection set since this work considers to start from the events detected by LIGO network with MBTA, and to include the less sensitive detector information to the trigger. More specifically, the 248 BNS injections were selected with the following procedure:

1. originally the locations of 10,000 sources were random and isotropic over the sky, and uniform in distance cubed based on an astrophysically motivated population[1]. The source distribution was cut off at a distance which aws far enough away compared to the considering detector sensitivities. The component masses were uniformly distributed between $1.2M_{\odot}$ and $1.6M_{\odot}$, and dimensionless component spins of up to 0.05. 250 events were randomly selected from the events obtained by analyzing the data using LIGO network with GstLAL. This was done in [50].

[1] As the distance increases, the number of the BNS is also increased.

2. Using the above 250 injections, MBTA found 248 of them in its re-analysis [3], and the corresponding injection set is what we have used in this thesis work.

Although the original population of injections composed of 10,000 events was isotropically distributed in space, we consider 248 injections which are detected in the two LIGO detectors, which biases the source directions toward directions favorable for the LIGO detectors. The distribution of the 248 injections is summarized in Figure 3.3 with the LIGO antenna pattern. Figure 3.4 also shows same 248 injection distribution but with the Virgo and KAGRA antenna patterns.

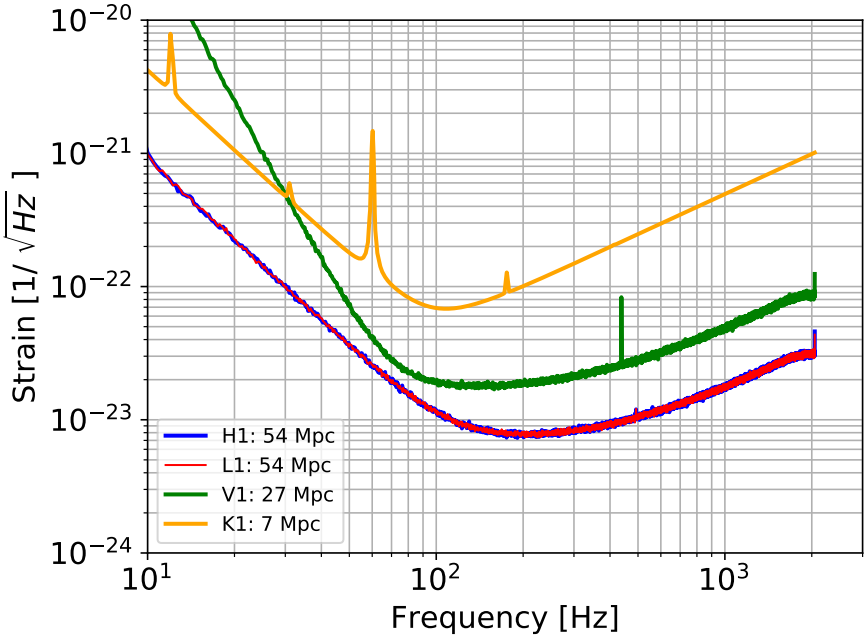

Figure 3.2: The assumed noise curves of the network detectors in amplitude spectral density (ASD). H1, L1, V1, K1 denote the name of the network detectors, i.e., LIGO-Hanford detecotr, LIGO-Livingston detector, Virgo detector and KAGRA detector, respectively. The distances show the BNS range of each detector. The Virgo and KAGRA PSDs were rescaled to correspond to various relative values of the BNS range with respect to LIGO.

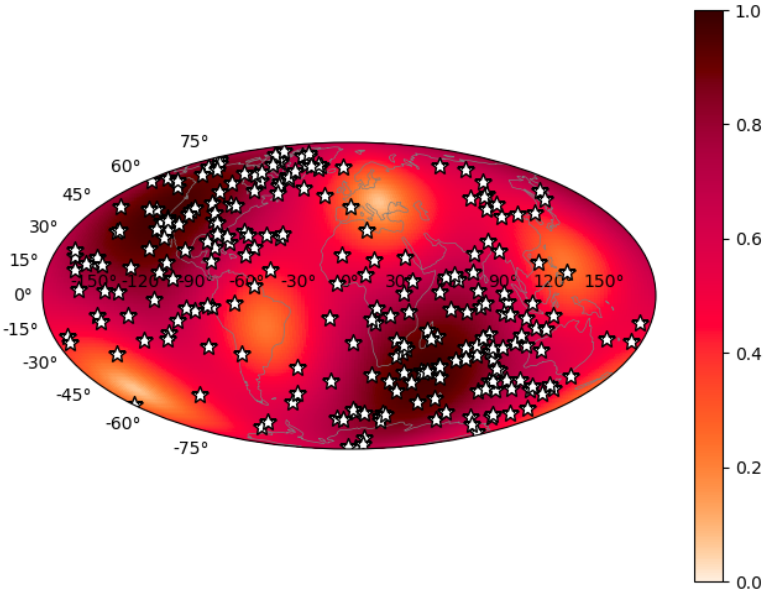

Figure 3.3: The sky locations of the 248 injections considered in this work are shown as stars on top of the color-coded combined antenna pattern of the two LIGO detectors. The sources are not uniformly distributed across the sky, but more favorably positioned with respect to the LIGO antenna pattern.

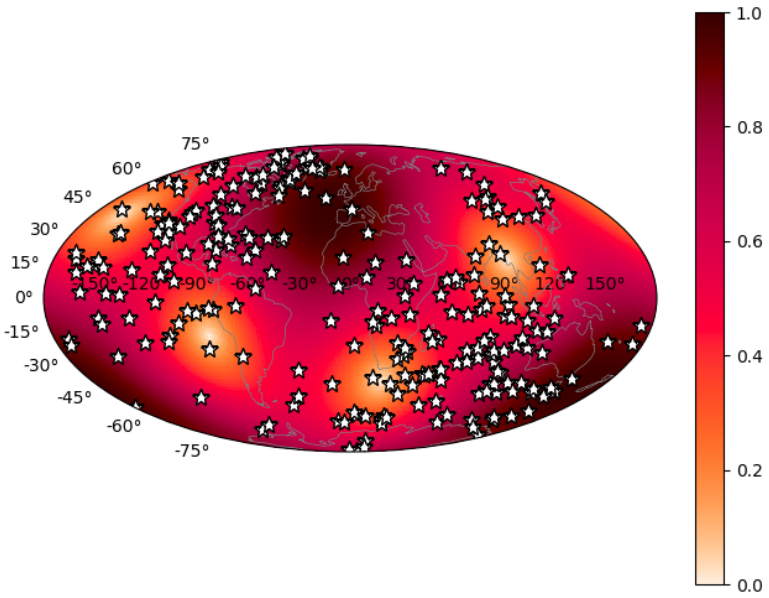

(a) With antenna pattern of Virgo detector

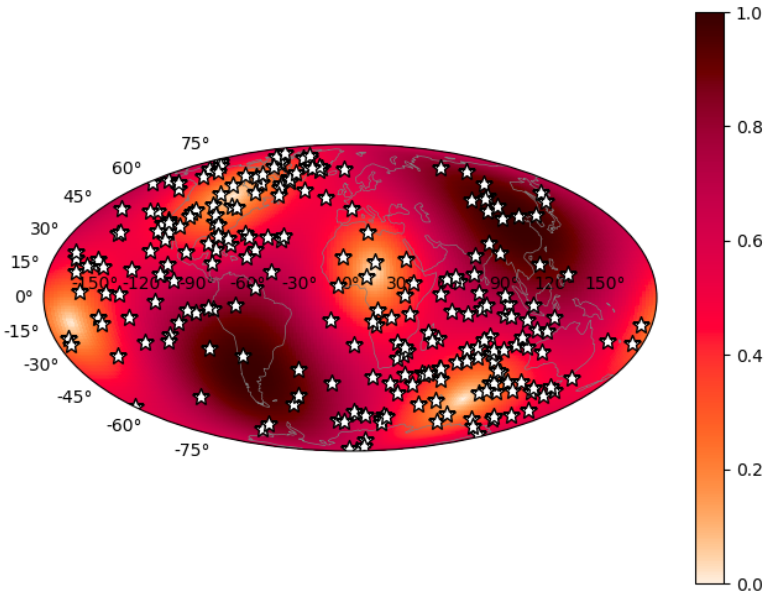

(b) With antenna pattern of KAGRA detector

Figure 3.4: The sky locations of the 248 injections considered in this work are shown as stars on top of the color-coded antenna pattern of Virgo detector (a) and KAGRA detector (b).

3.2.2 Generating artificial triggers for Virgo

We start from 248 injections detected as HL double coincidences. Depending on the outcome of the targeted search in the Virgo data obtained by looking for a trigger occurring close in time and with the same parameters as the HL coincidence, each of these can either remain a double coincidence if no trigger is found in Virgo (HL case), or else become a triple coincidence (HLV case). The latter case can appear in either one of two possibilities: the trigger found in Virgo is actually related to the injected signal (V_i case) or is related to detector noise (V_n case). The first step of the procedure is therefore to construct a set of injections with appropriate fractions of HL, V_i and V_n cases.

To assess the probability to get a V_n trigger, we need an estimate of the false alarm probability (FAP) in Virgo above a given SNR threshold, for a single template and a time window of 70 ms since we consider Virgo triggers within $\pm$ 35 ms of the LIGO triggers. This is derived from the SNR distribution obtained by running MBTA on representative subsets of O1 data, with about 2×10^5 templates, then assuming that the trigger rate is uniform across templates, and extrapolated below the SNR threshold of 6 applied in these analyses. The extrapolation used a Gaussian function, known to be a good approximation for the distribution of triggers at low SNR, which was confirmed by running small-scale analyses with lower SNR thresholds. We use two data sets, one corresponding to Virgo showing nominal behavior (quiet case) and one corresponding to a time of excess noise (noisy case). The SNR distributions are shown in Figure 3.5, along with the FAP as a function of SNR threshold that is derived from them.

For each injection, we estimate the SNR expected in Virgo $SNR_{\mathrm{V}}^{\mathrm{expected}}$ from the known effective distance $D_{\mathrm{eff}}^{\mathrm{V}}$, allowing for some statistical uncertainty:

$$SNR_{\mathrm{V}}^{\mathrm{expected}} = 2.26 \times (\text{detection range}) \times 8/D_{\mathrm{eff}}^{\mathrm{V}} + \mathrm{Gauss}(0,1), \qquad (3.1)$$

where $\mathrm{Gauss}(\mu, \sigma)$ is a random number derived from a Gaussian distribution with mean μ and standard deviation σ. More details about the effective distance are given in section A.1. In this formula, the factor 8 is the SNR threshold used to define the horizon distance for an optimally located and oriented source, and the factor 2.26 connects horizon distance to detection range by averaging on source's location and orientation. The V_i case applies if $SNR_{\mathrm{V}}^{\mathrm{expected}}$ is above the SNR threshold in Virgo $SNR_{\mathrm{V}}^{\mathrm{th}}$ and there is no louder noise trigger, i.e. a random number p_{V} drawn from a uniform distribution between 0 and 1 is smaller than FAP. The probability of the V_n case depends on the probability of getting a noise trigger above $SNR_{\mathrm{V}}^{\mathrm{expected}}$ or above $SNR_{\mathrm{V}}^{\mathrm{th}}$ if $SNR_{\mathrm{V}}^{\mathrm{expected}}$ is smaller than $SNR_{\mathrm{V}}^{\mathrm{th}}$, i.e. $\mathrm{FAP}(max(SNR_{\mathrm{V}}^{\mathrm{th}}, SNR_{\mathrm{V}}^{\mathrm{expected}}))$. The procedure is summarized in Table 3.1.

3.2.3 Attributing parameters to Virgo triggers in HLV-network

To produce sky maps for triple coincidences, we need to attribute parameters (SNR, time and phase of arrival) to the V_i or V_n triggers that supplement the

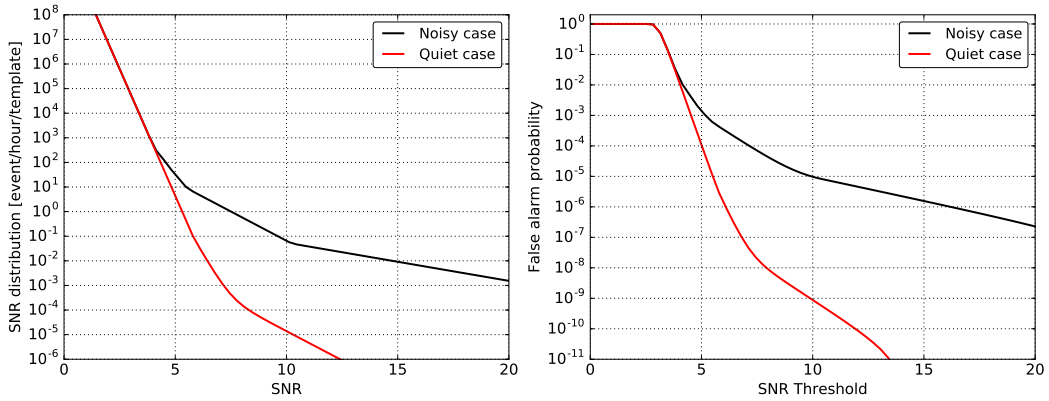

Figure 3.5: (*Left*) SNR distribution of noise triggers per hour and per template based on a measurement done during O1 and extrapolated for SNR below 6. The red curve was obtained on quiet data and the black curve on data with excess noise. (*Right*) False alarm probability (FAP) as a function of the SNR threshold, computed as FAP $= 1 - \exp(-R\,T)$, with R the rate of triggers above threshold per template, derived from the distribution on the left, and $T = 70$ ms. At low SNR threshold, FAP saturates at about 1 since the rate R becomes quite large.

HL double coincidence. This is done according to the procedure summarized in table 3.2. For V_i triggers we use parameters known from the injection metadata, and add ad-hoc statistical uncertainties. For the latter we started from educated guesses based on our experience of running the MBTA pipeline, which were then slightly adjusted to get consistent sky localization performances for HLV_i cases, i.e. making sure that the fraction of injections found within the area at a given confidence level matches that confidence level.

Table 3.1: Procedure for generating coincident events for LIGO-Virgo network. p_{V} is a random number from a uniform distribution between 0 and 1. $\mathrm{FAP_V}$ is the false alarm probability at a given SNR threshold in Virgo.

Conditions	Generated coincidences
if $p_{\mathrm{V}} < \mathrm{FAP_V}(\ max(SNR\ ^{\mathrm{th}}_{\mathrm{V}},\ SNR\ ^{\mathrm{expected}}_{\mathrm{V}})\ )$	H L $\mathrm{V_n}$
else	
if $SNR\ ^{\mathrm{expected}}_{\mathrm{V}} > SNR\ ^{\mathrm{th}}_{\mathrm{V}}$	H L $\mathrm{V_i}$
if $SNR\ ^{\mathrm{expected}}_{\mathrm{V}} < SNR\ ^{\mathrm{th}}_{\mathrm{V}}$	H L

Table 3.2: Procedure for attributing parameters to Virgo triggers. $t^{\mathrm{measured}}_{\mathrm{LIGO}}$ and $\phi^{\mathrm{measured}}_{\mathrm{LIGO}}$ represent, respectively, the measured time and phase of arrival at either the LIGO-Hanford or the LIGO-Livingston detector. For these parameters, we use the ones whose SNR is closer to the expected SNR of Virgo detector. $\Delta t^{\mathrm{injection}}$ and $\Delta\phi^{\mathrm{injection}}$ describe the simulated LIGO-Virgo differences of time and phase respectively. Random$[a : b]$ describes a random number uniformly drawn between a and b. We use 0.11 msec and 0.35 rad as typical measurement uncertainties at an SNR of 6 for the time and phase of arrival. These values have been adjusted so that the localization areas at a given confidence level are statistically self-consistent.

$\mathrm{V_n}$: Virgo trigger from noise	
SNR	randomly drawn from the distribution shown in figure 3.5
Time	$t^{\mathrm{measured}}_{\mathrm{LIGO}}$ + Random$[-35$ msec $: 35$ msec$]$
Phase	Random $[0 : 2\pi]$
$\mathrm{V_i}$: Virgo trigger from injections	
SNR	$2.26 \times$ (detection range) $\times\ 8/D^{\mathrm{V}}_{\mathrm{eff}} + \mathrm{Gauss}(0, 1)$
Time	$t^{\mathrm{measured}}_{\mathrm{LIGO}} + \Delta t^{\mathrm{injection}} + \mathrm{Gauss}(0,\ 0.11\ \mathrm{msec} \times 6/SNR\ ^{\mathrm{expected}}_{\mathrm{V}})$
Phase	$\phi^{\mathrm{measured}}_{\mathrm{LIGO}} + \Delta\phi^{\mathrm{injection}} + \mathrm{Gauss}(0,\ 0.35\ \mathrm{rad} \times 6/SNR\ ^{\mathrm{expected}}_{\mathrm{V}})$

3.2.4 Generating artificial triggers for KAGRA

The basic idea is same as described in section 3.2.2. I.e, we generate K_i and K_n triggers in the same manner as Virgo trigger generation with the parameters for KAGRA. The difference is the time window used for the calculation of the FAP for KAGRA. We used 80 ms as the time window since we consider KAGRA triggers within ± 30 ms and ± 40 ms, based on the light flight time between LIGO-Hanford to KAGRA and LIGO-Livingston to KAGRA respectively. Consequently the FAP for KAGRA is slightly different from the FAP for Virgo, as shown in Figure 3.6. Other parameters are defined as:

$$SNR_{\mathrm{K}}^{\mathrm{expected}} = 2.26 \times (\text{detection range}) \times 8/D_{\mathrm{eff}}^{\mathrm{K}} + \mathrm{Gauss}(0,1), \quad (3.2)$$

$$SNR_{\mathrm{K}}^{\mathrm{th}} = (\text{SNR threshold in KAGRA}), \quad (3.3)$$

where $D_{\mathrm{eff}}^{\mathrm{K}}$ is the effective distance for KAGRA. The procedure is summarized in Table 3.3.

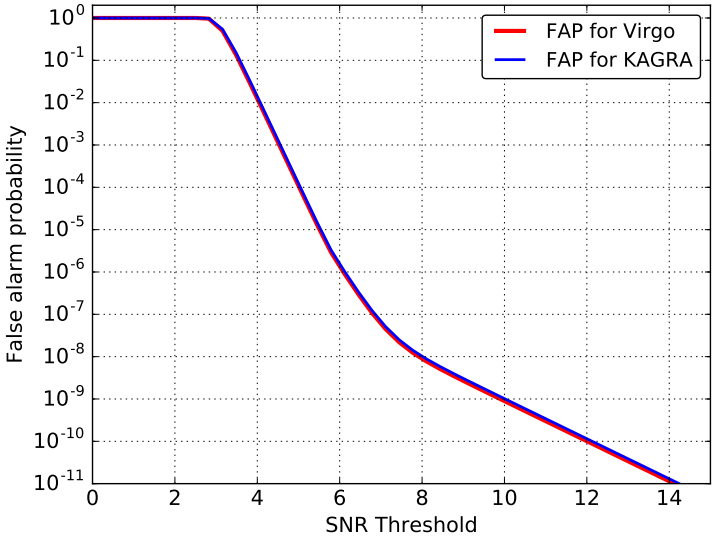

Figure 3.6: False alarm probability (FAP) fir Virgo and KAGRA as a function of the SNR threshold, computed as FAP $= 1 - \exp(-R\,T)$, with R the rate of triggers above threshold per template, derived from the distribution on the left of Figure 3.5, and T for Virgo and KAGRA is set to 70 ms and 80 ms respectively.

3.2.5 Attributing parameters to KAGRA triggers in HLK-network

This process is also done in the same manner as summarized in section 3.2.3. The procedure is summarized in Table 3.4.

Table 3.3: Procedure for generating coincident events for LIGO-KAGRA network. $p_{\rm K}$ is a random number from a uniform distribution between 0 and 1. $\mathrm{FAP_K}$ is the false alarm probability at a given SNR threshold in KAGRA.

Conditions	Generated coincidences
if $p_{\rm K} < \mathrm{FAP_K}(\ max(SNR\ {}^{\rm th}_{\rm K},\ SNR\ {}^{\rm expected}_{\rm K})\ )$	H L $\mathrm{K_n}$
else	
if $SNR\ {}^{\rm expected}_{\rm K} > SNR\ {}^{\rm th}_{\rm K}$	H L $\mathrm{K_i}$
if $SNR\ {}^{\rm expected}_{\rm K} < SNR\ {}^{\rm th}_{\rm K}$	H L

Table 3.4: Procedure for attributing parameters to KAGRA triggers. $t^{\rm measured}_{\rm LIGO}$ and $\phi^{\rm measured}_{\rm LIGO}$ represent, respectively, the measured time and phase of arrival at either the LIGO-Hanford or the LIGO-Livingston detector. For these parameters, we use the ones whose SNR is closer to the expected SNR of KAGRA detector. $\Delta t^{\rm injection}$ and $\Delta\phi^{\rm injection}$ describe the simulated LIGO-KAGRA differences of time and phase respectively. Random$[a : b]$ describes a random number uniformly drawn between a and b. Again we use 0.11 msec and 0.35 rad as typical measurement uncertainties at an SNR of 6 for the time and phase of arrival. These values have been adjusted so that the localization areas at a given confidence level are statistically self-consistent.

$\mathrm{K_n}$: KAGRA trigger from noise	
SNR	randomly drawn from the distribution shown in figure 3.5
Time	$t^{\rm measured}_{\rm LIGO}$ + Random$[-30$ msec $: 30$ msec$]$, for HK-case
	$t^{\rm measured}_{\rm LIGO}$ + Random$[-40$ msec $: 40$ msec$]$, for LK-case
Phase	Random $[0 : 2\pi]$
$\mathrm{K_i}$: KAGRA trigger from injections	
SNR	$2.26 \times$ (detection range) $\times\ 8/D^{\rm K}_{\rm eff} + \mathrm{Gauss}(0, 1)$
Time	$t^{\rm measured}_{\rm LIGO}$ + $\Delta t^{\rm injection}$ + Gauss(0, 0.11 msec $\times\ 6/SNR\ {}^{\rm expected}_{\rm K}$)
Phase	$\phi^{\rm measured}_{\rm LIGO}$ + $\Delta\phi^{\rm injection}$ + Gauss(0, 0.35 rad $\times\ 6/SNR\ {}^{\rm expected}_{\rm K}$)

3.2.6 Generating artificial triggers for Virgo and KAGRA

This is a setting for the investigation of the four-detector case. The artificial trigger generation is processed in accordance with section 3.2.2 and 3.2.4. We also consider the triggers found in Virgo and KAGRA which are actually related to the injected signal (V_i and K_i case), and which are related to detector noise (V_r and K_r case). Parameters are attributed to these triggers as described in section 3.2.3 and section 3.2.5. The procedure is summarized in table 3.5.

Table 3.5: Procedure for generating coincident events for LIGO-Virgo-KAGRA network. p_V and p_K is a random number from a uniform distribution between 0 and 1. FAP_V and FAP_K is the false alarm probability at a given SNR threshold in Virgo and KAGRA respectively.

Conditions	Generated coincidences
if $p_V < \mathrm{FAP}_V(\ max(SNR_V^{th}, SNR_V^{expected})\ )$	
if $p_K < \mathrm{FAP}_K(\ max(SNR_K^{th}, SNR_K^{expected})\ )$	H L V_n K_n
else	
if $SNR_K^{expected} > SNR_K^{th}$	H L V_n K_i
else	H L V_n
else	
if $SNR_V^{expected} > SNR_V^{th}$	
if $p_K < \mathrm{FAP}_K(\ max(SNR_K^{th}, SNR_K^{expected})\ )$	H L V_i K_n
else	
if $SNR_K^{expected} > SNR_K^{th}$	H L V_i K_i
else	H L V_i
else	
if $p_K < \mathrm{FAP}_K(\ max(SNR_K^{th}, SNR_K^{expected})\ )$	H L K_n
else	
if $SNR_K^{expected} > SNR_K^{th}$	H L K_i
else	H L

3.2.7 Figures of merit

We use the 90% confidence area and the so-called searched area [52][2] as figures of merit for the performance of the sky localization. The searched area is the area of the highest confidence region around the pixel of maximum probability, that includes the sky location of the injected GW signal. The 90% confidence area

[2]More details can be found in section 7.2 in [52].

gives the precision, whereas the searched area quantifies the accuracy of the sky localization.

3.3 Expected performance of heterogeneous HLV-network

3.3.1 Sky localization performance

Using the settings in section 3.2.2 and 3.2.3, we generate sky maps of 248 events and investigate the localization performance by collecting the median values of searched area and 90% confidence area. This calculation is repeated with different SNR thresholds in Virgo. First, we assumed that the two LIGO detectors have the same range while the Virgo detector has 39% of the range of the LIGO detectors to roughly mimic the O2 sensitivity. The calculated performance is shown in Figure 3.7. The dots show the median of the localization areas over the set of injections and the uncertainties report the interquartile range. In order to check that the results were not overly sensitive to a particular realization of the random numbers used in the simulation, the procedure was repeated twice, and since the results were consistent, the figure reports the average (quadratic average) of the medians (uncertainties) obtained in the two trials. The relative detector sensitivities are written down as 1-1-x, with x the ratio of the Virgo sensitivity compared to the two LIGO detectors.

The plots show that the optimal SNR threshold in Virgo is around 3. At this threshold, the localization is improved by about a factor of 4. In this configuration, about 51% of the 248 events are reconstructed as $\mathrm{HLV_i}$ triggers, 36% as $\mathrm{HLV_n}$ triggers, and 13% are HL triggers. The percentage of these three triggers changes depending on the Virgo threshold (these percentages depend on the Virgo sensitivity and threshold). In order to verify the artificial trigger generation in this work, we also actually run MBTA on Virgo data with a SNR threshold ranging from 5 to 10, and we obtained consistent median values for the searched area and 90% confidence area compared to the localization performance obtained with artificial Virgo triggers at those threshold as shown in Figure 3.8. Figure 3.7 also includes the localization performance when the lower sensitivity detector generates louder background triggers compared to a stable case. In this noisy case investigation, the SNR distribution and the FAP in Virgo are derived from the black curves instead of the red curves in Figure 3.5. This has no impact on the localization performance and in the following we work only in the quiet case.

3.3.2 Dependence on the sensitivity of Virgo detector

We calculate the localization performance for various BNS ranges of the Virgo detector. This is realized by scaling its expected SNR using (3.1) and its noise curve. The other settings are as described in section 3.2. The population of the HL, $\mathrm{HLV_i}$ and $\mathrm{HLV_r}$ events are summarized in section A.2. The expected performances in terms of searched area and 90% confidence area are shown in Figure 3.9. The hierarchical search with three detectors will improve the precision of the localization regardless of the value of the BNS range. On the other hand, if the BNS range for the lower sensitivity detector is too low, the accuracy of the localization will be slightly degraded since it will be more likely to get triple

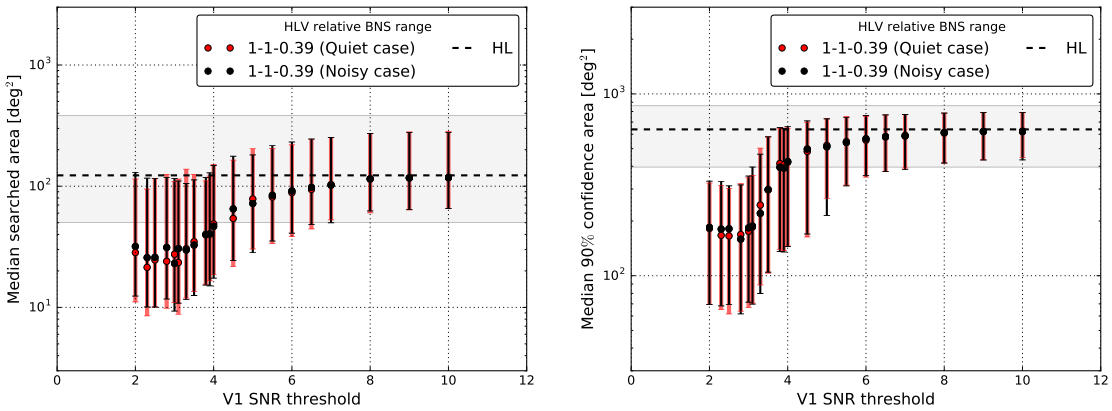

Figure 3.7: The sky localization performance of the heterogeneous network search by three detectors. These plots show the median with its interquartile range. The dashed black line shows the performance using the two LIGO detectors only. The red colored dots are for the case when the detector is quiet, while the black ones correspond to the noisy condition. The performances in the two cases are similar.

coincidences with Virgo noise triggers. However, this effect will not be so large; noisy Virgo triggers will mainly be found when the sensitivity is much lower than the sensitivities of the LIGO detectors. In this situation, the reconstructed sky maps will be similar to the ones obtained with the LIGO detectors only. Figure 3.8 shows the improvement in the performance for those events that become triple coincident events when Virgo is added to the network.

Based on Figures 3.8 and 3.9, the lower sensitivity detector begins to improve the localization performance as soon as its sensitivity is 20% of the more sensitive detectors. Then the optimal SNR threshold lies in the range from 3 to 3.5. We select the threshold in Virgo to 3.5 take into account the easiness of handling the data. The dependence on the sensitivity of Virgo detector at the threshold is equal to 3.5 is shown in Figure 3.10. We find that as the sensitivity of Virgo approaches half of the LIGO one, the accuracy and precision of the localization can be improved by about a factor of 7, compared to LIGO network.

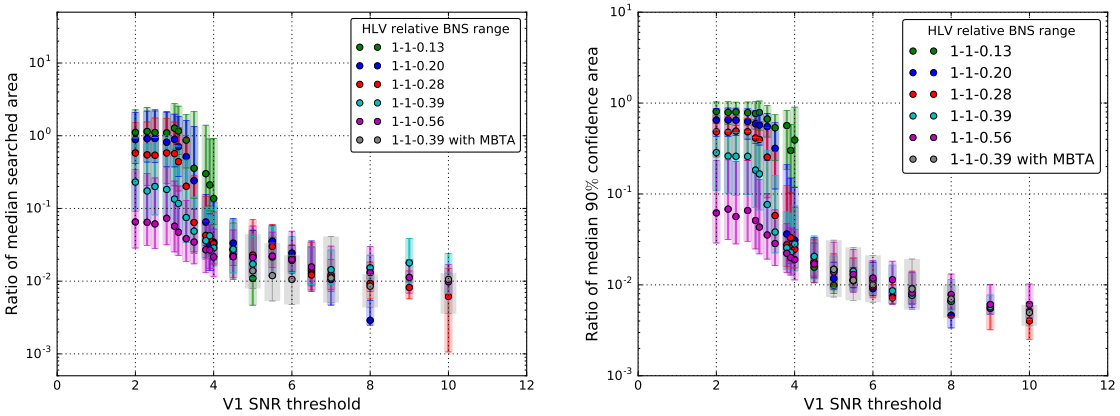

Figure 3.8: Ratio of the median searched area (*left*) and 90% confidence area (*right*) of HLV triggers to that of the same triggers treated as HL coincidences, with the interquartile ranges. As the sensitivity improves, $\mathrm{HLV_n}$ triggers become less likely whereas $\mathrm{HLV_i}$ triggers become more likely and benefit the localization performance.

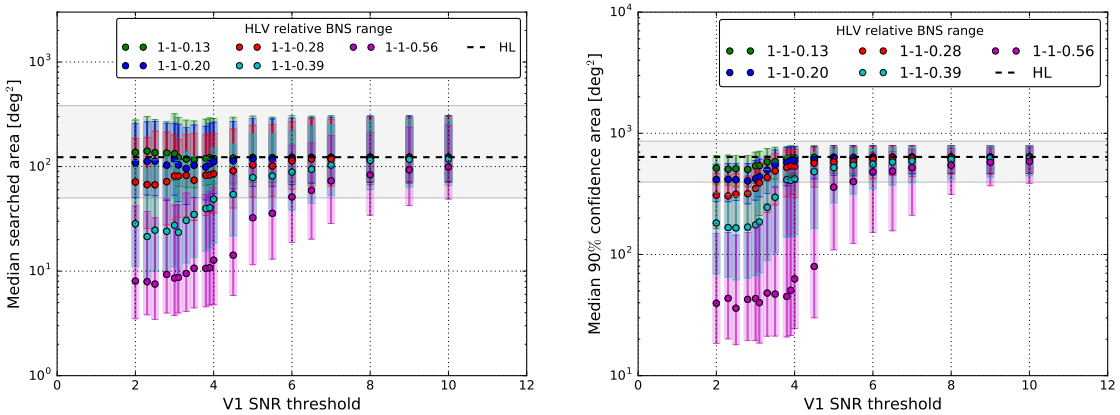

Figure 3.9: The median searched area (*left*) and 90% confidence area (*right*) with the interquartile ranges are shown as a function of the SNR threshold used in Virgo. Expected sky localization performance with the hierarchical search when the sensitivity of the Virgo detector is varied. The colors show the network configuration.

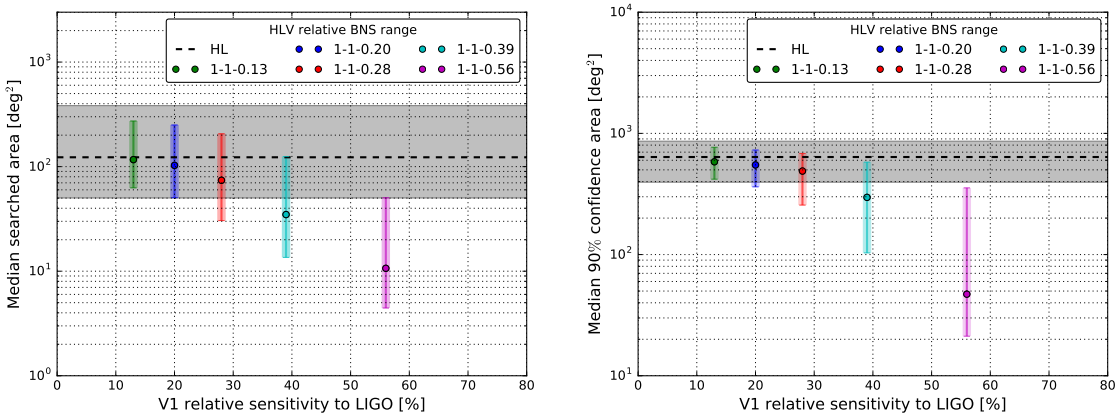

Figure 3.10: The median searched area (*left*) and 90% confidence area (*right*) with the interquartile ranges are shown as a function of the relative sensitivity of Virgo compared to the LIGO one where the Virgo threshold is set to 3.5. The colors show the network configuration.

Concerning the sky maps, the reconstructed region by HLV coincident triggers will be a fraction of the area reconstructed by the two LIGO detectors only. If a coincident trigger is built from two LIGO signals and a noise Virgo trigger, the area pointed by the HLV network starts to shift from the source position, mostly due to the error on the detection time in Virgo. However, if the range of Virgo detector is much lower than the LIGO ones, the reconstructed area remains similar to the ring shape region reconstructed by the two LIGO detectors only even when the Virgo trigger is due to noise. This hierarchical search will find ring-shaped sky maps when the sensitivity of the third detector is much lower than the higher sensitivity ones. As the sensitivity improves, the sky maps progressively turn into point-like regions inside the area by the two LIGO detectors.

3.4 Expected performance of heterogeneous HLK-network

With the same manner as HLV-network case, using the settings in section 3.2.4 and 3.2.5, we generate sky maps of 248 events and investigate the localization performance by collecting the median values of searched area and 90% confidence area. This calculation is repeated with different SNR thresholds in KAGRA, and also the procedure was repeated twice in order to check that the results were not overly sensitive to a particular realization of the random numbers used in the simulation. Based on the result shown in section 3.3.1, we consider a case where the less sensitive detector KAGRA generates background triggers stably in this calculation.

3.4.1 Dependence on the sensitivity of KAGRA detector

In the same way as in section 3.3.2, we calculate the localization performance for various BNS ranges of the KAGRA detector, by scaling its expected SNR using (3.2) and its noise curve. The population of the HL, $\mathrm{HLK_i}$ and $\mathrm{HLK_n}$ events are summarized in section A.2. The expected improvement ratio of the performance of HLK triggers to that of the same triggers treated as HL coincidences is shown in Figure 3.11. The expected performances in terms of searched area and 90% confidence area obtained from all the 248 events are shown in Figure 3.12. The relative detector sensitivities are written down as 1-1-x, with x the ratio of the KAGRA sensitivity compared to the two LIGO detectors.

The obtained results lead qualitatively to the same conclusions as in the HLV-network case. Based on Figures 3.11 and 3.12, the lower sensitivity detector begins to improve the localization performance as soon as its sensitivity is 28% of the more sensitive detectors. Then the optimal SNR threshold lies in the range from 3 to 3.5. By following the LIGO-Virgo network case, we select the threshold in KAGRA to 3.5 take into account the easiness of handling the data. The dependence on the sensitivity of KAGRA detector at the threshold is equal to 3.5 is shown in Figure 3.13. We find that as the sensitivity of KAGRA approaches half of the LIGO one, the accuracy and precision of the localization can be improved by about a factor of 3.5, compared to LIGO network.

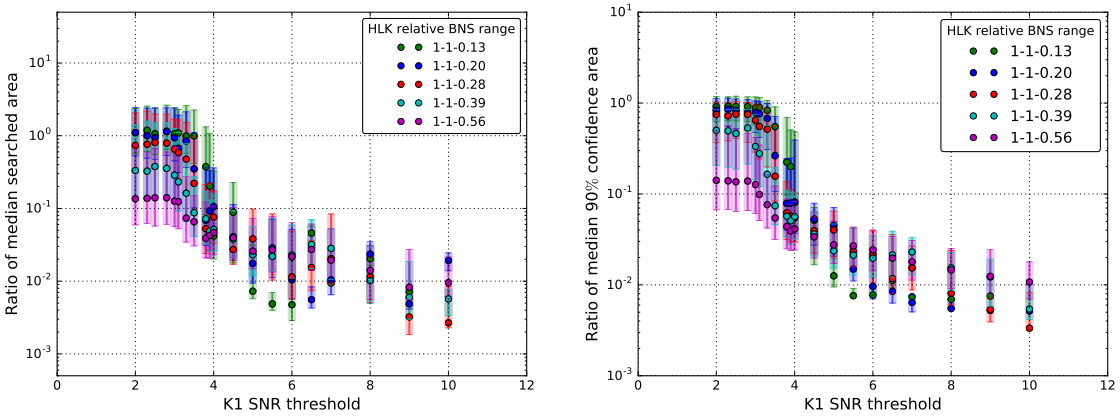

Figure 3.11: Ratio of the median searched area ($left$) and 90% confidence area ($right$) of HLK triggers to that of the same triggers treated as HL coincidences. As the sensitivity improves, $\mathrm{HLK_n}$ triggers become less likely whereas $\mathrm{HLK_i}$ triggers become more likely and benefit the localization performance.

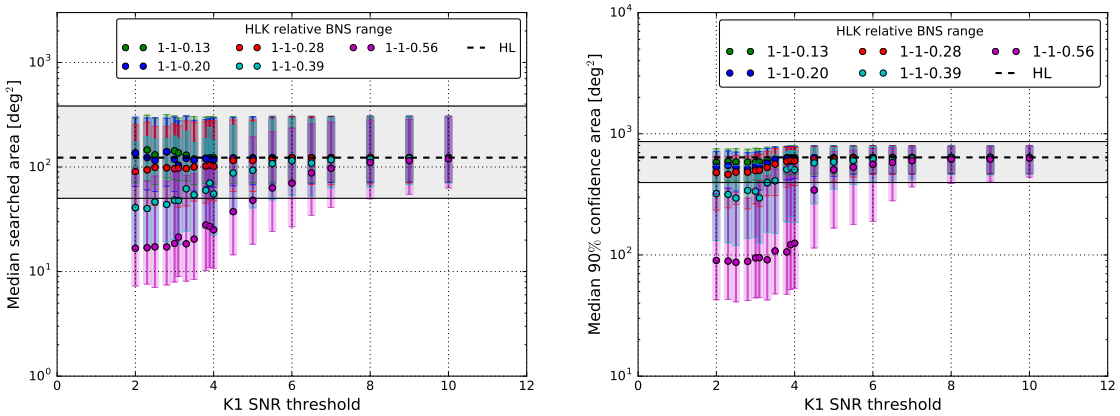

Figure 3.12: The median searched area ($left$) and 90% confidence area ($right$) are shown as a function of the SNR threshold used in KAGRA. Expected sky localization performance with the hierarchical search when the sensitivity of the KAGRA detector is varied. The colors show the network configuration.

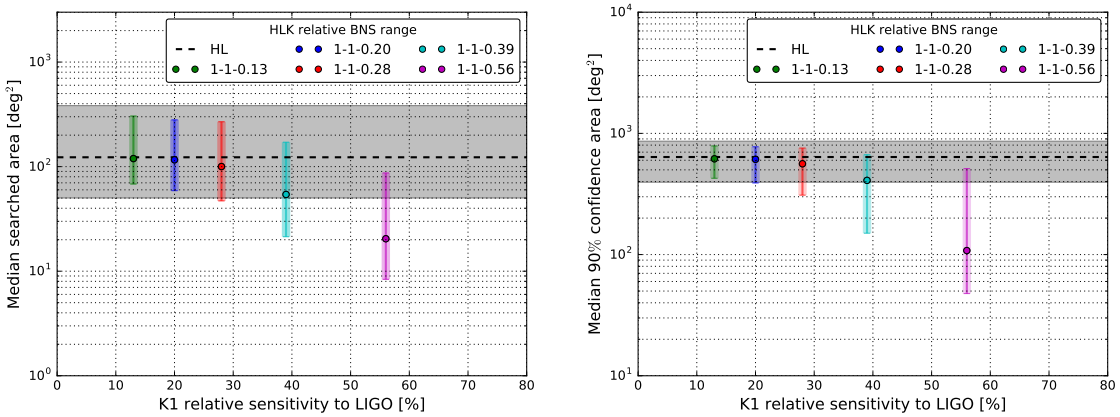

Figure 3.13: The median searched area ($left$) and 90% confidence area ($right$) with the interquartile ranges are shown as a function of the relative sensitivity of KAGRA compared to the LIGO one where the KAGRA threshold is set to 3.5. The colors show the network configuration.

3.4.2 Comparison to HLV-network performance

As seen in Figure 3.9 and 3.12, the size of the reconstructed sky maps by the HLK-network would become larger than that by the HLV-network, by roughly a factor of 2. This feature would come from the geometry of the network detector positions. The geometry of the HLK-network is slightly less favorable than the geometry of the HLV-network.

In order to test this statement, we confirm the followings.

1. The consistent sky localization performances for $\mathrm{HLK_i}$ are obtained, i.e. it is confirmed that the fraction of injections found within the area at a given confidence level matches that confidence level.

2. The population of HL, $\mathrm{HLK_i}$, $\mathrm{HLK_n}$ triggers are mostly similar to the ones of HL, $\mathrm{HLV_i}$, $\mathrm{HLV_n}$.

3. The SNR distributions of $\mathrm{HLK_i}$, $\mathrm{HLK_n}$ triggers are also similar to the ones of $\mathrm{HLV_i}$, $\mathrm{HLV_n}$.

4. This performance does not come from the difference of the used noise curves.

In addition, We investigate the performance by HLV-network and HLK-network with the events whose effective distances are close to each other as shown below.

Examination of localization performance with similar D_{eff} events

We select the HLV- and HLK-events whose difference of the effective distance is smaller than 10% (i.e, with a condition of $\mid 1 - D^{\mathrm{V}}_{\mathrm{eff}}/D^{\mathrm{K}}_{\mathrm{eff}} \mid < 0.1$). We then calculate the localization performance with the pure injection parameters without adding the small random number derived from a Gaussian distribution. The result is shown in Figure 3.14. Although we find just 28 such events, this shows that the HLK-network would give larger-reconstructed sky maps compared to the ones by HLV-network in average. One example of the sky maps are drawn in Figure 3.16. The sky maps would imply that the reconstructed region by HK or LK information comparably more parallel to the ring-shape by HL information than the ring by HV or LV information. As a result, the intersection tends to be larger. This seems to connect to the geometry of the detector position. The detector triangles composed of the two LIGO detectors with Virgo and KAGRA detector is shown in Figure 3.15. This figure shows that the triangle made by HLK-detectors are flatter than the one made by HLV-detectors. In addition, the difference of the determinants of a matrix $\boldsymbol{M}$ in section 2.1.3 as eq (2.11), is roughly by a factor of 2, which is consistent of the difference observed in the localization performance difference.

Based on the above, we would conclude that the performance by HLV-network would become better than that by HLK-network, due to the geometrical configuration of the detectors. The obtained results shown in Figure 3.12 are the counterpart for the performance by HLV-network in Figure 3.9.

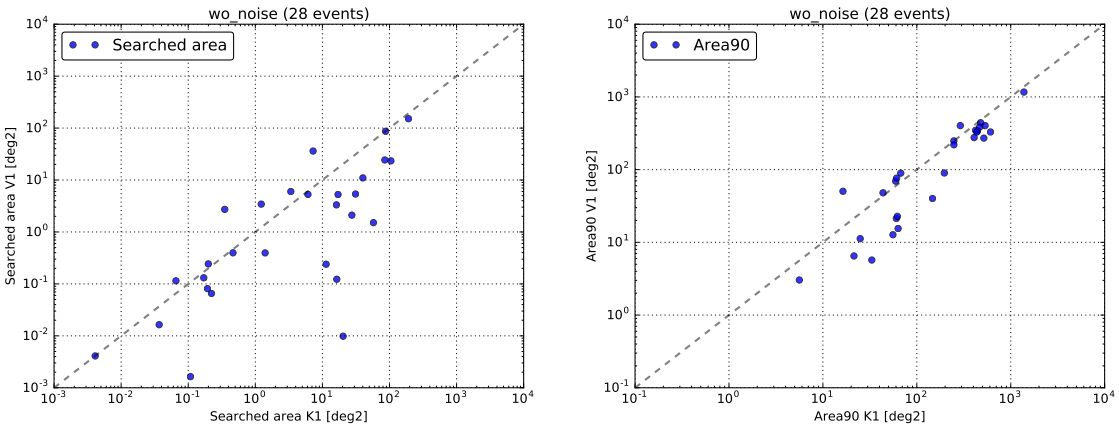

Figure 3.14: The sky localization performance by HLV- and HLK-network with similar $D_{\rm eff}$ events. These plots show the median values.

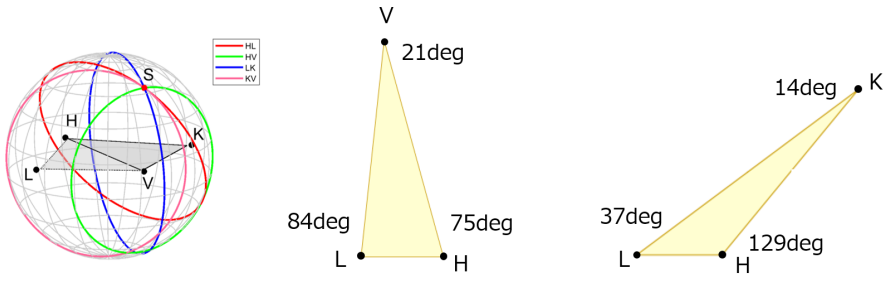

Figure 3.15: The triangles composed of the three detectors. H, L, V and K denote the LIGO Hanford detector, LIGO Livingston detector, Virgo detector and KAGRA detector. The triangle composed of the HLK detectors is more flatter than the triangle composed of the HLV detectors. The most left figure is from [53].

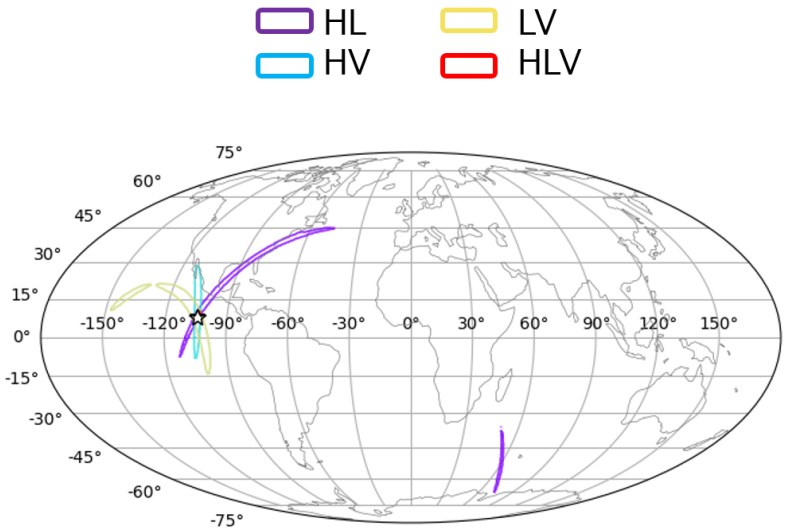

(a) Sky map example obtained by LIGO-Virgo network. The area reconstructed by HLV-network (red) is mostly hidden by the star.

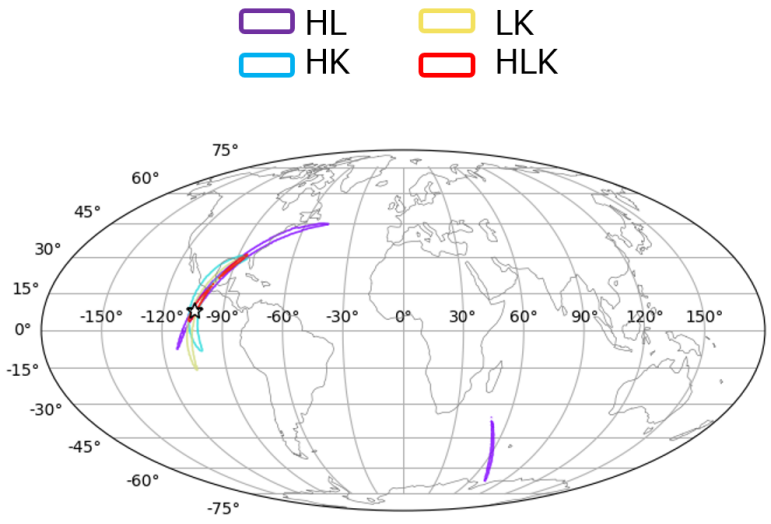

(b) Sky map example obtained by LIGO-KAGRA network

Figure 3.16: Sky map example obtained by LIGO-Virgo network (a) and by LIGO-KAGRA network (b).

3.5 Expected performance of heterogeneous HLVK-network

In accordance with HLV- and HLK-network case procedure, using the settings in section 3.2.3, 3.2.5 and 3.2.6, we generate sky maps of 248 events and investigate the localization performance by collecting the median values of searched area and 90% confidence area. In this calculation, we assume that the sensitivity of Virgo detector is half of the sensitivities of the two LIGO detectors. This calculation is repeated with different SNR thresholds in KAGRA (from 2 to 10), and also done in different SNR threshold in Virgo (3.0, 3.5, 4.0 and 5.0). The procedure was repeated twice in order to check that the results were not overly sensitive to a particular realization of the random numbers used in the simulation. We also consider a case where the less sensitive detectors Virgo and KAGRA generate background triggers stably in this calculation.

3.5.1 Dependence on the sensitivity of the fourth detector KAGRA

The expected performances of the searched area and the 90% confidence area by this network are shown in Figure 3.17 to 3.20. Figure 3.17 shows the expected improvement ratio of the performance of HLVK triggers to that of the same triggers treated as HLV coincidences. Figure 3.18 shows the expected performances of the searched area and the 90% confidence area obtained from all the 248 events. These two figures draws the case where the SNR threshold for Virgo is to 5.0. Figure 3.19 and 3.20 reports the performance when the SNR threshold of Virgo detector is set to 3.5, with the same manner as Figure 3.17 and 3.18. The expected performances with other configuration are summarized in section A.2.4. We calculate this performance for various BNS ranges of the KAGRA detector, by scaling its expected SNR and its noise curve. The relative detector sensitivities are written down as 1-1-0.5-x, with x the ratio of the KAGRA sensitivity compared to the two LIGO detectors. The population of the HL, $\mathrm{HLV_i}$, $\mathrm{HLV_n}$, $\mathrm{HLK_i}$, $\mathrm{HLK_n}$, $\mathrm{HLV_iK_i}$, $\mathrm{HLV_nK_n}$, $\mathrm{HLV_iK_n}$ and $\mathrm{HLV_nK_i}$ events are summarized in section A.2.

Similarly to the HLK-network case, the lowest sensitive detector begins to improve the localization performance as soon as its sensitivity is 28% of the more sensitive detectors, based on Figures 3.18 and 3.20. Then the optimal SNR threshold lies in the range from 3 to 3.5. In the case where the SNR threshold of Virgo detector is set to 5.0, i.e where the information of Virgo detector is not much reflected to the sky maps, KAGRA detector information will contribute to improvement of the localization performance relatively significantly. On the other hand, in the case where the SNR threshold of Virgo detector is set to 3.5, i.e where the information of Virgo detector is already reflected to the sky maps, KAGRA detector information would contribute less to improving the localization performance

It must be noted that, Figure 3.17 and 3.19 report that as the detector sensitivity of KAGRA increases, the averaged performance by HLVK-network at higher SNR threshold in KAGRA detector becomes worse. This happens since

we start from the events detection by the LIGO detectors, which is unfavorable to KAGRA detector, and thus that happens since KAGRA detector finds more events which are less aligned to KAGRA detector as its sensitivity is increased.

Consequently, the lowest sensitivity detector begins to improve the localization performance clearly as soon as its sensitivity is one third of the most sensitive LIGO detectors, which is two third of the sensitivity of the middle sensitive detector Virgo, with the optimal SNR threshold lies in the range from 3 to 3.5.

By following the LIGO-Virgo and LIGO-KAGRA network case, we select the threshold in Virgo and KAGRA to 3.5. The dependence on the sensitivity of KAGRA detector at the threshold is equal to 3.5 is shown in Figure 3.21. This performance is expected where Virgo has half of the LIGO sensitivity and its threshold is set to 3.5. In this configuration, we find that as the sensitivity of KAGRA approaches half of the LIGO one (same as Virgo one), the accuracy and precision of the localization can be improved by about a factor of 2 and 2.5, compared to LIGO-Virgo network.

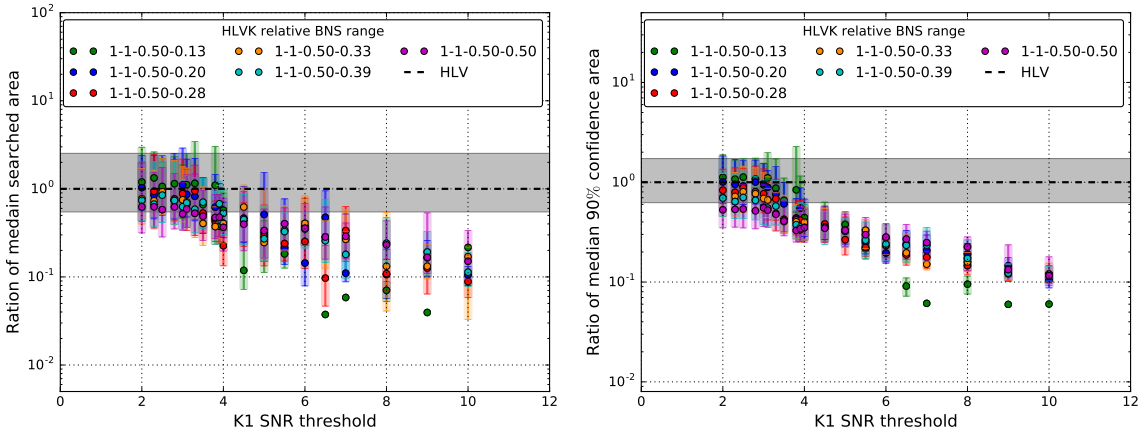

Figure 3.17: Ratio of the median searched area (*left*) and 90% confidence area (*right*) of HLVK triggers to that of the same triggers treated as HLV coincidences, when the sensitivity of the KAGRA detector is varied. The colors show the network configuration. This is the case where the SNR threshold for Virgo is set to 5.0.

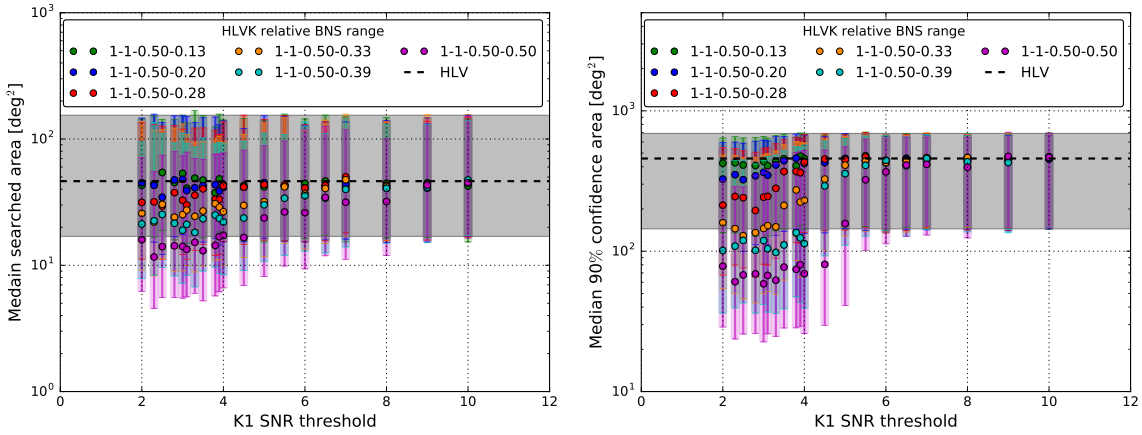

Figure 3.18: The median searched area (*left*) and 90% confidence area (*right*) are shown as a function of the SNR threshold used in KAGRA. Expected sky localization performance with the hierarchical search when the sensitivity of the KAGRA detector is varied. The colors show the network configuration. This is the case where the SNR threshold for Virgo is set to 5.0.

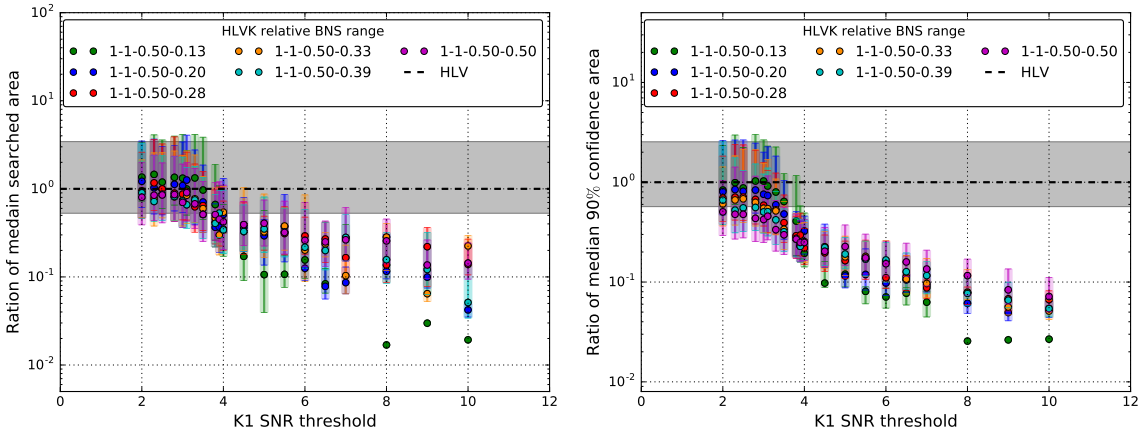

Figure 3.19: Ratio of the median searched area (*left*) and 90% confidence area (*right*) of HLVK triggers to that of the same triggers treated as HLV coincidences, when the sensitivity of the KAGRA detector is varied. The colors show the network configuration. This is the case where the SNR threshold for Virgo is set to 3.5.

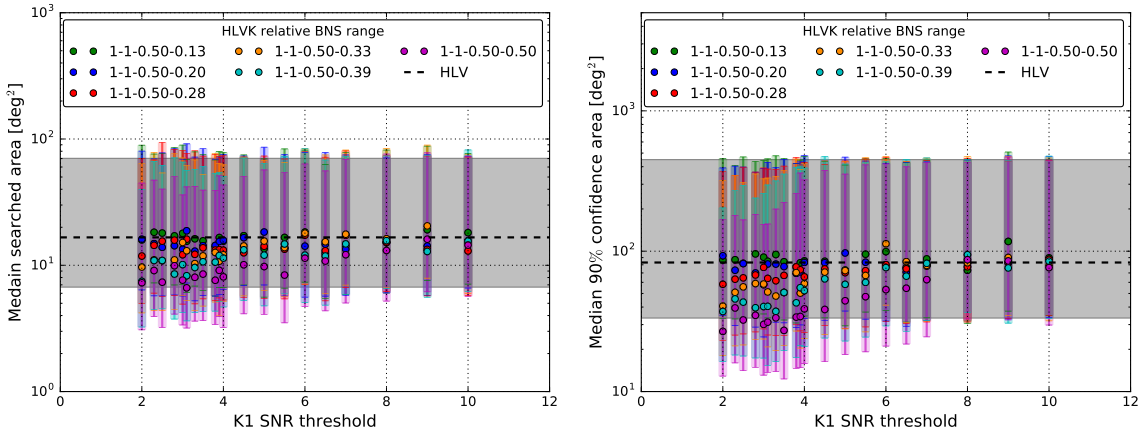

Figure 3.20: The median searched area (*left*) and 90% confidence area (*right*) are shown as a function of the SNR threshold used in KAGRA. Expected sky localization performance with the hierarchical search when the sensitivity of the KAGRA detector is varied. The colors show the network configuration. This is the case where the SNR threshold for Virgo is set to 3.5.

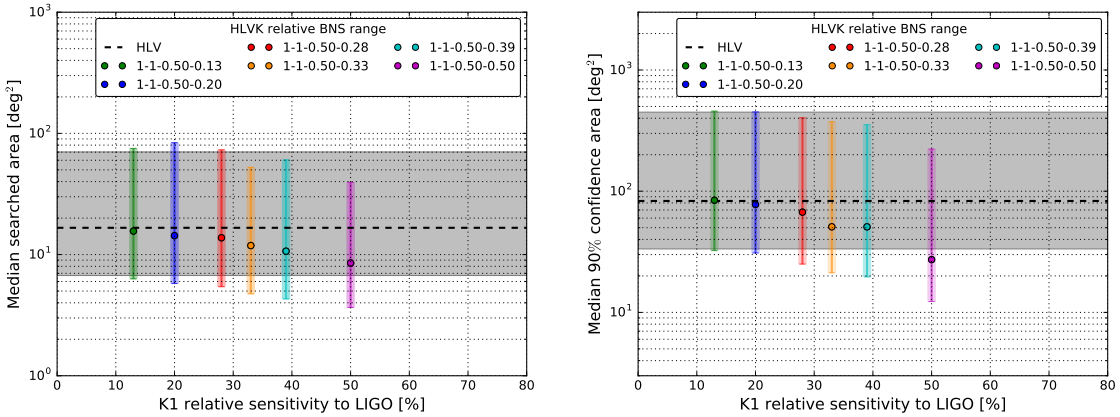

Figure 3.21: The median searched area (*left*) and 90% confidence area (*right*) with the interquartile ranges are shown as a function of the relative sensitivity of KAGRA compared to the LIGO one where the KAGRA threshold is set to 3.5. In this configuration, it is assumed that Virgo has half of the LIGO sensitivity and its threshold is set to 3.5. The colors show the network configuration.

3.6 Summary

Using MBTA and Bayestar, we show the expected fast localization performance for GWs from compact binary coalescence when a hierarchical search is implemented into a GW-EM follow-up pipeline. We confirm that the hierarchical search improves both the localization accuracy and precision in low-latency mode, compared to those achieved by a double coincidence search with the two LIGO detectors alone.

The hierarchical network effectively improves the localization accuracy and precision when threshold SNR for the lower sensitivity detector is set to around 3.5 provided that the BNS range of that the detector is greater than 20% of the more sensitive detectors in the case where the detector network is composed of the two LIGO detectors and the Virgo detector. We find that as the sensitivity of Virgo approaches half of the LIGO one, the accuracy and precision of the localization can be improved by about a factor of 7, compared to LIGO network.

In the case where the detector network is composed of the two LIGO detectors and KAGRA detector, we found a clear sky localization improvement when the relative sensitivity of KAGRA becomes greater than 28% of the more sensitive detectors. We find that as the sensitivity of KAGRA approaches half of the LIGO one, the accuracy and precision of the localization can be improved by about a factor of 3.5, compared to LIGO network.

In addition, the hierarchical network by four detectors will improve the localization accuracy and precision when threshold SNR for the lowest sensitivity detector is set to around 3.5 provided that the BNS range of that the detector is greater than 28% of most sensitive detectors. This result assumes that the sensitivity of the middle sensitive Virgo detector is half of the LIGO one. In this configuration, we find that as the sensitivity of KAGRA approaches half of the LIGO one (same as Virgo one), the accuracy and precision of the localization can be improved by about a factor of 2 and 2.5, compared to LIGO-Virgo hierarchical network.

Consequently, the search with this hierarchical approach will be most useful when adding new, less sensitive detectors to the network, as they are undergoing commissioning.

Realizing higher network duty cycle

This study did not consider the aspect of the network duty cycle. Indeed the probability to have at least three detectors up and running increases considerably when a fourth detector is added to the network. This is another benefit of adding detectors to the network and reduces the chances to miss detectable events. This comes from a fact that sometimes a GW detector is not operational due to interferomenter lock loss and/or maintenance operation. For example, assuming that all the detectors have an equal duty cycle of 80%, the duty cycle by three detectors in the three detector network would be about 51%. On the other hand, for a network made by four detectors, the duty cycle by three or four detectors becomes about 82%. This implies that in the three- and four-detector network, respectively about 49% and 18% of the detected events would have poor reconstructed sky position, even though all the network detectors have enough sensitivities. This is not suitable to the target of the EM follow up observation. This fact implies that operating a fourth robust interferometer is of paramount importance to achieve high network duty cycle.

The following chapter start to focuses on realizing a system to allow a robust interferometer operation for the fourth detector KAGRA.

Chapter 4

KAGRA seismic attenuation system (SAS)

In ground-based GW detectors, the main optics are suspended by a pendulum system called seismic attenuation system (SAS) in order to decouple them from the seismic vibration of the ground, as taking care of the mechanical resonances in order not to drastically decrease the duty cycle.

In KAGRA detector, three types of SAS are installed depending on the required displacement noise level above 10 Hz as detailed in sections 1.4.2 to 1.4.4.

This chapter briefly summarises the background information about KAGRA SAS needed to understand the work presented in the next chapters. This chapter also reports the measured/estimated sensor noise floors which is done for a preparation of building the target active control system (in the next chapter).

Section 4.1 describes each mechanical component which composes the KAGRA SAS. Section 4.2 introduces the sensors and actuators which are implemented in the KAGRA SAS. This subsection reports the measured/estimated noise floors of those sensors. Section 4.3 briefly summarizes the assembled KAGRA SAS mechanics and the expected mirror displacement. More details about the three suspension systems can be found in [48, 44, 54].

4.1 Building blocks of KAGRA SAS

As introduced in section 2.2.2, we realize sufficiently low resonant frequency system with a compact mechanics, using the anti-spring techniques. In this subsection the main components which constitute the three type of SAS are described.

4.1.1 Inverted pendulum (IP) stage

IP-stage is composed of a frame structure on the ground, three inverted pendulums (IPs) and the top-stage where a GAS filter (see section 4.1.2) is mounted. The overview of IP-stage is shown in Figure 4.1. The three IPs are 120° separated and they support the top-stage. The detailed structure of the IP leg in shown in

Figure 4.2. Each IP leg is supported by a cone bellows on a jack. The jacks are used for the tilt adjustment of the IP-stage.

IP-stage has three sets of coil-magnet actuators and two kinds of sensors mounted in a pinwheel geometry. The implemented sensors are displacement sensors and inertial sensors. More specifically, as displacement sensors, we use linear variable differential transducer called LVDT (see section 4.2.1). As inertial sensors, we use geophones L-4C for the two ETMs and accelerometers (which were developed for TAMA detector) for the ITMs[1]. The details about these inertial sensors are described in section 4.2.2. These two kinds of sensors on the IP-stage are originally used by combining their signals as introduced in section 2.2.3, in order to use LVDT signal at lower frequency and inertial sensor signal at higher frequency. The IP-stage can also be used to adjust the initial position of the suspended mirror in the horizontal direction by using a motorized blade spring system.

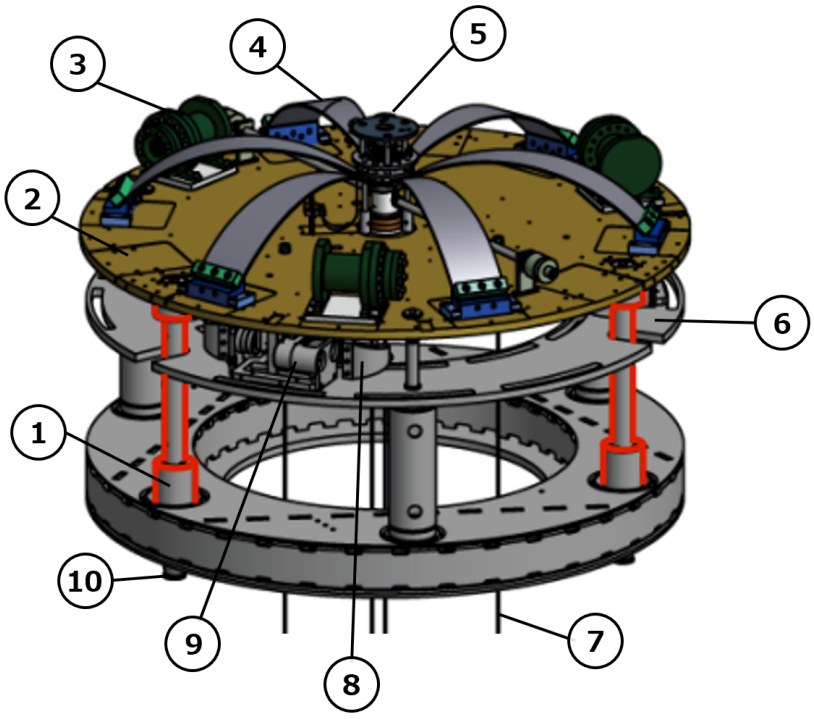

Figure 4.1: The overview of IP-stage. 1) IP leg, 2) top stage, 3) inertial sensor for sensing the IP top stage motion, 4) the cantilever of F0 GAS filter, 5) keystone of F0 GAS filter, 6) frame structure where one end of the LVDTs and the motorized blade spring are attached, 7) suspension wires, 8) motorized blade spring, 9) LVDT and the coil-magnet unit, 10) cup of cone bellows.

[1]For ITMs, we are planning to replace the TAMA accelerometers to geophones in observation before the next observing run.

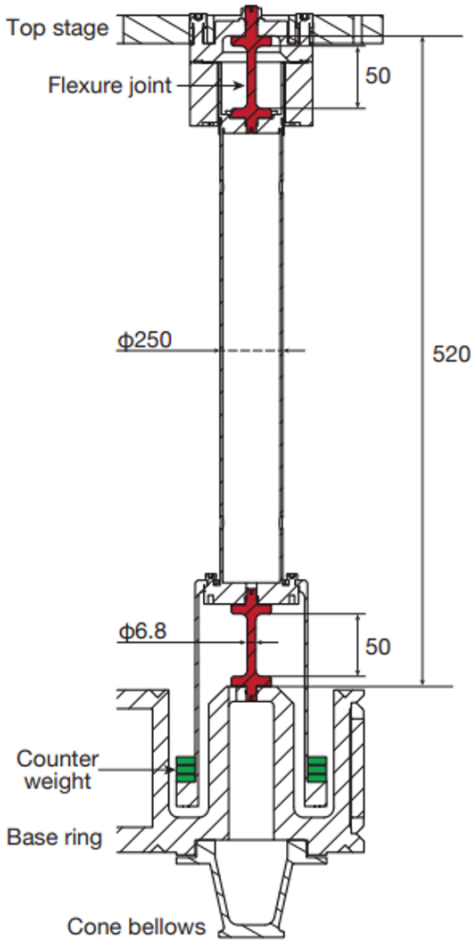

Figure 4.2: The details of the IP leg. The counter weight is implemented in order to the saturation level in the displacement transfer function as described in section 2.2.2 (This figure is from [44]).

4.1.2 GAS filters

As introduced in section 2.2.2, the GAS filter is composed by a set of symmetrically arranged cantilever blades. The cantilever blades are made of maraging steel [55]. This material is selected in order to avoid creep deformation, which is the tendency of a material to drift slowly when it is under high stress conditions. Figure 4.3 shows the detailed structure of a GAS filter, known as standard filter (SF). Figure 4.4 shows its cross-section. The width and number of the cantilever blades are tuned in accordance with the weight of the suspended masses. Each GAS filter is covered by a metal cup in order to realize the required mass load and to attach electrical cables on the surface of it. The multi-stage pendulum system in KAGRA is composed of a chain of GAS filters. The number of the GAS filters in the chain is selected with suspension type depending on the required vibration attenuation level.

Each GAS filter has a LVDT and a coil-magnet actuator to actively control it (see section 4.2). LVDT measures the relative height variation between the base plate and the keystone.

The GAS filter has a motorized position adjustment system for the keystone in vertical realized by using blade spring. This system is called fishing rod. The most top and bottom GAS filter have a motorized Yaw position adjustment system for the mirror torsional position.

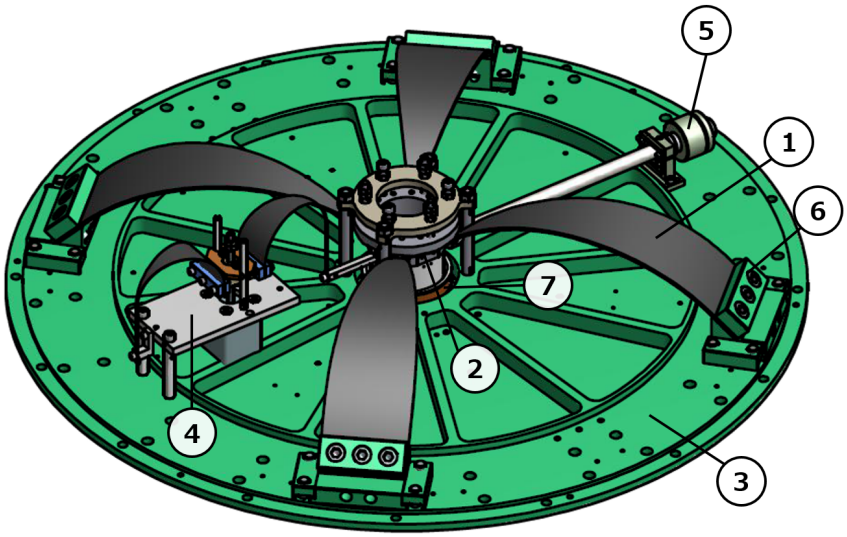

Figure 4.3: The mechanical overview of the typical GAS filter, called standard filter. 1) The cantilever blade, 2) the keystone, 3) the baseplate, 4) the motorized spring for initial positioning of the keystone, 5) the magic-wand for compensating CoP effect (see section 2.2.2), 6) the base clamp, 7) the LVDT to monitor the displacement of the keystone.

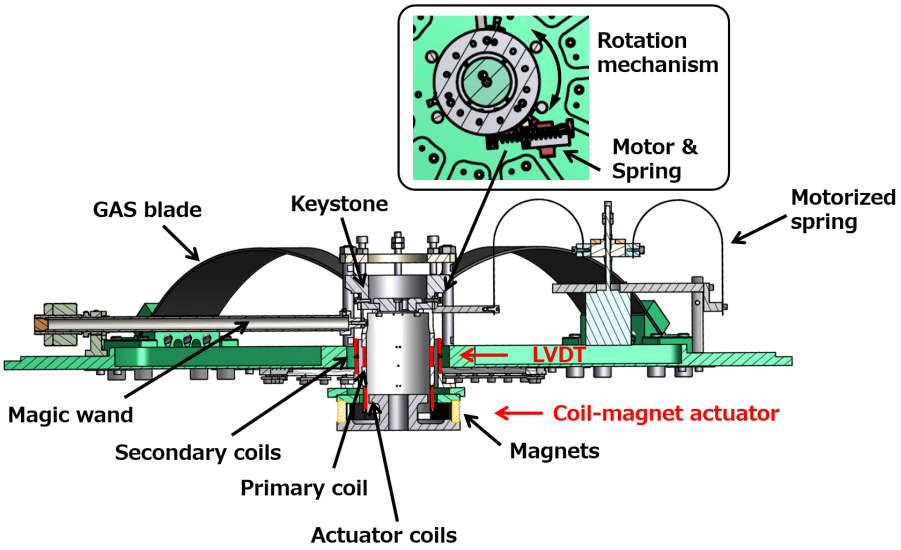

Figure 4.4: The cross-section of GAS filter [54].

Effect of blade compression

The compression of the GAS blades is tuned so that the keystone balances the suspended payload at the working point. According to eq (2.30), $k_{\rm eff}$ can have a negative value depending on the compression, in which case the system becomes unstable and the GAS filter does not work properly. This is explained with eq (2.30) and the following equation:

$$m - m_0 = -\frac{(k_z + k_x{}')z}{g} + \frac{k_x{}' l_{0x}}{g} \frac{z}{\sqrt{{x_0}^2 + z^2}}, \tag{4.1}$$

which is obtained assuming the keystone is at its equilibrium position in eq (2.28). Using these equations Figure 4.5 shows the working point and the resonant frequency as the function of the suspended mass load, with some compression $C = (l_{0x} - x_0)/l_{0x}$in the model. Typically, the compression is tuned so that the GAS behaves like the case of 9% compression in figure 4.5. Consequently, we have to tune the suspended load very carefully in the actual system.

Thermal drift

The keystone height can easily drift with slight temperature variation of the blade springs. The drift of the keystone due to the temperature dependence of the Young's modulus of the blade spring material can affect the GAS filter operation.

The impact can be estimated as follows. We assume that the GAS filter balances at the working point with a suspended mass of m. In this situation, the height change Δz when the load on the keystone is changed by Δm can be given by $\Delta z = g\Delta m/k$, where k and g are the effective stiffness of the GAS filter and

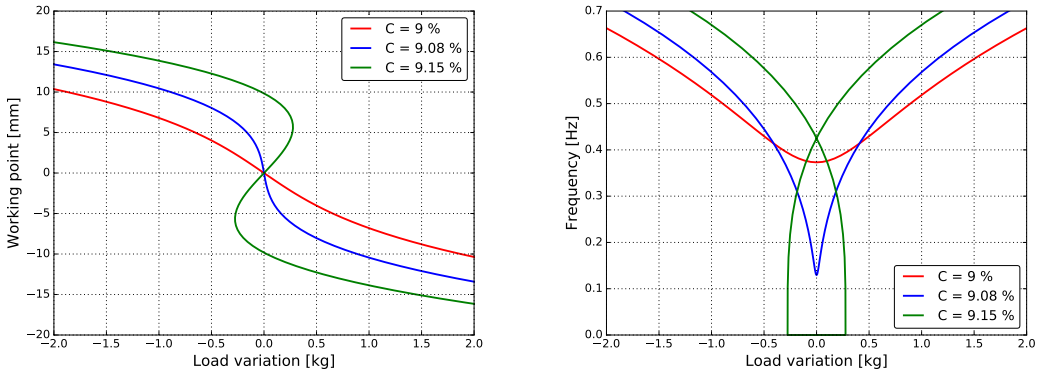

Figure 4.5: Working point height of the keystone (*left*) and its resonant frequency (*right*) as a function of suspended mass load, with various compression of the GAS blade, predicted with the model, when the following setting is used: $k_z = 1.0 \times 10^5$ N/m, $k_x{}' = 1.0 \times 10^6$ N/m and $l_{0x} = x_0$ =0.3 m. It is assumed $m_0 = 200$ kg in the *right* panel.

gravitational acceleration respectively. In addition, assuming $\Delta m/m = \Delta E/E$ is known (where E is Young's modulus of the blade), the temperature dependence of the keystone height is given by:

$$\frac{\Delta z}{\Delta T} = \frac{g}{k}\frac{\Delta m}{\Delta T} = \frac{mg}{kE}\frac{\Delta E}{\Delta T} = \frac{g}{\omega_0^2 E}\frac{\Delta E}{\Delta T}, \tag{4.2}$$

where T is the temperature of the blade. Experimentally this dependence was measured as [48]

$$\frac{\Delta z}{\Delta T} = 0.69\ [\mathrm{mm/K}] \left(\frac{0.33\ \mathrm{Hz}}{\omega_0/2\pi}\right)^2 \left(\frac{\frac{1}{E}\frac{\partial E}{\partial T}}{3.0 \times 10^{-4}\ [1/\mathrm{K}]}\right), \tag{4.3}$$

where ω_0 is the resonant angular frequency of GAS filter.

This implies that it is important not only to keep constant the environmental temperature but also to keep constant the height by using control system, in order not to give impact the inetrferometer operation.

4.1.3 Suspension wires

The mechanical components at room temperature are suspended by using wires made of maraging steel. Figure 4.6 shows their detailed structure. The wire has thicker diameter in its middle part compared to the ends. It is demanded to use larger diameter wire in order to obtain stronger torsional stiffness, which is good for the interferometer operation. On the other hand, if the diameter is too large, the longitudinal vibration attenuation performance can be degraded. This is due to a fact that the elastic force of the wire can become non-negligible compared to the gravitational restoring force. Based on this fact, the shape is selected, and the diameter is adjusted depending on the suspended mass.

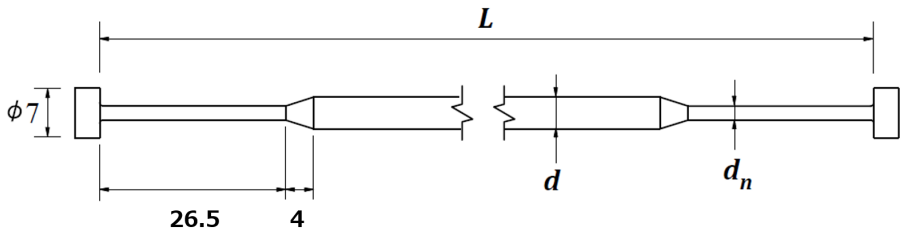

Figure 4.6: Overview of the typical suspension wire made of maraging steel.

4.1.4 Magnetic damper

A passive damper which utilizes the eddy-current as introduced in section 1.3.1 is called magnetic damper. The braking force works between two ring-shaped plates. One plate includes an array of magnets (72 magnets in total) as shown in Figure 4.7. A magnetic damper works effectively when the displacement gap between the two plates are set to about 2.5 mm in KAGRA SAS.

4.1.5 Bottom filter

The GAS filter at the lowest stage in the GAS-filter chain is called bottom filter (BF). BF has motorized tilt adjustment system, and is used to set the gap between the recoil mass and intermediate mass for the room-temperature payload (see section 4.1.6) for the initial alignment. By adjusting the pitch and roll of BF, we can adjust the gap between IM and IRM (see section 4.1.6) respectively in the longitudinal and transverse direction. The schematic of this system is show in Figure 4.8.

Damping system at BF

Depending on the suspension, we also have an active damping system at BF stage. We implement six sets of LDVTs and coil-magnet actuators around the BF body in order to damp the resonant modes which cannot be damped with

the upper stages. The LVDT and actuator unit used for the BF-stage damping is called BF-LVDT (see section 4.2.1).

We have two types of implementation. In one case, one end of BF-LVDT unit is mounted on the ground, i.e, on the security frame structure. In the other case, the end is mounted on a suspended mass. The overview of this system is shown in Figure 4.9.

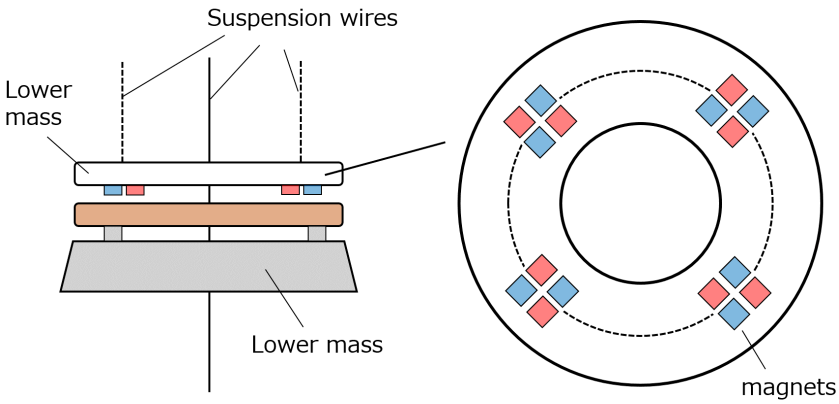

Figure 4.7: Over view of magnetic damper. The magnets are arranged as shown in the picture on the *right*, and the difference of the colors denotes the difference of magnetic pole.

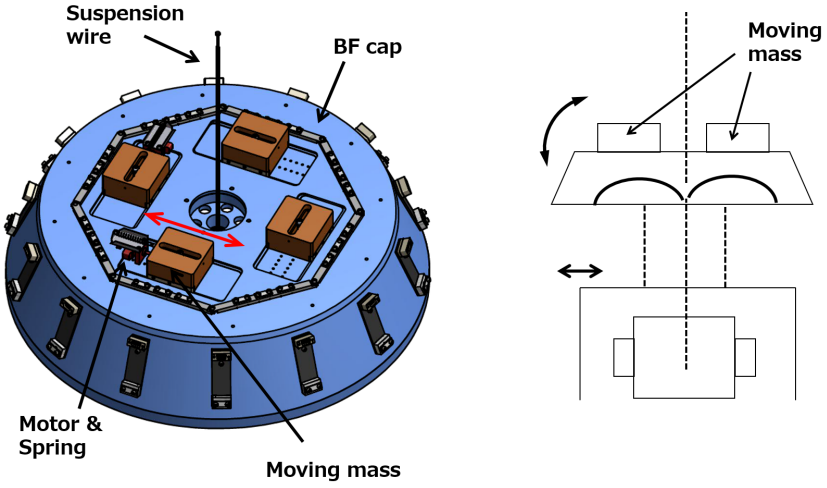

Figure 4.8: Overview of BF tilt adjustment system [54].

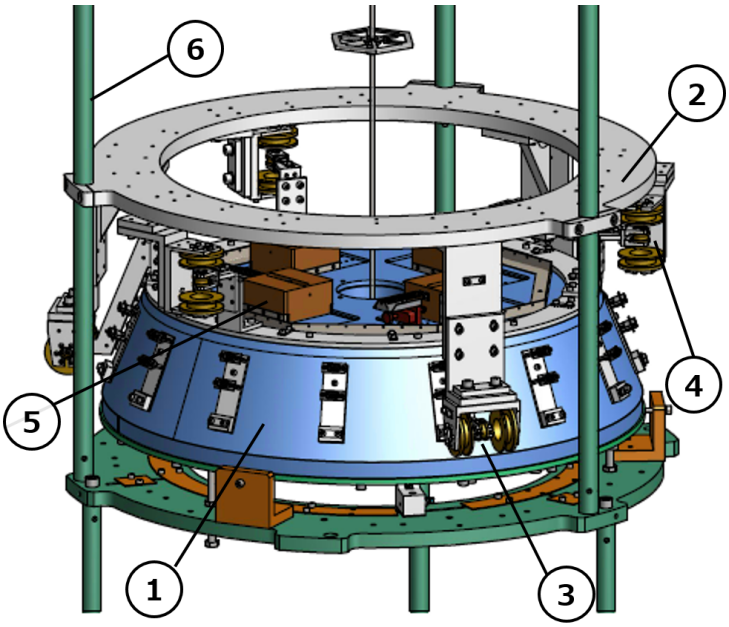

(a) 1) The body of the bottom GAS filter, 2) the BF-damper structure attached to the security frame, 3) the horizontal BF-LVDT and coil-magnet actuator unit, 4) the vertical BF-LVDT and coil-magnet actuator unit, 5) the motorized BF-tilt adjustment system, 6) the security frame.

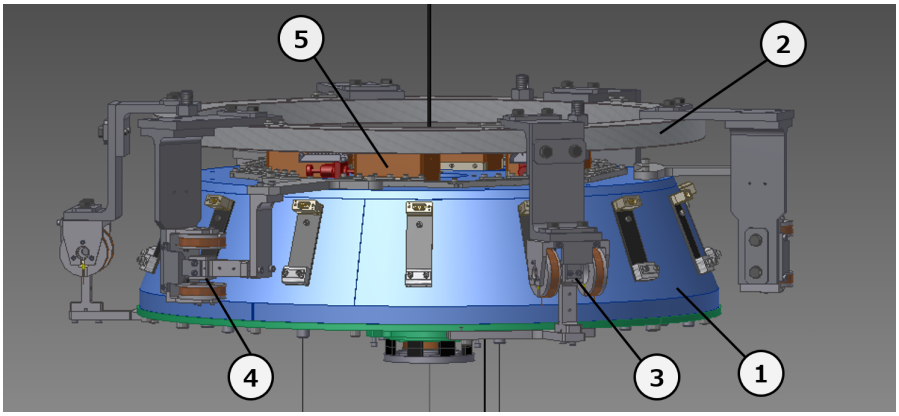

(b) 1) The body of the bottom GAS filter, 2) the suspended recoil mass for the bottom GAS filter, 3) the horizontal BF-LVDT and coil-magnet actuator unit, 4) the vertical BF-LVDT and coil-magnet actuator unit, 5) the motorized BF-tilt adjustment system [54].

Figure 4.9: Overview of damping system at BF where one end of the sensor and actuator unit is mounted on the security frame structure (a) and where one end is mounted on a suspended mass (b).

4.1.6 Payload

The lowest part of the suspension system is called payload. The payload is used for:

1. steering the mirror in pitch and yaw for the interferometer alignment,
2. additional seismic attenuation,
3. damp the payload resonances.

Depending on the suspension, we have two types of payload; one is used at room-temperature, and the other one is used at cryogenic temperature.

Room-temperature payload

Room-temperature payload has two stages and is composed of:

1. an intermediate mass (IM) and an intermediate recoil mass (IRM),
2. a test mass (TM), a recoil mass (RM),

as shown in Figure 4.10. IM is suspended by single maraging wire from BF keystone, and IRM is suspended by three magaring wires from the underneath of BF. TM and RM are suspended from IM by two loop-shaped tungsten wires. As local sensors and the actuators, we use an optical sensor and electro-magnetic actuator called OSEM (see section 4.2.3). OSEMs are implemented at the IM-stage and measure/actuate the relative motion between IM and IRM in six dofs. Also TM stage has OSEMs but they are only used as actuators. The detailed OSEM positions are shown in Figure 4.11. As additional local sensor, TM stage has also an optical lever (see section 4.2.4) to measure its motion in longitudinal, pitch and yaw direction.

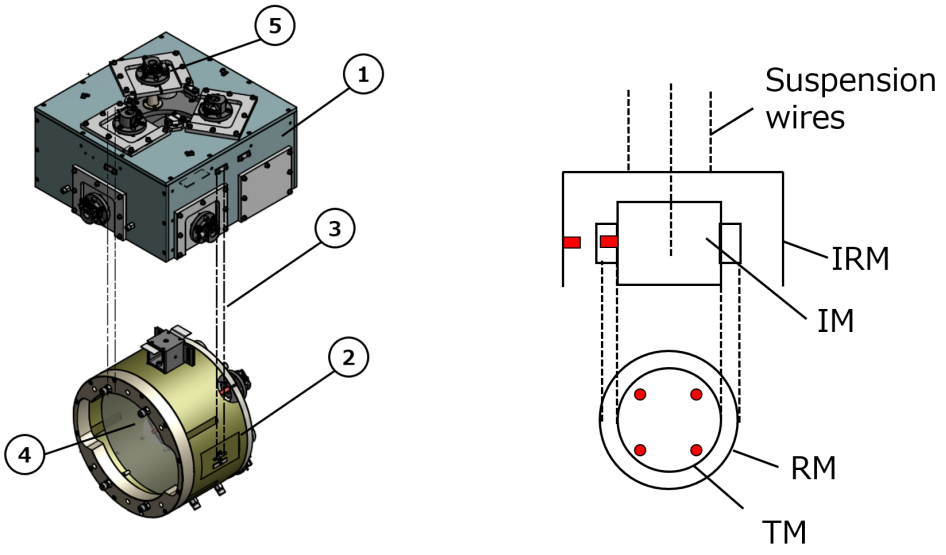

Figure 4.10: Overview of room-temperature payload. 1) intermediate recoil mass (IRM), 2) recoil mass (RM), 3) tungsten wires to suspend RM from IM, 4) test mass (TM), 5) OSEM at IM-stage (in *left*) The red colored dots and the rectangles schematically show OSEM unit positions (in *right*).

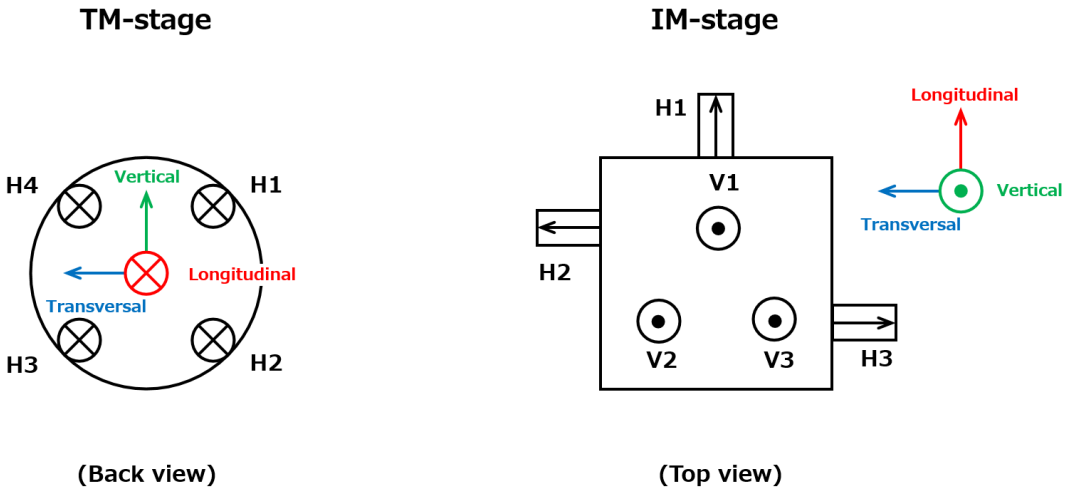

Figure 4.11: Detailed OSEM location. H1, H2, H3 and H4 denote the position of OSEM for horizontal motion, and V1, V2 and V3 show the OSEM position for vertical motion. The arrows show the sensor and actuator polarities. TM-stage has only actuators.

Cryogenic payload

Cryogenic payload is developed to operate at cryogenic temperature and, as shown in Figure 4.12, consists of four stages:

1. platform (PF)
2. marionette (MN), recoil marionette (RMN)
3. intermediate mass (IM) and intermediate recoil mass (IRM),
4. test mass (TM) and recoil mass (RM)

In this payload, PF is suspended by maraging wire from BF, and two suspension chains are suspended from PF. These two chains are called TM chain and RM chain respectively. One chain includes MN, IM and TM, and the other chain suspends RMN, IRM and RM. MN is suspended from cantilever blades at PF-stage by single maraging wire (of thinner diameter). IM is suspended from MN by four copper-beryllium wires, and the TM is suspended by four sapphire fibers from IM. The sapphire fibers are hooked to a sapphire blades at IM-stage. On the other hand, RMN is suspended from the underneath of the PF by three wires, IM is suspended from RMN by four wires, and RM is suspended by two loop wires from IRM. All the RMN, IRM and RM are suspended by copper-beryllium wires. Each stages are connected with high purity aluminum wires, which is called heat links (see cooling system in section 4.3.1).

As local sensors and the actuators in cryogenic payload, we use reflective photo sensors (PS) and coil-magnet actuators developed for this cryogenic payload (see section 4.2.5). PS measure the relative motion between TM-chain and RM-chain in six dofs. The detailed PS and the actuator positions are shown in Figure 4.11. As additional local sensor, TM-stage and MN-stage have an optical lever (see section 4.2.4), measures the MN-, TM- chain motion in pitch and yaw. Only at TM-stage, another optical lever which measure TM-chain motion in longitudinal (see section 4.2.4) is implemented.

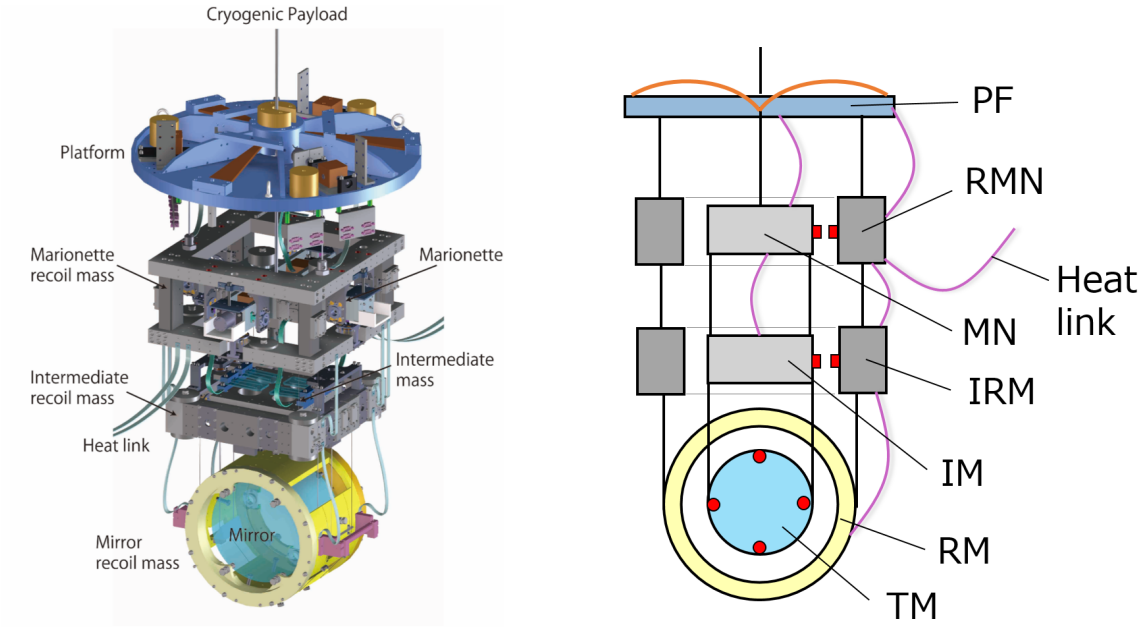

Figure 4.12: Overview of the cryogenic payload. The red colored dots and the rectangles schematically show photo-sensor (PS) and actuator unit positions. For TM-stage, only actuators are implemented.

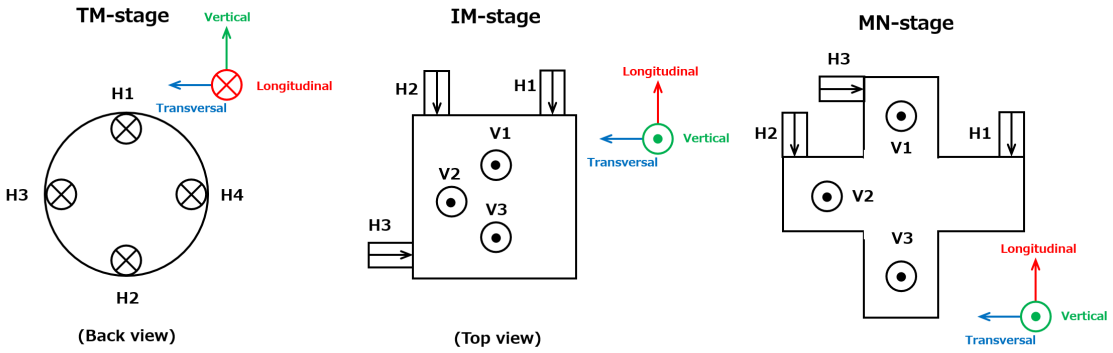

Figure 4.13: Detailed PS and actuator location. H1, H2, H3 and H4 denote the position of PS for horizontal motion, and V1, V2 and V3 show the photo-sensor (PS) position for vertical motion. The arrows show the sensor and actuator polarities. TM-stage has only actuators.

4.2 Sensors and Actuators

The sensors and actuators implemented in the KAGRA SAS are briefly introduced. The measured/estimated noise floors of those sensors are also reported in this subsection. Those measurement/estimation is done for a preparation of building the active control system (in the next chapter).

4.2.1 Linear Variable Differential Transducer (LVDT)

Linear Variable Differential Transducer (LVDT) is a non-contacting relative position sensor using coil inductance and modulating magnetic fields [56]. LVDT is composed of three coaxial coils, more concretely, composed of a small coil and 2 larger diameter coils as shown in Figure 4.14. The smaller coil and the two larger coils are called primary and secondary coil(s) respectively. LVDT measures the displacement of the primary coil from the center of the secondary coils.

We have two kinds of LVDTs; one type consists of the three coils, and the other type has a magnet inside the primary coil holder. The first type is called LVDT and the other type is called BF-LVDT since they are used for the damping system at BF-stage. BF-LVDT shares the coils for sensing and actuation [57]. In LVDT case, we have another coil (and magnet) for actuation, on the other hand, in the BF-LVDT case, we use the coils for both sensing and actuation purpose. The typical noise floor and the linear range are shown in Figure 4.15.

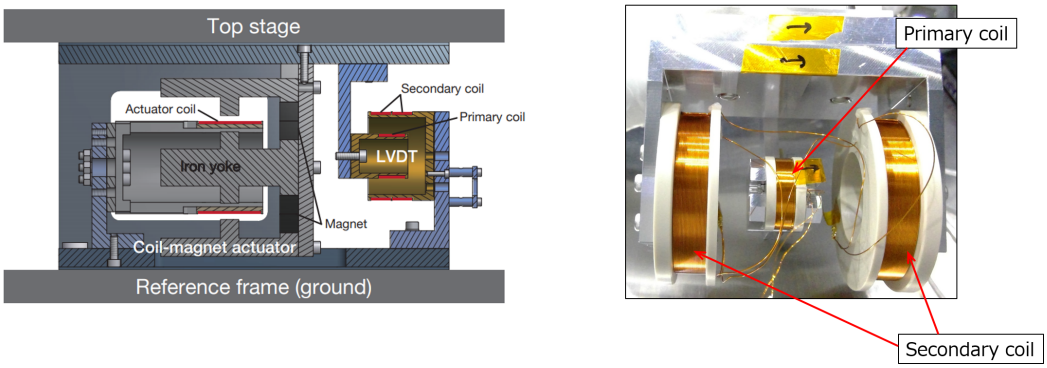

Figure 4.14: The detailed structure of LVDT from [44] (*left*) and that of BF-LVDT (*right*). The structure of GAS-LVDTs is shown in Figure 4.4.

4.2.2 Inertial sensor

Due to planning constrain, two different kind of inertial sensor are currently used. One is an accelerometer developed for TAMA-SAS [43] and the other one is a commercial speedmeter, geophone L-4C. The TAMA-accelerometers are used in the two ITM suspensions, while the geophones are implemented in the two ETM suspensions.

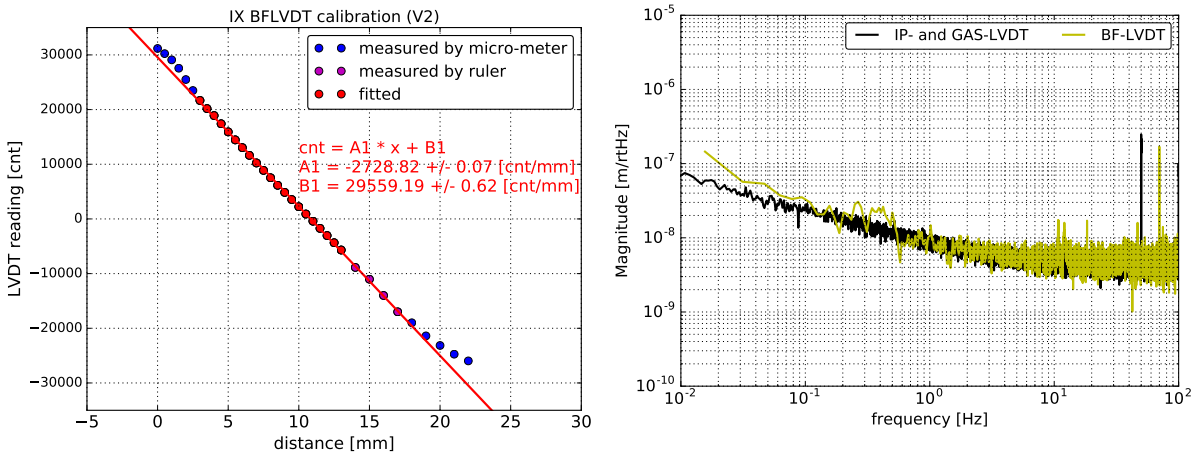

Figure 4.15: The typical linear rage (*left*) and the noise floor (*right*) of the LVDTs. The *left* panel shows a measured calibration curve where the value of the vertical axis is proportional to the LVDT output voltage. In the *right*, measured noise floors of the LVDTs (referred as IP- and GAS-LVDT) and the floor of the BF-LVDTs are shown.

TAMA accelerometer

The accelerometers are originally developed for TAMA-SAS [58]. They have folded pendulum geometry, and its proof mass is supported by two legs. The leg at one end of the proof mass is a normal pendulum with a normal restoring force. The other side of the proof mass is supported by an equal-length inverted leg which produces an anti-spring force. The mechanical resonant frequency can be tuned to about 0.5 Hz. We obtained the acceleration signal of the proof mass from a feedback control force.

The measured noise floor of the implemented ITMX-accelerometer[2] estimated by the three-channel correlation analysis [59] is shown in Figure 4.16.

Geophone L-4C

A geophone L-4C is a speedmeter and its response in frequency domain is given by

$$H_{\rm geo}(\omega) \;=\; \frac{G_e\omega^2}{\omega_0^2 + 2i\eta\omega_0\omega + \omega^2}, \tag{4.4}$$

where G_e is the generator constant, η is the damping coefficient, ω and ω_0 are the angular frequency and angular resonant frequency, respectively. Figure 4.17 shows the response in eq (4.4) with typical parameters. The actual geophones are

[2]Due to some technical problems, the accelerometers did not achieve their expected sensitivities. Especially the noise floor of the ones for ITMY suspension was much worse than that of ITMX suspension.

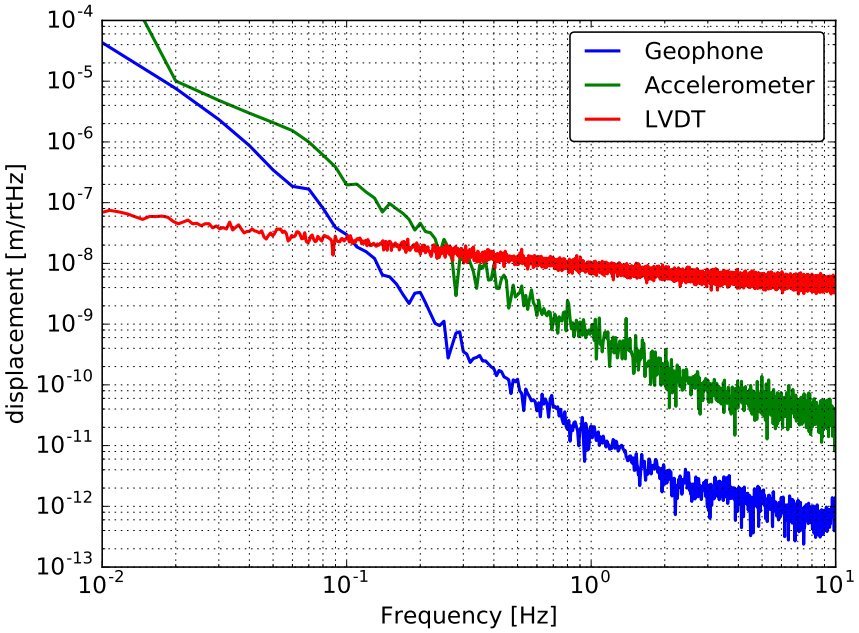

Figure 4.16: The measured noise floor of the implemented inertial sensors compared to that of LVDTs.

calibrated with already calibrated seismometers described in section 4.2.7. The typical noise floor of a geophone estimated with the three-channel correlation analysis [59] is also shown in Figure 4.16.

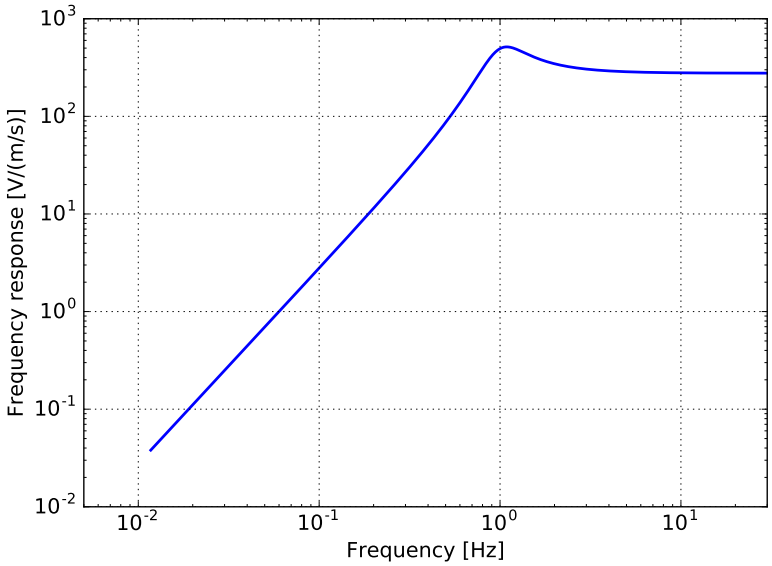

Figure 4.17: The geophone frequency response with the typical parameters. In this plot G_e, f_0, η are set to 276.8 V/(m/s), 1.0 Hz and 0.28 respectively.

4.2.3 Optical sensor and electro-magnetic actuator (OSEM)

Optical sensor and electro-magnetic actuator (OSEM) is a unit composed of a shadow sensor and a coil magnet actuator [60]. Typical configuration and its noise floor are shown in Figure 4.18 and 4.19 respectively.

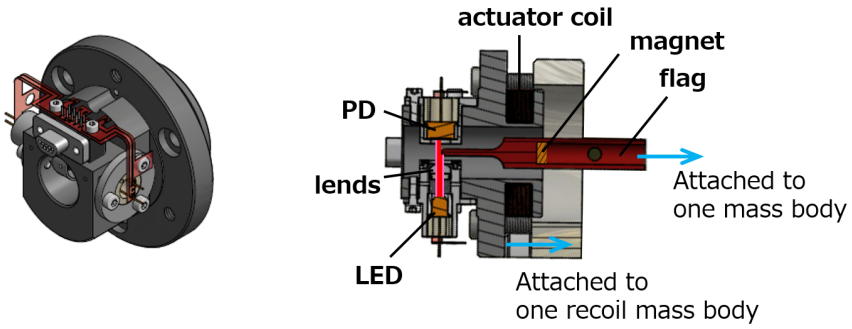

Figure 4.18: Detailed structure of OSEM.

4.2.4 Optical levers

Optical lever (oplev) consists of a light source and a quadrant photo diode (QPD). We sine fiber-collimated light from a super luminescent diode (SLD) on a mass,

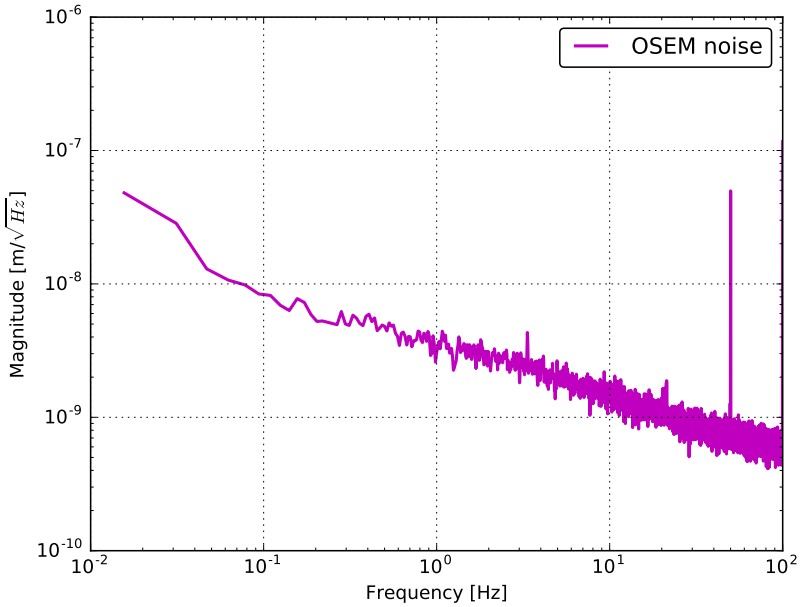

Figure 4.19: Detailed structure of OSEM.

and from the change in the position of the reflected light on the QPD, we can measure the mirror motion. An example of the geometry is shown in Figure 6.2. The oplev system is implemented outside the vacuum chamber, and an air-shield is installed around both the light source and QPD.

We have two types of oplevs; one is used for sensing the angular motion, and the other one is for the longitudinal motion. The oplev for the longitudinal motion is called length-sensing oplev (length-oplev), and it shares the light source with oplev (for angular motion) however uses another QPD and a lend. The details on the working principle can be found in [61]. The linear range of oplev is typically about a few hundred μrad. The noise floor of the optical lever and the length-sensing optical lever estimated from a measurement is shown in Figure 4.20. The noise floors are estimated from a interpolation of free-swinging mirror spectra with the air-shield.

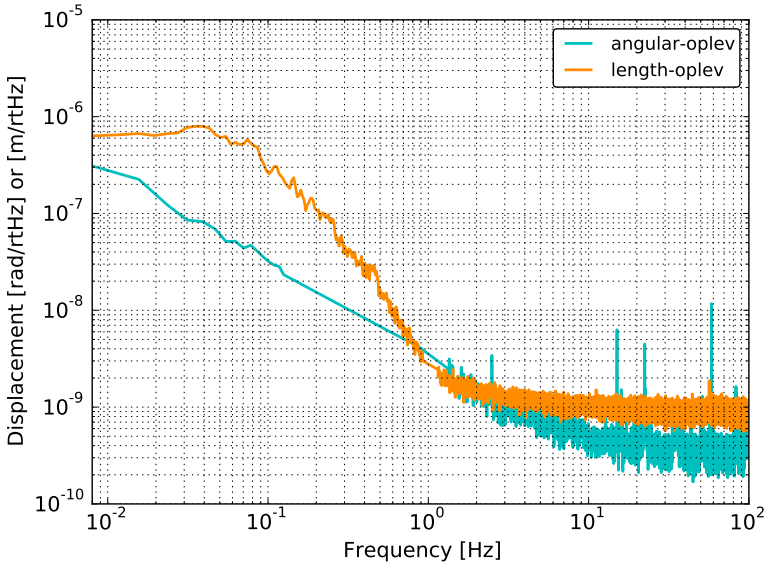

Figure 4.20: An estimated noise floor of the angular optical lever and the length-sensing optical lever. This plot includes the environmental noise.

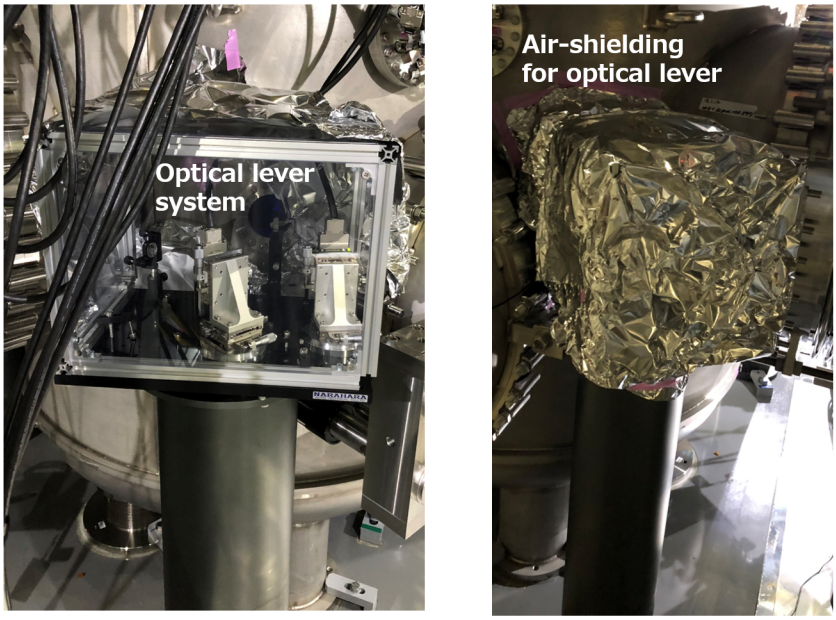

Figure 4.21: An example of the air-shield for the optical levers. The system at PR3 suspension without the shield is shown in *left*, with the shield is in *right*.

4.2.5 Reflective photo sensor

The reflective photo sensor (PS) is a non-contacting sensor which works even at the cryogenic temperature 20 K. It was developed mainly for the purpose of mechanical resonance damping of the RM-chain modes [62]. A photo-sensor unit consists of a LED and 2 photo-detectors, and six of this photo-sensor units are arranged at each MN- and IM-stage so that they can sense the 6 dofs. Even though the calibration factor depends on the operation temperature, it was experimentally confirmed that the calibration factor at the cryogenic temperature is obtained by multiplying a factor to the calibration factor at measured room-temperature.

It is also known that this photo-sensors have individual differences in the calibration factors. According to a measurement, the difference can come form the difference of the beam profile of the LED. An estimation of the noise floor of the implemented photo-sensor[3] is shown in Figure 4.22.

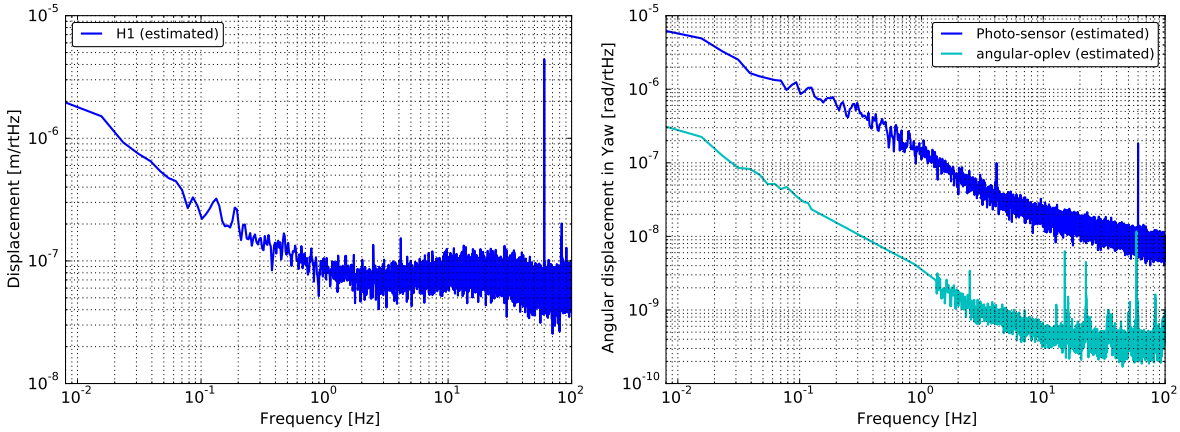

Figure 4.22: An estimation of the noise floor of the implemented photo-sensor (*left*) and a comparison of the noise floor to that of angular optical lever in Yaw dof (*right*).

[3]Due to time constrain, we could not calibrate each photo-sensor. The calibration factor has been estimated by comparing two force transfer functions. According to a simulation, the low-frequency-gains of the following two transfer functions becomes equal; the transfer function from MN-Yaw excitation to MN-Yaw with PS, and that from MN-Yaw excitation to MN-Yaw with oplev. The calibration factor is obtained by assuming this fact. The noise floor of one PS is then calibrated from the result.

4.2.6 Coil-magnet actuator

For the suspension controls, it is demanded to use non-contacting actuators in order not to transmit the external vibration to the suspended masses. For this purpose, we implement coil-magnet actuators which are composed of a permanent magnet and a solenoid coil. The magnet is attached on the mirror, and the coil is attached on the recoil mass, for example. By inputting current to the coil, we obtain a magnetic field with electromagnetic induction which apply a force on the magnet. The actuator design details are summarized in [63].

4.2.7 Seismometer

The ground vibration at each front- and end- station is measured by a seismometer Trillium120QA [34]. For the Type-A system, the seismometer is set at the second floor of each station. Its self-noise level compared to the typical noise level of LVDT is shown in Figure 4.23. The noise floor itself is relatively low for the suspension related control even at frequency between 10 mHz to 100mHz, however, the seismometer is affected by local tilt change at frequencies below 0.1 Hz. Due to this fact the use of seismometers below 0.1 Hz is usually avoided.

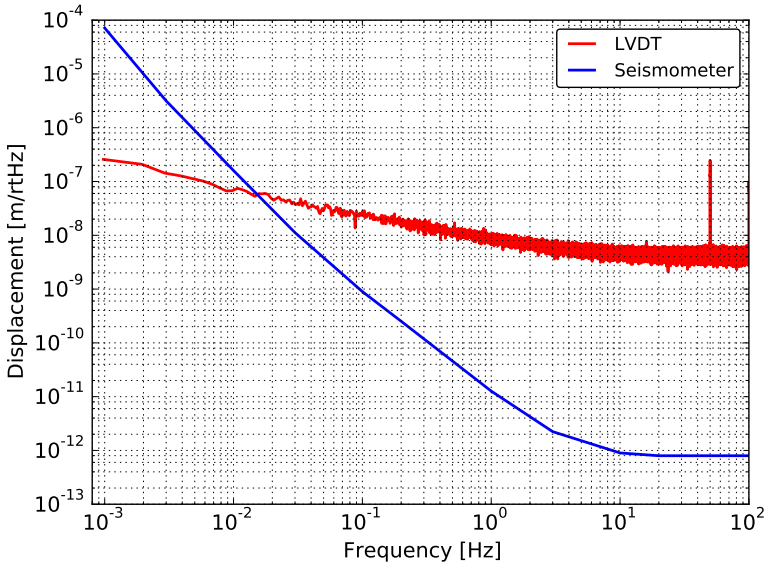

Figure 4.23: Self-noise level of Trillium120QA compared to the typical noise level of LVDT.

4.2.8 Data acquisition and signal processing

The data acquisition and the active control system implementation in KAGRA are realized by using a real-time digital system developed for KAGRA project. The voltage from the sensors are digitalized by Analogto-Digital Converters (ADCs), and then the correction signals are calculated in the digital system. Finally the correction signals are converted to voltage by Digital-to-Analog Converters (DACs) and then the voltage signals are sent to the actuators via appropriate electric circuits. The anti-aliasing and anti-imaging filters which aims to cut the noise due to the digitalization, are realized by using analog circuits. In the digital system for the suspension system, we use 16kHz and 2 kHz as sampling rate for the payload and the other part respectively, which are enough for the purpose of the KAGRA SAS controls. The sensing and the actuation is limited by the available range of the ADCs and DACs, which are ±20V and ±10V respectively. All the control filters have to be build to avoid voltage saturation. More details of the KAGRA digital system is summarized in [48].

An example of signal flow of the KAGRA digital system especially for the suspensions is shown in Figure 4.24. Each sensor signals are digitalized by ADC and then converted to displacement/velocity/acceleration by digital calibration filter. The calibrated signals are aligned to Cartesian coordinate by matrix operation (with sensor matrix), and then we apply feedback filters for each dof. Finally we send the correction signals to each actuators through a matrix (actuator matrix).

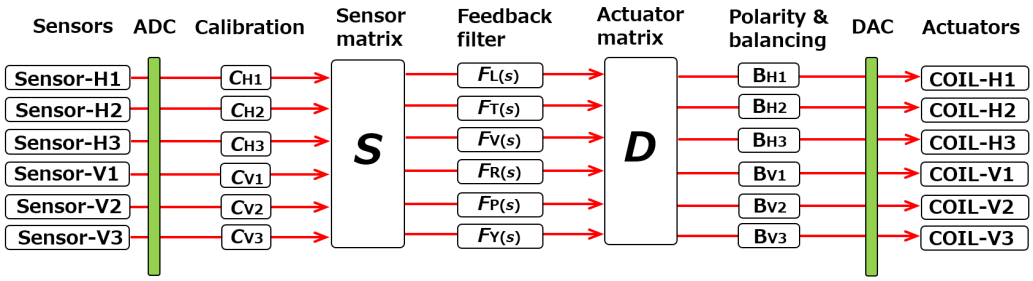

Figure 4.24: An example of signal flow of the KAGRA digital system especially for the suspensions. This is a case where six sensors and actuators are implemented.

4.3 Overview of KAGRA SAS

As described in section 1.4.4, in KAGRA detector, three types of SAS are installed depending on the required mirror displacement noise level above 10 Hz. They are called Type-A (section 4.3.1), Type-B (section 4.3.2) and Type-Bp SAS (section 4.3.3). The required displacement of the Type-A SAS is the most restrict, and it becomes looser for the Type-B and Type-Bp SAS in order.

In order to lock DRFPMI, all these suspensions have to be finely controlled as desired. Especially for the first step we need to lock FPMI, and for the purpose we have to acquire the lock of arm-cavities first. For this process, to actively control the Type-A SASs, which holds the arm-cavity mirrors, is of paramount importance. Then controlling BS, which is suspended by the Type-B SAS, plays an important role to acquire/keep the FPMI lock. After the FPMI is acquired, controlling finely the Type-Bp and the other Type-B SASs becomes crucial in order to acquire/maintain the PR/SR cavity lock.

This subsection describes the detailed mechanical systems of those suspensions which are assembled with the mechanical components, sensors and actuators introduced above.

This subsection includes the expected mirror displacement spectrum. For the estimation of the mirror displacement, we assume that 1 % of vertical motion couples to the longitudinal displacement. This assumption come from an empirical estimation for the vertical to longitudinal coupling of the mechanics of 0.1-1 % depending on the assembled mechanics. In addition, this is due to a fact that specifically in KAGRA, at least 0.3 % vertical-to-horizontal coupling will be found due to a fact that the arm tunnel has a tilt of 1/3000 for the purpose of drainage. In addition, we use 90 percentile seismic motion in Figure 1.11 assuming that the ground motion level is high.

4.3.1 Type-A suspension

Type-A suspension consists of nine stages. The mechanical system of Type-A suspension and its schematic overview are shown in Figure 4.25. The upper five stages are operated in room-temperature and the other (lower) four stages are operated at cryogenic temperature. From upper stage, Type-A suspension consists of IP-stage, five GAS filters with the damping system at BF-stage, and the cryogenic payload. The five GAS filters are called F0, F1, F2, F3 and BF from the top. Each GAS filter and MN are suspended by single maraging wire from their upper stage. At the upper surface of F1, we implement the magnetic damper. The magnet plate is suspended from the underneath of the IP-stage, and the other copper plate is attached on the F1 cup. For the BF-stage damping system, we use BF-LVDTs with one end attached on the security frame. In the payload part, each stage is connected with heat links as introduced in section 4.1.6. Heat links are implemented to reduce the cooling down time making use of conductive heat transfer [64, 65].

Cooling system

The cryogenic payload is cooled down by utilizing both the radiation and conductive cooling. For cooling we use four units of pulse-tube cryocoolers. The payload is surrounded by two layered shield whose temperatures are at 8 K and 80 K from inside, and the structure is housed in a cryostat. For heat extraction, the heat links surrounded around the payload are connected to the cryostat via a vibration isolation system in order not to transmit the vibration of the cryostat to the payload. The overview of the system inside the cryostat and the heat links is called heat link vibration isolation system (HLVIS) are shown in Figure 4.26 and 4.27.

Expected mirror displacement

The expected displacement of a mirror suspended by a Type A system is shown in Figure 4.28. In this plot, it is also assumed that the cryostat vibrates as much as the ground. The expected vibration transmitted from the cryostat via HLVIS is also included. In this calculation, we assume that that the cryostat displacement spectra is the same as the ground vibration, however, cryostat can enhance the vibration at frequency above a few Hz due to its internal resonances and cryocooler operations [66]. Thus the actual mirror displacement especially at above 10Hz is to be investigated by using a sensitive interferometer.

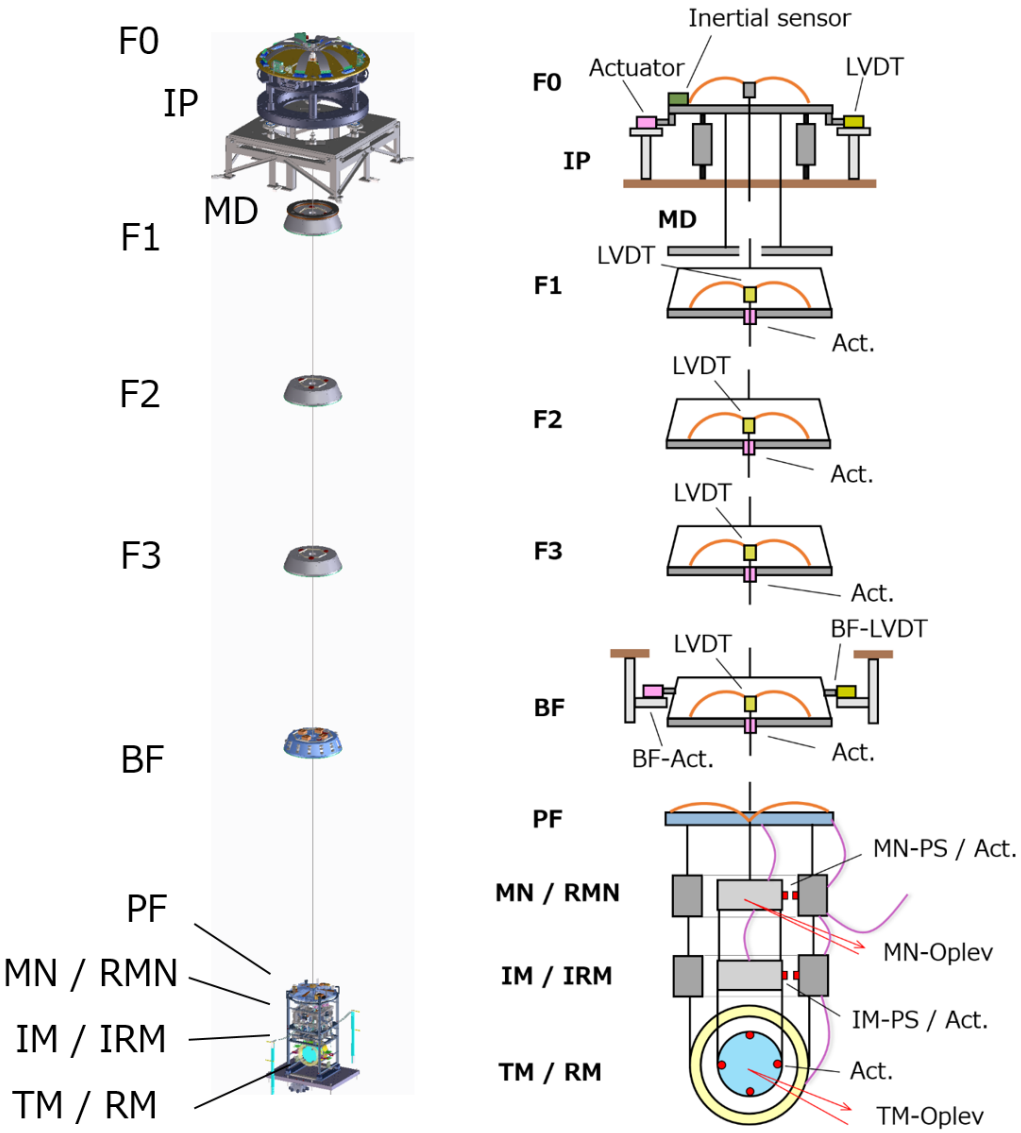

Figure 4.25: The overview of the Type-A suspension system. In the schematic view (*right*), the information about sensors and actuators, described in section 4.2, is included. The boldfaced letters represent the names of the suspension stages, while the small characters show the implemented sensors and actuators.

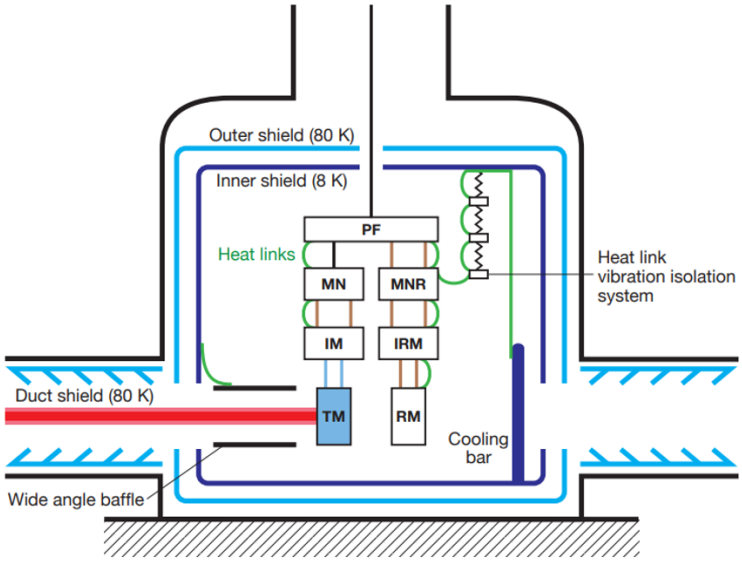

Figure 4.26: A schematic view inside the cryostat from [44].

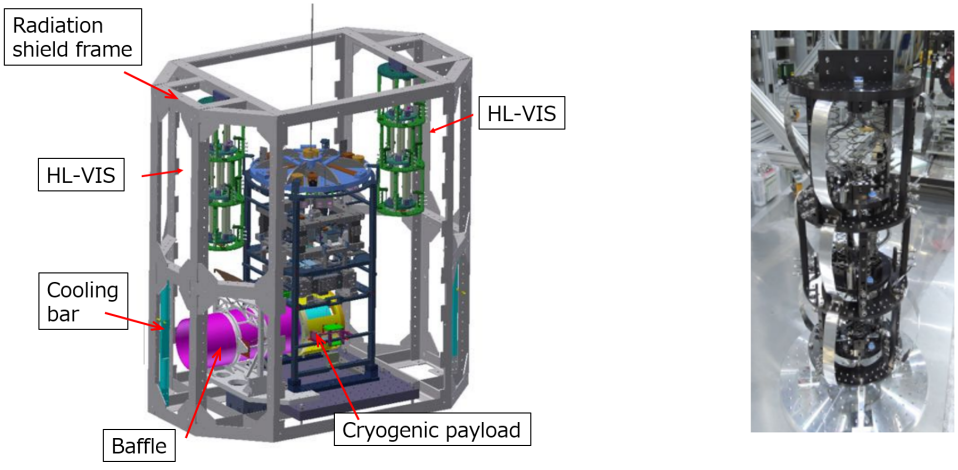

Figure 4.27: 3D-CAD drawing of the system inside the cryostat (*left*) and the actual structure of the vibration isolation system for the heat links (*right*).

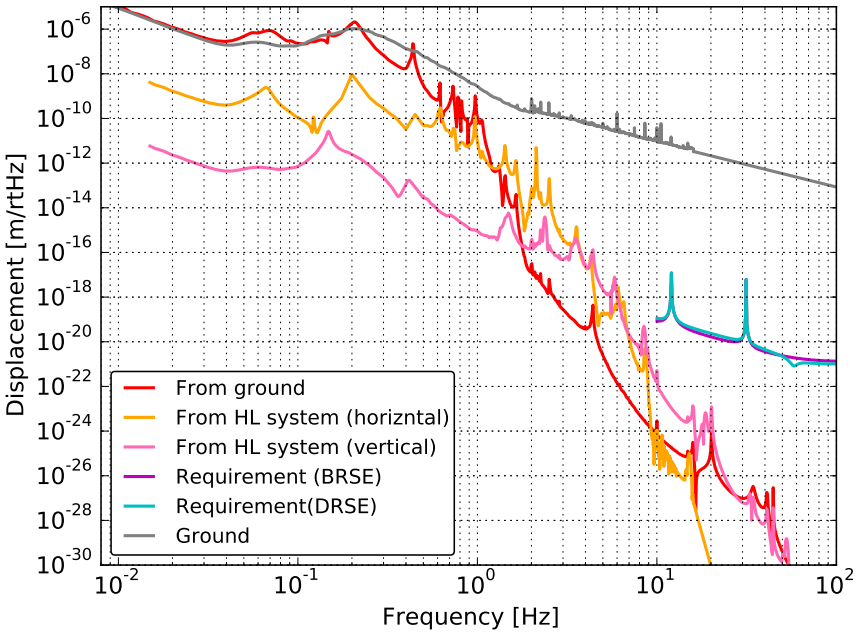

Figure 4.28: Expected mirror displacement spectrum of a mirror suspended by Type-A suspension, assuming 1% vertical to horizontal coupling. The red curve shows the TM displacement induced by ground, and this curve includes the vertical coupling. The orange and pink curves show the horizontal and vertical vibration transmitted from the cryostat via HLVIS respectively, assuming 1% coupling for vertical dof.

4.3.2 Type-B suspension

Type-B suspension consists of five stages. All the stages are operated in room-temperature, and Type-B suspension consists of IP-stage, three GAS filters without the damping system at BF-stage, and the room-temperature payload. The three GAS filters are called F0, SF[4] and BF from the top. Each GAS filter and IM are suspended by single maraging wire from their upper mass. At the upper surface of F1, we implement the magnetic damper as in the Type-A SAS. For Type-B, we do not have the BF-stage damping system. The mechanical system of Type-B suspension and its schematic overview are shown in Figure 4.29.

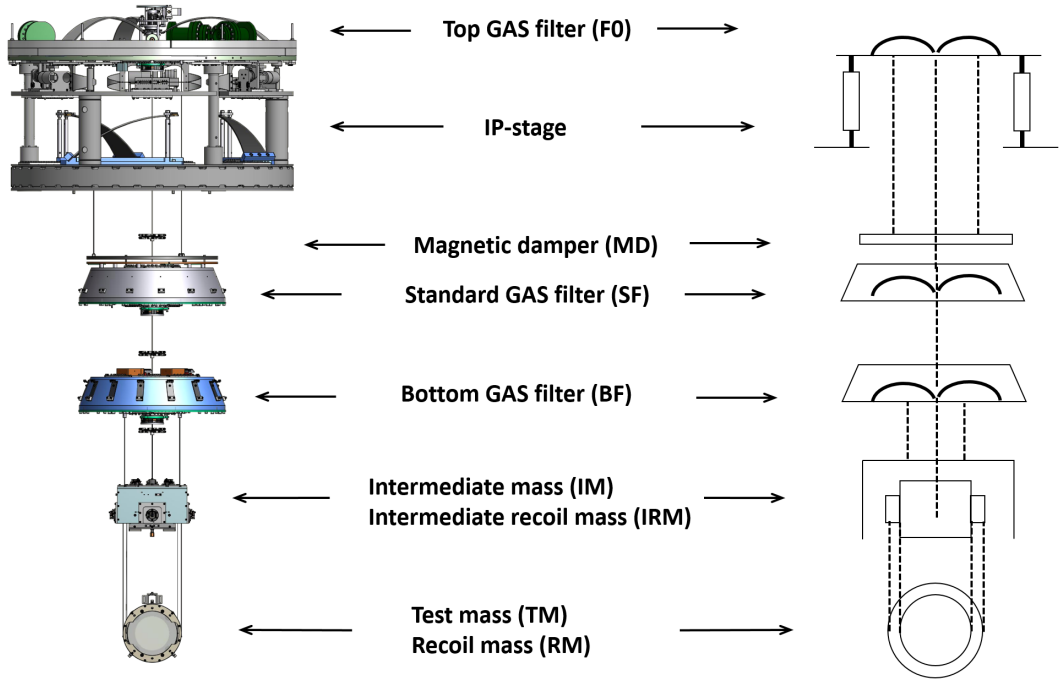

Figure 4.29: The overview of the Type-B suspension system.

Expected mirror displacement

The expected mirror displacement suspended by Type-B suspension is shown in Figure 4.30.

[4]SF is an abbreviation of standard filter.

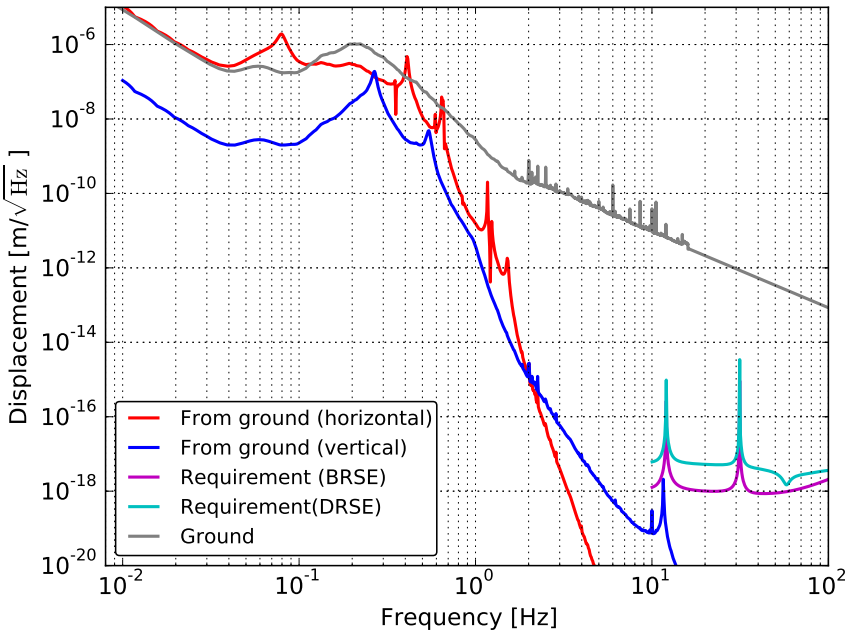

Figure 4.30: Expected mirror displacement spectrum of a mirror suspended by Type-B suspension, assuming 1% vertical to horizontal coupling. The red and blue curves shows the TM displacement induced by ground in horizontal and vertical respectively.

4.3.3 Type-Bp suspension

Type-Bp suspension consists of four stages. The mechanical system of Type-Bp suspension and its schematic overview are shown in Figure 4.31. All the stages are operated at room-temperature, and Type-Bp suspension consists two GAS filters with the damping system at BF-stage, and the room-temperature payload. The two GAS filters are called SF and BF from the top. Each GAS filter and IM are suspended by single maraging wire from their upper mass. In this system, SF is installed on mechanical ground, without IP-stage. For the static horizontal position adjustment, we use a motorized stage which is called traverser, as shown in Figure 4.32. For the BF-stage damping system, we use BF-LVDTs, with one end mounted on the suspended mass which is called BF-recoil mass (RBF). In this system, we do not have the magnetic damper.

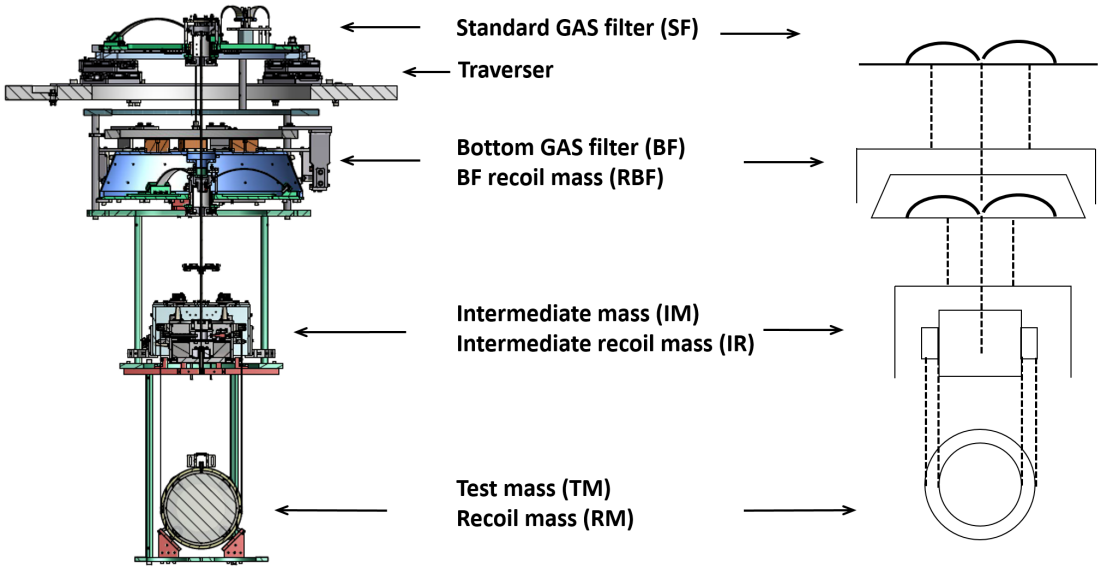

Figure 4.31: The overview of the Type-Bp suspension system (from [54]).

Expected mirror displacement

The expected displacement of a mirror suspended by Type-Bp suspension is shown in Figure 4.33.

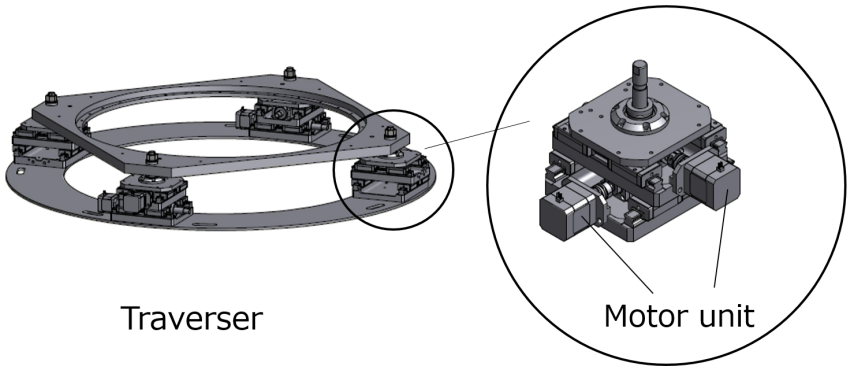

Figure 4.32: Overview of the traverser for Type-Bp suspension.

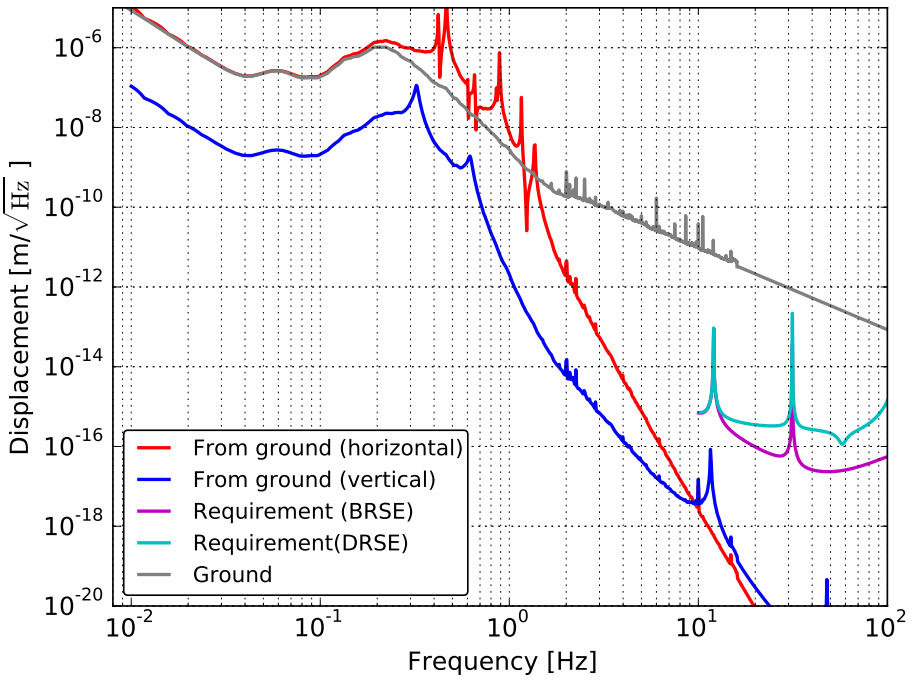

Figure 4.33: Expected mirror displacement spectrum of a mirror suspended by Type-Bp suspension, assuming 1% vertical to horizontal coupling. The red and blue curves shows the TM displacement induced by ground in horizontal and vertical respectively.

4.4 Integration/maintenance of KAGRA SAS

The eleven KAGRA SASs have been assembled and later transferred into their vacuum chamber where sensors and actuators have been connected to the real-time digital system in order to be able to actively control them. After the mechanical installation has been finished, it is necessary to perform several adjusting and repairing operations on the mechanics working inside the small vacuum chambers.

Indeed I've devoted more than one and half year of my time to this activity of assembly, installation and repairing for all the three types of suspension from 2018 March[5]. This subsection briefly describes some of the installation steps and my contribution to those works.

4.4.1 Mechanical installation

As the first step, KAGRA SAS is assembled outside its vacuum chamber. The assembly starts from the lower stage (TM and IM stages) and goes to the upper stages, especially for the Type-B and Type-Bp SAS. In the Type-A SAS, the assembly of the room-temperature part and later the cryogenic payload is done independently and they are connected inside its vacuum chamber. More details can be found in [67, 68].

History

The first KAGRA SAS installation had been done from 2015 October to 2016 February for the initial KAGRA test run (so-called iKAGRA run). At that time only one mirror, the PR3, was suspended by KAGRA SAS, with a simplified Type-Bp configuration. After iKAGRA period, the installation for KAGRA operation started with three assembly teams for Type-A, Type-B and Type-Bp suspensions.

The three Type-Bp suspensions had been installed from 2016 December to 2017 December including test period to assess the installation procedure. Concerning the Type-B suspensions, the test installation of BS suspension started in 2016 June and the installation of all the four suspensions had been finished on 2018 December. For type-A suspension, the installation had started on 2017 January, and then all the four Type-A suspension installation had been finished on about 2019 January including the cryogenic payload part, heat links and their HLVIS.

Sensor calibration

We calibrate OSEMs, accelerometers, Geophones and BF-LVDTs, which are used in room-temperature part, before they are mounted on the suspensions. The

[5]In master's, I have spent a half year in the tunnel for iKAGRA PR3 installation and its test. I could obtained a knowledge about the mechanics of the actual KAGRA suspension.

LVDTs for IPs and GAS stages are calibrated during the installation procedure.

Cabling inside/outside chambers

For the purpose of obtaining (sending) the sensor (actuator) signals from (to) the suspension, We lay electrical cables around each stages inside vacuum chamber. It is important to lay the cables loosely so that the additional stiffness due to the laid cables do not become dominant. Figure 4.35 shows examples of in-vacuum cabling around IP-stage of the Type-A SAS and IM-stage of the Type-Bp SAS.

The cables from inside the chamber are connected to ADC/DAC trough appropriate electrical circuits as shown in Figure 4.36.

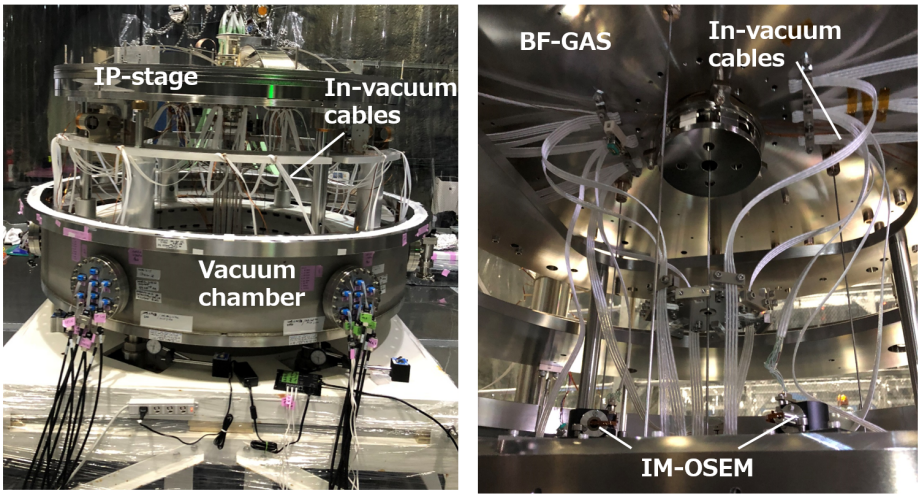

Figure 4.34: Examples of in-vacuum cabling; around IP-stage of the Type-A SAS (*left*) and around IM-stage of the Type-Bp SAS (*right*).

Figure 4.35: An example of in-air cabling.

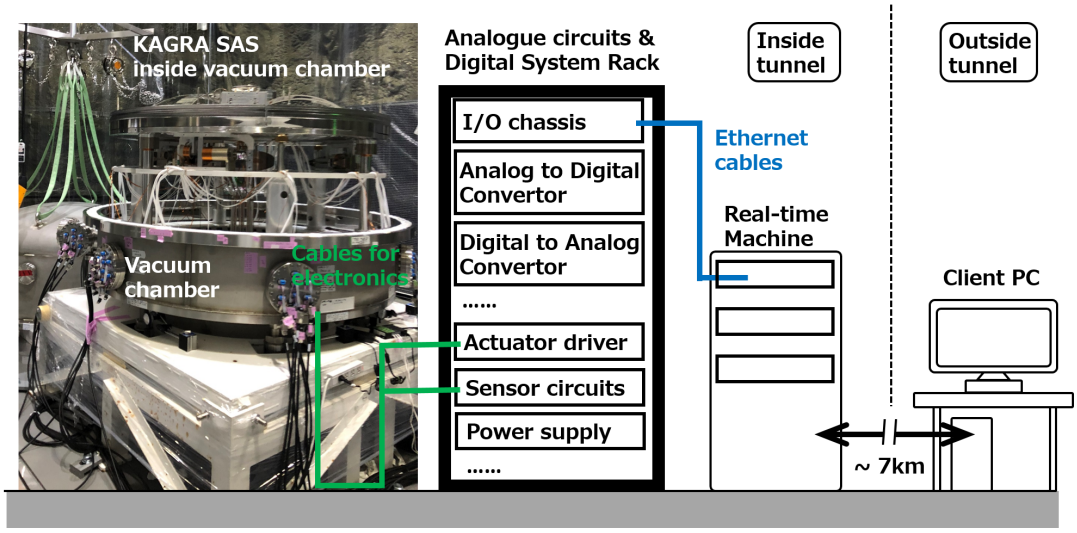

Figure 4.36: Overview of cabling including the digital system connection.

4.4.2 Development of real-time digital system model

As described in section 4.2.8, we use real-time digital system to acquire the sensor signals and to send the actuation signals. We first decide/program how the sensor/actuation signals flow before starting the program running. After starting the run, we then develop/implement finite impulse response filters during the running. The operation of the suspensions are conducted remotely if not problems are reported.

We first develop the real-time system which enables to sense/actuate the suspensions in order to use the real-time system during mechanical assembly period.

4.4.3 Characterization

At every time when we finish assembling one stage, we measure the transfer functions from the actuators to the implemented sensors, and then confirm that the mechanical system has been assembled as designed.

After this step is achieved, we can start to implement feedback control systems for the suspensions, by developing the finite impulse response filters.

4.4.4 Maintenance and repairing

During the initial interferometer alignment period, some problems are reported around the suspension system. Some of the examples, which are reported oftenly, are listed in the following. More details are found in [69].

LVDT circuit replacement

Sometimes the electrical circuits which drives the LVDT (for its sensor part) become broken and the circuits have to be replaced to new one. Since the calibration of the LVDT sensors are depended on the circuit, we have to re-calibrate the LVDTs every time when the circuits become broken.

re-cabling

Soldering point of some cables, which has been already laid inside the vacuum chambers in complicated way, are sometimes disconnected and they have to replaced to new ones.

OSEM body positioning

For the OSEM shadow sensors, it was required to finely adjust the relative position between the OSEM body and the flag so that they were at the center of its linear range (about 1 mm). This position adjustment is done in outside the

vacuum chamber, however, we have to work on this even after installing the suspension inside the chamber due to the mirror slip as described below. An example of the unsuitable/suitable case is shown in Figure 4.37.

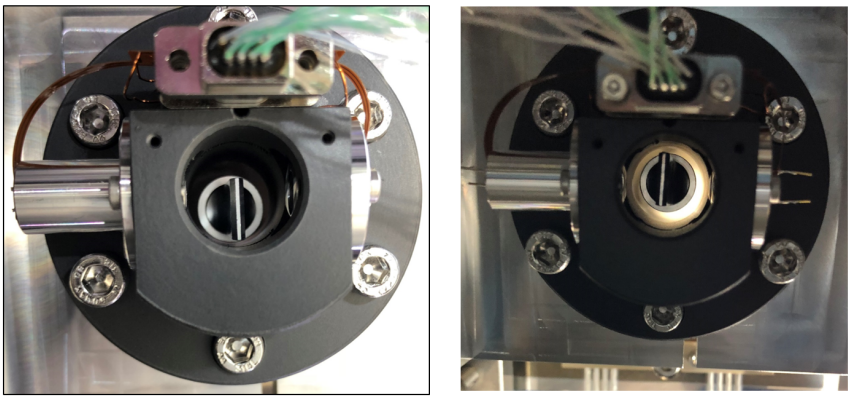

(unsuitable case) (suitable case)

Figure 4.37: Example of OSEM positioning at IM-stgae of the Type-Bp SAS. The *left* and *right* figures show unsuitable and suitable cases respectively.

Mirror slip compensation

Sometimes the mirrors, especially for the PR mirrors which are suspended by the Type-Bp SAS, has been slipped when the mirrors are kicked by a large external disturbance. The mirror orientation is recovered by tilting the upper stage, i.e, IM. After finely adjust the orientation, we work on the OSEM positioning. Basically we have to iterate this IM tilt tuning and the OSEM positioning.

For mechanical rubbing of GAS-keystone

It is found that the GAS keystone, more concretely the primary coil holder, is rubbing to the other coil holder. The tilt of the secondary coil holder have to be finely adjusted.

Magnet re-gluing for TM of Type-Bp SAS

In PR2 and PRM suspension, it is reported that some of the magnets (flag-shaped) are come off form the mirror surface and the we are not able to actuate the TM. We then re-glue the detached magnets to the suspended mirror.

4.4.5 Contribution to integration

I have worked on the followings for the KAGRA SAS integration/maintenance for the mechanical part in the mine:

- PR2: in-vacuum cable repairing, LVDT circuit replacement, magnet re-gluing for TM, IM-OSEM positioning, rubbing-debugging at BF-GAS
- PR3: Upgrading the air-shield for the optical lever (see Figure 4.21), IM-OSEM positioning
- PRM: LVDT circuit replacement, magnet re-gluing for TM, IM-OSEM positioning
- SR2: Geophone pod assembly[6] and calibration/noise estimation
- SR3: Geophone pod assembly and calibration/noise estimation, GAS blade compression tuning, rubbing-debugging at TM-stage
- SRM: Geophone pod assembly and calibration/noise estimation, TM assembly
- ITMX: mechanical installation of the tower part, BF-LVDT calibration/ noise estimation, in-air cabling for the room-temperature part, accelerometer/LVDT noise estimation, payload-tower connection[7]
- BS: rubbing-debugging at TM-stage
- ITMY: in-vacuum cable repairing, in-air cabling for the room-temperature part, payload-tower connection, accelerometer noise estimation
- ETMX: in-air cabling for the room-temperature part
- ETMY: Geophone pod assembly and calibration/noise estimation, in-air cabling for the room-temperature part.

In addition to the above, I have also measure the Q factors of PR3 mechanical resonances for its characterization. Concerning the IM-OSEM positioning, its rubbing part localization and for the debugging is done by myself alone in the most of part, especially for the Type-Bp SASs.

Indeed these works were the main tasks in the time period from 2018 March to 2019 July, oftenly I have stayed inside the small vacuum chambers.

Thanks to this, however, I've gained a good knowledge about the mechanics of KAGRA SAS. I have also realized how crucial it is to design the mechanical systems in order to make easier the repairing and maintenance of such a complex system.

[6]Since the Geophone L-4C is not vacuum compatible and it has to be installed inside a pod in order to use in pumped-down condition.

[7]The cryogenic payload of the Type-A SAS is mechanically connected to the already installed upper (tower) part.

After the integration has been finished, I have focused on realizing the most important local control system, which is the control system for KAGRA Type-A SAS. The following chapters describe that topic.

Chapter 5

Development of Type-A SAS control system

This chapter focuses on development of an active control system for the Type-A suspension. The active control system is based on a digital servo systems and uses feedback loops with the local sensors and non-contacting actuators described in the previous chapter. The main targets for the suspension control are to damp the mechanical resonances as rapidly as possible, and to keep the mirror in the proper position and orientation. Such control system is realized by implementing appropriately shaped feedback filters. These filters are developed based on the idea described in section 2.2.3. More concretely we shape/implement the feedback filters (F_{fb} in section 2.2.3) in *zpk* expression in the KAGRA digital system.

Section 5.1 describes the interferometer control phases, since the requirements for the suspension local control system depends on the interferometer control phase. Section 5.2 summarizes the requirements for the suspension local control system for each interferometer control phase. Section 5.3 briefly introduces how the suspension is modeled as the plant in simulation. Section 5.4 describes the overview of the suspension control system. Sections 5.5 to 5.7 summarizes the development of the control system for each interferometer control phase, and those expected performance based on simulation.

5.1 Interferometer control phases

The interferometer control phases can be described by the following three phases:

- the calm-down phase,
- the lock-acquisition phase,
- the observation phase.

The interferometer operation phases are summarized in Figure 5.1.

The calm-down phase denote a phase where the suspended mirror is oscillating at the resonances with large amplitude due to an external disturbance or the kick by the interferometer lock loss. Thus the target of the local control system in this

phase is to damp the mechanical resonances as rapidly as possible. Minimizing the decay time of the resonances allow having fast interferometer lock recovery and, consequently, reducing lock loss time.

The lock-acquisition phase represents the phase where the interferometer lock trials are applied. In this phase, it is required to reduce the mirror displacement and its velocity in L dof and then to bring the operation points so that the mirror is trapped into the linear regime of the interferometer. It is also required to suppress the angular residual motion, in order to close other control loop with more sensitive sensors such as the wave front sensors.

The aim of the observation phase is, first, to suppress the mirror fluctuation due to technical noise such as sensor noise couplings at the frequency higher than 10 Hz, which is the detection band of GWs. The second aim is to keep the mirror position and the orientation at the proper interferometer operating point.

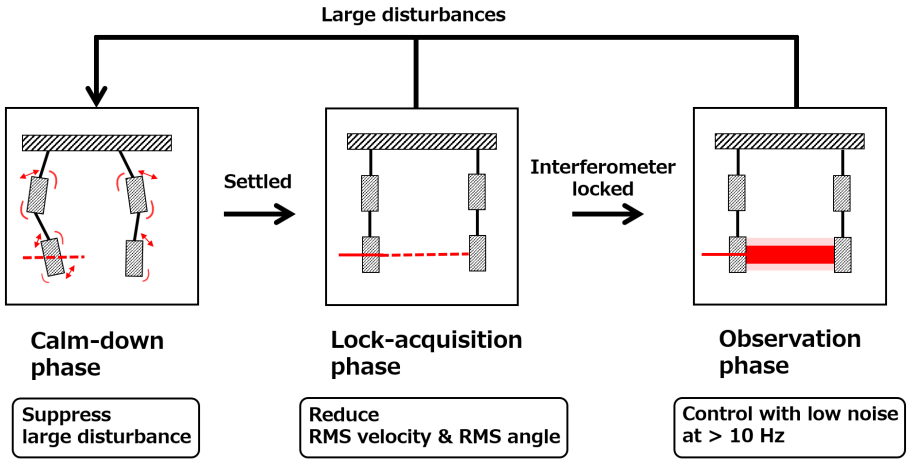

Figure 5.1: Suspension control operation phases categorized into the three phases. The main purposes of the active suspension controls are included.

5.2 Requirements

The description in section 5.2.1 to section 5.2.4, describes each requirement. Section 5.2.5 summarizes the requirements for the local control system and it is summarized in Table 5.2 consequently.

5.2.1 Requirement on damping time

In order to reduce the lock loss time, it is required to damp the the excited mechanical resonances of the suspension rapidly. The requirement is set that the $1/e$ decay time of the mechanical resonances disturbing the interferometer lock

acquisition is less than 1 minute. This requirement is set in order to avoid waiting for a long period of time before starting the following lock acquisition trial.

5.2.2 Requirement on RMS velocity

As described in section 1.3.5, the mirror displacement has to be reduced at the level of nm in order to keep the interferometric-locked condition. Since the finesses are set at 38 for the signal recycling cavity, 57 for the power recycling cavity and 1550 for the arm cavities, and the wavelength of the laser is 1064 nm for the KAGRA detector, the effective width of the linear range ΔL_{lin} is calculated as 14 nm, 9.93 nm and 0.34 nm for the signal recycling cavity, for the power recycling cavity and for the arm cavities.

In order to lock the interferometer, it is necessary to reduce the velocity of the mirrors sufficiently. Since the feedback control is available only when the mirrors are in the width ΔL_{lin}, the permitted incident mirror velocity is limited by the control bandwidth. In addition, the maximum actuation force limits the permitted mirror velocity.

Control bandwidth limit

Based on the consideration of control bandwidth, the requirement on the incident mirror velocity is obtained as

$$v_{\mathrm{mirror}} \lesssim \omega_b \Delta L_{\mathrm{lin}} = \omega_b \frac{\lambda}{2\mathcal{F}}, \tag{5.1}$$

where ω_b represents control bandwidth. The maximum incident velocities based on the control bandwidth limit for the power recycling, signal recycling, arm cavities are summarized Table 5.1.

Actuation force limit

Following the consideration in [63], the force F required in order to stop the mirror can be obtained by,

$$F = \frac{m v_{\mathrm{mirror}}}{\Delta t}, \tag{5.2}$$

where m, v and Δt are the mass, the velocity of the mirror and the time it takes to pass the linewidth ΔL_{lin} of the cavity, respectively. Since the time the mirror takes to pass the width can be given by $\Delta t = \Delta L_{\mathrm{lin}}/v_{\mathrm{mirror}}$, the requirement on vincident mirror velocity limited by the actuation force can be given by

$$v_{\mathrm{mirror}} \lesssim \sqrt{\frac{F_{\mathrm{max}} \Delta L_{\mathrm{lin}}}{m}}, \tag{5.3}$$

The permitted maximum velocities based on the actuation force limit for the power recycling, signal recycling, arm cavities are also summarized Table 5.1. Since we use the green-lock technique for the arm cavity locking as described in section 1.3.5, the velocity for the arm cavity mirrors is not included in that table.

Table 5.1: Requirements on the velocity of the cavity length variation. The control band width is set to 50 Hz, and the values of actuation limit is obtained from [63]. For the lock-acquisition of the arm cavities, The control band width and the finesse are set to 10 kHz and 50 respectively assuming to use the laser frequency actuator of the arm-length stabilization system.

Cavity	BW limit [μm/s]	Actuation limit [μm/s]
Arm cavity	330	–
Power recycling cavity	2.9	7.3
Signal recycling cavity	4.4	0.44

RMS velocity requirement

Based on the requirement on the mirror velocity v_{mirror}, we set the requirement on the RMS velocity of the mirrors v_{rms}.

Since the mirrors of the optical cavities oscillate randomly, the mirror velocity changes randomly as well. If the mirror velocity has a Gaussian distribution, the probability distribution of the mirror's velocity $f(v)$, when passing through the resonance point, is given by [70]

$$f(v) = \frac{v}{v_{\mathrm{rms}}^2} \exp\left(-\frac{v^2}{2v_{\mathrm{rms}}^2}\right), \tag{5.4}$$

where v_{rms} means the RMS velocity of the cavity length variation. Assuming such velocity probability distribution, the RMS velocity that allows acquiring lock with probability p is:

$$v_{\mathrm{rms}} = \left(\sqrt{(-2\log(1-p)}\right)^{-1} v_{\mathrm{mirror}}. \tag{5.5}$$

In order to have a lock acquisition probability higher than 50%, the RMS velocity v_{rms} has to be lower than 0.72 v_{mirror}. Based on these conditions, the requirements on the RMS mirror velocity of the KAGRA suspensions is set to 2.0 μm/s for the type-A SAS, 0.31 μm/s for the type-B SAS and 2.0 μm/s for the type-Bp system. The velocity requirement for the type-A suspensions comes from a fact that PR and SR cavities include the input test masses (ITMs). Even though the requirement on the velocity for the arm cavity mirrors is set to 240 μm/s, the two ITMs are also part of the power and signal recycling cavities. The vibration of these ITMs affect the length variation of these cavities, and thus more strict requirement is used for the type-A SAS mirror RMS velocity, based on the bandwidth limit of PR and SR cavities.

5.2.3 Requirement on RMS angular fluctuation

For the stable operation of the interferometer, and also for preventing degradation of the sensitivity due to the mode mismatch, we have to suppress the mirror angular fluctuation. This requirement applies to the pitch and yaw dof, since these angular motions can have a huge impact on the interferometer.

For the lock-acquisition phase, the angular motion has to be reduced below 880 nrad RMS, in order to avoid that the intra-cavity power degrades by more than 5 % [71]. During the observation phase, the angular motion has to be smaller than 200 nrad RMS in order to avoid that the beam spot motion on the mirrors becomes larger than 1 mm RMS [72]. In addition, in order to keep the interferometer locked for 1 day, angular beam position drift is required to be smaller than 400 nrad/h [72].

5.2.4 Requirement on longitudinal displacement

In the lock acquisition phase and the observation phase, the mirror longitudinal displacement has to be suppressed so that the interferometer lock is kept. In order to keep the lock, the amplitude of the actuation force should be smaller than the maximum force of the actuators. It was reported in [63] that the actuation efficiency at MN-, IM- and TM-stage were 3.9×10^{-7} m/V, 1.7×10^{-8} m/V and 1.8×10^{-9} m/V respectively at low frequency. Since the maximum voltage that the digital-to-analogue converter (DAC) can provide is 10 V (se described in section 4.2.8), the maximum permitted longitudinal displacements for each stage are 3.9 μm, 1.7×10^{-1} μm and 1.8×10^{-2} μm at MN-, IM- and TM-stage respectively. By assuming that the longitudinal displacement compensation is done at the MN-stage, and considering a margin of a factor of 10, the requirement on the longitudinal displacement can be set to 0.39 μm.

5.2.5 Requirement on Type-A suspension control

The requirements for the active controls of the Type-A SAS are summarized in Table 5.2. The requirement for the mirror transverse and vertical displacement is set to 0.1 mm in order to avoid a mis-centering of the beam spot on the mirror. Based on section 5.2.4 and 1 % vertical-to-horizontal coupling, the permitted requirement of the mirror vertical displacement in the lock acquisition and the observation phase is set to 39 μm RMS. The RMS value is defined as integration of the spectrum density down to 0.01 Hz. This value is selected assuming the corresponding time scale ($\sim$ 100 sec.) is sufficiently long to cover the lock-acquisition process. A large contribution to the velocity and the angular motion is given by the micro-seismic peak around 0.2 $\sim$ 0.5 Hz.

In addition, the control system noise coupling to the mirror longitudinal displacement in the observation band (above 10 Hz) has to be lower than the required vibration level by the KAGRA design sensitivity (see section 1.4.2).

Table 5.2: Requirements on the Type-A suspension control. The column labeled as ref. describes the section which explains the reason of the requirements.

Items	Requirements	ref.
The calm-down phase		
$1/e$ decay time	< 1 min.	§ 5.2.1
RMS displacement (transverse, vertical)	< 0.1 mm	§ 5.2.5
The lock acquisition phase		
RMS velocity (longitudinal)	< 2.0 μm/sec.	§ 5.2.2
RMS angle (pitch, yaw)	< 880 nrad	§ 5.2.3
RMS displacement (longitudinal)	< 0.39 μm	§ 5.2.4
RMS displacement (transverse)	< 0.1 mm	§ 5.2.5
RMS displacement (vertical)	< 39 μm	§ 5.2.5
The observation phase		
Control noise at 10 Hz (longitudinal)	$< 8.0 \times 10^{-20}$ m/$\sqrt{\text{Hz}}$	§ 1.4.2
RMS displacement (longitudinal)	< 0.39 μm	§ 5.2.4
RMS displacement (transverse)	< 0.1 mm	§ 5.2.5
RMS displacement (vertical)	< 39 μm	§ 5.2.5
RMS angle (pitch, yaw)	< 200 nrad	§ 5.2.3
DC angle drift (pitch, yaw)	< 400 nrad/h	§ 5.2.3

5.3 Mechanical system modeling

In KAGRA, the mechanical frequency responses of a suspension system is calculated with a simulation tool [73], which is based on a three-dimensional rigid body model. For the KAGRA SAS the rigid body modeling describes properly the suspension up to about 50 Hz [48]. The simulation tool calculates the frequency response by using the linearized equation of motion around the equilibrium point of the system:

$$\boldsymbol{M}\ddot{\boldsymbol{x}} \ + \ \boldsymbol{G}\dot{\boldsymbol{x}} \ + \ \boldsymbol{K}\left(\boldsymbol{x} - \boldsymbol{x_{eq}}\right) \ = \ \boldsymbol{0}, \tag{5.6}$$

where $\boldsymbol{M}$, $\boldsymbol{G}$, $\boldsymbol{K}$ represent the mass matrix, the damping matrix and the stiffness matrix respectively. These matrices are calculated with:

$$K_{ij} \ = \ \left.\frac{\partial^2 U(\boldsymbol{x})}{\partial x_i \partial x_j}\right|_{\boldsymbol{x}=\boldsymbol{x}_{eq}}, \tag{5.7}$$

$$G_{ij} \ = \ \left.\frac{\partial^2 R(\boldsymbol{x}, \dot{\boldsymbol{x}})}{\partial \dot{x}_i \partial \dot{x}_j}\right|_{\boldsymbol{x}=\boldsymbol{x}_{eq}}, \tag{5.8}$$

$$M_{ij} \ = \ \left.\frac{\partial^2 T(\dot{\boldsymbol{x}})}{\partial \dot{x}_i \partial \dot{x}_j}\right|_{\boldsymbol{x}=\boldsymbol{x}_{eq}}, \tag{5.9}$$

where $U(\boldsymbol{x})$, $R(\boldsymbol{x}, \dot{\boldsymbol{x}})$ and $T(\dot{\boldsymbol{x}})$ denote the potential energy, dissipation function and kinetic energy of the system, and the derivatives are calculated at the equilibrium point $\boldsymbol{x}_{eq}$.

The simulation for the control system of KAGRA SAS is addressed by linear control theory. For this purpose, the equation of motion of the suspension system is transformed into state-space representation. Using the calculation framework, we simulate the suspension system with control system, and tune/select the parameters of the control filters. More detailed information about the modeling of the KAGRA suspension can be found in [44].

5.4 Overview of control system

The control loops for local suspensions are developed based on feedback control with implemented sensors and actuators. We adopt only single-input-single-output (SISO) system in the control system. An example of the signal flow of the feedback control system, which is for the IP-stage, is shown in Figure 5.2. We first sense the suspension motion using the implemented sensors, and then convert the sensor-basis signals to the Cartesian signals (in Figure 2.6) by using a matrix. The feedback filters are applied to the Cartesian signals. Then the correction signals are distributed to each actuators by applying the proper matrix, i.e. the matrix that allows transforming the signals from Cartesian basis to the actuator coil basis. Finally we apply the forces to the suspension with the actuators by sending the filtered signals. In order to realize the active control system,

we shape the feedback filters for each required Cartesian dof and each suspension stage. In the development we estimate the control performance for each feedback loops, such as the noise couplings, which is calculated in accordance with the treatment in section 2.2.3. The stability of the feedback loop are estimated using the open loop gain in Bode plot as described in section 2.2.3.

The basic idea of the control system is summarized in Figure 5.3. At the IP stage, we control the static mirror position by controlling the DC position of the IP-sage, and damping the translational resonance. The IP stage is also used by the control system to suppress the mirror residual motion in the lock-acquisition and observation phases.

We implement either DC compensation filter or DC coupled damping filter for the GAS filter stage control, in order to keep the keystone height and to damp the vertical resonances.

For the BF control, we only control the torsion dof (Yaw dof), in order to compensate the low frequency torsional drift and to damp the whole chain resonances which cannot be sensed by IP-stage.

At the payload level, we implement control loops to compensate for the TM and MN angular drift in Pitch and Yaw. In addition, the control damps the payload internal resonances that cannot be sensed by the upper stages.

Figure 5.2: An example of the signal flow of the feedback control system: the case of the IP-stage. H1, H2 and H1 represent each coil. L, T and Y denote longitudinal, transverse and yaw respectively.

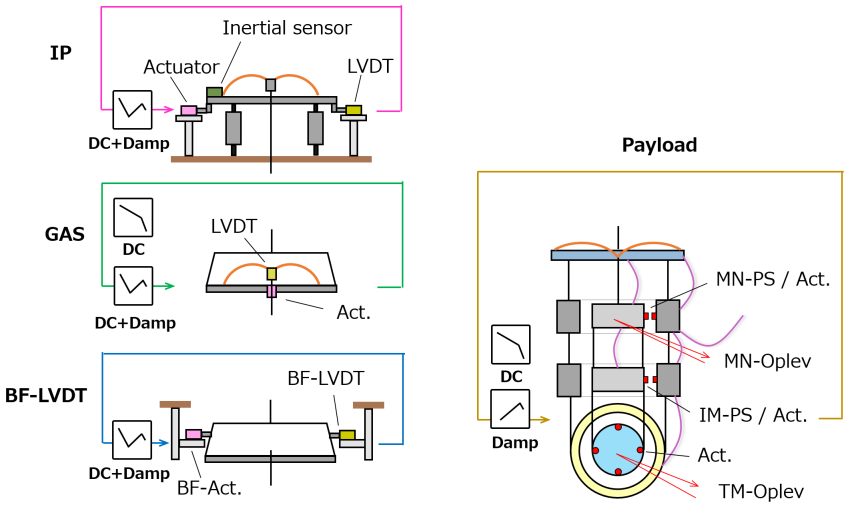

Figure 5.3: Overview of the control system for the Type-A suspension. The curves in the square windows show the schematic view of the filter shapes.

5.5 Controls for calm-down phase

As described in section 5.1, the primary target of the calm-down phase is to reduce large-amplitude motion of the mechanical resonances excited by external disturbances. In this phase, the active controls are required to damp resonances so that the $1/e$ decay time of the mechanical resonances disturbing the interferometer lock acquisition, is less than 1 minute.

According to the rigid-body simulation described in section 5.3, the Type-A suspension has 75 resonant modes; these are listed in section B.1. In this model, the assumption is made that the heat links do not affect the suspension dynamics. In this work, however, we concentrate on the resonances at frequencies lower than 30 Hz, since the resonant modes that impact the lock acquisition are the lower frequency modes rather than the higher frequency ones. The value of 30 Hz is set since the suspension sensors/actuators can sense/actuate the system up to around that frequency. As one note about the higher frequency modes above 30 Hz, we might have to work on their damping if such resonances degrade the detector sensitivity. However for this purpose we need to have another system to damp them since the local sensors/actuators are not enough to damp such modes.

In addition, some modes that do not affect the lock-acquisition are excluded from this discussion. Consequently the total number of resonances to be damped becomes 54.

5.5.1 Servo system

Table 5.3 shows the feedback filters designed for the calm down phase. To estimate the damping performance, the $1/e$ decay time constant with and without the controls has been calculated. The results are summarised in Figure 5.4. There are four remaining resonances below 30 Hz that exceed the requirement of 1 minute. However, since these are the tilt modes of the F1 and F2 GAS stages (mode #25, #26, #29 and #30 in section B.1) and the coupling to the mirror is small, we do not consider them here[1]. Based on this, this control system will satisfy the requirement for the calm-down phase.

[1] According to the model prediction, the mode #29 and #30 seems to slightly connect to the mirror tilt motion. However exciting the F1/F2 motions by actuating payload is not feasible, and thus we do not consider them.

Table 5.3: The servo loops for the calm down phase with the used sensors. In the below oplev and PS represent the optical lever and the photo sensor. We have the optical levers at MN- and TM-stages and they are labeled as MN-oplev and TM-oplev respectively.

Loop	Loop dof	Sensor	Actuation dof	Purpose
IP	L, T, Y	LVDT	IP	DC and damp
BF	Y	BF-LVDT	BF	DC and damp
F0	GAS	LVDT	F0	DC and damp
F1	GAS	LVDT	F1	DC
F3	GAS	LVDT	F3	DC and damp
BF	GAS	LVDT	BF	DC
MN	L, T, V, R, P, Y	PS	MN	damp
from TM to MN	P	TM-oplev	MN-P	DC and damp
from TM to IM	P	TM-oplev	IM-P	damp
from TM to MN	Y	TM-oplev	MN-Y	DC
from TM to IM	Y	TM-oplev	MN-Y	damp

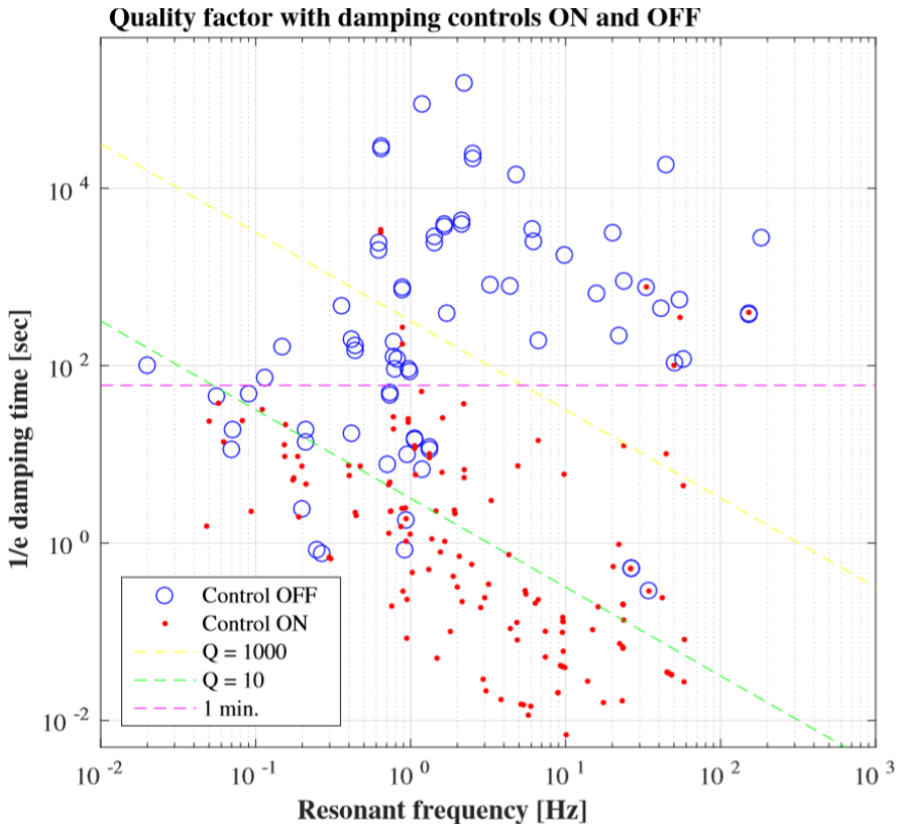

Figure 5.4: $1/e$ decay time constant with and without the designed controls. The blue-edged points and the red dots show the decay time constant without and with the control system. This control loop takes care below 30 Hz.

5.6 Controls for lock-acquisition phase

In order to stably acquire/keep the interferometer lock, RMS velocity, RMS displacement and RMS angular displacement of the mirrors are required to be smaller than the requirement in the table 5.2. Typically the biggest contribution to such mirror residual motion comes from the ground motion in a frequency band around 0.2 Hz, which is called micro-seismic peak.

In order to sufficiently suppress the mirror residual motion at low frequency, we consider a feedback system with feed-fowrading as introduced in section 2.2.3 (especially in Figure 2.17). In the calm-down phase, we use LVDTs for IP-stage control. However, the LVDTs measures the relative displacement between the ground and the IP-stage. This implies that the control loops with the LVDTs inject the seismic noise to the suspension and then shakes the suspension at low frequency, especially at the microseicmic region.

In order to avoid the re-injection of the seismic noise to the suspension, we consider to remove the seismic motion signal from the LVDTs. For this purpose, we use a seismometer Trillirum120QA (see section 4.2.7) on the ground. By combining the LVDT and seismometer signals, we subtract the ground motion signal from the LVDTs. We call this technique sensor correction. The expected suppression is discussed in this subsection. In addition, we assume that the sensor correction system is implemented to the upper stages such as IP-stage. For the other control loop, especially for the payload and the GAS stages, we assume to use same ones as the ones used in the calm-down phase. In the following subsection, the sensor correction system at the IP-stage is abbreviated as IP_{sc}.

5.6.1 Suppression with sensor correction technique

Filter for sensor correction at IP-stage

The block diagram of the IP-stage feedback control system with the sensor correction system is shown in Figure 5.5. This system is the one in Figure 2.17 but without the path from the seismometer to the actuator (which corresponds to the case where $F_{\mathrm{ff}} = 0$). In this system, the sensor correction part is shown by blue-colored part, and is additionally implemented to the feedback control of the IP-stage. In this configuration, the seismic noise coupling will be most effectively subtracted when the sensor correction filter F_{sc} satisfies $F_{\mathrm{sc}} = -S_{\mathrm{L}}/S_{\mathrm{s}}$ where S_{L} and S_{s} are the sensor response of the LVDT and the seismometer, as discussed in section 2.2.3 (especially in the topic of feedback control with feed-forwarding).

Assuming the inter-calibration between the IP-LVDT and the seismometer sensors are perfectly done, i.e, $S_{\mathrm{L}}/S_{\mathrm{s}} = 1$, the sensor correction filter F_{sc} should have gain of 1 at the frequency band where we want to subtract the seismic motion. In addition, since the seismometer becomes more sensitive to the local tilt motion at the frequency below 0.1 Hz, the F_{sc} should also have a high-pass filter which keeps the phase shift as 0 deg as much as possible in the demanded frequency band. Based on this using a elliptic high-pass filter, the F_{sc} can be

shaped as shown in Figure 5.6.

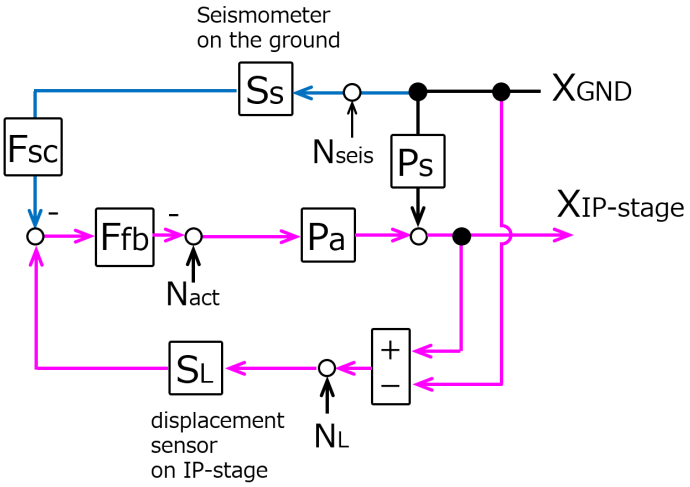

Figure 5.5: Block diagram of the feedback control with the sensor correction system at the IP-stage. Each parameters are defined with the same manner as in section 2.2.3. This is the case where F_{ff} is set to zero. By implementing filter for the sensor correction F_{sc}, we realize the sensor correction system, that subtract the seismic noise from the displacement sensors (LVDTs).

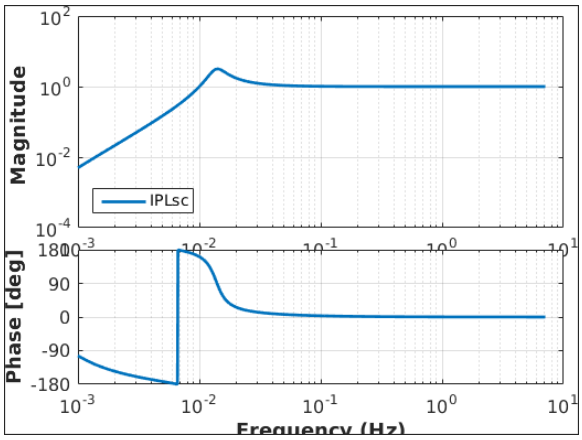

Figure 5.6: Designed sensor-correction filter for IP-stage. The horizontal axis shows frequency in Hz.

Expected mirror suppression

Using the filter shown in Figure 5.6 and the filter sets used in the calm-down phase, we calculate the expected velocity and displacement in L dof. The results are shown in Figure 5.7. In this calculation, high seismic noise level (90 percentile seismic motion level) is assumed. The blue colored curves show the case where no controls are applied. The orange ones represent the case where the IP-stage is controlled with IP-LVDTs (without $IP_{\rm sc}$). The red ones show the case where the IP-stage is controlled with IP-LVDTs with $IP_{\rm sc}$.

Table 5.4 summarizes the RMS velocity and displacement integrated down to 10 mHz. Figure 5.7 and Table 5.4 indicate that the RMS velocity satisfies the requirement for the lock acquisition phase, independent on the sensor correction system at IP-stage. On the other hand, the RMS displacement requirement will not be satisfied if the integration is done down to 10 mHz due to the seismometer self-noise contribution. If the RMS integration is stopped at 13.5 mHz (time scale is about 75 sec), the RMS displacement requirement will be satisfied. Since this displacement amplitude enhancement comes from the tilt motion coupling from the seismometer Trillium120QA, we have to implement another system for the further stabilization at such frequency. For example, this issue can be solved by implementing a sensor correction system for the seismometer using a sensor which senses the local tilt motion. As another option, we can compensate the displacement drift by feeding back the interferometer signal to the upper stage such as IP-stage, once the interferometer lock is acquired. Since the interferometer lock can be acquired within such time scale (about 1 minute) and the displacement drift compensation in can be treated in the control system in the observation phase, for the lock-acquisition control system, we consider to realize a system which sufficiently suppresses the mirror motion in velocity/displacement at least in the time scale of 1 minute. Indeed the primary target is to suppress the motion at the frequency region where the micro seismic peak is dominant, will be realized by implementing of this sensor correction system.

Figure 5.8 shows the expected mirror velocity/displacement in L dof with $IP_{\rm sc}$ where the inter-calibration between IP-LVDTs and the seismometer Trillium120QA is not perfect. From these plots, the permitted maximum mismatch between those sensors is obtained as 40 %, based on the RMS values at about 15 mHz. In addition, the target inter-calibration mismatch is then set to smaller than 10 %.

Consequently taking care of the displacement compensation system whose time scale is longer than 1 minute is set as a work for the observation phase control, and the control system in the lock-acquisition phase focuses on the suppression at the frequency around the microseismic peak.

Based on this assumption, the calculated results indicates that this sensor correction system at IP-stage will suppress the RMS velocity/displacement of the mirror and will satisfy the RMS requirement for both the velocity and the

displacement. In addition, it is confirmed that the sensor correction system at IP-stage will also satisfy the displacement requirement at 10 Hz.

Table 5.4: The estimated RMS displacements and velocities of the mirror with the integration down to 10 mHz. IP_{sc} in the labels denote the sensor-correction system in this work.

Configuration	velocity [μm/s]	Displacement [μm]
Without any controls	0.48	0.56
with IP control, without IPsc	1.1	0.99
with IP control, with IPsc	0.15	0.75

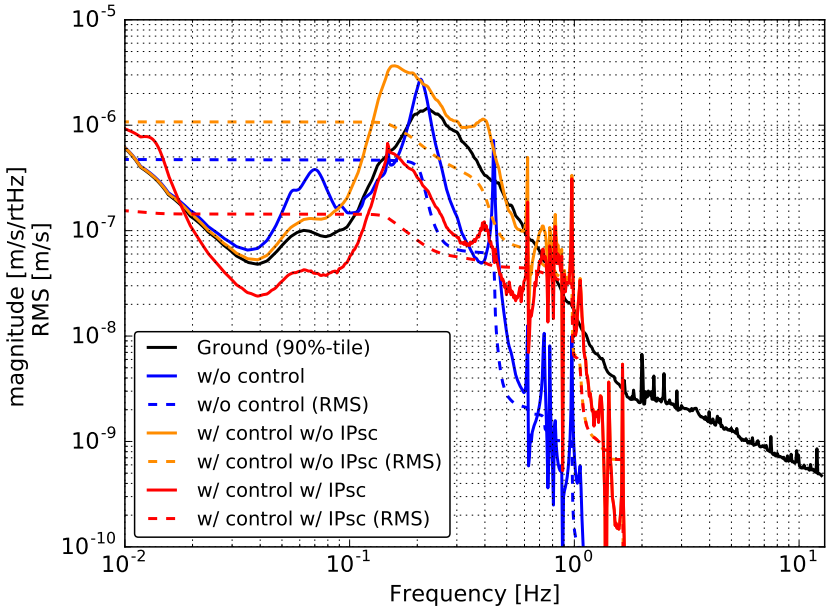

(a) Expected mirror velocity

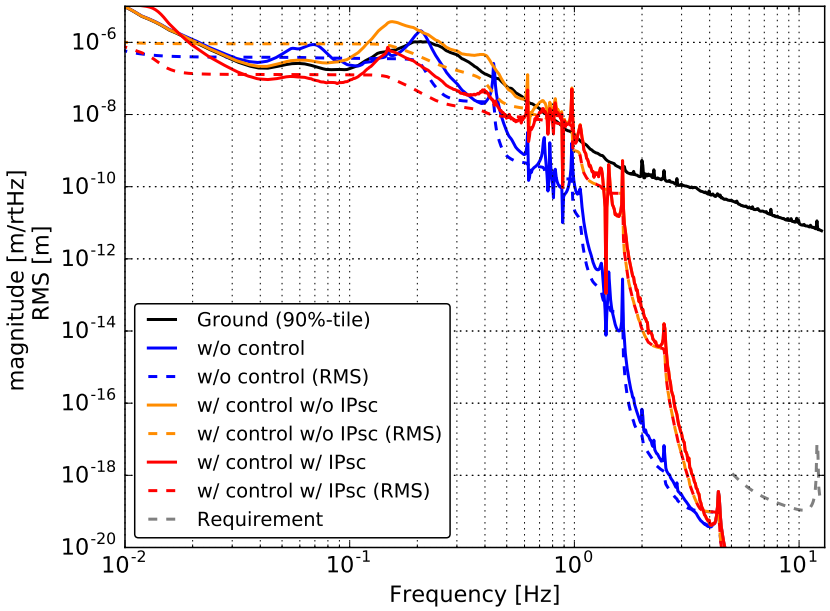

(b) Expected mirror displacement

Figure 5.7: Expected mirror residual motion in L dof in velocity (*top*) and in displacement (*bottom*) with and without the IP-stage control. The colors show the difference of the control configuration. The dashed curves draw the RMS integrated down to 10 mHz. In this calculation, high seismic noise level (90 percentile seismic motion level) is assumed. The grey colored dashed curve at around 10 Hz shows the requirement of the mirror displacement.

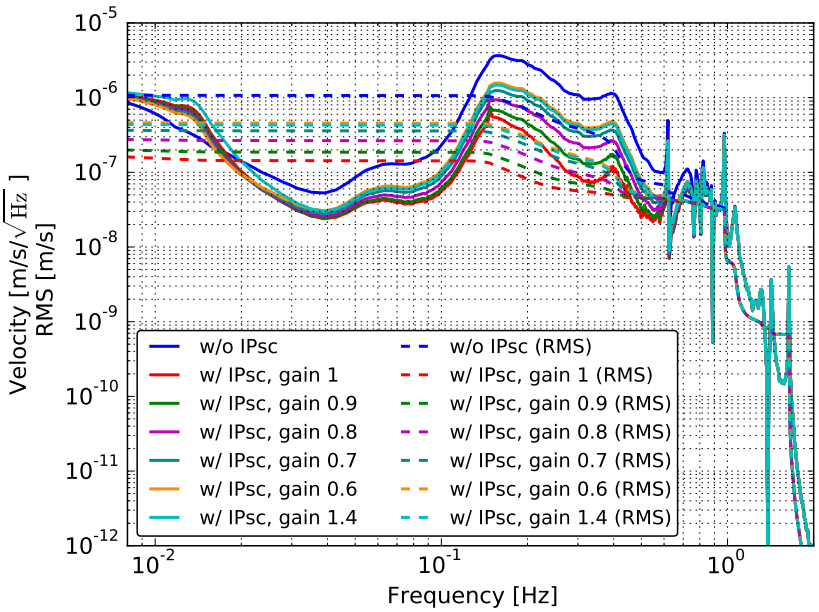

(a) Expected mirror velocity

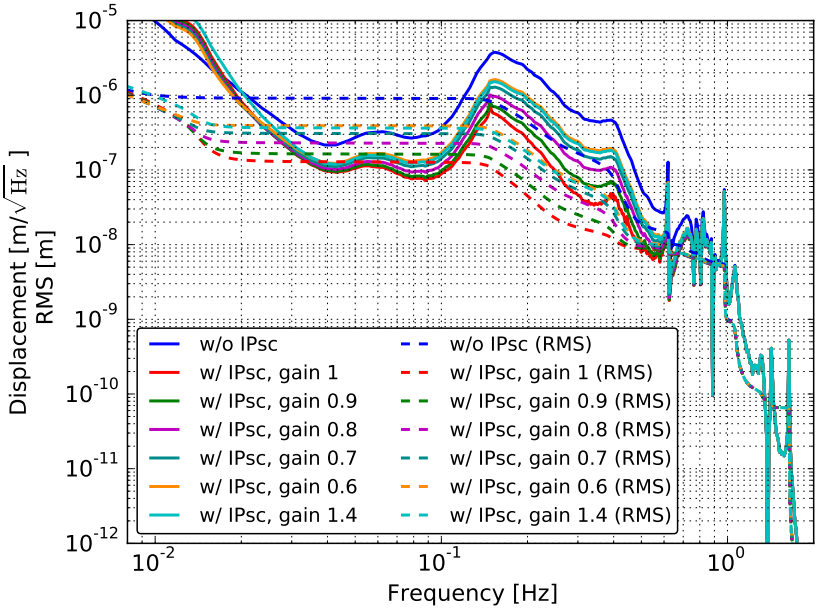

(b) Expected mirror displacement

Figure 5.8: Expected mirror residual motion in L dof in velocity (*top*) and in displacement (*bottom*) with IP-stage control with $IP_{\rm sc}$. The colors show the mismatch of the inter-calibration between the IP-LVDTs and the seismometer Trillium120QA. The dashed curves draw the RMS values integrated down to 10 mHz. In this calculation, high seismic noise level (90 percentile seismic motion level) is assumed. The gain denotes the mismatch level between the LVDTs and the seismometer.

5.7 Controls for observation phase

In this phase, we do not need strong damping since the mirror motion is already calmed down enough. Rather than damping, we need to keep the mirror position/orientation without injecting control noises to the mirror motion. For this purpose, the mirror displacement at above 10 Hz have to be sufficiently suppressed in order to meet the requirement. Especially for the Type-A SAS, the permitted maximum mirror displacement at 10 Hz is 8.0×10^{-20} m$/\sqrt{\text{Hz}}$ (as described in section 1.4.2).

Figure 5.9 shows an estimated mirror displacement in L dof with the controls used in the lock acquisition phase (that is developed in sections 5.5 and 5.6). In this figure, the dashed black curve show the requirement, and the other colored curves represent the couplings to the mirror displacement from all the sensors used in the controls. According to this plot, the contribution from the following loops exceed that required displacement noise level at above 10 Hz:

1. MN to MN loop with the photo-sensors (PSs),
2. TM to MN loop with TM optical lever
3. F3GAS to F3GAS and F0GAS to F0 loops with the LVDTs.

Based on this calculation, it is found that the control loops by PSs have to be opened in the observation phase. This is since their contribution above 10 Hz is much larger than the requirement (by factor of 10^8 at 10 Hz), and since realizing such suppression with mathematical filters are not feasible. It is also required to use the only DC-filters for the GAS filter loops, without damping-coupled filters. In addition, the filter shape of the optical lever loop is also have to be tuned, or to be opened.

Since to the control system for the observation phase depends on the main interferometer control and the control scheme has not been under development in 2019, realizing the control system for the observation phase is set at further step after this thesis. However, it is expected that the above listed loops will be issues in the control in the observation phase, and the filter shapes and the control dofs are to be further considered/developed.

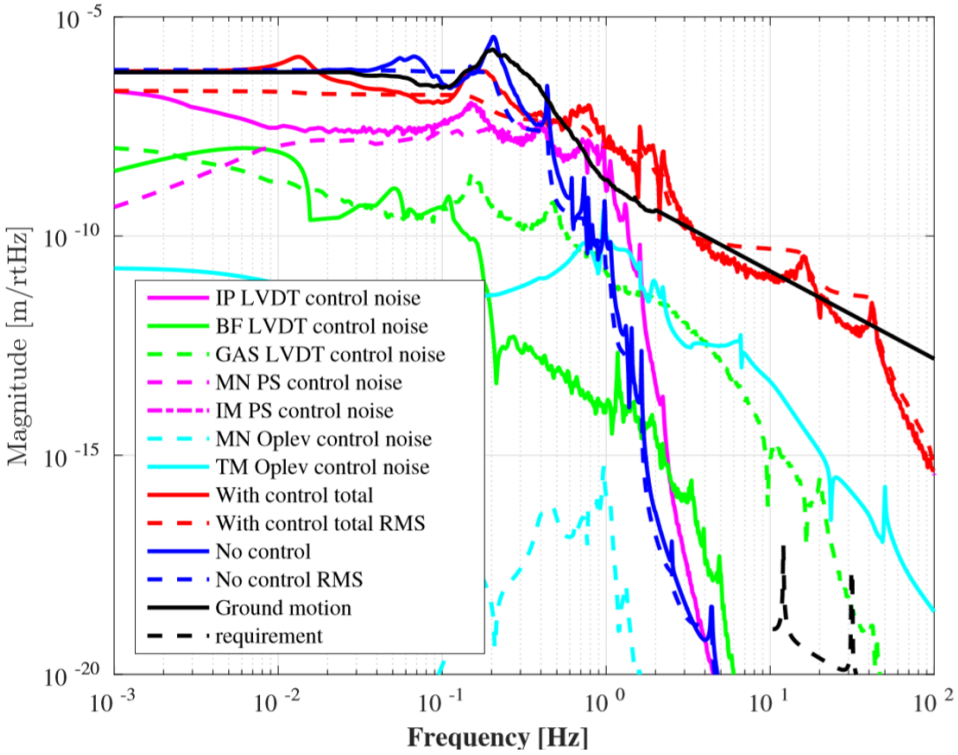

Figure 5.9: Expected mirror residual motion in L dof in displacement including the contribution from all the control loops in the lock-acquisition phase. The blue and red colored dashed curves show the RMS values integrated down to 1 mHz, and the other curves show the spectra of mirror displacement induced by each control loop.

Chapter 6

Implementation of Type-A SAS control system

This chapter describes the performance of the implemented active control system (developed in chapter 5) and its evaluation. The target is to realize the local control system for the Type-A SAS that allows to acquire the interferometer lock. The more concrete goal is to confirm that the suspensions have the designed mechanical response, and also to verify if the control system meets the requirements for the calm-down phase and lock-acquisition phase summarised in section 5.2, especially in Table 5.2. This implementation/evaluation is conducted with ETMX suspension which is one of the Type-A SAS.

Section 6.1 gives the information about ETMX suspension configuration during the measurement. Section 6.2 describes the characterization of the mechanical responses of the Type-A SAS. This is done in order to confirm if the suspension has the characteristics of pendulum as a preparation for building the active control system. Section 6.3 describes the performance of the implemented controls filters for the calm-down phase control. This section confirms that all the mechanical resonances disturbing the interferometer lock are damped within the required time in the lock recovery mode. Section 6.4 summarizes the performance of the control system for the reduction of the mirror residual motion focusing on the frequency region around the micro-seismic peak. This is done to realize a robust interferometer operation.

Since the FPMI lock is achieved by implementing the above active control system, it becomes available to investigate the vibration isolation performance of the suspension at higher frequencies, compared to the measurement with the local sensors. Section 6.5 reports the result of the mechanical vibration isolation performance measured with the interferometer.

6.1 Suspension configuration

6.1.1 Mechanical and environmental configuration

During the measurement, it was known that one of GAS filter, which is the third GAS filter from the top and is called F2-filter, was mechanically stacked for a technical reason[1]. It was also known that this could not be solved unless disassembling the upper structure, and there was not enough time to solve this issue. We then decided to keep using the ETMX suspension with the F2 GAS filter stacked, since the requirement for the displacement noise at 10 Hz should be satisfied even with the configuration as shown in Figure B.7.

Concerning the other setting, the temperature of the payload during the test was about 250 K.

[1]Nevertheless all the coils of the sensors and actuators were electrically connected and the expected resistances were measured, no free-swinging was observed when a actuation was sent. In addition to this, it seemed that one peak disappeared from the force transfer function in vertical dof. We then started to believe that the keystone of the GAS filter somehow hit the lock screws which had been installed for a safety.

6.1.2 Sensor and actuator arrangement

The implemented sensor positions for ETMX suspension are summarized as shown in Figure 6.1 and Figure 6.2.

IP and BF stage

In ETMX suspension, the positions of each inertial sensor, LVDT and actuator unit at IP-stage are arranged as shown in *left* of Figure 6.1. As introduced in section 4.2.2, ETMX has three geophones as the inertial sensor at IP-stage. The sensor actuator unit at BF-stage is distributed as in *right* of Figure 6.1.

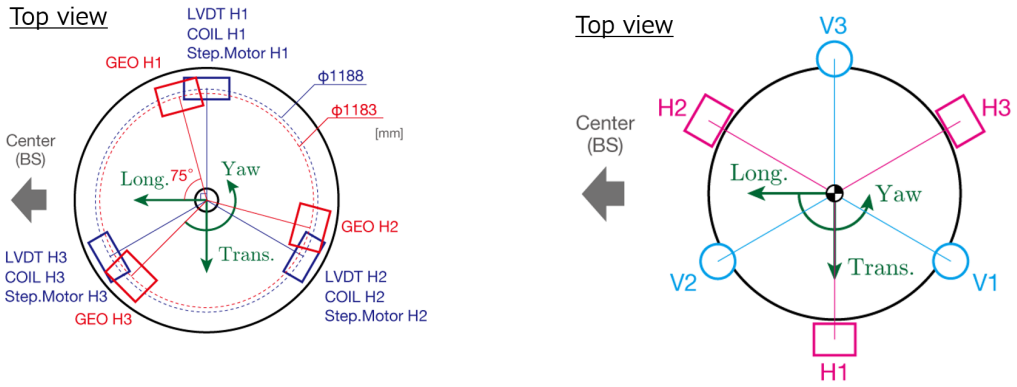

Figure 6.1: Geometrical position of the installed sensors and actuators at IP-stage(*left*) and BF-stage (*right*) for ETMX suspension case [74]. GEO and COIL denote the geophone and actuator respectively. Three LVDTs are installed at IP-stage and measure the horizontal 3 dofs (longitudinal, pitch and yaw). Six BF-LVDTs senses the displacement in the six dof.

Optical levers

An angular optical lever and length-sensing optical lever are installed at the TM-stage, and they sense the TM motion in the three dofs, i.e, longitudinal, pitch and yaw. On the other hand, only the angular optical lever is implemented at the MN-stage. In the MN-stage optical lever, the incident light beam is sent to the mirror attached on the MN-body and it is reflected to the same place where it is injected. In addition, the mirror is mounted onto the MN-body with an angle, the sensor output of this MN-stage optical lever in pitch dof becomes a superposition of the MN-body motion in pitch and roll. Those signals are degenerated and cannot be distinguished.

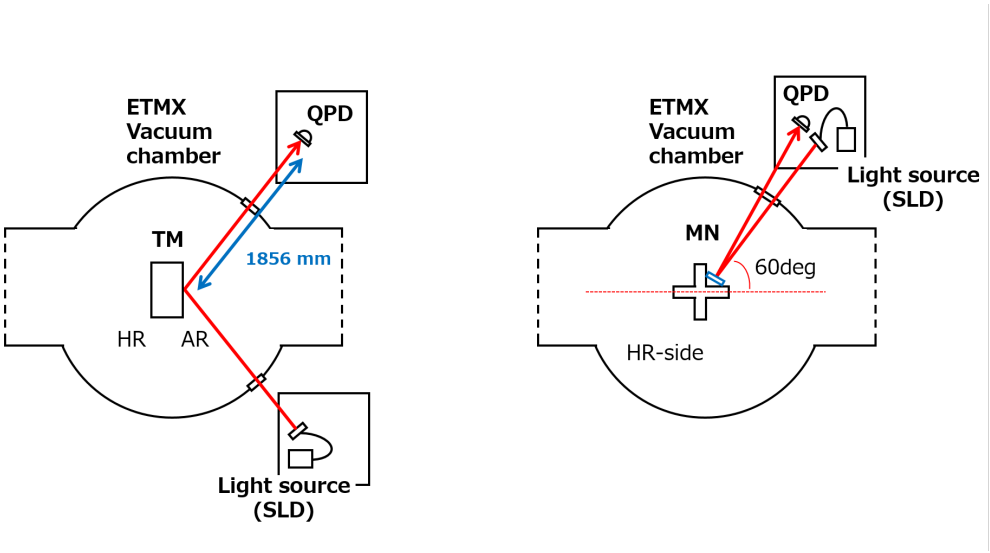

Figure 6.2: Geometrical configuration of the installed optical lever systems at the TM-stage (*left*) and MN-stage (*right*). HR and AR denote high-reflectivity coating and anti-reflectivity coating respectively.

6.2 Mechanical response

In order to confirm if the assembled suspension works as designed, its mechanical response is investigated by comparing to the simulation.

6.2.1 ETMX suspension model

In this check, we use a rigid-body simulation without considering the heat link system including HLVIS, assuming that the heat link system has sufficiently soft stiffness and it does not make any impact to the main suspension. In addition, one spring for F2 GAS is removed in the simulation in order to take into account that the F2 GAS stage is mechanically stacked.

6.2.2 Diagonal transfer functions

We measure the force transfer function of each component by injecting white noise at each component actuator, and compared to the simulation.

IP stage

Before the measurement, at the IP-stage, the LVDT sensors are diagonalized to the Cartesian basis by measuring the geometrical position. The coil-magnet actuators are diagonalized along with the LVDTs by checking the transfer function from each actuator to the L, T and Y dof defined by LVDTs with an injection of a sinusoidal signal at 2 Hz. This frequency is selected since the highest mechanical resonance is about at 1 Hz. The inertial sensors, i.e, geophones for ETMX suspension, are then inter-calibrated to LVDTs by comparing the transfer function from LVDT signal in yaw dof to each geophone signal. After the operation, the sensor matrix for the geophone is diagonalized by referring the transfer function from LVDT signal in L, T, Y to each geophone signal with an injection of a sinusoidal signal at 2 Hz.

After the above procedure, we measure the mechanical transfer functions and the results are shown in Figure 6.3. Even though it is found that the Q factors of some of the peaks in the model have to be tuned more precisely, basically the measured resonant frequency and the slope at higher frequencies agree with the rigid-body simulation.

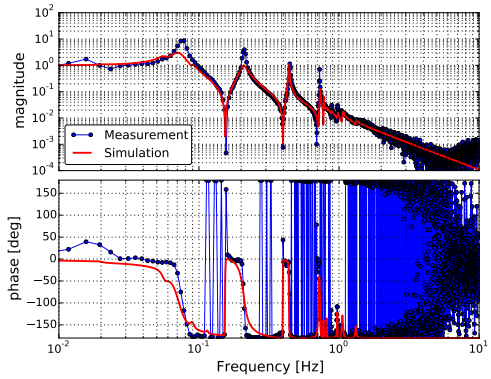

(a) Longitudinal

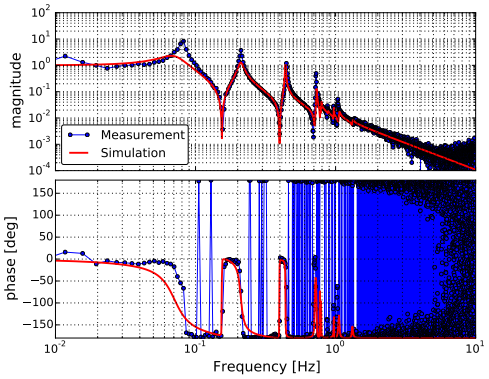

(b) Transverse

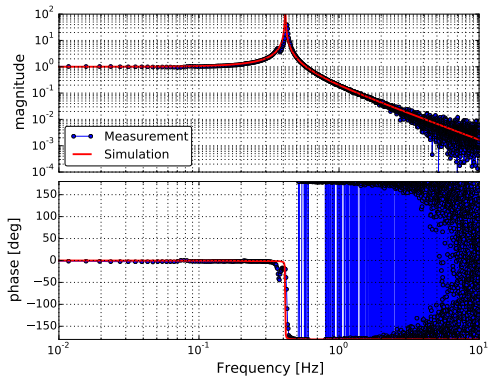

(c) Yaw

Figure 6.3: Diagonal mechanical transfer functions of the IP-stage in longitudinal (a), transverse (b) and Yaw (c) dof with the simulated curve. The dots and the curves show the measured result and the simulated one.

GAS stages

The measured transfer functions of each GAS stage are shown in Figure 6.4. The noise becomes dominant at frequency higher than about 7 Hz. As Figure 6.4 indicates clearly, the model fails to explain the actual system. This is since the resonant frequencies of each GAS filter are not estimated well enough. For the lowest three modes (about the 180 mHz, 410 mHz and 480 mHz modes) in the model could be tuned based on the current model with system identification. However, the model fails to predict the the resonances at 1.29 Hz and 1.44 Hz, and also a peak at 4.4 Hz mode, which is the payload vertical resonance, is not found. In addition, a resonance at 9.7 Hz is found.

Consequently, the current model cannot explain the actual GAS filter responses and it has to be modified for more precise modeling. We also might have to investigate further about the system and to confirm if the discrepancies are well affected with the heat link system, and if the F2-GAS treatment is reasonable enough, in a case where this issue limits the interferometer sensitivity.

Even though this model fails to explain the actual resonant frequencies, the measured slopes at higher frequency agreed with the model. This implies that the vibration isolation performance at above 10 Hz will satisfies the requirement, as shown in Figure B.7. The details of the higher frequency performance will be confirmed with high sensitive sensor such as the main interferometer.

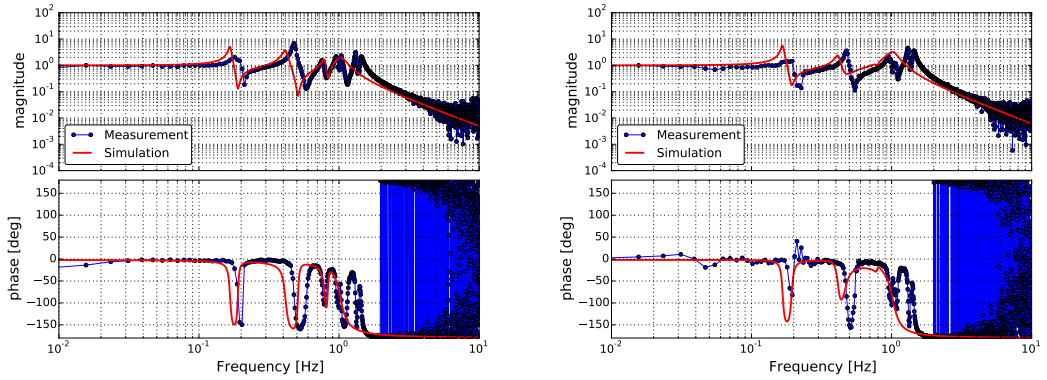

(a) F0 GAS (b) F1 GAS

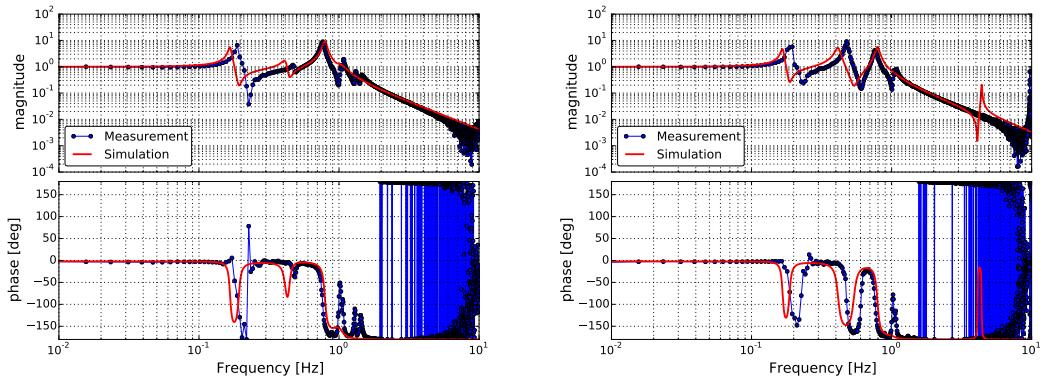

(c) F3 GAS (d) BF GAS

Figure 6.4: Mechanical transfer functions of F0 GAS (a), F1 GAS (b) F3 GAS (c) and BF GAS stage with the simulated curve. The dots and the curves show the measured result and the simulated one.

BF stage

In the BF-stage, both the sensors and actuator are diagonalized by measuring the geometrical LVDT-unit position. Figure 6.5 shows the measured transfer function in the 3 horizontal dofs. At high frequencies above about 1.5 Hz in L/T, 2 Hz in Y dof, all the tranfer functions have f^2 dependency. This is known as a spurious coupling in the BF-LVDT. The actuation signals directly couple to the sensor coils.

For L and T dof, the measurement agrees with the simulation, except for the Q factors and the resonant frequencies of the first and the second modes, similar to the IP-stage case. Concerning the yaw dof, the used model totally fails to predict the frequency response. In addition, for all the L, T, Y dofs, this measurement do not agree with the previous measurement which was conducted when payload and the heat link system were not installed. This issue is discussed in section 6.2.3.

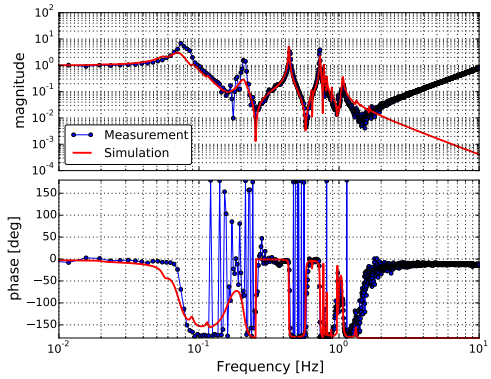

(a) Longitudinal

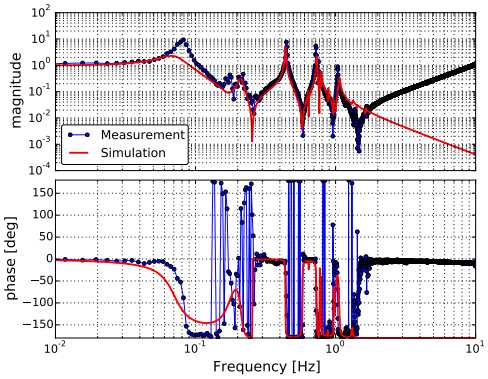

(b) Transverse

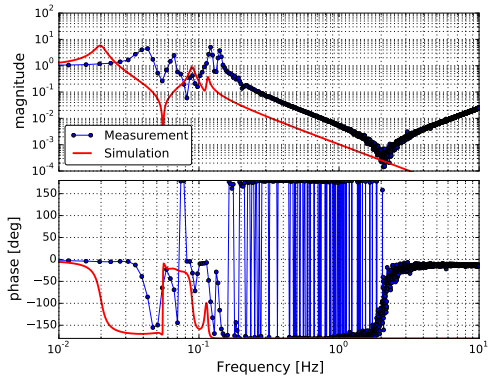

(c) Yaw

Figure 6.5: Diagonal mechanical transfer functions of the BF-stage in longitudinal (a), transverse (b) and Yaw (c) dof with the simulated curve. The dots and the curves show the measured result and the simulated one.

MN stage

For the payload part, the actuators are balanced by using the already calibrated optical lever so that the each coil pushes/pulls the mass by the same amount. The photo-sensor diagonalization is done geometrically. Figure 6.6 and 6.7 show the measured response of the MN-stage sensed by the optical lever and by the photo-sensors respectively. The noise becomes dominant at frequency higher than about 20 Hz for the transfer functions by optical lever and above a few Hz for the ones by the photo-sensors.

Figure 6.6 indicates that the model can explain the actual system, except for the two modes observed at 0.32 Hz in yaw dof and 7.5 Hz in pitch dof. The 0.32 Hz in yaw dof can come from the discrepancy of the material parameters since this model uses the parameters at 20 K. Another possible reason would be the heat link system, however, we do not have good explanation for this in this work. The discrepancy of the 7.5 Hz in pitch dof, which is the TM-chain mode, can be connected to the hanging situation. Since the TM is suspended with four rods of the sapphire fiber and it is glued on the mirror with ears [65], and we do not have much experience the suspension system with that rods. The material parameter can be also one of this reason.

Figure 6.7 shows that the model agrees with the measurement except for:

1. the two modes observed in Figure 6.6, i.e, the 0.32 Hz mode in yaw dof and 7.5 Hz in pitch dof,

2. the highest resonance in L and T dof at 5.2 Hz and 5.0 Hz respectively as shown in Figure 6.7a and 6.7b,

3. vertical dof as shown in Figure 6.7c.

The discrepancy of the L and T dof, which are the RMN resonances, might come from the hanging condition. This can be happen if one of the wires is floating, the effective stiffness in pitch and roll can become softer, even though for more detailed explanation for this, we have to do further investigation. The failure of the vertical dof come from the failure of the photo-sensor diagonalization. The vertical photo-sensor signal obtained by the matrix operation based on the geometrical factors, actually it senses the yaw motion as shown in Figure 6.7c and as shown in Figure 6.7f. Thus the vertical dof cannot be tested with the photo-sensor. In order to sense the vertical motion with the photo-sensors further sensor matrix diagonalization is necessary.

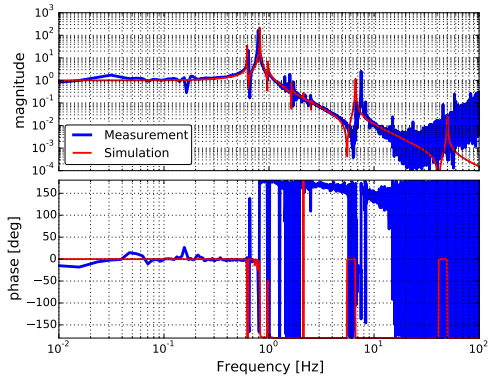

(a) MN to MN in pitch

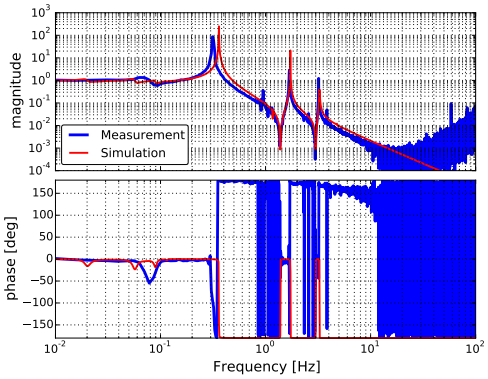

(b) MN to MN in yaw

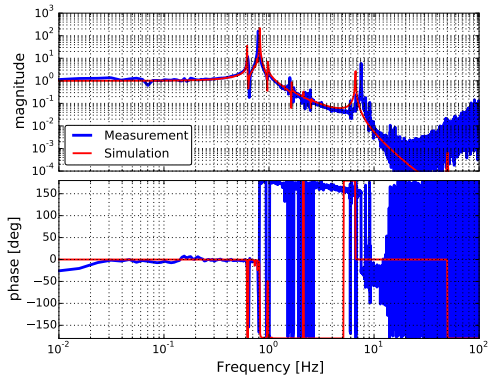

(c) MN to TM in pitch

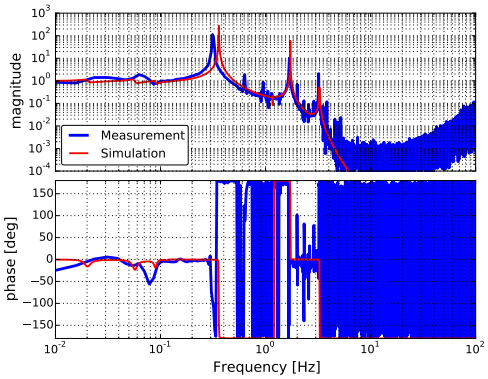

(d) MN to TM in yaw

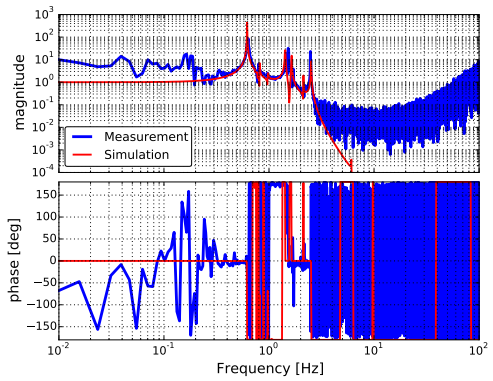

(e) MN to TM in longitudinal

Figure 6.6: Diagonal mechanical transfer functions of the MN-stage in pitch (*left*) and yaw (*right*) sensed by the optical lever. The upper panels show the response from MN to MN, while the lower panels represent the ones from MN to TM.

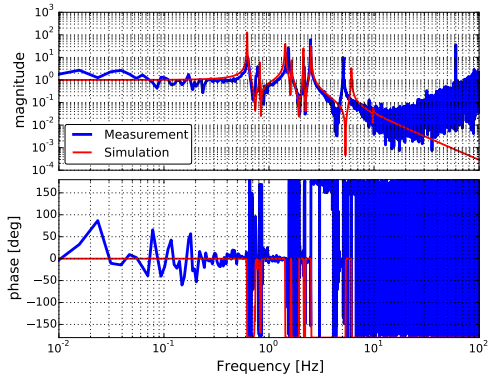

(a) Longitudinal

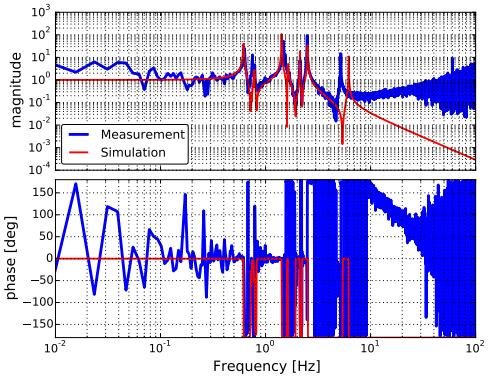

(b) Transverse

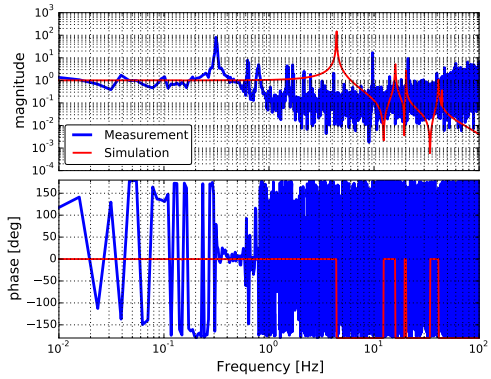

(c) Vertical

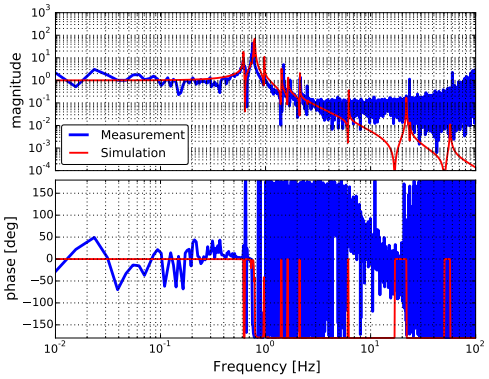

(d) Roll

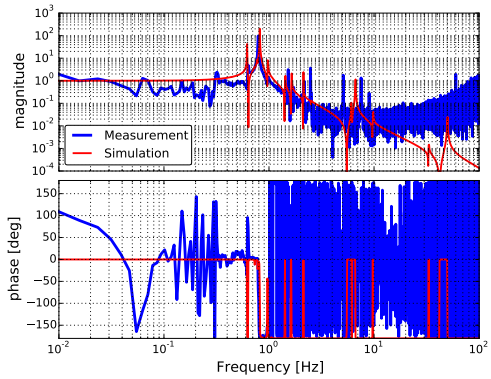

(e) Pitch

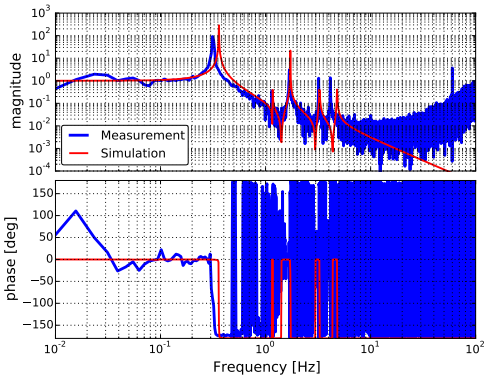

(f) Yaw

Figure 6.7: Diagonal mechanical transfer functions of the MN-excitation to MN-stage sensed by the photo-sensors.

IM stage and TM stage

Basically the model agrees with the actual system except for the two modes at 0.32 Hz in yaw dof and 7.5 Hz in pitch dof. These transfer functions are measured with the optical levers at the TM stage.

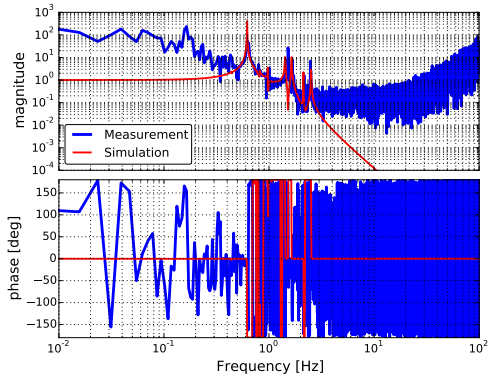

(a) Longitudinal

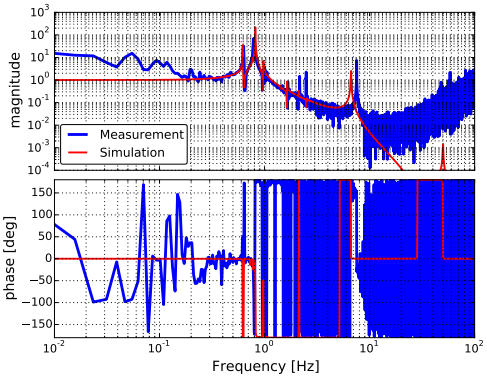

(b) Pitch

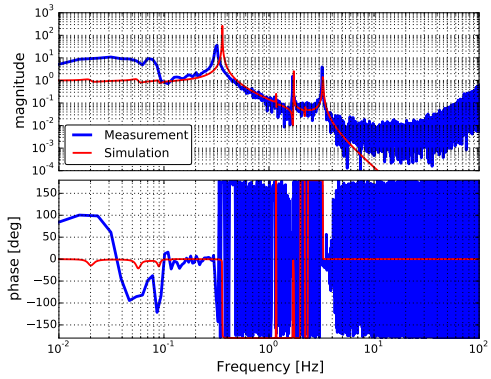

(c) Yaw

Figure 6.8: Diagonal mechanical transfer functions from IM-stage excitation to TM in longitudinal (a), transverse (b) and Yaw (c) dof with the simulated curve. They are measured with the optical levers at the TM stage.

TM stage

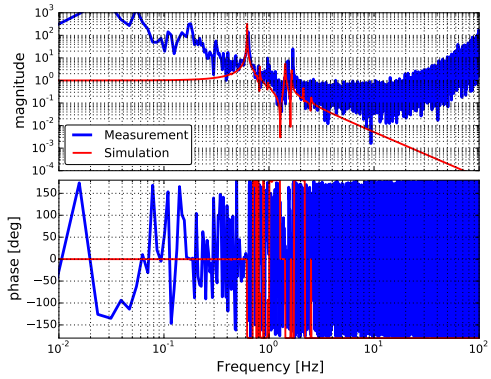

(a) Longitudinal

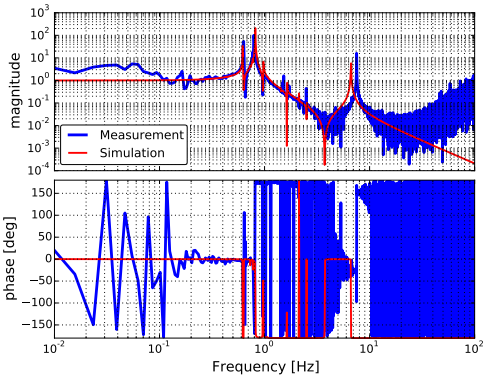

(b) Pitch

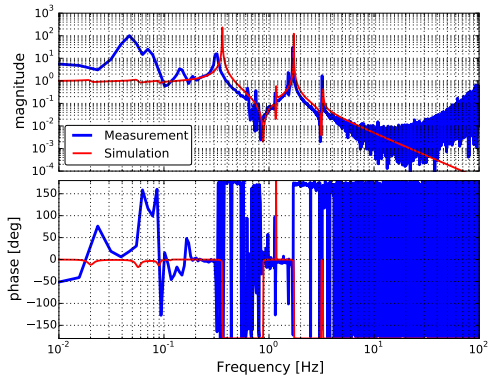

(c) Yaw

Figure 6.9: Diagonal mechanical transfer functions from TM-stage excitation to TM in longitudinal (a), transverse (b) and Yaw (c) dof with the simulated curve. They are measured with the optical levers at the TM stage.

6.2.3 Effect of heat-links and its vibration isolation system

According to the force transfer function measurement in the above, some significant discrepancies from the model without heat link system are reported at the BF-stage measurement as follows:

- The first resonant frequency of the BF-stage excited transfer functions in Yaw degree of freedom become higher than the those predicted by the model. The measured first resonant frequencies for Yaw dof is 40 mHz while that by model is 20 mHz.
- One peak at 0.14 Hz is newly found in the BF-stage excited transfer functions in Yaw degree of freedom. This peak is found in all the equipped sensors when the BF-stage is excited in Yaw. On the other hand, this peak is not observed with Optical levers when the lower stage such as MN-stage is excited.

Similar measurement was already done in [44] and it reports that if there is not payload, heat link nor the heat link vibration isolation system, the first resonant frequency in L, T and Yaw was dof measured at 55 mHz, 65 mHz and 20 mHz, respectively. On the other hand, the newly measured frequencies in this work are 74 mHz, 82 mHz and 40 mHz for L, T and Yaw dof respectively. It also reported the measured results were in agreement with simulation. Compared to the suspension configuration in [44], the total length of the suspension becomes longer in this work, it is more natural to predict that the fist resonance would be found at lower frequencies. The resonant frequency depends on the temperature, and the temperature during the measurement is actually lower than the room-temperature, 250 K. However, this is not enough to explain the difference of the elastics constant by factor of about 4 (in yaw case). Thus this implies that the current system should have additional springs to the current model. The most possible origin of this additional spring is the heat link system.

6.2.4 Summary of mechanical system characterization

The measured characteristics in terms of the frequency response agrees with the rigid-body simulation (which does not include the heat link system) except for the BF-stage and GAS filters, with some exception of resonant frequency and the Q factors. The model fails in predicting the frequency response of the BF-stage, especially in the yaw dof.

Consequently, it is confirmed that the each suspension component has the characteristics of a pendulum, and this is enough for the purpose of realizing the local control system to allow the interferometer lock. However, the details of the mechanical system will have to be more precisely identified and modeled. Especially the rigid-body modeling without including heat link system fails to explain some of the actual Type-A suspension response and resonant frequencies.

6.3 Performance of damping control

The installed feed-back servo system for the calm-down phase is summarized in section6.3.1 and its performance test is described in the section6.3.2.

6.3.1 Servo system

As shown in Figure 5.3, the upper part (IP and BF) has DC-coupled damping filters for the horizontal and the vertical dof, and lower part (payload) is more focused on the payload mode damping and mirror angular DC control. The implemented servo loops with the used sensors is summarized in Table 6.1 and the open loop transfer functions are show in Figure 6.10. In this system we use optical lever at MN-stage to sense the MN motion in the roll dof. We also use the optical levers at two stages; MN- and TM-stage. Oplev at the MN-stage (MN-oplev) senses the two angular motion in P and Y, while the optical lever at TM-stage (TM-oplev and TM-length oplev) senses the L, P and Y dof.

Table 6.1: The implemented servo loops with the used sensors. The loops for the IP- and BF-stage and the GAS filters are closed in each stage. In the below oplev represents the optical lever. We have the optical levers at MN- and TM-stages and they are labeled as MN-oplev and TM-oplev respectively.

Loop	Loop dof	Sensor	Actuation dof	Purpose
IP	L, T, Y	LVDT	IP	DC and damp
BF	Y	BF-LVDT	BF	DC and damp
F0	GAS	LVDT	F0	DC and damp
F1	GAS	LVDT	F1	DC
F3	GAS	LVDT	F3	DC and damp
BF	GAS	LVDT	BF	DC
from MN to MN	Y	MN-oplev	MN-Y	damp
from TM to MN	Y	TM-oplev	MN-Y	DC
from TM to MN	P	TM-oplev	MN-P	DC and damp
from TM to IM	P	TM-oplev	IM-P	damp
from MN to MN	R	MN-oplev	MN-R	damp

In this control system for the payload, due to a technical issue found in the PS signal of ETMX suspension shown in section 6.3.3, the control system for the payload is basically built with the optical levers, even though it has smaller linear range compared to the photo-sensors. The resonant modes of #51, #52, #55, #56 and #57 are the exception and they are taken care by the photo-sensors at the MN-stage. The implemented filters are shown in $left$ of Figure 6.11.

Based on this, we additionally use fourth order Butterworth band-pass filters for the payload damping [75]. We refer to this as band-pass comb filters. This

control system is implemented in order to damp the RM chain modes which are to be sensed by the photo-sensors in the design. This band-pass filter can also minimize the control noise re-injection at higher frequency region. The filter is designed with band-pass frequency around the target frequency $(f_0 - \Delta f_1, f_0 + \Delta f_2)$ where f_0 is the target frequency, Δf_1 and Δf_2 decide the frequency band-width. We select an optical lever signal which observes the target resonance and tuned the phase by tweaking Δf_1, Δf_2 and the gain. The optimization is done manually so that the decay time of the mode becomes smaller than the requirement. The implemented band-pass comb filters are summarized in Table 6.2 and shown in *right* of Figure 6.11.

Table 6.2: The implemented band-pass comb filters for the payload modal damping with the used sensors and actuators. The frequencies of the target resonance are included. The combination of the stage and the dof is written by stage-dof.

ID	Sensing	Actuation	Target frequency [Hz]
BP-comb 1	TM-P	MN-L	1.53 Hz (#44)
BP-comb 2	MN-P	MN-R	23.5 Hz (#63)
BP-comb 3	TM-L	IM-L	2.17 Hz (#49)
BP-comb 4	TM-P	MN-V	9.69 Hz (#59)
BP-comb 5	TM-L	MN-L	2.5 Hz (#52)
BP-comb 6	TM-P	MN-P	7.5 Hz (#58)
BP-comb 7	TM-Y	MN-Y	3.21 Hz (#53)
BP-comb 8	TM-Y	MN-Y	1.15 Hz (#39)

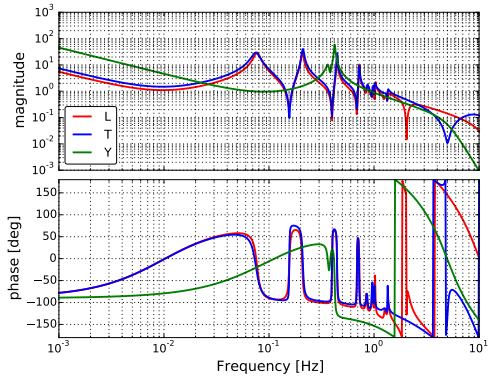

(a) IP loops in L, T and Y dof.

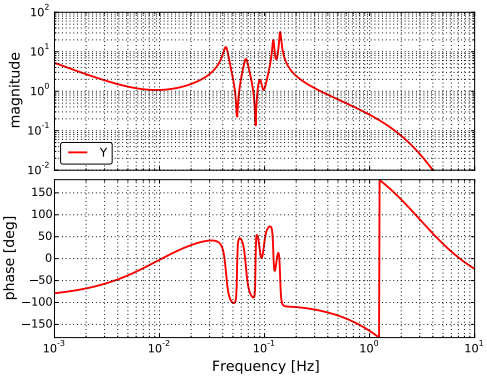

(b) BF loops in Y dof.

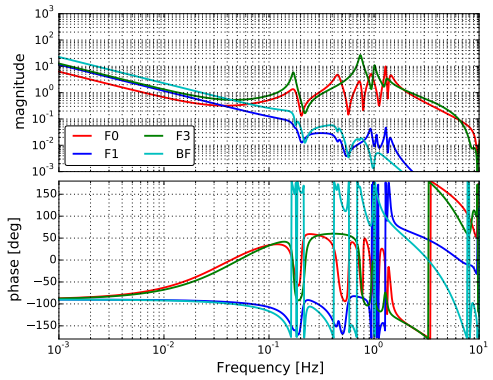

(c) F0, F1, F3 and BF GAS loops.

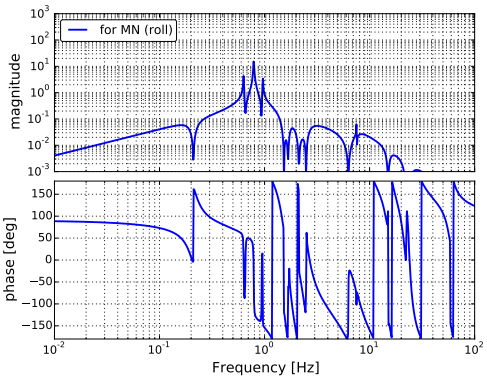

(d) Payload loops in R dof.

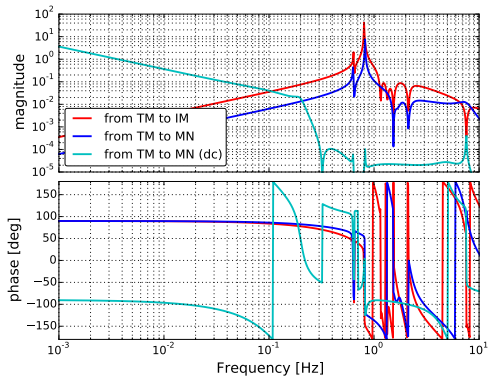

(e) Payload loops in P dof.

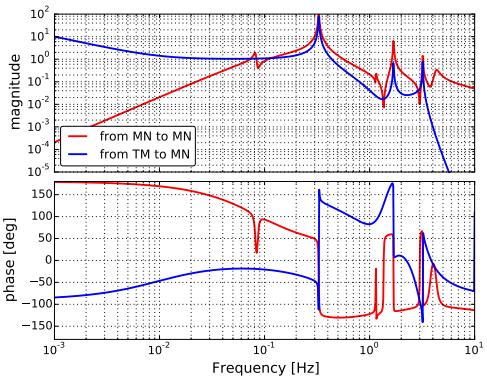

(f) Payload loops in Y dof.

Figure 6.10: Open loop transfer functions of the implemented servo filters for the calm-down phase.

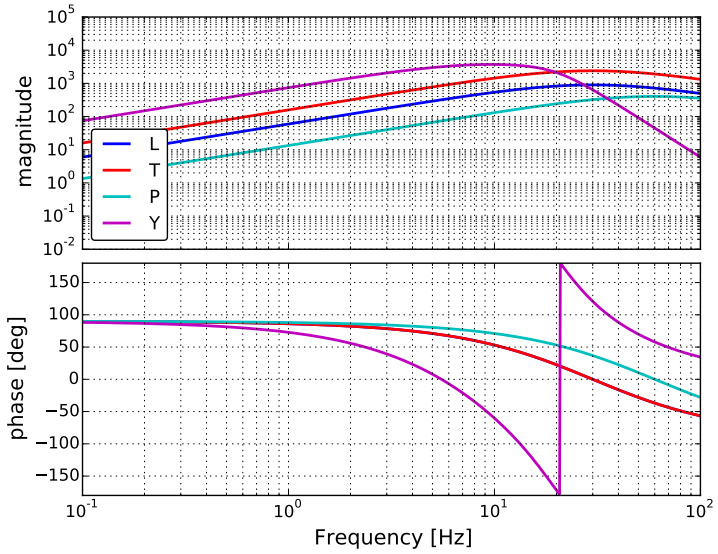

(a) PS loop filters at MN-stage in L, T, P and Y dof.

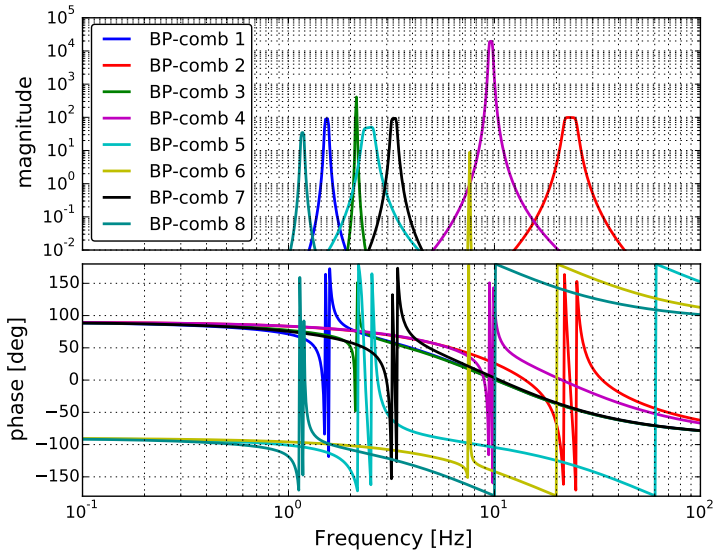

(b) Implemented band-pass comb filters.

Figure 6.11: Implemented servo filters in addition to the ones in Table 6.1.

6.3.2 Decay time measurement

In order to check that the installed control system satisfy the requirement ($1/e$ decay-time constants < 1 min.), the decay-time constant of each mechanical resonance is measured. Since the target for the system is to damp all the mechanical resonances which disturbs the lock acquisition, some of the mode which are expected to less couple to the mirror such as shown in Figure 6.12 (a), are not considered. In addition, only the modes whose resonant frequency are lower than 30 Hz are examined, since the resonances which disturbs interferometer locking are basically the lower frequency modes. As another reason that frequency is selected since it is difficult to sense the resonances higher than 30Hz with the local sensors and also to actuate them. Then the total number of the measured resonances are 53.

The decay time measurement was conducted as follows: first, we excite a target resonant mode by using an appropriate actuator with a sinusoidal signal at the target frequency. Then after confirming the resonance is sufficiently excited, we turned off the actuation and measure the decay signal by the built-in sensors. The measured decay time series is approximately fitted by an exponential-decay sine wave function eq (6.1): When a beating signal of two or three resonances is measured, a double or a triple decay sine wave function is used for the fitting. This situation occurs when some modes have close resonant frequencies.

$$f(t) = \sum_{i}^{n} \left[A_i \exp\left(-\frac{t}{\tau_{e,i}}\right) \sin\left(2\pi f_{0,i} t\right) \right] + x_0, \quad (n = 1, 2 \text{ or } 3) \tag{6.1}$$

where τ_e is the $1/e$ decay time.

An example of this measurement is shown in figure 6.13. These are obtained by exciting MN-stage in Yaw dof and by measuring with the optical lever.

The measured decay time constants for each resonance without and with the control are summarized in section B.5. They include the resonance modes whose resonant frequencies are below 30 Hz. The measured $1/e$ decay time constants for each resonant frequency are plotted in figure 6.14. According to the plot, the requirement is satisfied except for the two cases. I note that one resonance predicted at 4.4 Hz reported in in Figure 6.12 (b), is not found in this work. The investigation for that mode is ignored since no vertical resonances which would disturb the lock acquisition, are observed at around 4 to 5 Hz region.

For the one case found at 1.5 Hz, this would not be a problem for the lock acquisition since the resonance is the mode in roll and transverse dof labeled mode #43 in section B.1. Even if this mode becomes problematic, we can damp it using the optical lever at the MN-stage and the virtual actuator in roll dof at MN-stage for example. Thus the case at 1.5 Hz does not break the requirement.

Concerning the case at 0.14 Hz, this mode is found at Yaw motion of the BF-stage, and is not identified by the model which does not have the information of the heat-link system The counterpart of this mode is not found in the table in section B.1. This is the highest mode observed in the force transfer function

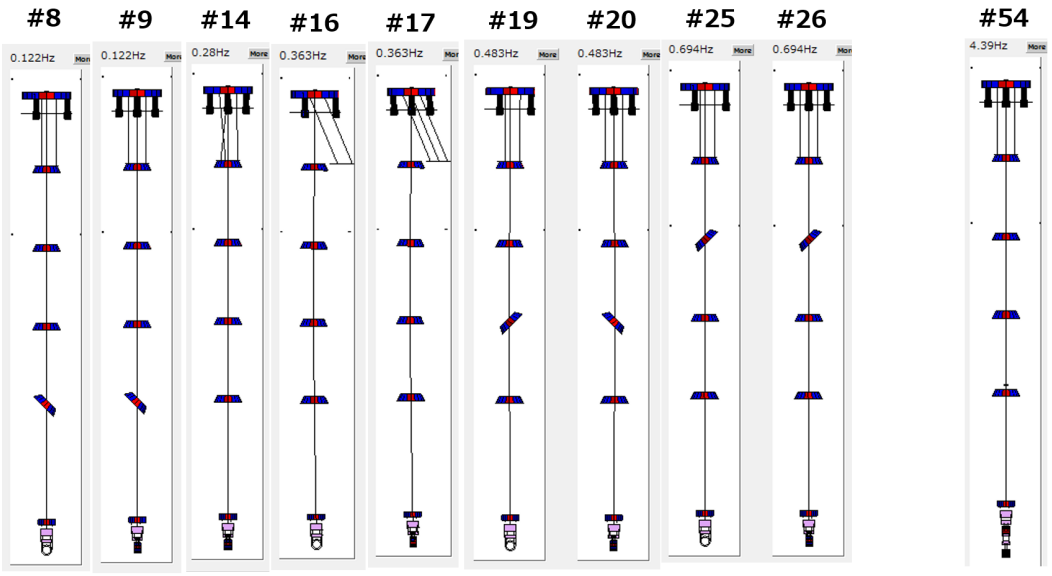

Figure 6.12: Eigen modes which are not considered in this test (a), and the eigen mode which is not found (b), at the frequency region lower than 30 Hz.

from BF-stage excitation in Yaw dof to BF-stage in Yaw dof in Figure 6.5c. Based on the fact that the BF-stage Yaw control loop failed to damp this mode effectively nevertheless the open loop gain is larger than 1 as in Figure 6.10b, it implies that this issue is connected to payload part especially the heat-link system. Generally speaking, further investigation would be necessary for more details about this resonance. However, this peak is visible at the BF-Yaw and TM-chain-Yaw sensors, when the BF-stage is excited in Yaw as in Figure 6.15a. On the other hand, when the MN-stage is excited in Yaw, the peak is observed in only BF-stage and both the optical lever at MN-stage and the photo-sensor do not sense the peak as shown in Figure 6.15b. This implies that unless the BF-stage is not kicked, this resonance would not be excited. Since the feedback signals for the global control is fed back to the TM- and MN-stage in the current interferometer control, we do not kick BF-stage at the lock loss.

These observed facts lead a conclusion that this mode would not be problematic for the lock acquisition in the lock-recovery mode. Although this 0.14 Hz Yaw motion would be problematic when the upper stages such as BF- and IP-stages are used for the interferometer control, that consideration is to be done as further improvement. Consequently, the installed control system satisfies the requirement in the lock-recovery mode.

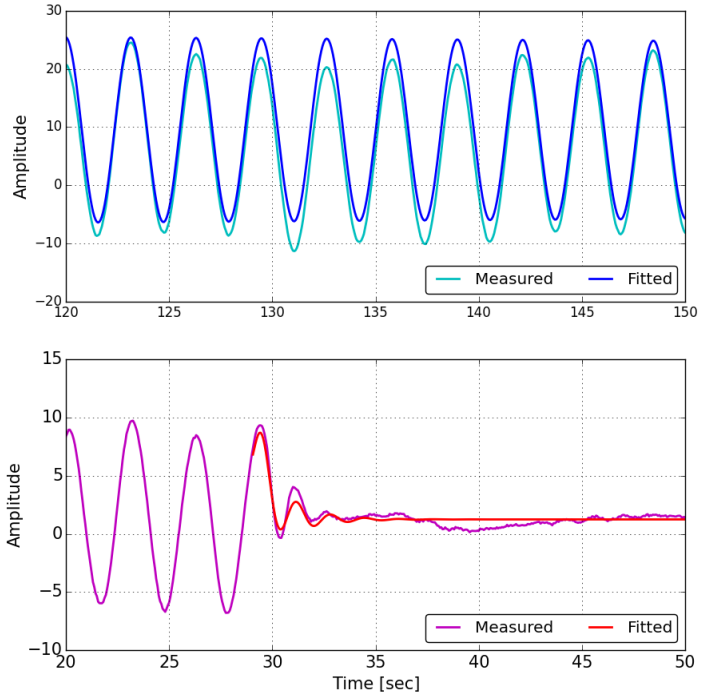

Figure 6.13: An example of the $1/e$ decay-time measurement. The time series, when one resonant mode is excited by a sinusoidal injection and when it is cut off, is drawn in. The upper and the lower panel show the case where the control is off and on respectively. Yaw motion excited at MN-stage and sensed by the optical lever. The (cyan, magenta) colored curves show the measured time series, while the (blue, red) colored time series represent the fitted time series.

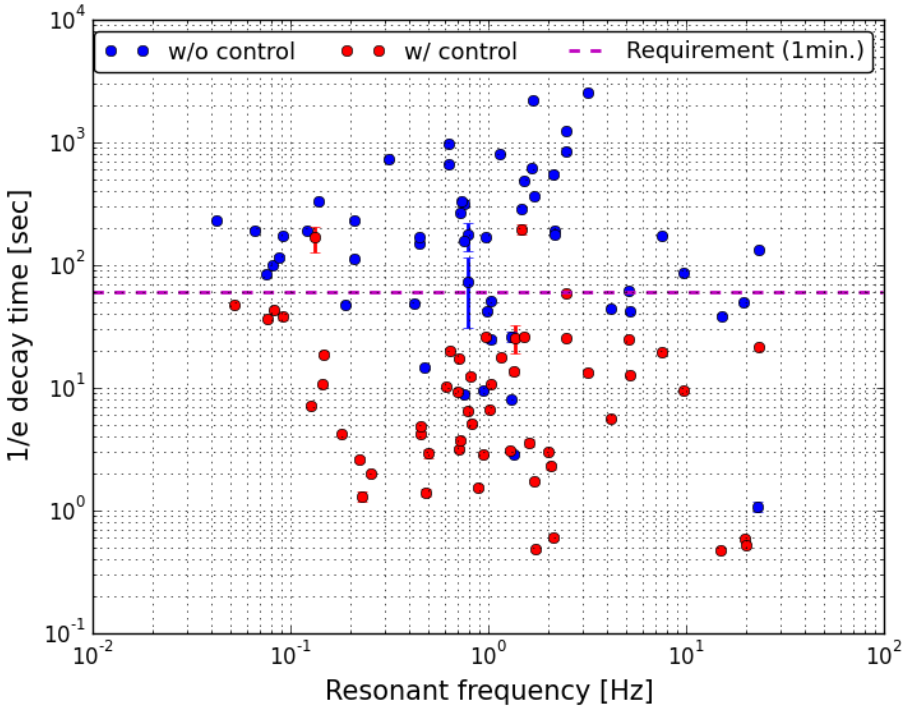

Figure 6.14: The result of the $1/e$ decay time constant as the function of the measurable mechanical resonances. The dashed line shows the requirement of 1 minute.

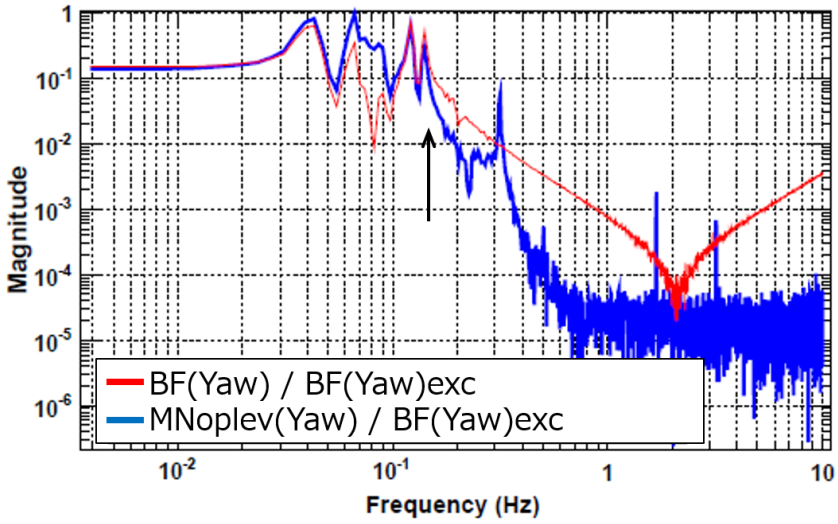

(a) Force transfer function from BF-Yaw excitation to BF-Yaw (blue) and to MN-Yaw measured by the optical lever (red). The unit is a.u.

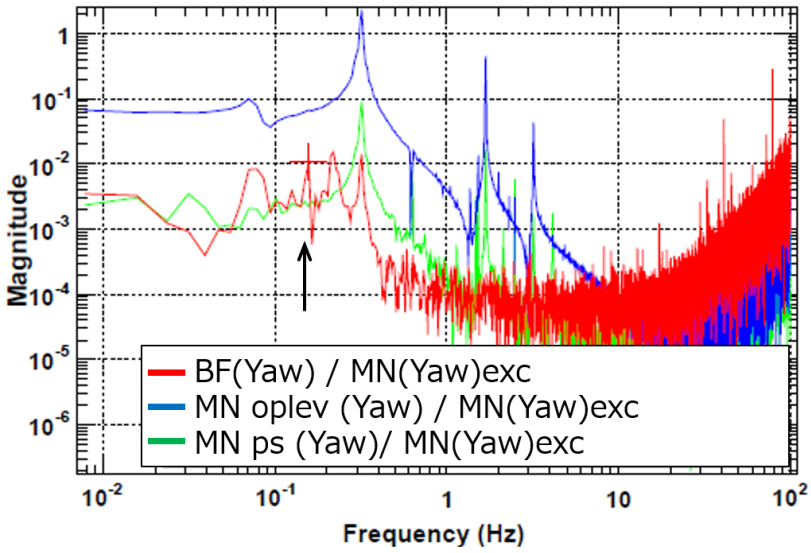

(b) Force transfer function from MN-Yaw excitation to BF-Yaw (blue), and to MN-Yaw with the optical lever, and to MN-Y with the reflective photo-sensors at MN-stage (blue and green respectively.).

Figure 6.15: The measured force transfer functions in Yaw. The unit is a.u. The arrows point the peak at 0.14 Hz.

6.3.3 Further steps for the damping system

In this work, it is failed to find one resonance which is the vertical motion predicted at 4.4 Hz with the model which does not have heat-link system. Investigation for this mode would be also important to understand the whole suspension system, however, the corresponding resonance should have smaller decay time since such vertical mode is never appeared during this work.

In addition, this control system uses mainly optical levers in order to avoid to use the reflective photo-sensors due to the technical issue that the photo-sensors sometimes becomes unstable depends on time[2] and has a spectra such as shown in Figure 6.16.

The implemented control system based on the optical levers satisfied the requirement, however, since the linear range of the optical lever is relatively small (typically about a few hundred μrad) and the signal easily goes outside the available range when a big disturbance happens such as large earthquakes, a large kick is happened at a lock loss. In order to construct a more robust damping system, it is demanded to use the photo-sensors effectively especially when the relatively large disturbance happens, since the linear range is larger than the that of the optical lever.

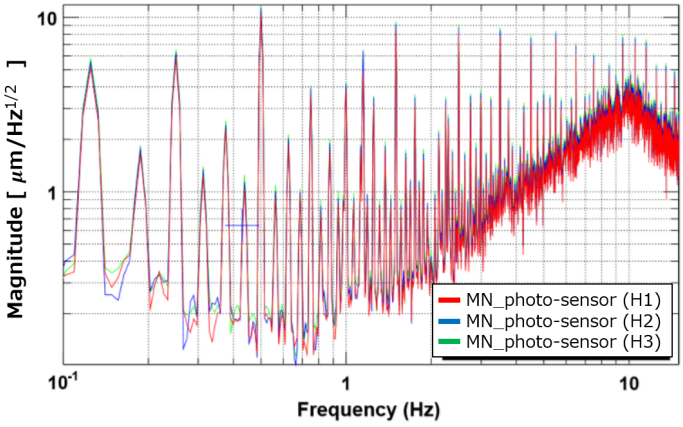

Figure 6.16: Spectra of the photo-sensor when it becomes noisy. The unit is calibrated based on an estimation.

In addition, we want to improve the sensitivity of the photo-sensors, or we want to have sensors which observes the RM-chain motion and whose sensitivity is comparable to the optical lever. Since the current photo-sensors are not enough to measure the mass motion when the mirror motion becomes smaller than typically

[2]It was known that this issue came from somewhere in the electrical circuits, however, it was impossible to solve the issue during my available time at the site.

1μm and 1μrad. If we can solve the issue shown in Figure 6.16 and also improve the sensitivity, we can utilize the photo-sensors effectively. Implementing better-sensitivity photo-sensors (or optical lever for the RM-chain) would also help to reduce the current work load on the designing the band-pass comb filters[3].

[3]Since the band-pass comb filter is so sensitive to the resonant frequency, and thus the temperature of the payload is changed (this can cause the resonant frequency shift), we have to tune the filter accordingly. In a situation where the commissioning is ongoing, this makes the situation quite inconvenient.

6.4 Performance of seismic noise suppression control

In order to reduce the RMS velocity and displacement of the mirror at the frequency around 0.2 Hz, the feedback control with sensor-correction system, which is described in section 5.6.1 is implemented to the actual Type-A system. As in the designing part, the sensor correction system is additionally implemented to the feedback controls at the most upper stage, i.e the IP-satge. For the other control loop such as the payload and the GAS stages, we use same ones as the ones used in the calm-down phase.

6.4.1 Control system

The ground vibration signal measured by a seismometer Trillium120QA [34] at the second floor of the X-end station is sent and added to the LVDT signal with a sensor correction filter $F_{\rm sc}$. Then the corrected LVDT signals are used for the feedback control system. Figure 6.17 show the main signal flow of the system, while Figure 6.18 draws the corresponding block diagram with a schematic view of the actual control system. The signals sensed at each IP-LVDTs are converted to the Cartesian signals with the sensor matrix. The filtered seismometer signal on the ground is added to the Cartesian signals and then the combined signals are used as the error signal of the feedback system. The correction signals are sent to each coils after applying the force distribution matrix.

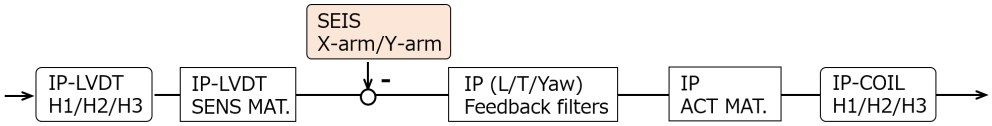

Figure 6.17: Main signal flow of the feedback control with the sensor correction system at the IP-stage. The signals sensed at each IP-LVDTs are converted to the Cartesian signals with the sensor matrix (SENS MAT.). The filtered seismometer signal on the ground is added to the Cartesian signals and then the combined signals are used as the error signal of the feedback system. The correction signals are sent to each coils after applying the force distribution matrix (IP ACT MAT.).

Filter shaping

Since the optimal sensor-correction filter is obtained by $F_{\rm sc} = -S_{\rm L}/S_{\rm s}$ where $S_{\rm L}$ and $S_{\rm s}$ are the sensor response of the LVDT and the seismometer, we inter-calibrate the signals between the IP-LVDT and of the seismometer on the ground so that the seismometer signal has same unit as the LVDT one. This is done by measuring the mechanical displacement transfer function from ground to IP-stage by LVDT and then tuned the gain by finding a frequency region which should be

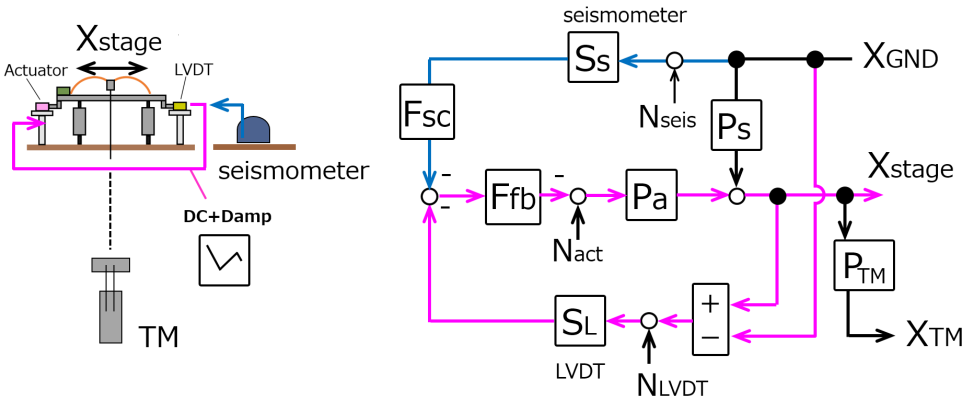

Figure 6.18: Block diagram of the feedback control with the sensor correction system at the IP-stage with its schematic view. Each parameters are defined with the same manner as in section 2.2.3. This is the case where $F_{\rm ff}$ is set to zero. $P_{\rm TM}$ denotes the displacement transfer function from IP-stage to TM-stage.

equal to 1, which is around at 0.6 Hz, as shown in Figure 6.19. As the result, we obtain the factors 0.99 and 0.93 for the L and T dof respectively.

After tuning the gain, we apply the high-pass filter with cut-off frequency of 10 mHz in order not to send too much noise of the seismometer. In order to avoid large amount of phase shift at above 0.1 Hz, we select a second order elliptic high-pass filter whose passband ripple and attenuation are set to 10 dB and 100 dB respectively. In addition we add one more high-pass filter at 0.5 mHz. A forth order Butterworth filter has been chosen to this purpose in order to cut-off the seismometer noise. This filter is necessary since the used seismometer measure the velocity and for this we have to additionally implement f^{-1} component for the conversion to the displacement signal. Since we wanted to avoid to enhance the noise at low frequency, we selected Butterworth filter for the lower high-pass filter.

The sensor-correction filter shape which is applied to the displacement seismometer signal is shown in Figure 6.20. The phase shift due to this filter shown in Figure 6.20 is 3.3 deg which gives 0.2 % difference compared to the ideal signal which we want to subtract. The sensor-correction filter shape which is applied to the velocity seismometer signal is obtained by applying a pure integration filter $1/s$ where s is the Laplace variable.

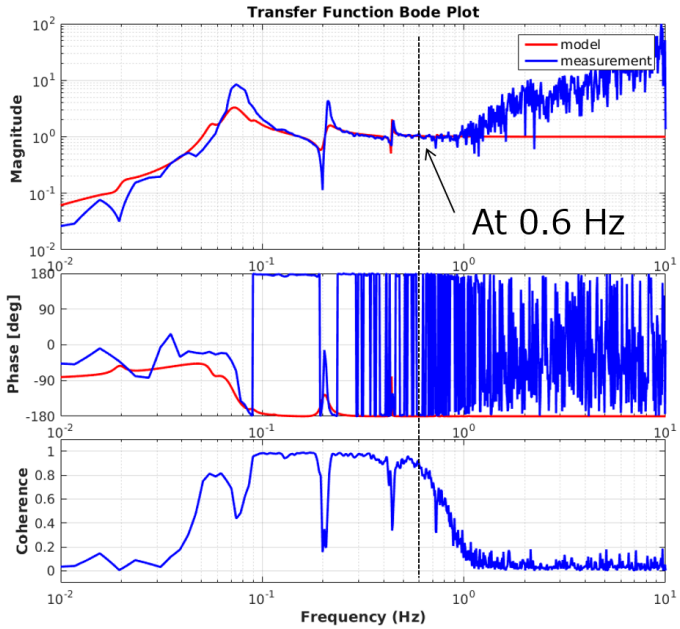

Figure 6.19: Displacement transfer function from ground to IP-stage by LVDT.

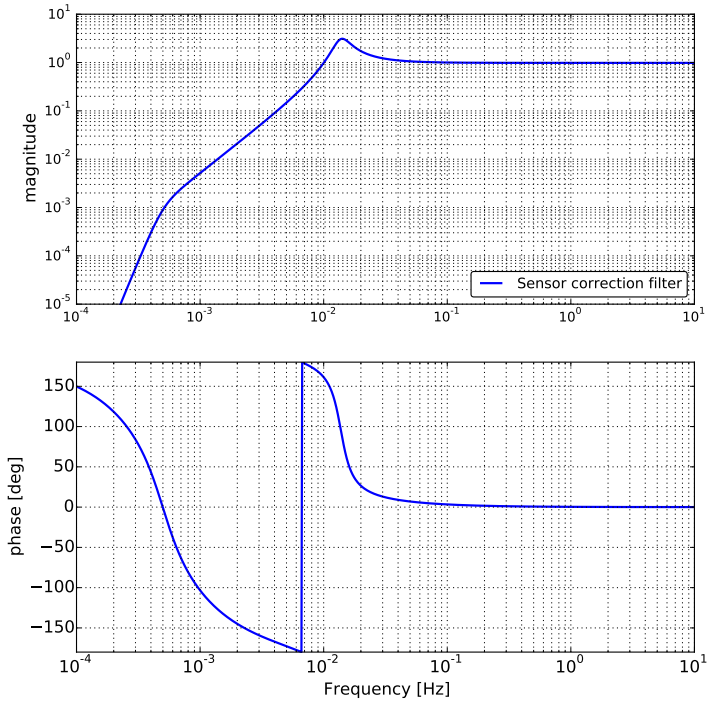

Figure 6.20: The sensor-correction filter shape which is applied to the displacement seismometer signal. This is the filter used in ETMX suspension. since the output of the used seismometer is velocity, $1/s$ is applied to this filter practically and then the seismometer signal is filtered.

6.4.2 Impact on a local suspension

After implementing the sensor-correction filter at the IP-stage, we investigate the suppression performance with the local sensors which are implemented around the ETMX suspension, and test if the residual mirror RMS velocity and displacement satisfy the requirements on them. In the following subsections the sensor-correction system at the IP-stage by the seismometer on the ground is abbreviated to IPsc. First we test the performance with the situation where the IPsc is implemented to only the L dof.

IP-stage performance

Figure 6.21 shows the comparison of the IP-stage displacement spectrum measured by the inertial sensor, geophone ($left$) and by the LVDT ($right$), when the IPsc is on and off. The seismometer signals are included in order to confirm the ground motion can be regarded as identical between the two measurements, since the ground motion always affect the shape of the spectra. Figure 6.21 ($right$) shows that the IP-stage motion as measured by the LVDT is suppressed by the IPsc at the frequencies below 1 Hz. where the LVDT signal had larger than its noise level when the IPsc was off. Indeed in this frequency range, the LVDT signal is above noise in both conditions (IPsc ON/OFF). On the other hand, however, the sensor-corrected IP-LVDT signal indicates that the LVDT is less corrected at the frequency below 70 mHz. Especially at the frequency below 40 mHz, the amplitude becomes larger compared to the case where the IPsc is off, due to the seismometer noise and the sensor-correction filter shape. This performance at such low frequency region is unavoidable in the sensor-corrected system with a seismometer which looses the sensitivity to the horizontal motion at such frequency region. Since the main target of this work is to reduce the RMS connected to the micro-seismic peak, which is around 0.1 to 0.5 Hz, we do not discuss the lower frequency displacement fluctuation here.

Figure 6.22 reports the comparison between the sensor-corrected IP-LVDT signal and the geophone signal when the IPsc is on. This figure reports that there is a discrepancy between the geophone signal and the sensor-corrected IP-LVDT signal. The amplitude is different by factor of 2 at around 0.2 Hz. In addition, the frequencies of the dips are also different each other. This seems to connect to the fact that the geophone can sense the tilt motion, while the LVDT does not see the tilt. This happens since the two sensors are sensing other motion. The more detailed investigation for this issue will be necessary, however, in this work we assume the geophone observes the IP-stage motion at that frequency and test the RMS requirements.

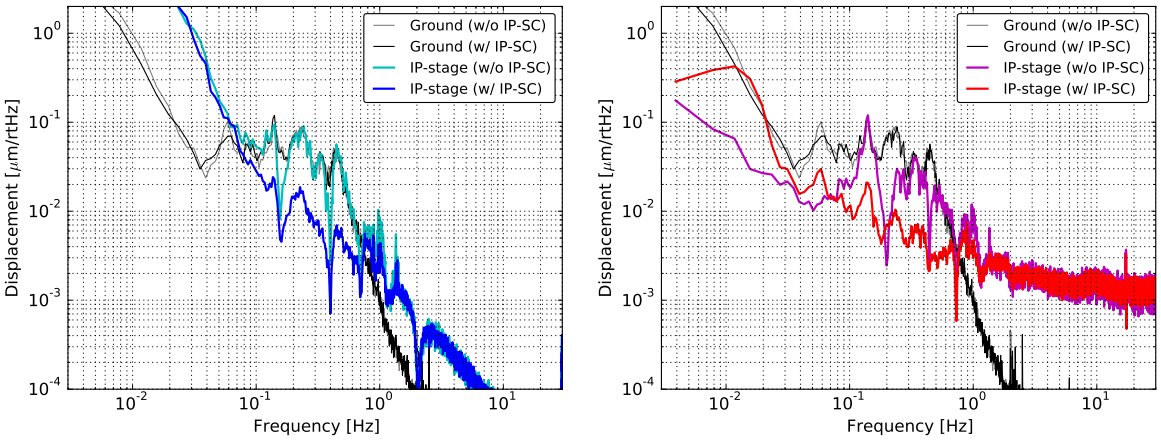

Figure 6.21: Comparison of the IP-stage displacement spectrum measured by the inertial sensor geophone (*left*) and by the LVDT (*right*) when the IPsc is on and off. I note that in the *right* panel, the LVDT signal with and without IPsc is not compatible since one measures the displacement, while the other one observes the inertial motion basically.

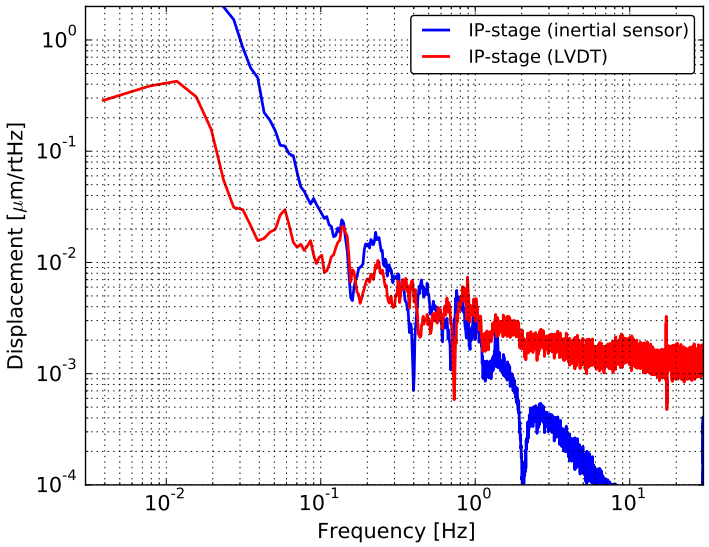

Figure 6.22: Comparison between the sensor-corrected IP-LVDT signal and the geophone signal when the IPsc is on.

BF-stage and TM-stage performance

Figure 6.23 (*left*) shows the comparison of the BF-stage displacement spectrum measured by the LVDT, when the IPsc is on and off. The BF-LVDTs in this measurement are not sensor-corrected and thus they observes the relative motion between the security frame (mechanical ground) and the BF-body. This figure implies that the IPsc works for the whole upper part, since it is observed that the amplitude of the spectra in the frequency region between 0.1 Hz to 1 Hz is suppressed with the IPsc, and the amplitude at the frequency below about 40 mHz is enhanced due to the seismometer self-noise and the correction filter. Since the motion of the BF-body becomes smaller than seismic motion, all the feature of the BF-body displacement is buried into the seismic spectrum.

On the other hand, Figure 6.23 (*right*) shows the comparison of the TM-stage displacement spectrum measured by the length-optical lever when the IPsc is on and off. A consistent improvement is observed, however, the sensitivity of the TM length optical lever is not good enough to measure the TM motion.

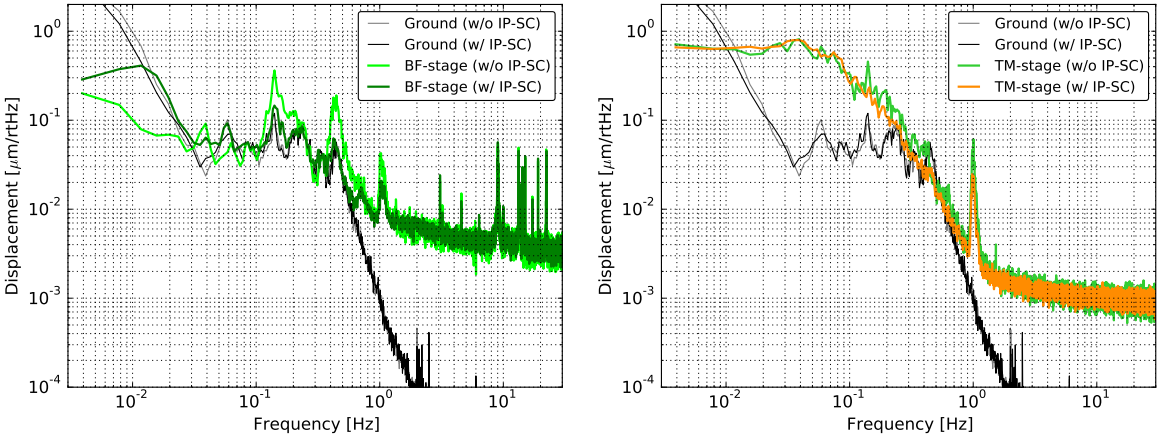

Figure 6.23: Comparison of the BF-stage displacement spectrum measured by the LVDT (*left*), and comparison of the TM-stage displacement spectrum measured by the length-optical lever when the IPsc is on and off. (*right*) when the IPsc is on and off.

Displacement transfer function measurement in L dof

After testing the single-dof correction system, we installed the IPsc to both L and T dof, and investigate the mirror motion suppression performance. In order to evaluate the suppression performance, the displacement transfer function from the ground to the mirror in L dof is measured by combining two displacement transfer functions; the displacement transfer function from the ground to the IP-stage, and that from the IP-stage to the TM-stage. The first transfer function is passively measured with the seismometer on the ground and the geophone on

the IP-stage. The second one is measured by exciting IP-stage and the geophone signal is used at frequency higher than 0.1 Hz, while LVDT signal is used at frequency lower than 0.1 Hz. Those signals are selected based on the measured coherence. The obtained transfer function from the ground to the mirror in L dof is shown in Figure 6.24. Using these transfer functions and the measured ground motion at KAGRA site, Figure 6.25 estimates the mirror displacement and velocity with the 90 percentile ground motion in Figure 1.11. The estimated RMS displacements and velocities of the mirror with the integration down to 20 mHz are summarized in Table 6.3. RMS velocity can satisfy its requirement even without the IPsc though, the RMS velocity is suppressed by factor of 5 using the IPsc technique. On the other hand, RMS displacement satisfy the requirement at 20 mHz though, this is not the case at 10 mHz and the RMS value can become larger than 1 μm.

Table 6.3: The estimated RMS displacements and velocities of the mirror with the integration down to 20 mHz.

Configuration	velocity [μm/s]	Displacement [μm]
Without IPsc	0.79	0.64
With IPsc	0.14	0.23

Comparison with simulation

Figures 6.26 and 6.27 show the comparison between the measurement and the simulation, where the IP-stage is controlled by IP-LVDTs without IP_{sc}, and by IP-LVDTs and with IP_{sc} respectively. These simulated curves are obtained by assuming that the inter-calibration between the IP-LVDTs and the seismometer is perfect.

In the case without IP_{sc} (shown in Figure 6.26), there is mismatch in the velocity/displacement spectrum (by factor of about 1.5 in RMS) especially at below about 0.5 Hz even though the measurement quantitatively agrees with the simulation. Taking into account the additional stiffness due to the cabling condition might explain the difference though, the details are to be investigated for further step.

On the other hand, in the case with IP_{sc} (shown in Figure 6.27), the measurement agrees with the simulation at below about 0.5 Hz. The discrepancy between the measurement and the simulation comes from a fact that this simulation does not include the feedback loops for the payload, which affects to the spectrum especially at above 0.5 Hz.

Consequently, it is confirmed that the implemented IP_{sc} suppresses the mirror RMS velocity/displacement as designed.

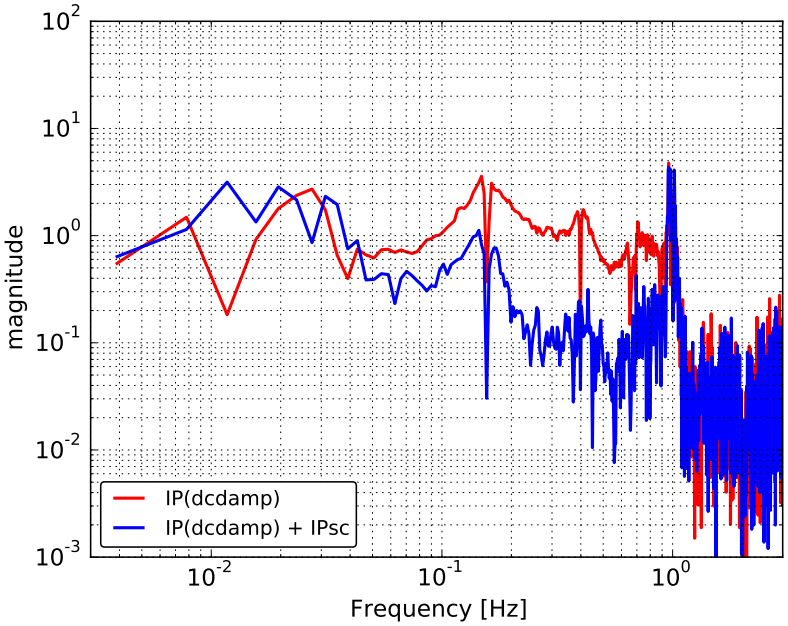

Figure 6.24: The measured displacement transfer function from the ground to the mirror in L dof. The colors show the difference of the configuration. At the frequency region higher than 1 Hz the sensor noise becomes dominant.

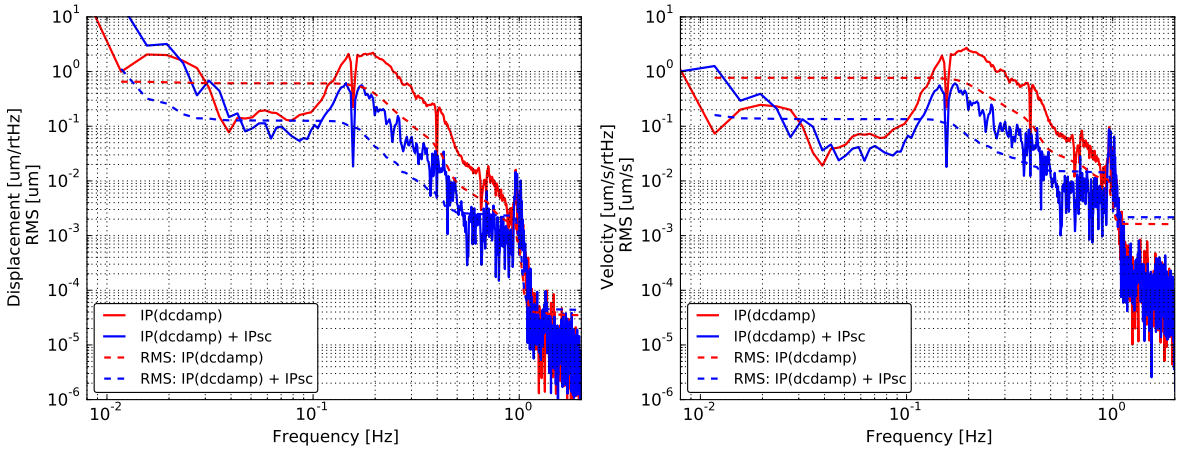

Figure 6.25: Comparison of the expected TM residual displacement (*left*) and TM velocity (*right*) in L dof when the IPsc is on and off. In this calculation 90 percentile ground motion is used.

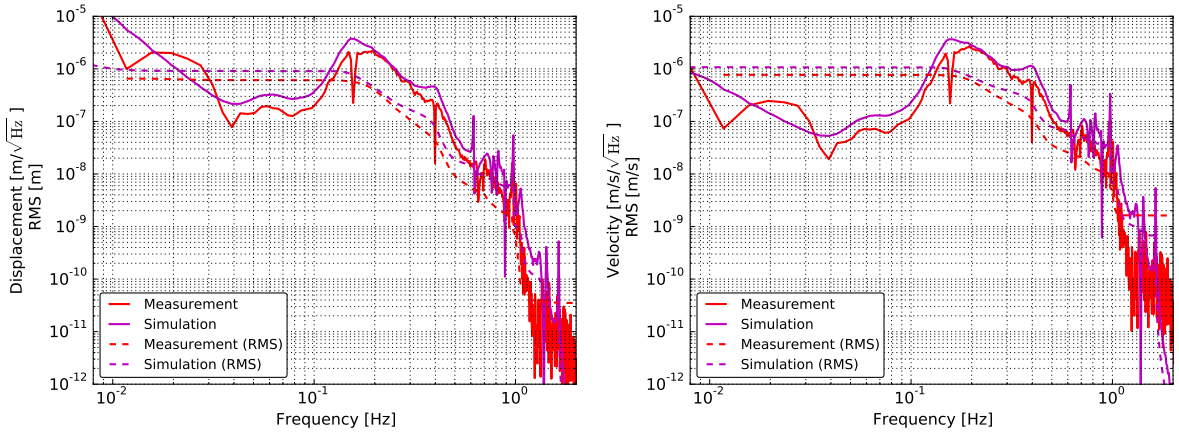

(a) Mirror displacement (b) Mirror velocity

Figure 6.26: Measured expected mirror residual motion in L dof, compared to the simulation described in section 5.6.1 in displacement (*left*) and in velocity (*right*) with IP-stage controls *without* IP_{sc}. The dashed curves draw the RMS values integrated down to about 10 mHz. In this calculation high seismic noise level (90 percentile seismic motion level) is assumed.

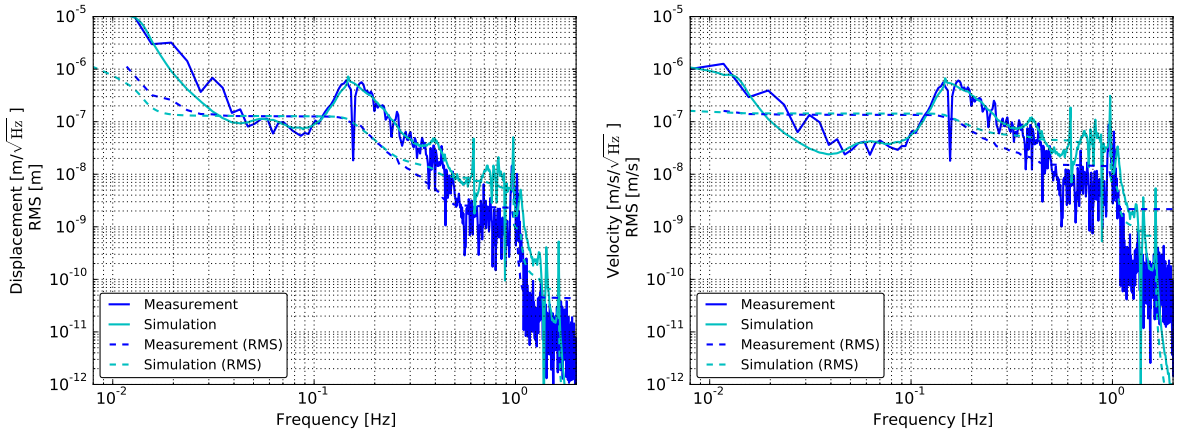

(a) Mirror displacement (b) Mirror velocity

Figure 6.27: Measured expected mirror residual motion in L dof, compared to the simulation described in section 5.6.1 in displacement (*left*) and in velocity (*right*) with IP-stage controls *with* IP_{sc}. The dashed curves draw the RMS values integrated down to about 10 mHz. In this calculation high seismic noise level (90 percentile seismic motion level) is assumed.

Performance summary

Consequently, the implemented IPsc suppresses the residual motion of the mirror and it gives RMS displacement which satisfies the requirement for the lock acquisition phase, in the time-scale of 1 minute, which corresponding to the integration down to 20 mHz. The RMS velocity satisfies the requirement for the lock acquisition phase, independent on the IPsc system.

Since the RMS is estimated with the inertial sensor geophone which looses the high signal-to-noise ratio at such low frequency, those values can be upper limits. It is expected that the geophone spectra contain the tilt coupling which cannot be distinguished with the current setting. For further performance improvement, finely tweaking the high-pass cut-off frequencies of the shape of the sensor-correction filter F_{sc} can slightly help to realize the system which satisfies the requirements on RMS velocity and displacement down to 10 mHz. However, this makes the time-scale longer by a factor of 2, from 50 sec to 100 sec which does not make drastic change (practically it also becomes difficult to measure the performance with the currently implemented local sensors).

Based on this fact, it is more natural to have another system which compensates such longer-tern drift on the suspensions, which uses the baseline signal[4] in DC and feeds back to the upper part of the suspension, such as IP-stage, at the end-station so that the ETMX/Y move along with the ITMX/Y respectively, for example (as described in section 5.6.1).

In addition, this sensor-correction system is developed from a motivation that the inertial sensors on IP-stage are not effectively useful in some of the suspensions. This low-frequency drift issue can be solved if we build a inertial control system, by using the inertial sensors which has enough sensitivity at frequency below 0.1 Hz, at least same level as that of the current seismometers Trillium120QA. As a reference, The typical noise floors of such inertial sensors compared to the mirror displacement due to the seismic noise, are summarized in Figure B.13. However, it is expected that we need to compensate the tilt-coupling of the inertial sensors at low frequencies.

In conclusion, the implemented IPsc suppresses the residual motion of the mirror and satisfies the requirement for the lock acquisition phase in the time-scale of 1 minute, which is enough to acquire the interferometer lock. In order to a realize more stabilized control system at frequencies below 0.1 Hz in the time scale of much longer than 1 minute, another displacement drift compensation system is necessary. Building such drift compensation system is set as the next step after this thesis work.

[4] such as interferometer signal or stain meter signal along with the arms.

6.4.3 Residual motion

Figure 6.28 shows the spectra of mirror residual motion in L, Pitch and Yaw dof, observed by the optical lever at the TM-stage. The TM motion in L dof is covered by the seismic motion and the spectrum does not show the TM motion. Instead the P and Y motion of the TM is measureable. The RMS angular motion in Pitch and Yaw dof is measured 0.20 μrad and 0.17 μrad respectively. The RMS of Pitch motion is on the requirement for the observation phase though, in the usual case, the requirement should be satisfied since this is measurement is done when the seismic motion level is high at around 50 mHz.

On the other hand, Figure 6.29 reports the spectra of the residual motion the IP-stage in T dof measured by the inertial sensor geophone and that of the BF-body in V dof measured by the displacement sensor LVDT. The residual RMS displacement of transverse IP-stage and vertical BF-body is measured at 0.3 μm and 0.13 μm. Even though the suspension system does not have any sensors which can sense the T and V dof at the TM stage, however, the RMS will be limited by the upper part of the suspension. Assuming that the RMS displacements down to 10 mHz in these plots are the ones of TM, the requirement is satisfied. Even though the vertical spectra is measured when the seismic motion level is low, the RMS requirement will be also satisfied even if the amplitude increases by one order of magnitude (assuming that the ground moves as same level as the 90 percentile ground motion).

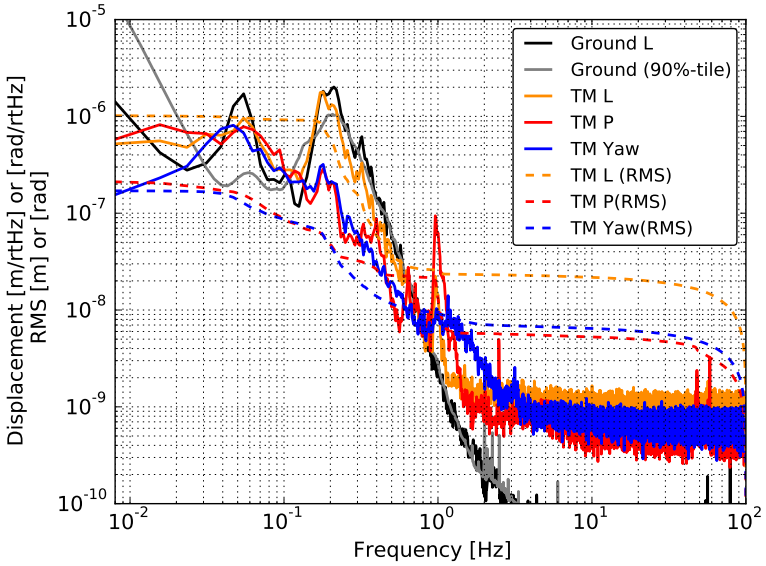

Figure 6.28: Spectra of mirror residual motion in L, Pitch and Yaw dof, observed by the optical lever at the TM-stage. The solid curves show the amplitude spectral density and the dashed ones indicate the amplitude in RMS.

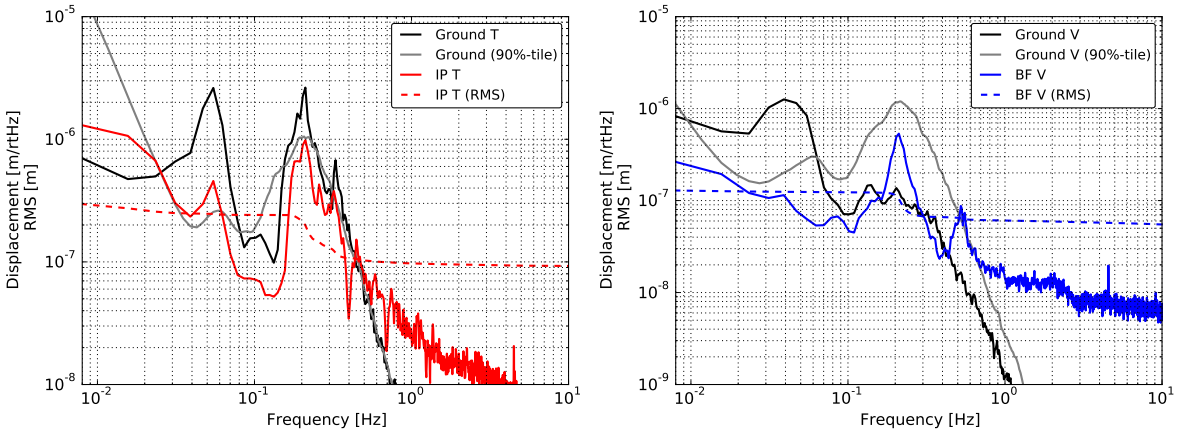

Figure 6.29: Spectra of residual motion the IP-stage in T dof measured by the inertial sensor geophone (*left*) and that of the BF-body in V dof measured by the displacement sensor LVDT (*right*)

6.5 Performance of mechanical vibration isolation

By using the implemented filters described in the above, the inteferometer lock is achieved with FPMI[5] configuration. Since a better sensitivity sensor for the mirror displacement is acquired, I have measured the overall vibration isoaltion performance.

In order to measure the overall performance in L dof, transfer functions from the upper stages to the mirror motion has been investigated (including FPMI signal).

6.5.1 Measurement set up

For this purpose, force transfer functions are measured by actuating on the IP- and BF-stages and sensing the mirror motion with either the length-optical lever or the FPMI[6] with green and IR laser.

For evaluating the vibration isolation performance, we can measure either the displacement transfer function from a sensor to a sensor, or force transfer function from an excitation to a sensor. Since we use the LVDT for this measurement and also since it was observed that in the LVDT signal, the direct coupling between the sensor and the actuator becomes dominant at frequencies above a few Hz when that stage is excited, as shown in Figure 6.5a for example, we select the force transfer function for this measurement.

For the lower frequency part (< 1 Hz), white noise is injected to the upper stages and then the length-optical lever is used as the sensor. On the other hand, for the higher frequency part (> 1 Hz), a sinusoidal noise is injected and the FPMI is used as the sensor. In the sinusoidal noise injection measurement, the length-optical lever signal is also measured as a reference.

Control configuration

During the measurement with the local optical lever, all the local controls are off in order to get the open loop mechanical response. On the other hand, during the measurement with the FPMI, some of the loops which does not disturb the measurement are kept closed. This is necessary in order to avoid the mirror angular drift especially in yaw dof, since otherwise we cannot keep the locked condition of the interferometer. For this purpose, during the FPMI measurement, all the payload controls are opened, however, the controls for each GAS stage, BF-stage in Yaw dof and IP-stage in T and Yaw dof are kept closed (The details about these filters are summarized in section 6.3.1). These loops are kept closed since the controlled dof is different from the target L dof, and the coupling levels

[5]FPMI stand for Fabry-Perot Michelson Interferometer.

[6]The difference of the wave length of the laser corresponds to the difference of the sensitivity of the sensors (interferometers). During this measurement, the ETMY is globally controlled for keeping its lock.

are not large. In addition to this, a DC-control filter for the longitudinal dof at IP-stage whose unity gain frequency (UGF) is lower than about 0.3 Hz is closed. The LVDT is used for this loops. This is done since the measurement with FPMI focuses on the frequency only higher than 1Hz, and also otherwise the lock of the FPMI was easily lost in the timescale of a few minutes due to the drift. The open loop transfer function used for the IP-stage in L dof is shown in $left$ of Figure 6.30. Since the seismic motion enhanced the residual motion in the period when the measurement by FPMI with IR laser was conducted, the filter shape is changed so that the filter can damp the 0.2 Hz mode accordingly.

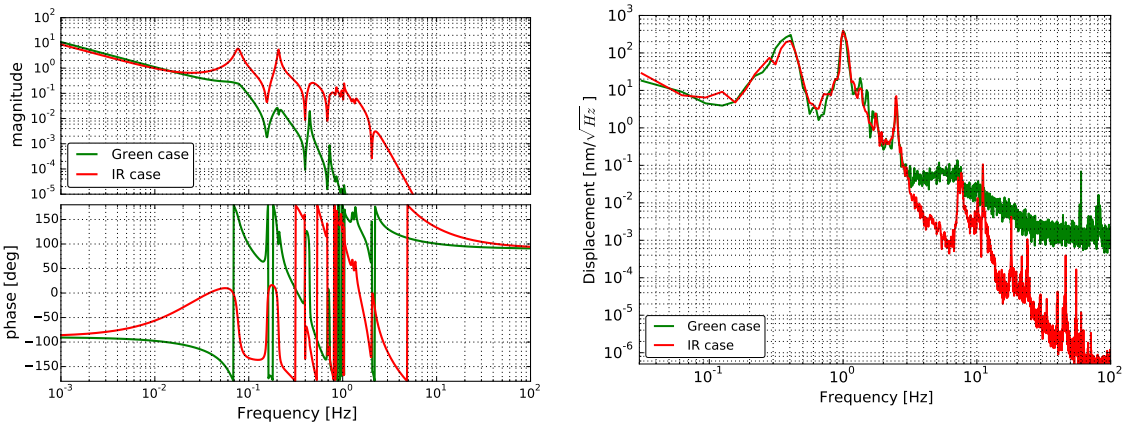

Figure 6.30: The used open loop transfer function used for the IP-stage in L dof ($left$) and the typical noise floor of the FPMI with green and IR laser during the measurement ($right$).

6.5.2 Measurement

The measured force transfer functions when the IP- and BF-stage is excited in L dof are shown in *top* and *bottom* of Figure 6.31 respectively.

As described above, the response at frequency below 1.1 Hz and 1.8 Hz is measured by the length-optical lever with white noise injection for IP- and BF-stage excitation respectively. The response above those frequencies is measured by both the length-optical lever and FPMI with one sinusoidal noise injection. For the measurement with single sinusoidal injection, we selected the measurements whose coherence is higher than 0.7. The FPMI measurement fails above 1.4 Hz for IP-stage excitation and 4.2 Hz for the BF-stage excitation since the induced mirror displacement becomes comparable to the FPMI noise level. At frequencies higher than 3 Hz, the coupling from the other dofs becomes dominant in the length-optical lever signal as shown in Figure 6.31b

Figure 6.31a indicates that except the IP-excited measurement in the frequency band between 1.1 Hz to 1.4 Hz, the model used in section 6.2, can explain the actual suspension response in both excitation cases, except for the Q factors

of the lowest and the second lowest resonances. As shown in Figure 6.31a, in the frequency band between 1.1 Hz to 1.4 Hz, there is no agreement among the model, the measurement by length-optical lever and that by FPMI, even though the slopes are mostly consistent. This could come from the coupling with the other dofs and that makes the coupling ratio difference to the length-optical lever and to the FPMI. For the more details, further investigation will be necessary. On the other hand, Figure 6.31b reports that the actual system agrees with the model up to 4.2 Hz.

This would imply that even though the designed mechanical transfer function might not be realized in the actual system in the the frequency band between 1.1 Hz to 1.4 Hz[7], the vibration isolation performance is realized at 4.2 Hz.

6.5.3 Summary

A direct vibration isolation performance is tested in terms of the force transfer function measurement. The measurement indicates that the response of the actual system is consistent with the prediction by the model used in section 6.2 except for that at the frequency higher than 1.1 Hz in the IP-excited measurement. The result would imply that the designed vibration isolation performance at 4.2 Hz agrees with the model. For more the details, we have to conduct further investigation.

[7] Assuming that the discrepancy does not comes from the coupling from the other degree of freedoms

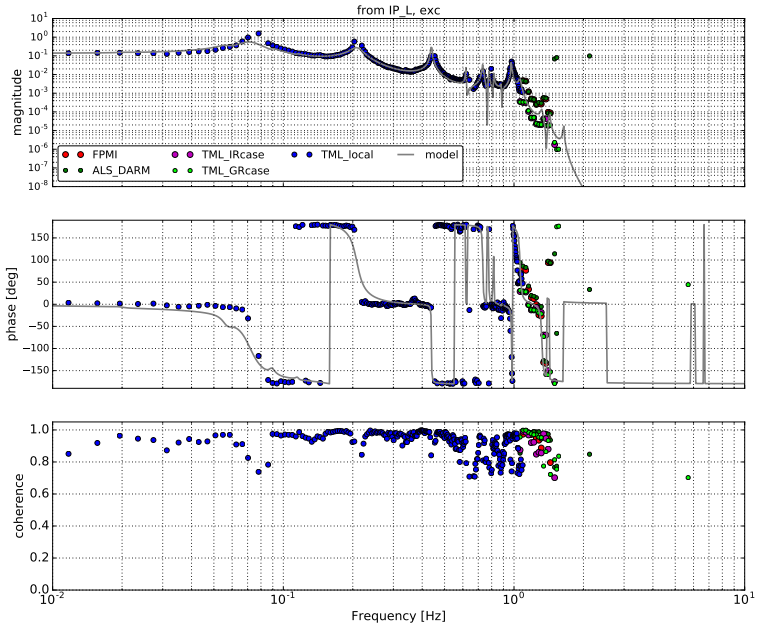

(a) From the IP-stage excitation

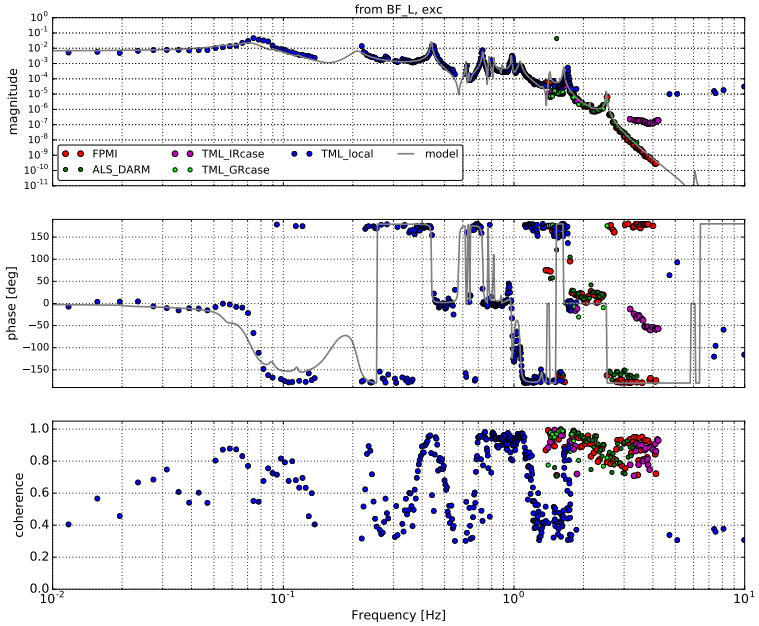

(b) From the BF-stage excitation

Figure 6.31: Measured force transfer functions from the IP-stage excitation (a) and from the BF-stage excitation (b) in L dof. The grey colored curves show the prediction of the model used in section 6.2. The blue dots represents the measurement with the length-optical lever and with white noise injection. The other colored dots show the results by sinusoidal noise injection. The green and red dots are obtained from FPMI while the magenta and lime dots are the measurements by the length-optical lever when the FPMI measurements are conducted.

6.6 Summary of the performance

In this work we conduct the following tests for the evaluation of the suspension and its control system:

1. suspension mechanical response,
2. damping control performance for the calm-down phase,
3. RMS suppression control performance for the lock-acquisition phase.

Based on the first test, we conclude that the assembled Type-A suspension has the characteristics of the pendulum, although some of the unexpected resonances which would related to the heat link system are observed. From this issue, we find that we have to include the heat link system in the model of the suspension mechanics for the further precise estimation.

From the second test, we confirm that the installed damping control system satisfies its requirement for the lock-recovery mode.

The third test demonstrates the feedback control system using displacement sensors by a feed-forward system with seismometer on the ground effectively suppressed the mirror residual motion and it satisfies the requirement in the time scale of 1 min. The measured performance is summarized in Table 6.4.

In conclusion, it is confirmed that the control system which allows to lock the interferometer has been realized. This is the first time to control the full Type-A suspension system.

Table 6.4: Requirements on the Type-A suspension control. The column labeled as ref. describes the section which explains the reason of the requirements. The result written as (*1) is the RMS value measured at 20 mHz. The results noted as (*2) and (*3) are the RMS value of IP-stage in T measured by its inertial sensors, and the RMS value of BF-body in V by BF-LVDT, respectively.

Items	Requirements	Achieved results	ref.
The calm-down phase			
$1/e$ decay time	< 1 min.	< 59 sec.	§ 6.3.2
RMS displacement (T, V)	< 0.1 mm	(0.3 μm, 0.13 μm) (*2, 3)	§ 6.4.3
The lock acquisition phase			
RMS velocity (L)	< 2.0 μm/sec.	0.14 μm/s	§ 6.4.2
RMS angle (P, Y)	< 880 nrad	(200 nrad, 170 nrad)	§ 6.4.3
RMS displacement (L)	< 0.39 μm	0.23 μm (*1)	§ 6.4.2
RMS displacement (T)	< 0.1 mm	0.3 μm (*2)	§ 6.4.3
RMS displacement (V)	< 39 μm	0.13 μm (*3)	§ 6.4.3
The observation phase			
Control noise at 10 Hz (L)	$< 8.0 \times 10^{-20}$ m/$\sqrt{\text{Hz}}$	not measured	
RMS displacement (L)	< 0.39 μm	0.23 μm (*1)	§ 6.4.2
RMS displacement (T)	< 0.1 mm	0.3 μm (*2)	§ 6.4.3
RMS displacement (V)	< 39 μm	0.13 μm (*3)	§ 6.4.3
RMS angle (P, Y)	< 200 nrad	(200 nrad, 170 nrad)	§ 6.4.3
DC angle Drift (P, Y)	< 400 nrad/h	not measured	

Chapter 7

Conclusion and future works

7.1 Conclusion

7.1.1 Fast localization with heterogeneous detector network

We investigate the expected performance regarding fast sky localization of coalescing binaries with a network of three or four GW detectors having heterogeneous sensitivities, such as the LIGO-Virgo, LIGO-KAGRA and LIGO-Virgo-KAGRA network by using a hierarchical search. In the hierarchical approach, the presence of an event seen in coincidence in the two more sensitive detectors triggers a focused search in the data of the third (and fourth), less sensitive, detector(s) with a lower SNR threshold. In this work, we show the expected fast localization performance for GWs from CBC when a hierarchical search is implemented into a GW-EM follow-up pipeline using MBTA and Bayestar.

We confirm that the hierarchical search improves both the localization accuracy and precision compared to those achieved by a double coincidence search with the two LIGO detectors alone with low-latency analysis pipeline.

The hierarchical network effectively improves the localization accuracy and precision when threshold SNR for the lower sensitivity detector is set to around 3.5 provided that the BNS range of that the detector is greater than 20% of the more sensitive detectors in the case where the detector network is composed of the two LIGO detectors and the Virgo detector. As the sensitivity of Virgo approaches half of the LIGO one, the accuracy and precision of the localization can be improved by about a factor of 7.

In the case where the detector network is composed of the two LIGO detectors and KAGRA detector, we found a clear sky localization improvement when the relative sensitivity of KAGRA becomes greater than 28% of the more sensitive detectors. As the sensitivity of KAGRA approaches half of the LIGO one, the accuracy and precision of the localization can be improved by about a factor of 3.5.

In addition, the hierarchical network by four detectors improves the localization accuracy and precision when threshold SNR for the lowest sensitivity detector is set to around 3.5 provided that the BNS range of that the detector is greater than 28% of most sensitive detectors. This result assumes that the

sensitivity of the middle sensitive Virgo detector is half of the LIGO one. As the sensitivity of KAGRA approaches half of the LIGO one, the accuracy and precision of the localization can be improved by about a factor of 2 and 2.5 compared to LIGO-Virgo hierarchical network.

Consequently, we conclude that once the sensitivity of the third or fourth detector reaches the required one, the search with this hierarchical approach will be most useful when adding new, less sensitive detectors to the network, as they are undergoing commissioning.

7.1.2 Type-A local suspension control

In this work we conduct the following tests for the evaluation of the suspension and its control system:

1. suspension mechanical response,
2. damping control performance for the calm-down phase,
3. RMS suppression control performance for the lock-acquisition phase.

Based on the first test, we conclude that the assembled Type-A suspension has the characteristics of the pendulum, and it is enough to build the local control system. However, some of the unexpected resonances which would related to the heat link system are observed. From this issue, we find that we have to include the heat link system in the model of the suspension mechanics for the further precise estimation.

From the second test, we confirm that the installed damping control system satisfies its requirement for the lock-recovery mode.

From the third test, it is confirmed that the feedback control system using displacement sensors by a feed-forward system with seismometer on the ground effectively suppressed the mirror residual motion and it satisfies the requirement in the time scale of 1 min.

Consequently, we have realized the local control system for the Type-A suspension to allow interferometer locking.

In conclusion, including the first part about the fast localization in heterogeneous network, this research contributed to the KAGRA joining to the network as the fourth detector.

7.2 Future works

7.2.1 Type-A local suspension control

Mechanical suspension characterization

During this test we face on a fact that the model without the heat link system cannot fully explain the actual mechanical system, especially the BF motion in Y dof. The most possible origin is the heat ink system. We have to include the heat link system in the model of the suspension mechanics for the further precise estimation.

In addition this work could not investigate the feature of the suspension system at frequencies above 4.2 Hz, where the heat link system can introduce external vibration from the inner shield of the cryostat. We have to confirm that the vibration induced by the actual heat link system satisfies the displacement requirement at 10 Hz.

Payload control

For the more robust operation, utilizing higher sensitive photo-sensors are demanded. The control system only with the optical levers is possible with the band-pass comb (BP-comb) filters. However, since it takes time for the tuning and maintain the BP-comb filters. Since the filters are much sensitive to the target resonant frequency and the mechanical resonant frequency can be shifted by the temperature change. The higher sensitive photo-sensors can reduce such work load.

Residual motion suppression control

In this work, a seismometer on the ground is used for the suppression control and we observe that the displacement residual at below 10 mHz enhanced due to the noise relate to the used seismometer. In order to avoid this, we should have inertial sensors which is sensitive enough at below 100 mHz.

Long-term tidal compensation

Even though the mirror displacement is suppressed locally with the sensor correction technique, the arm cavity drift related to the tidal deformation have to be compensated with the sensors which can sense the strain of the arm in order to keep the locked condition longer. This would be realised by sending the interferometer signal to the IP-stage actuators.

Chapter A

Supplemental note for study of fast localization

A.1 Typical parameters for data analysis

Effective distance

The effective distance $D_{\rm eff}$ is the distance of an optimally located and oriented source that would produce the same signal strength. The distance $D_{\rm eff}$ is defined as

$$D_{\rm eff} = \frac{R}{\sqrt{\frac{1}{4}{F_+}^2(1+\cos^2\iota)^2 + {F_\times}^2\cos^2\iota}}, \tag{A.1}$$

where R is the actual physical distance to the source, ι is the inclination angle of the source.

Horizontal distance

The horizontal distance $R_{\rm H}$ is the distance at which an optimally located and oriented source would produce a certain SNR ρ_0 in a detector. Usually, the ρ_0 is set at 8. The horizontal distance is defined by using sensitivity of a detector. Using an inner product is defined as:

$$(a|b) = 4Re\left[\int_0^\infty df\ \frac{\tilde{a}(f)\tilde{b^*}(f)}{S(|f|)}\right], \tag{A.2}$$

the SNR of the detector ρ for a given signal h is calculated by

$$\rho^2(t) \ = \ (h|h)\,. \tag{A.3}$$

The corresponding detector sensitivity σ in dimension of length is expressed by

$$\sigma^2 \ = \rho^2 \times {D_{\rm eff}}^2. \tag{A.4}$$

The signal amplitude ρ is proportional to the ${D_{\rm eff}}^{-1}$. Then, the horizontal distance, which is described as the effective distance at the SNR $\rho_0 = 8$, is described by

$$R_{\rm H} \ = \ D_{\rm eff}(\rho = \rho_0) \ = \ \frac{\sigma}{\rho_0} \ = \ \frac{\sigma}{8}. \tag{A.5}$$

Detection range

The detection range $R_{\rm det}$ is the spherical radius, whose volume is equal to the volume surrounded by detection radius $r_{\rm det}$. The detection radius $r_{\rm det}$ is the distance that the detector can sense the signals in each direction for an orientation of the source. The detection radius $r_{\rm det}$ is defined as

$$r_{\rm det} = R_{\rm H}\sqrt{\frac{1}{4}{F_+}^2(1+\cos^2\iota)^2 + {F_\times}^2\cos^2\iota}, \tag{A.6}$$

where $R_{\rm H}$ is the horizontal distance. By using the detection radius $r_{\rm det}$, the detection range $R_{\rm det}$ is obtained as follows.

$$\begin{aligned} R_{\rm det}(\iota,\psi) &= \left(\frac{3}{4\pi}V(\iota,\psi)\right)^{1/3} \\ &= \left(\frac{3}{4\pi}\int_0^{r_{\rm det}(\theta,\phi,\iota,\psi)} dr\int_0^{\pi} d\theta\int_0^{2\pi} d\phi\; r^2\sin\theta\right)^{1/3} \\ &= \left(\frac{1}{4\pi}\int_0^{\pi} d\theta\int_0^{2\pi} d\phi\; \left(r_{\rm det}(\theta,\phi,\iota,\psi)\right)^3\sin\theta\right)^{1/3}. \end{aligned} \tag{A.7}$$

Relation between Horizontal distance and detection range

Due to the directional sensitivity or antenna pattern of the detectors, the detection range $R_{\rm det}$ is smaller than the horizontal distance $R_{\rm H}$ by a factor of 2.26, for the same SNR threshold[37, 76]. Then the relation is given by

$$\frac{R_{\rm H}}{R_{\rm det}} = 2.26. \tag{A.8}$$

Expected SNR

The SNR of a detector is deduced from the detection range and the effective distance. By combining (A.4), (A.5), (A.8), the SNR ρ is given by

$$\rho = \frac{\sigma}{D_{\rm eff}} = \frac{\rho_0\; R_{\rm H}}{D_{\rm eff}} = \frac{\rho_0\;\times\;2.26\;\times R_{\rm det}}{D_{\rm eff}} = \frac{8\;\times\;2.26\;\times R_{\rm det}}{D_{\rm eff}}. \tag{A.9}$$

A.2 Triggered event population

A.2.1 LIGO-Virgo network case

The population of the HL, HLV_i and HLV_n events are summarized in Figure A.1. In these plots, V_r denotes V_n triggers.

A.2.2 LIGO-KAGRA network case

The population of the HL, HLK_i and HLK_n events are summarized in Figure A.2. In these plots, K_r denotes K_n triggers.

A.2.3 LIGO-Virgo-KAGRA network case

The population of the HL, HLV_i, HLV_n, HLK_i, HLK_n, HLV_iK_i, HLV_nK_i, HLV_nK_i and HLV_nK_n events are summarized in Figure A.3 to A.8. In these plots, V_r and K_r denote V_n and K_n triggers respectively.

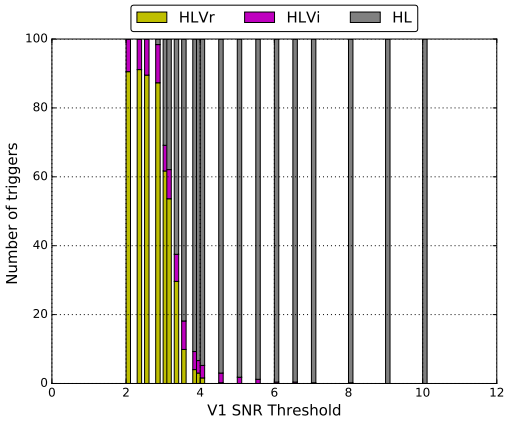

(a) HLV: 1-1-0.13 case

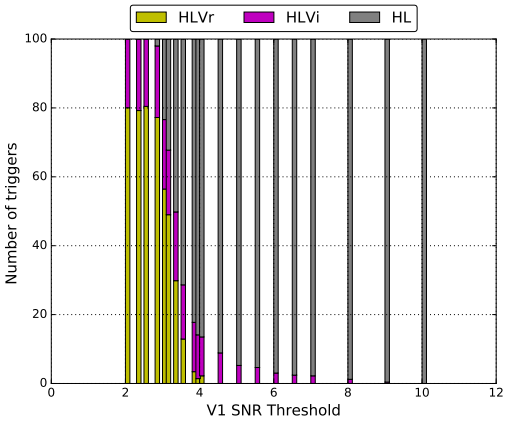

(b) HLV: 1-1-0.20 case

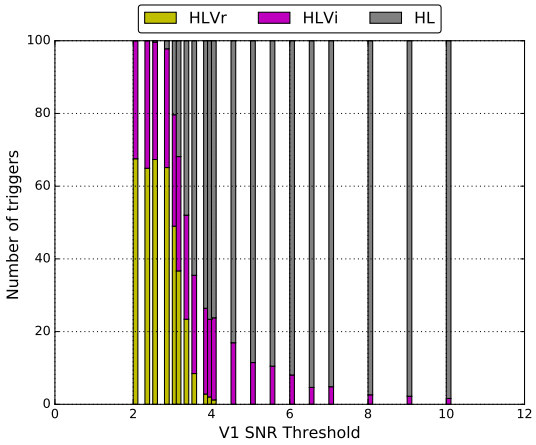

(c) HLV: 1-1-0.28 case

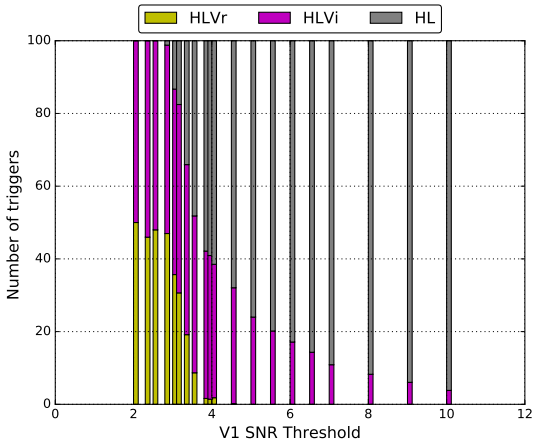

(d) HLV: 1-1-0.39 case

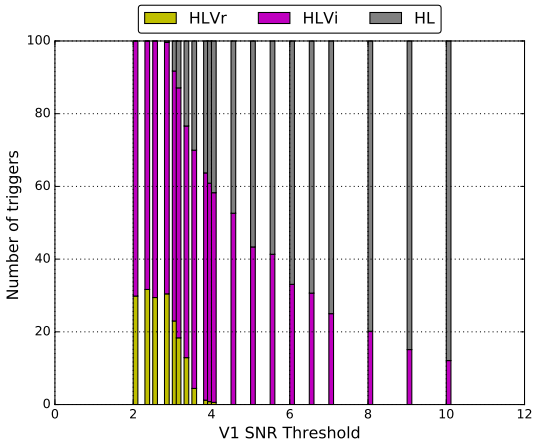

(e) HLV: 1-1-0.56 case

Figure A.1: The trigger population, HL, $\mathrm{HLV_i}$ and $\mathrm{HLV_r}$ events, in percentage with LIGO-Virgo network. The relative detector sensitivities are written down as 1-1-x, with x the ratio of the Virgo sensitivity compared to the two LIGO detectors.

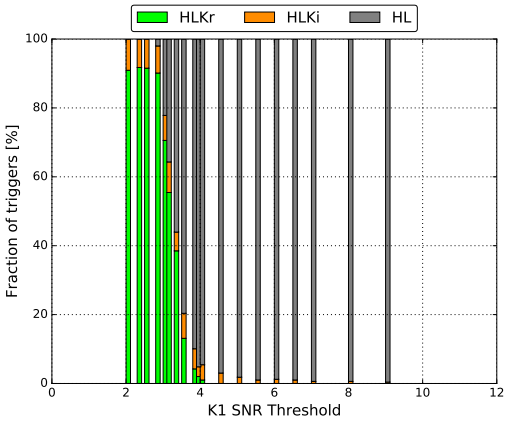

(a) HLK: 1-1-0.13 case

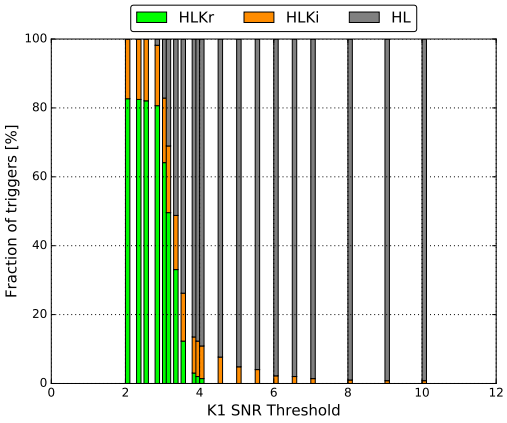

(b) HLK: 1-1-0.20 case

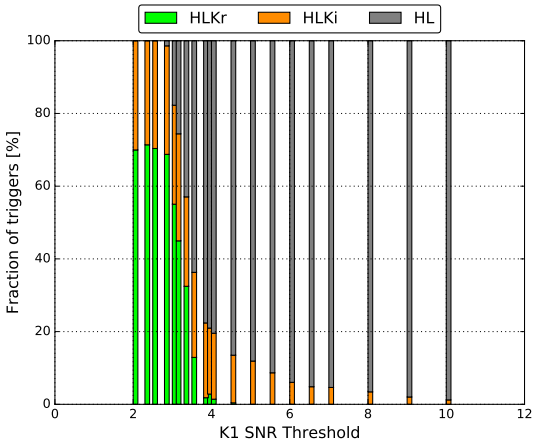

(c) HLK: 1-1-0.28 case

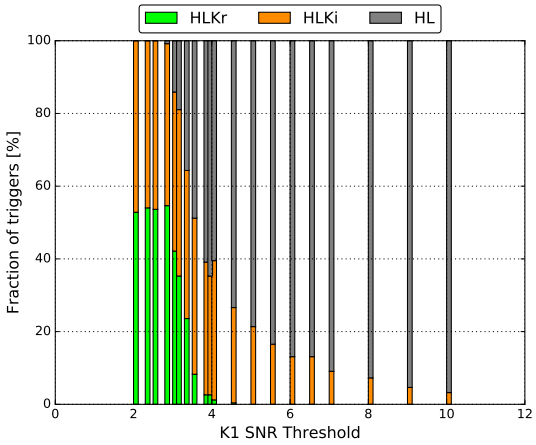

(d) HLK: 1-1-0.39 case

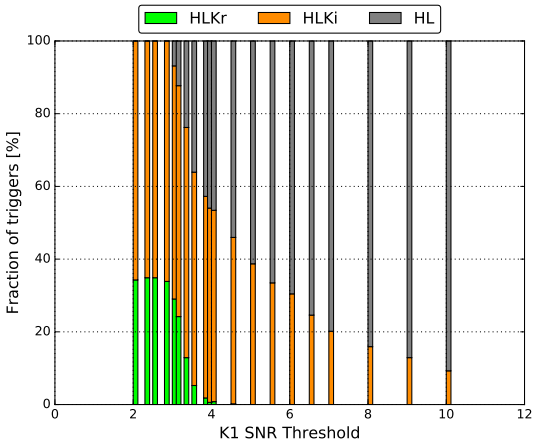

(e) HLK: 1-1-0.56 case

Figure A.2: The trigger population, HL, HLK_i and HLK_r events, in percentage with LIGO-KAGRA network. The relative detector sensitivities are written down as 1-1-x, with x the ratio of the KAGRA sensitivity compared to the two LIGO detectors.

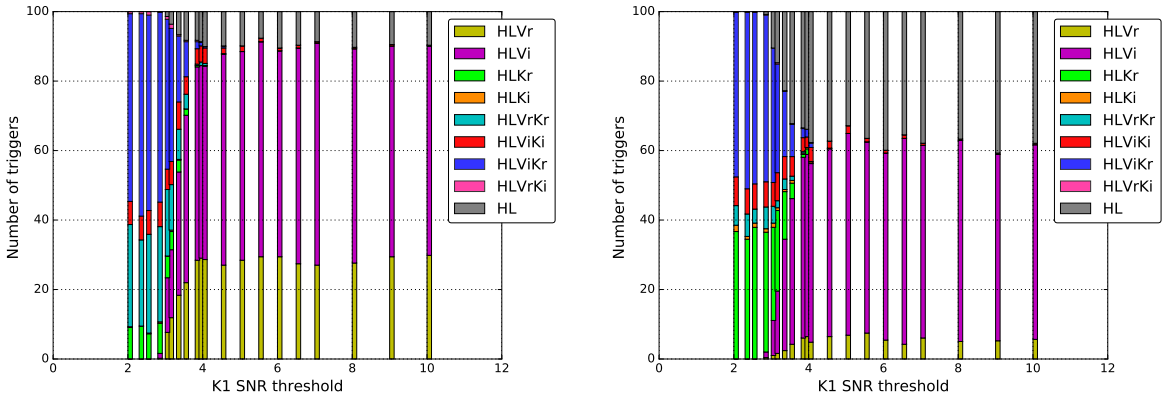

(a) SNR threshold for HLV: 5-5-3.0 case (b) SNR threshold for HLV: 5-5-3.5 case

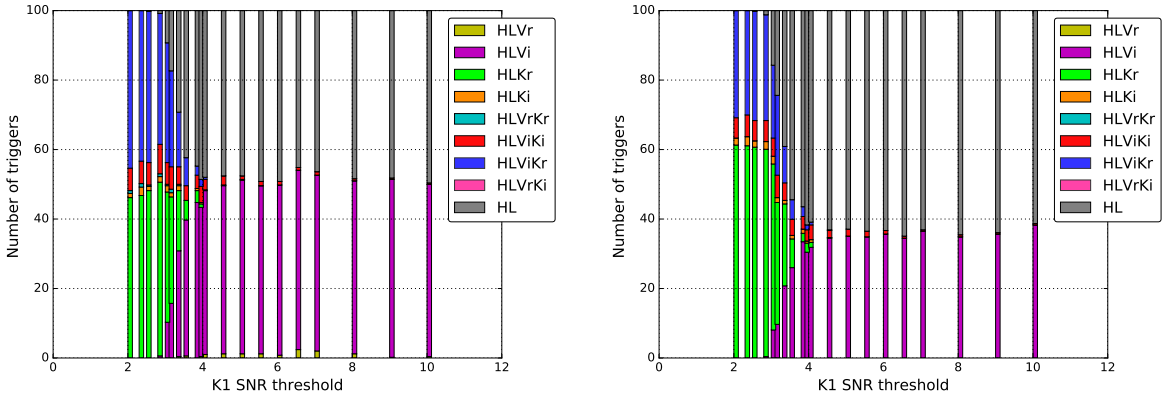

(c) SNR threshold for HLV: 5-5-4.0 case (d) SNR threshold for HLV: 5-5-5.0 case

Figure A.3: The trigger population in percentage with LIGO-Virgo-KAGRA network, where the relative detector sensitivities are set to HLVK: 1-1-0.5-0.13, with the ratio of the Virgo and KAGRA sensitivities compared to the two LIGO detectors.

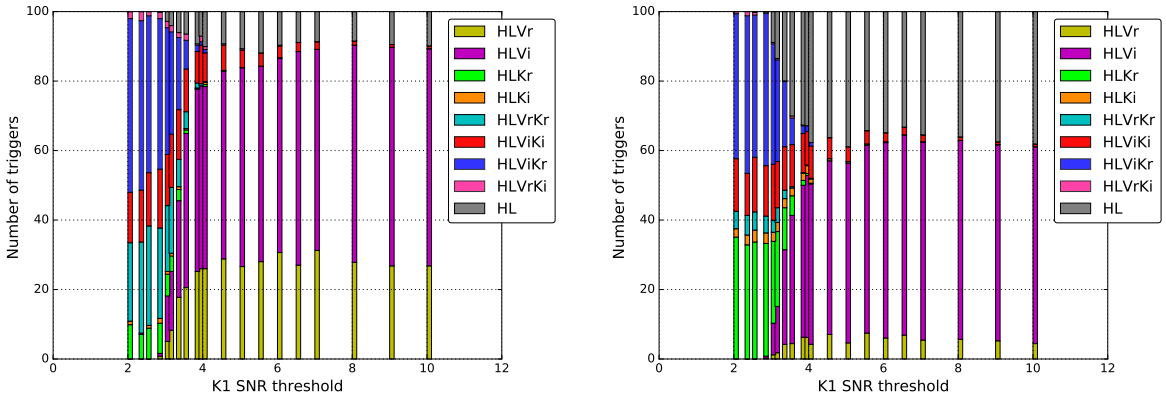

(a) SNR threshold for HLV: 5-5-3.0 case (b) SNR threshold for HLV: 5-5-3.5 case

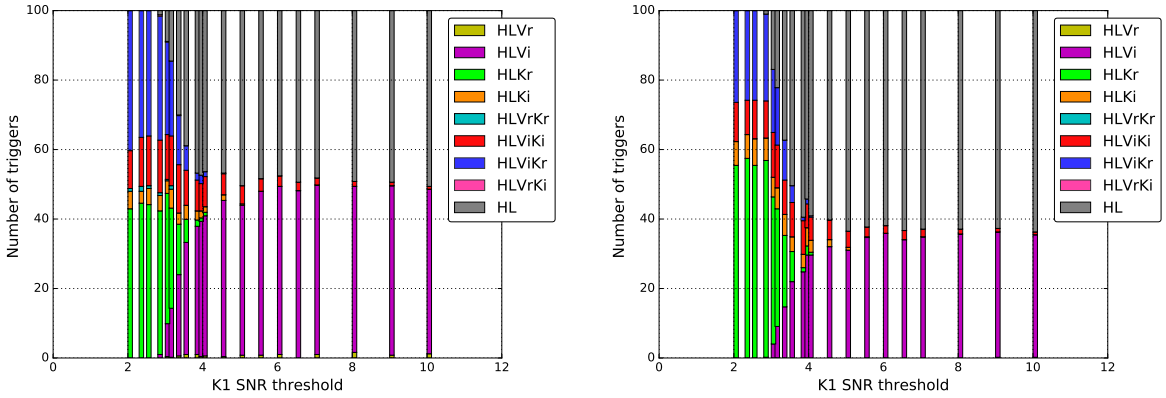

(c) SNR threshold for HLV: 5-5-4.0 case (d) SNR threshold for HLV: 5-5-5.0 case

Figure A.4: The trigger population in percentage with LIGO-Virgo-KAGRA network, where the relative detector sensitivities are set to HLVK: 1-1-0.5-0.20, with the ratio of the Virgo and KAGRA sensitivities compared to the two LIGO detectors.

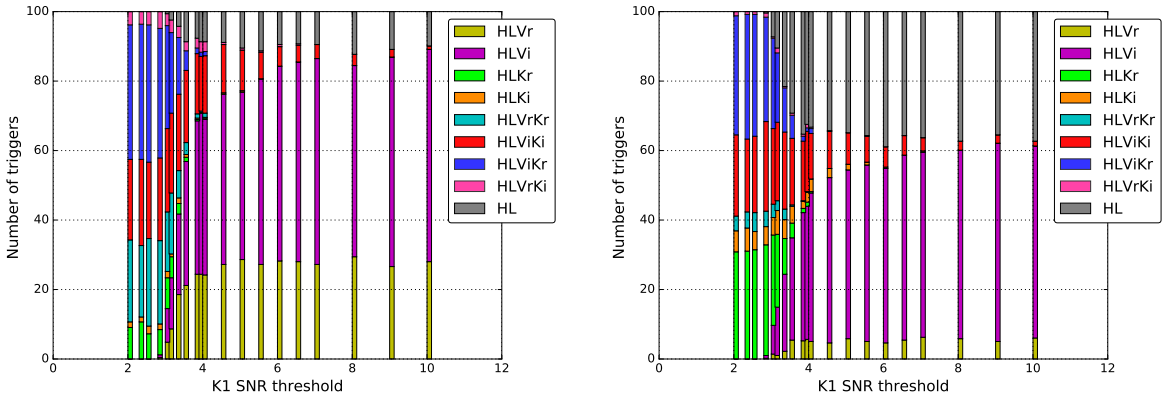

(a) SNR threshold for HLV: 5-5-3.0 case (b) SNR threshold for HLV: 5-5-3.5 case

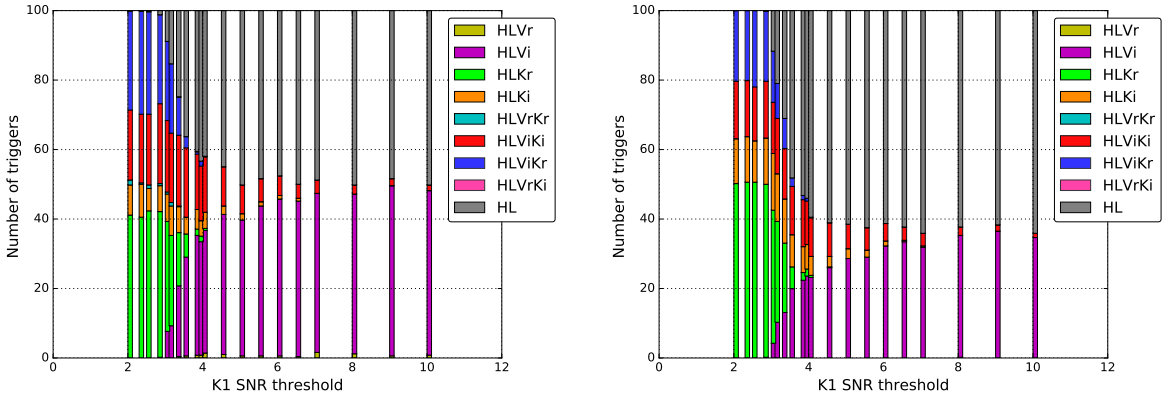

(c) SNR threshold for HLV: 5-5-4.0 case (d) SNR threshold for HLV: 5-5-5.0 case

Figure A.5: The trigger population in percentage with LIGO-Virgo-KAGRA network, where the relative detector sensitivities are set to HLVK: 1-1-0.5-0.28, with the ratio of the Virgo and KAGRA sensitivities compared to the two LIGO detectors.

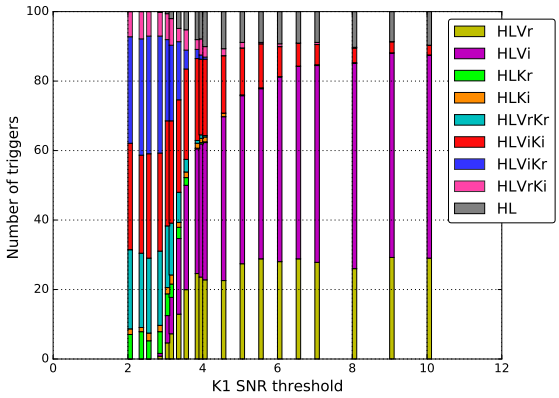

(a) SNR threshold for HLV: 5-5-3.0 case

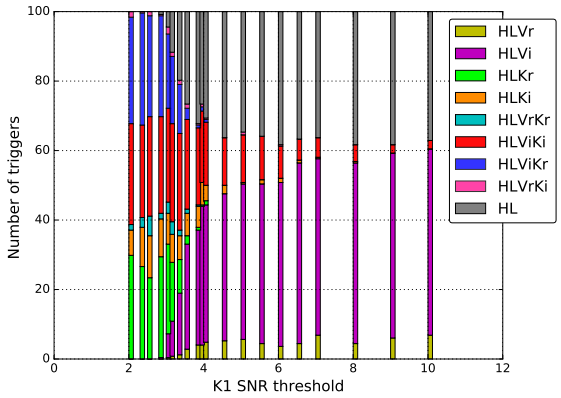

(b) SNR threshold for HLV: 5-5-3.5 case

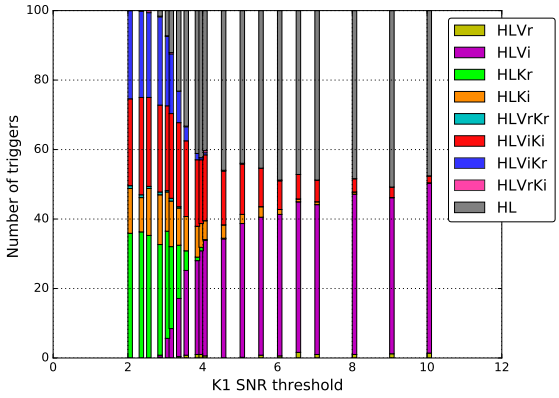

(c) SNR threshold for HLV: 5-5-4.0 case

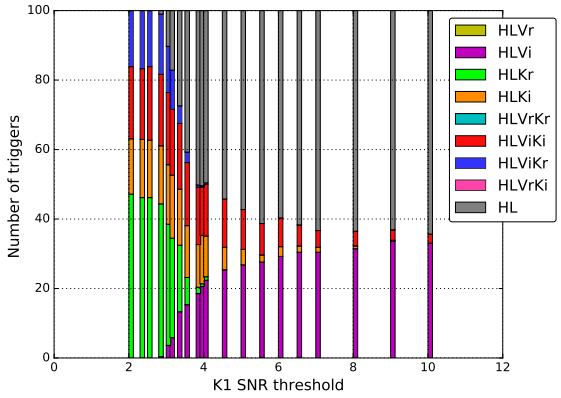

(d) SNR threshold for HLV: 5-5-5.0 case

Figure A.6: The trigger population in percentage with LIGO-Virgo-KAGRA network, where the relative detector sensitivities are set to HLVK: 1-1-0.5-0.33, with the ratio of the Virgo and KAGRA sensitivities compared to the two LIGO detectors.

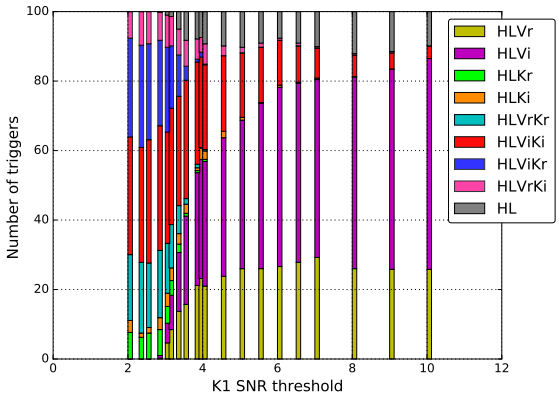

(a) SNR threshold for HLV: 5-5-3.0 case

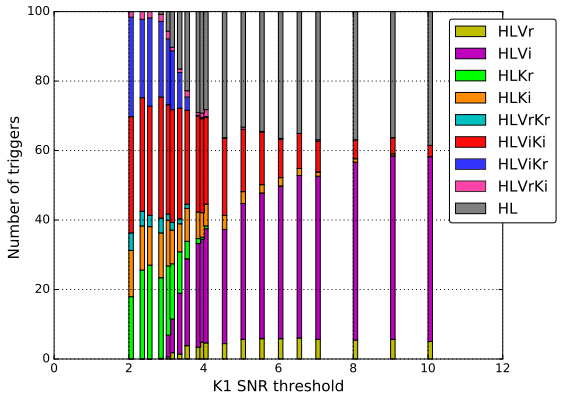

(b) SNR threshold for HLV: 5-5-3.5 case

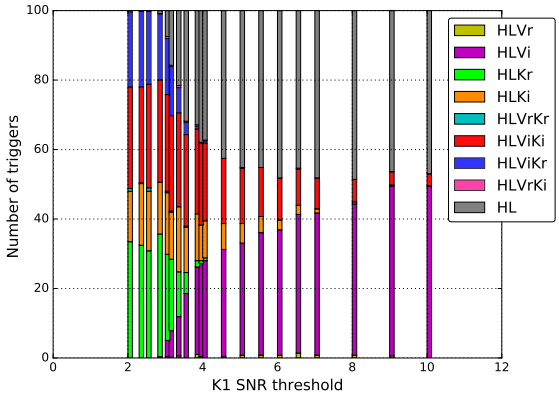

(c) SNR threshold for HLV: 5-5-4.0 case

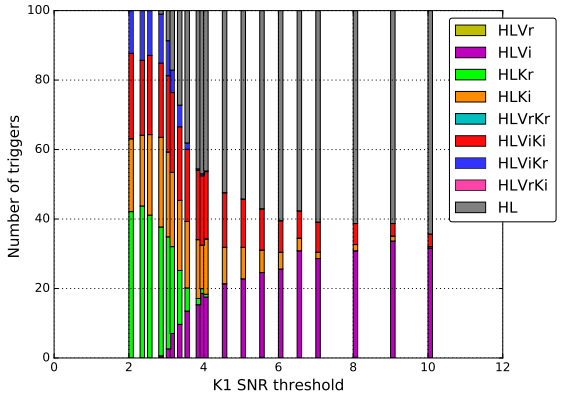

(d) SNR threshold for HLV: 5-5-5.0 case

Figure A.7: The trigger population in percentage with LIGO-Virgo-KAGRA network, where the relative detector sensitivities are set to HLVK: 1-1-0.5-0.39, with the ratio of the Virgo and KAGRA sensitivities compared to the two LIGO detectors.

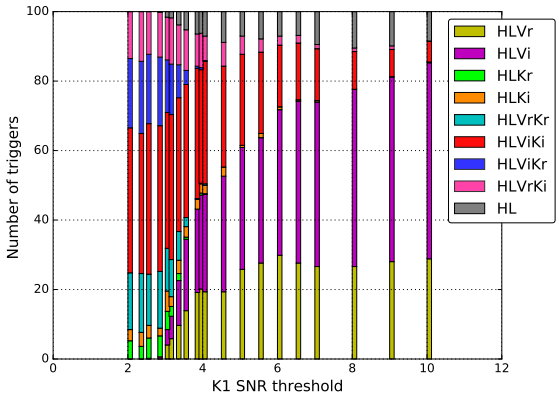

(a) SNR threshold for HLV: 5-5-3.0 case

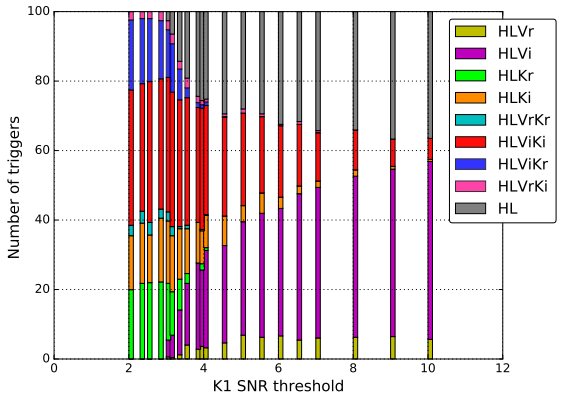

(b) SNR threshold for HLV: 5-5-3.5 case

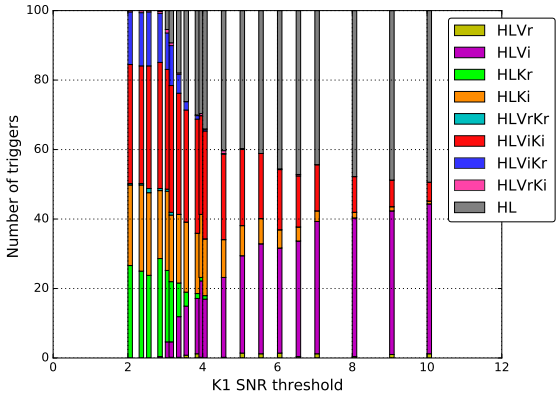

(c) SNR threshold for HLV: 5-5-4.0 case

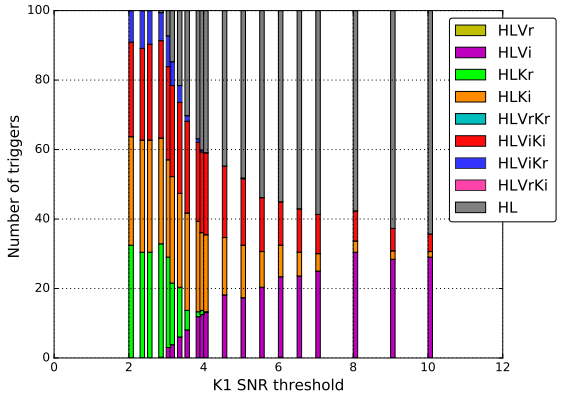

(d) SNR threshold for HLV: 5-5-5.0 case

Figure A.8: The trigger population in percentage with LIGO-Virgo-KAGRA network, where the relative detector sensitivities are set to HLVK: 1-1-0.5-0.5, with the ratio of the Virgo and KAGRA sensitivities compared to the two LIGO detectors.

A.2.4 Dependence on the sensitivity of the fourth detector KAGRA with different SNR thresholds in Virgo

The expected performances of the searched area and the 90% confidence area with different SNR thresholds in Virgo are summarized in this subsection. Figure A.9 and A.10 are the case where the SNR threshold for Virgo is set to 4.0, while Figure A.11 and A.12 are the case where it is set to 3.0.

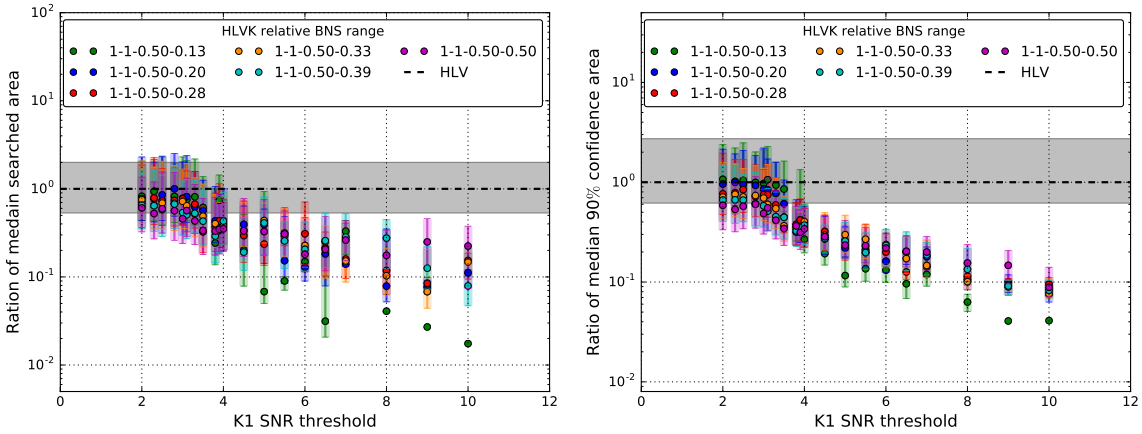

Figure A.9: Ratio of the median searched area (*left*) and 90% confidence area (*right*) of HLVK triggers to that of the same triggers treated as HLV coincidences, when the sensitivity of the KAGRA detector is varied. The colors show the network configuration. This is the case where the sub-threshold for Virgo is to 4.0.

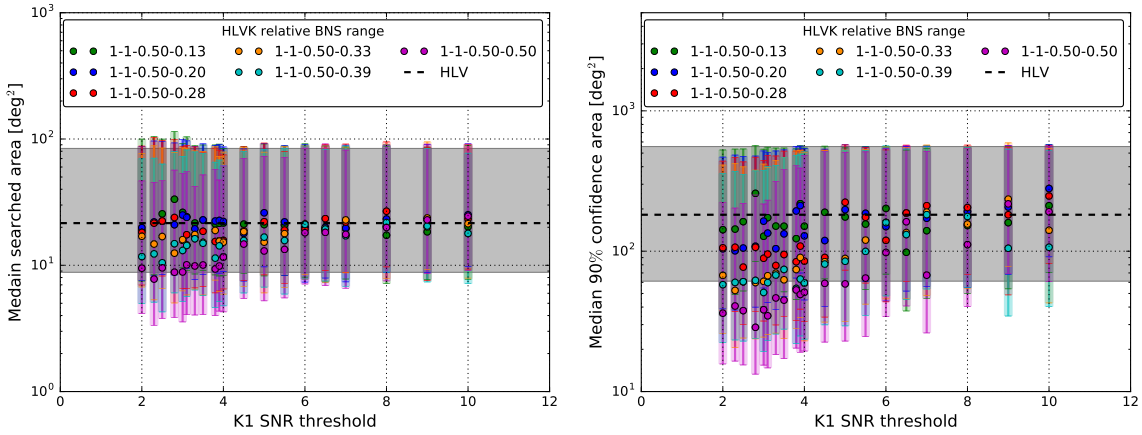

Figure A.10: The median searched area (*left*) and 90% confidence area (*right*) are shown as a function of the SNR threshold used in KAGRA. Expected sky localization performance with the hierarchical search when the sensitivity of the KAGRA detector is varied. The colors show the network configuration. This is the case where the sub-threshold for Virgo is to 4.0.

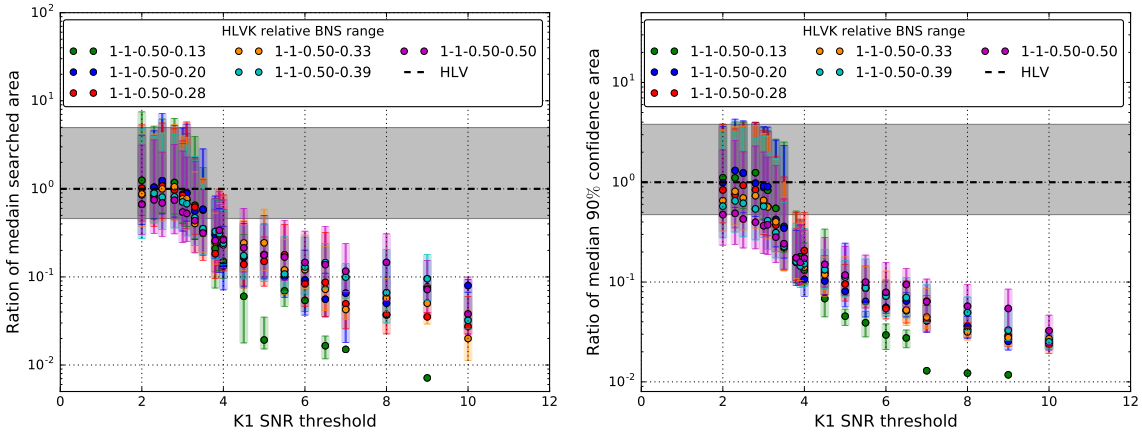

Figure A.11: Ratio of the median searched area (*left*) and 90% confidence area (*right*) of HLVK triggers to that of the same triggers treated as HLV coincidences, when the sensitivity of the KAGRA detector is varied. The colors show the network configuration. This is the case where the sub-threshold for Virgo is to 3.0.

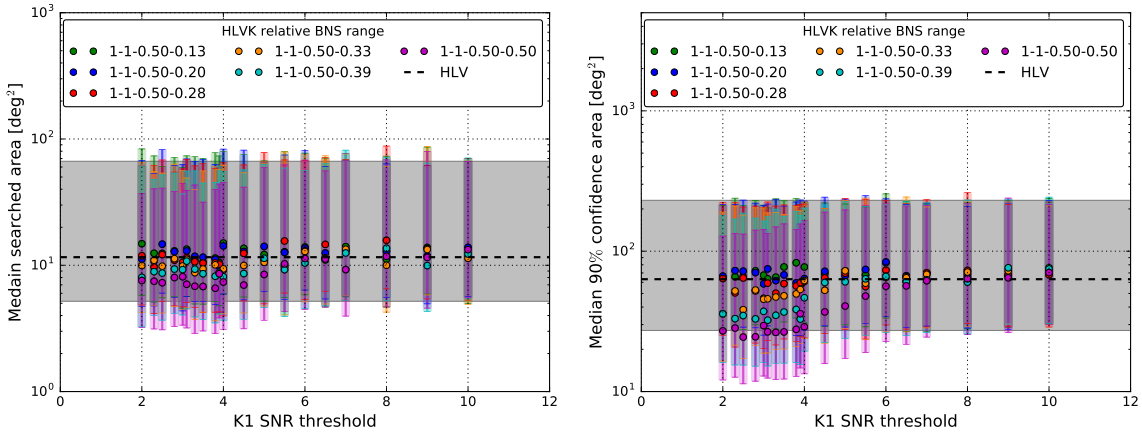

Figure A.12: The median searched area (*left*) and 90% confidence area (*right*) are shown as a function of the SNR threshold used in KAGRA. Expected sky localization performance with the hierarchical search when the sensitivity of the KAGRA detector is varied. The colors show the network configuration. This is the case where the sub-threshold for Virgo is to 3.0.

Chapter B

Detailed characteristics of Type-A suspension

B.1 Simulated eigen mode list of Type-A suspension

The eigen mode shapes of the designed Type-A suspension is listed here.

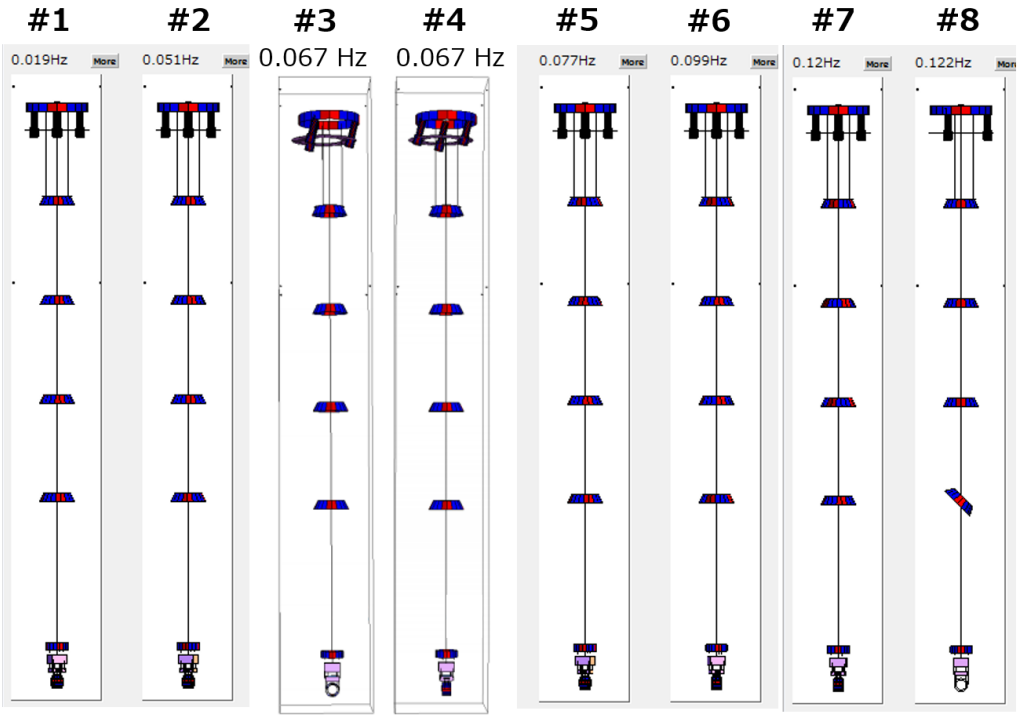

#9

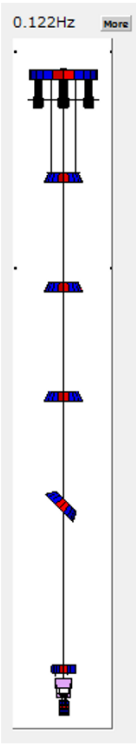

#10

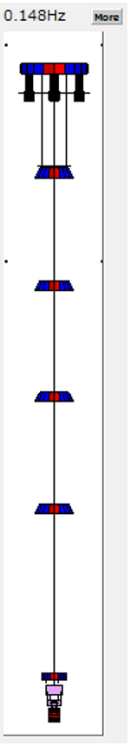

#11

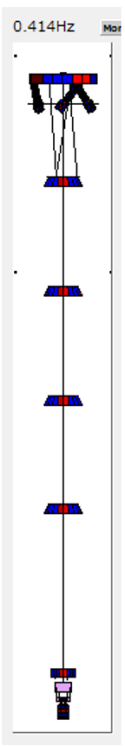

#12

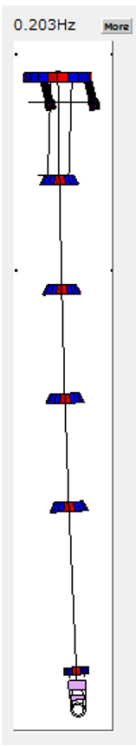

#13

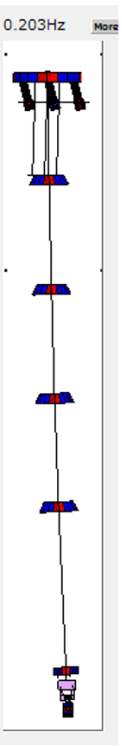

#14

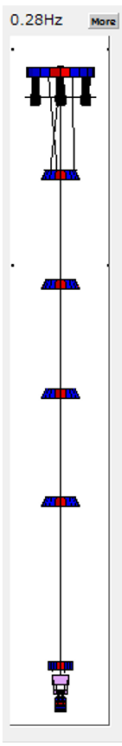

#15

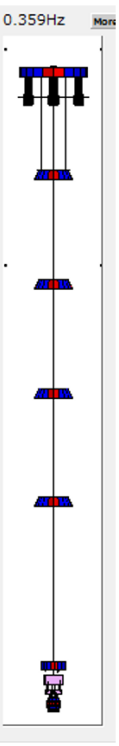

#16

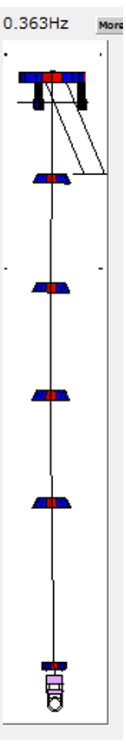

#17

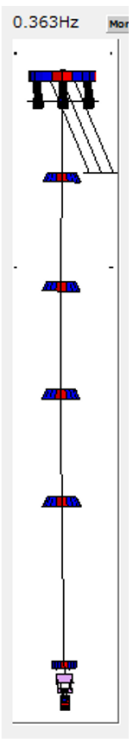

#18

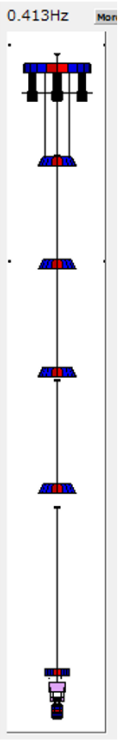

#19

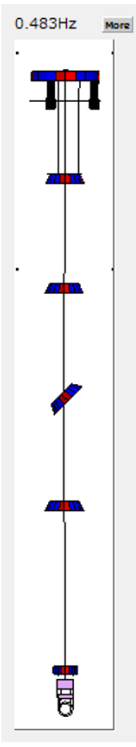

#20

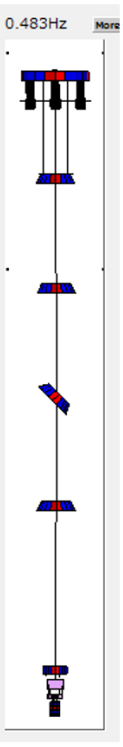

#21

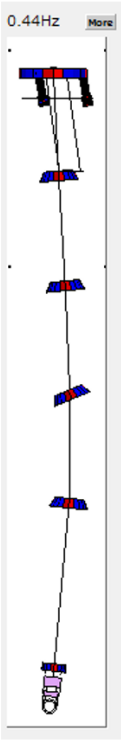

#22

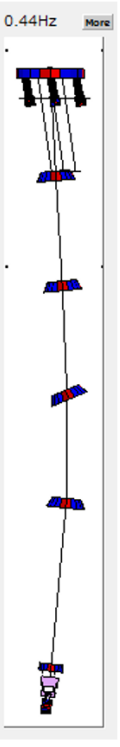

#23

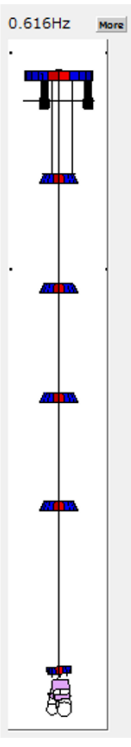

#24

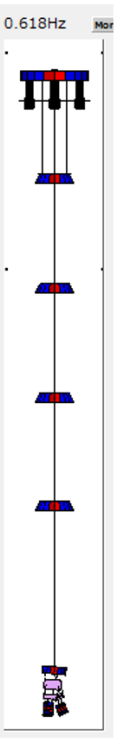

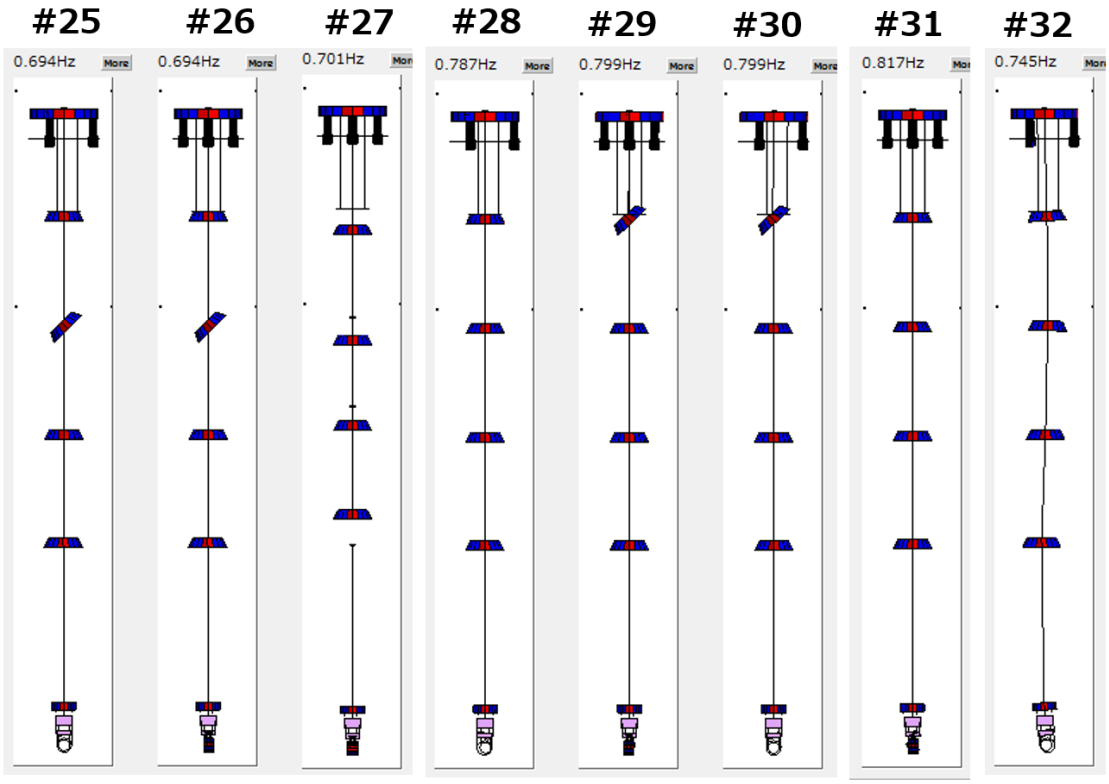
#25
0.694Hz
#26
0.694Hz
#27
0.701Hz
#28
0.787Hz
#29
0.799Hz
#30
0.799Hz
#31
0.817Hz
#32
0.745Hz

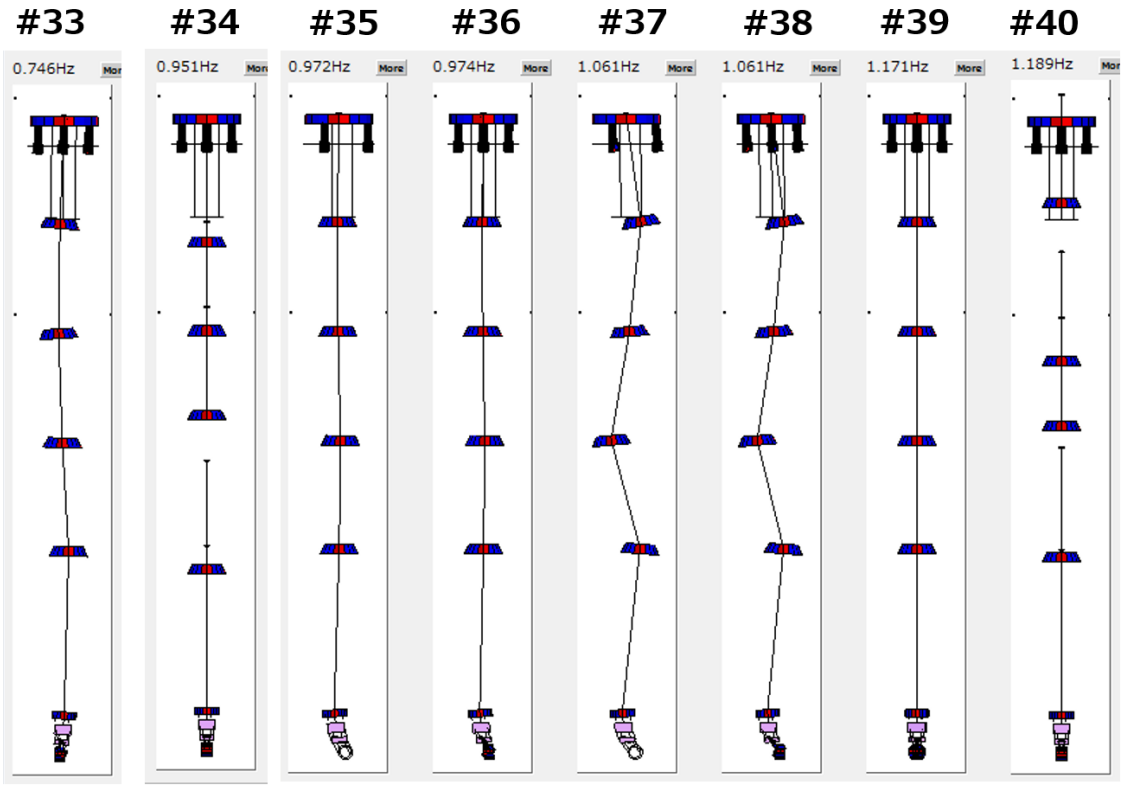
#33
0.746Hz
#34
0.951Hz
#35
0.972Hz
#36
0.974Hz
#37
1.061Hz
#38
1.061Hz
#39
1.171Hz
#40
1.189Hz

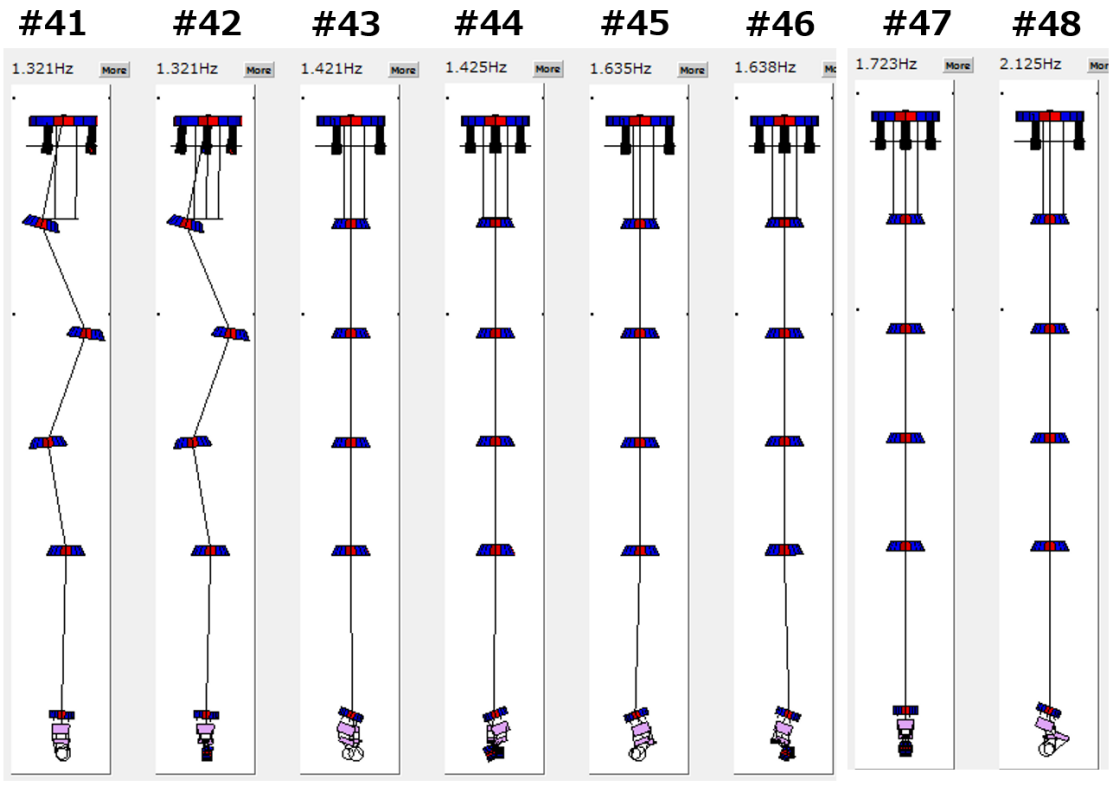
#41
1.321Hz
#42
1.321Hz
#43
1.421Hz
#44
1.425Hz
#45
1.635Hz
#46
1.638Hz
#47
1.723Hz
#48
2.125Hz

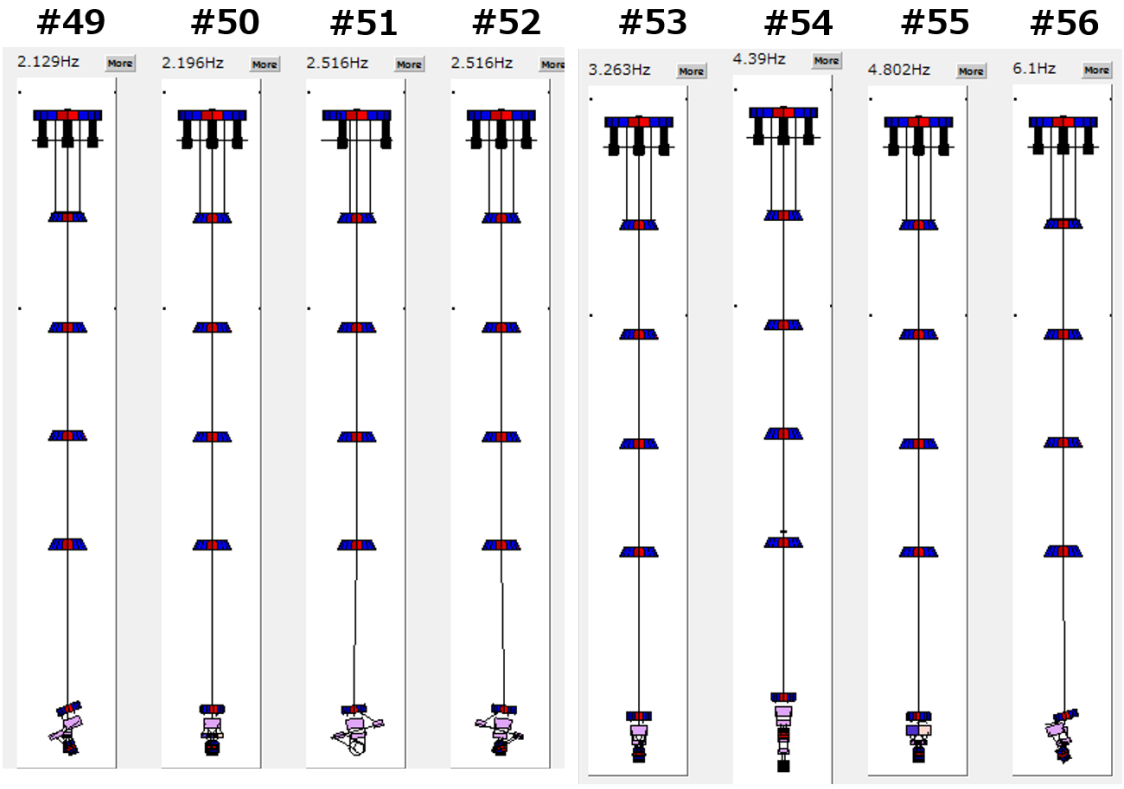
#49
2.129Hz
#50
2.196Hz
#51
2.516Hz
#52
2.516Hz
#53
3.263Hz
#54
4.39Hz
#55
4.802Hz
#56
6.1Hz

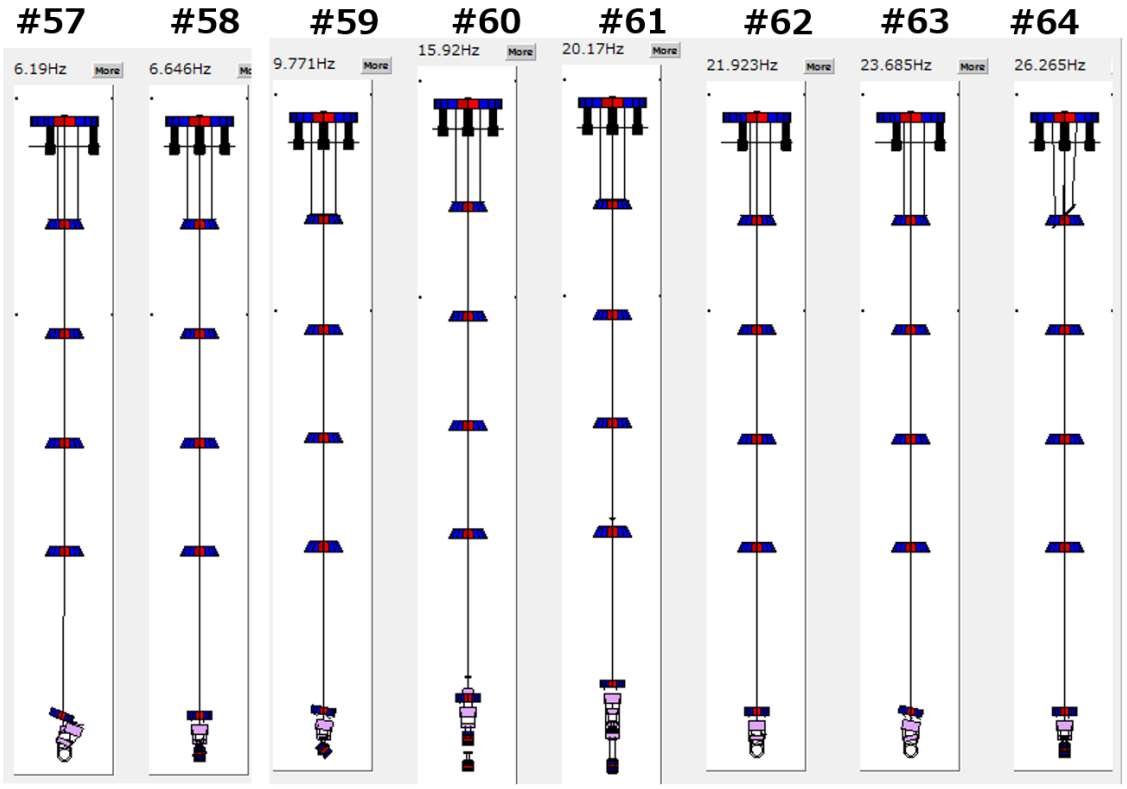
#57
#58
#59
#60
#61
#62
#63
#64
6.19Hz
6.646Hz
9.771Hz
15.92Hz
20.17Hz
21.923Hz
23.685Hz
26.265Hz
More

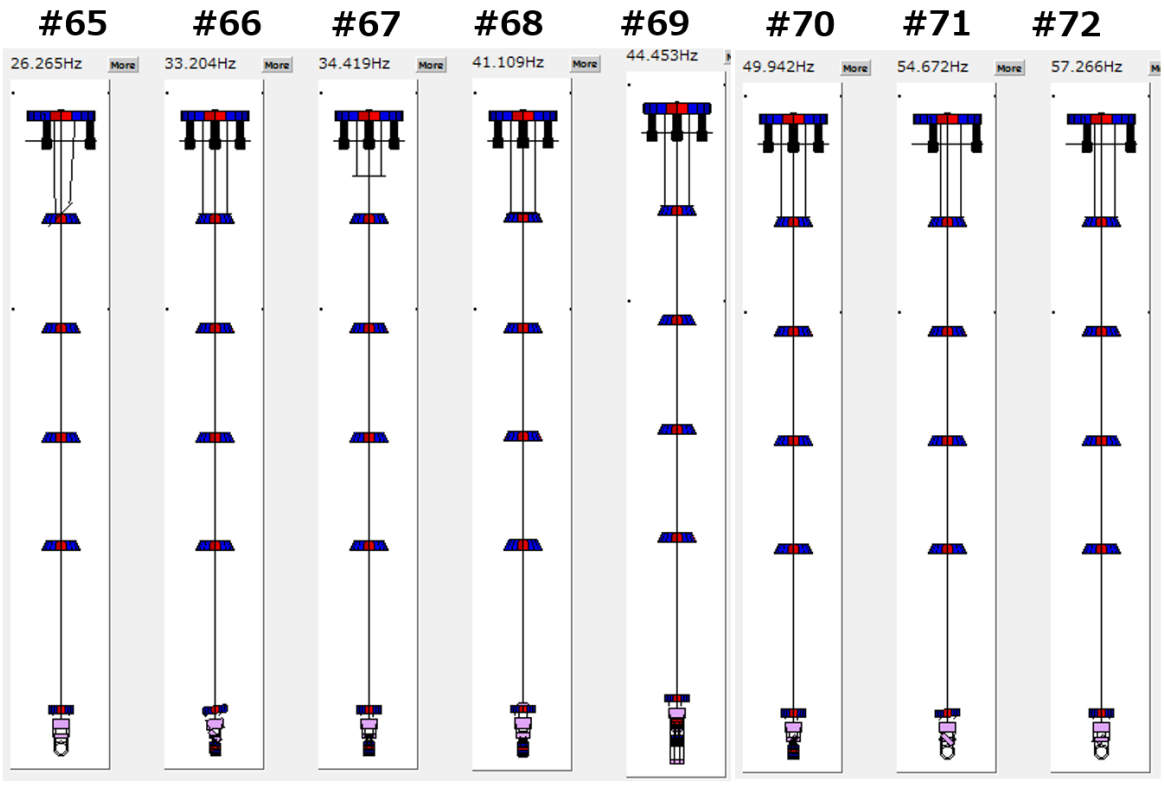
#65
#66
#67
#68
#69
#70
#71
#72
26.265Hz
33.204Hz
34.419Hz
41.109Hz
44.453Hz
49.942Hz
54.672Hz
57.266Hz
More

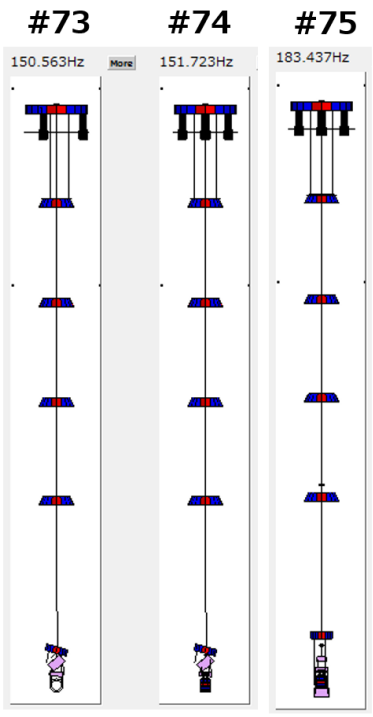
#73
#74
#75
150.563Hz
More
151.723Hz
183.437Hz

B.2 Type-A suspension configuration during the measurement

During the measurement period, we had to faced on a situation where at least on GAS filter is mechanically stacked or locked in all the Type-A suspensions. Concerning ETMY suspension, we found that second and third GAS stages seemed to be mechanically stacked with same reason as the issue of ETMX F2-GAS filter. For the two input suspensions, we had to intentionally lock the first GAS filter (called F0-GAS) keystone in order to hold the other suspension components, especially the mirror, at the target height[1]. For all these suspensions we decided to keep using them with such configuration for the O3 period. Figure B.7 shows the expected mechanical seismic attenuation performance where one or two GAS stage are not working as spring, assuming the vertical mirror vibration couples to the longitudinal dof by 1%.

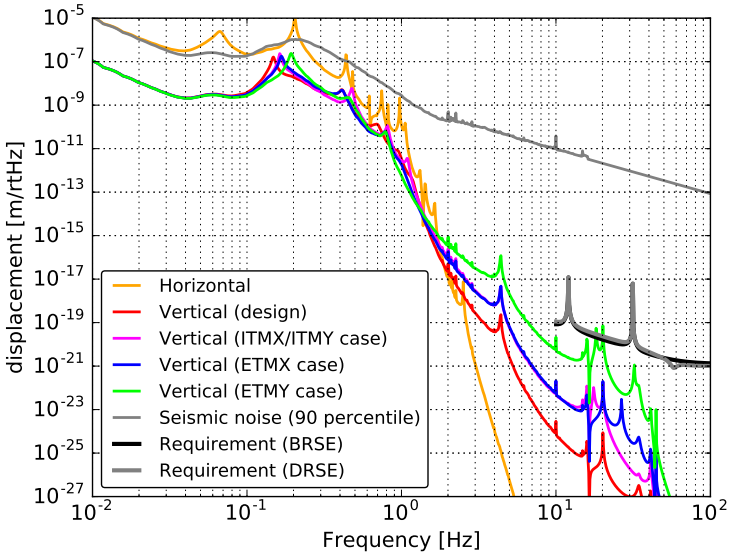

Figure B.7: Expected mechanical seismic attenuation performance where one or two GAS stage are not working as spring, assuming the vertical mirror vibration couples to the longitudinal dof by 1%.

[1]This issue has the following history: we originally had GAS blades made in abroad which would suspend the mirror properly. We then found that the original blade was actually broken, cracked because of hydrogen embrittlement in Maraging steels [77]. We remade and replaced the blades with the new ones made in Japan, we finally found that the newly made GAS blades were too weak to hold the whole suspension at the desired height.

B.3 Axis difference among the X-arm cavity and X-arm suspensions

As a preparation of the transfer function measurement with the FPMI signals, which is called DARM, the difference of the X-arm cavity axis and the local sensor axes of the X-arm suspension is investigated. The angle offset is estimated by comparing two displacement transfer functions at 10 mHz; one is from longitudinal vibration of the mass to the X-arm displacement signal, and the other one is from transverse vibration of the mass to the X-arm displacement signal. For example, for the IP-stage case, the angle offset θ is obtained by

$$\theta \;=\; \arctan\left(\frac{X_{\mathrm{arm}}}{IP_{\mathrm{T}}} \Big/ \frac{X_{\mathrm{arm}}}{IP_{\mathrm{L}}}\right). \tag{B.1}$$

During this measurement, the X-arm cavity was locked with IR laser and the displacement signal is reconstructed from its control signal. The estimated angle offset is summarized in Figure B.8. The angle offset from the X-arm cavity axis to the longitudinal axis of the ITMX-IP and ETMX-IP is obtained as 8.2 deg and 5.0 deg. This implies that the ITMX-IP motion and ETMX-IP motion in L dof couples to the motion in the orthogonal axis of X-arm cavity axis by 1% and 0.4% respectively.

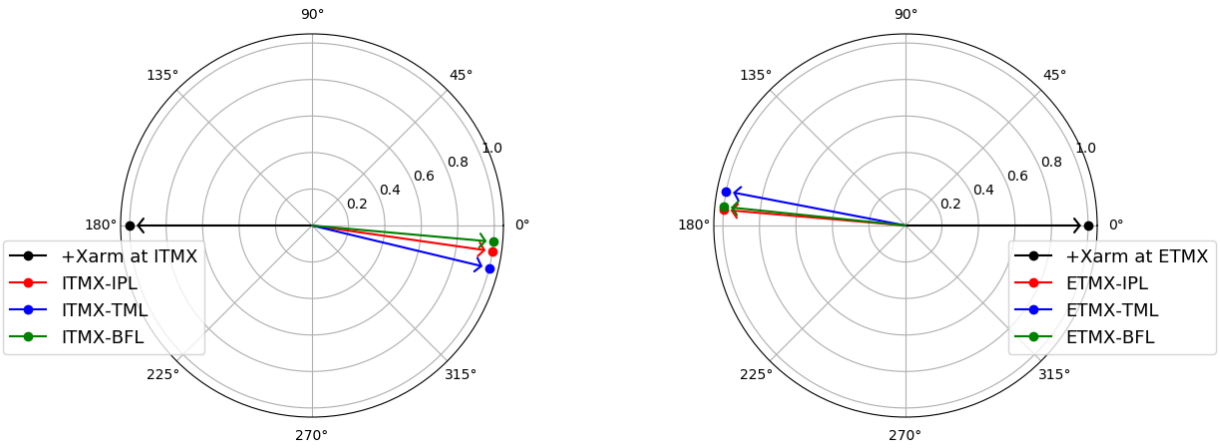

Figure B.8: Estimated angle offset of X-arm suspensions compared to the X-arm cavity axis.

B.4 Position dependence of LVDT noise floor

The sensor noise floor of the LVDT at several point inside its linear range is measured as illustrated in Figure B.9 and B.10. This reports that of the primary coil is much close to the secondary one (at the edge of the linear range), the noise floor can be enhanced by factor of 10 in the current system.

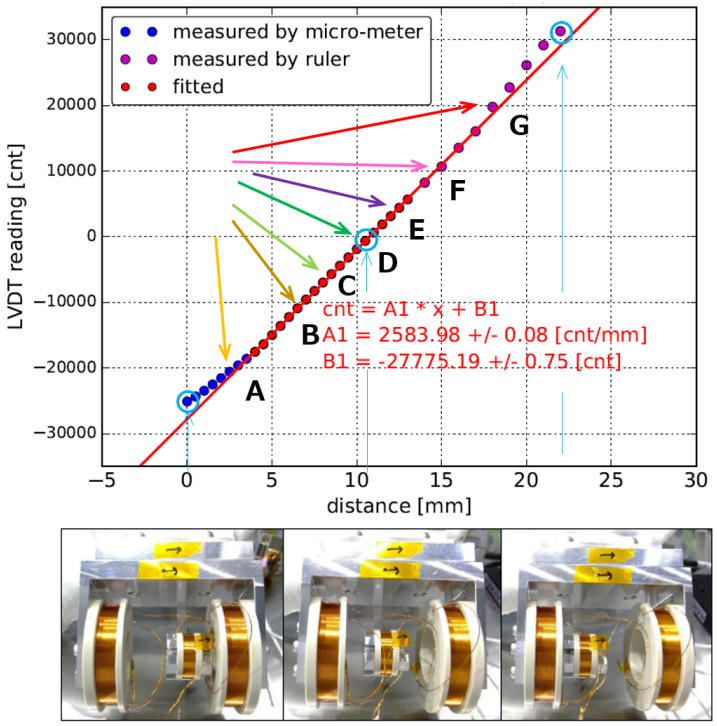

Figure B.9: A LVDT calibration curve. he noise floor is measured at the points which are denoted by the alphabets from A to B.

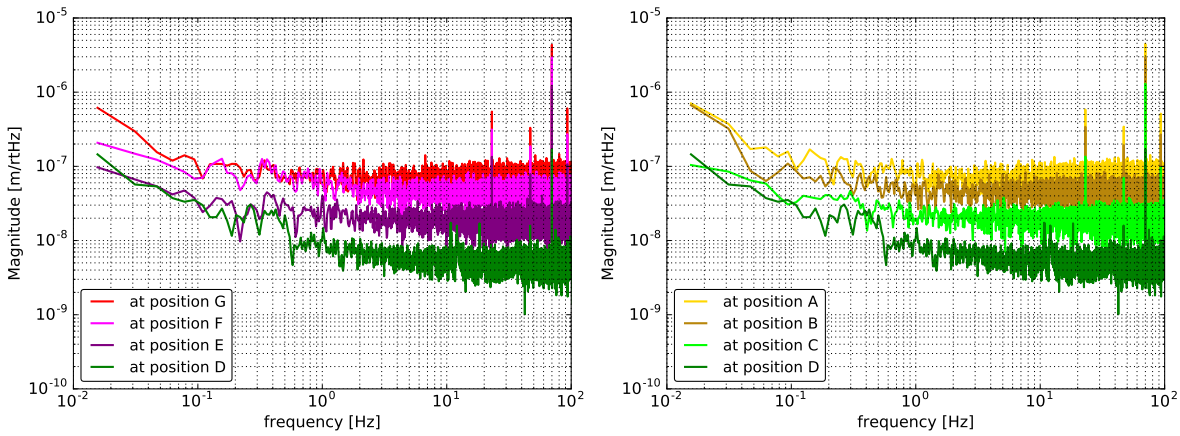

Figure B.10: LVDT sensor noise floors measured at the points shown in Figure B.9.

B.5 Measured decay time constant table

The measured resonant frequencies and the decay time constants are listed in Figure B.11 andB.12. The yellow colored modes are the ones which we pay less attention, while the red colored one is the mode which is not found in this work. The mode numbers correspond to ones in section B.1. Standard deviations are removed from the below figures however, they are included in Figure 6.3.2.

mode number	fitted frequemcy[Hz]	decay time [s]	excittion point
#1	0.04	233.6	BFY
#2	0.07	193.2	BFY
#3	0.08	83.9	IPT
#4	0.08	100.9	IPL
#5	0.09	116.0	BFY
#6	0.09	174.1	BFY
#7	0.12	191.8	MNoplevY
#8			
#9			
#10	0.19	48.1	F0GAS
#11	0.42	49.1	IPY
#12	0.21	233.1	IPT
#13	0.21	111.5	IPL
#14			
#15	0.32	726.6	IMY
#16			
#17			
#18	0.47	14.7	F0GAS
#19			
#20			
#21	0.45	152.0	IPT
#22	0.45	169.3	IPL
#23	0.63	671.4	MNR
#24	0.63	982.3	MNR
#25			
#26			
#27	0.76	8.9	F3GAS
#28	0.75	316.9	IPT
#29	0.79	73.3	MNP
#30	0.79	177.2	MNR
#31	0.75	157.7	MNR
#32	0.72	268.8	IPT
#33	0.73	328.7	IPL
#34	0.94	9.5	F1GAS
#35	0.97	167.6	IPT
#36	0.98	42.6	IPL

mode number	fitted frequemcy[Hz]	decay time [s]	excittion point
#37	1.03	51.4	IPT
#38	1.04	24.7	IPL
#39	1.15	811.7	MNY
#40	1.31	8.0	F1GAS
#41	1.34	2.9	IPT
#42	1.31	26.3	IPL
#43	1.48	288.2	MNR
#44	1.52	488.6	MNP
#45	1.71	365.9	MNP
#46	1.67	615.8	MNP
#47	1.68	2201.1	MNY
#48	2.16	192.2	MNT
#49	2.16	176.6	MNL
#50	2.12	555.2	MNY
#51	2.49	845.5	MNT
#52	2.49	1241.0	MNL
#53	3.20	2552.2	MNY
#54			
#55	4.14	44.6	MNY
#56	5.20	42.2	MNT
#57	5.09	61.3	MNL
#58	7.52	172.9	MNP
#59	9.70	86.9	BFGAS
#60	15.05	38.6	MNR
#61	19.39	49.6	BFGAS
#62	22.89	1.1	MNR
#63	23.49	134.9	MNR
#64			
#65			
#66			
#67			
#68			
#69			
#70			
#71			
#72			
#73			
#74			
#75			
NOT_IDed	0.14	329.6	MNoplevY

Figure B.11: Measured decay time constants without controls.

mode number	fitted frequemcy[Hz]	decay time [s]	excittion point
#1	0.05	47.1	BFY
#2	0.08	36.6	BFY
#3	0.15	18.8	IPT
#4	0.15	10.6	IPL
#5	0.08	42.9	BFY
#6	0.09	37.9	BFY
#7	0.13	7.2	BFY
#8			
#9			
#10	0.18	4.2	F0GAS
#11	0.48	1.4	IPY
#12	0.25	2.0	IPT
#13	0.22	2.6	IPL
#14			
#15	0.23	1.3	MNY
#16			
#17			
#18	0.50	2.9	F0GAS
#19			
#20			
#21	0.46	4.2	IPT
#22	0.45	4.9	IPL
#23	0.61	10.2	MNR
#24	0.64	20.1	MNP
#25			
#26			
#27	0.82	5.1	F3GAS
#28	0.71	17.2	MNR
#29	0.71	3.2	MNP
#30	0.81	12.4	MNR
#31	0.79	6.5	MNP
#32	0.70	9.2	IPT
#33	0.72	3.7	IPL
#34	0.89	1.5	F1GAS
#35	0.95	2.9	IPT
#36	0.97	26.2	IPL

mode number	fitted frequemcy[Hz]	decay time [s]	excittion point
#37	1.03	10.8	IPT
#38	1.01	6.7	IPL
#39	1.16	17.7	MNY
#40	1.29	3.1	F1GAS
#41	1.36	25.7	IPT
#42	1.36	13.5	MNP
#43	1.48	197.4	MNT
#44	1.52	26.3	MNL
#45	1.73	0.5	MNR
#46	1.60	3.6	MNP
#47	1.70	1.7	MNY
#48	2.08	2.3	MNR
#49	2.00	3.0	MNP
#50	2.13	0.6	MNY
#51	2.49	58.6	MNT
#52	2.49	25.6	MNL
#53	3.19	13.3	MNY
#54			
#55	4.19	5.6	MNY
#56	5.20	12.6	MNT
#57	5.09	25.1	MNL
#58	7.53	19.7	MNP
#59	9.68	9.5	BFGAS
#60	14.97	0.5	MNR
#61	19.85	0.6	MNR
#62	20.17	0.5	MNR
#63	23.48	21.8	MNR
#64			
#65			
#66			
#67			
#68			
#69			
#70			
#71			
#72			
#73			
#74			
#75			
#NOT_IDed	0.13	168	BFY

Figure B.12: Measured decay time constants with controls.

B.6 Typical noise floors of inertial sensors

The typical noise floors of the inertial sensors used for current Type-A SAS, compared to the mirror displacement due to the seismic noise, are summarized in Figure B.13. This plot includes the spectra of the displacement of the mirror suspended by the Type-A SAS where the seismic noise level is high/low.

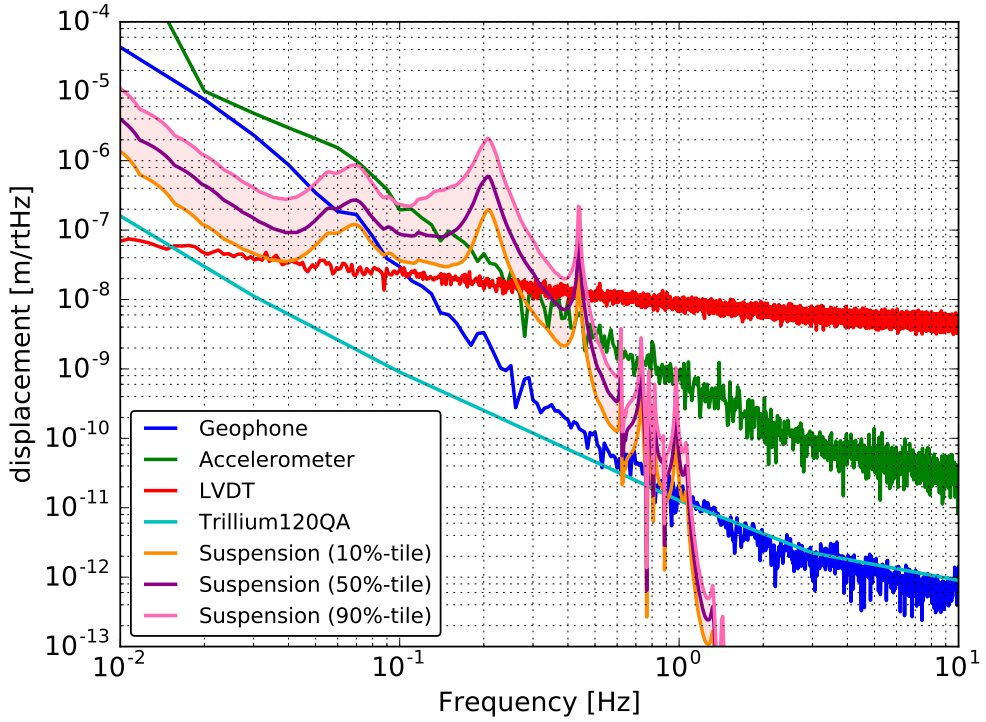

Figure B.13: The typical noise floors of such inertial sensors compared to the mirror displacement due to the seismic noise.

Chapter C

Supplementary note for sensor correction system

C.1 Impact on X-arm cavity displacement signal

After implementing the same sensor-correction system at the IP-stage by a seismometer which senses the local ground motion (named IPsc), to the ITMX suspension, the impact of the IPsc to the X-arm cavity displacement is investigated. During this measurement, the X-arm cavity was locked with IR laser and the displacement signal is reconstructed from its control signal.

C.1.1 Setting for ITMX suspension

The high-pass filter cut-off of the sensor-correction filter for ITMX suspension is tweaked since the seismometer noise coupling at the frequency about below 0.1 Hz is more dominant compared to the ETMX case. The filter used is the obtained by multiplying high-pass filter at 0.5 mHz with forth order of Butterworth and an elliptic high-pass filter with 20 mHz cut-off whose order, passband ripple and the attenuation are set to second,10 dB and 80 dB respectively. The phase shift due to this filter is given by 6.3 deg, which give 0.6 % difference. This filter is applied to the seismic displacement signal. The inertial sensors on the ITMX IP-stage are the accelerometers which are introduced in section 4.2.2.

The impact on the local ITMX suspension is is shown in Figure C.1 to C.2. The TM-stage signal is not included since the measured spectra show only the self noise.

C.1.2 Impact on X-arm cavity displacement

The impact of the IPsc to the X-arm cavity displacement signal is summarized in Figure C.3. This figure shows the spectra and the coherence between some signals when the IPsc is off (*left*) and on (*right*). In this plot, differential and common motion of the IP-stages and the seismometers of ETMX (X-end station) and ITMX (X-front station) are denoted as $diff.\_IP\_inertial$, $diff\_seis$ and $common\_IP\_inertial$. The signals labeled sc_out show the sensor-correction filtered signals which sent to the LVDT signals, and one labeled gif shows the

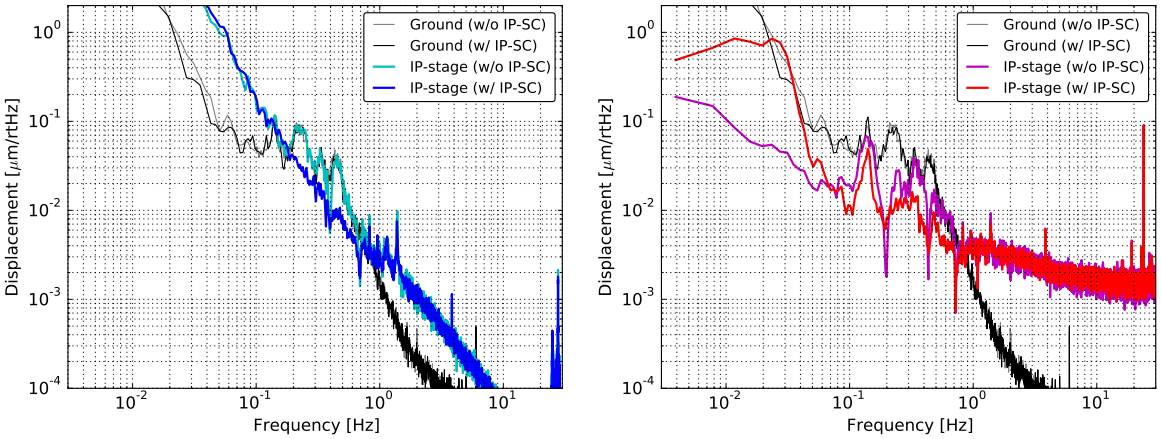

Figure C.1: Comparison of the IP-stage displacement spectrum measured by the inertial sensor, the accelerometer ($left$) and by the LVDT ($right$) when the IPsc is on and off at ITMX suspension. I note that in the $left$ panel, the LVDT signal with and without IPsc is not compatible since one measures the displacement, while the other one observes the inertial motion basically.

strian meter signal which observes the differential motion of the ground along with the X-arm axis.

By comparing the spectra of common and differential IP-stage motion measured by the inertial sensors, it is observed both the amplitudes are suppressed with the IPsc as expected, even though this signals are reliable only in the frequency band between about 0.2 Hz to 1 Hz. In addition, the amplitude of X-arm cavity displacement signal becomes larger by roughly factor about 10 at 30 mHz due to the seismometer related noise.

Thus the sensor correction system with the local seismomters suppresses the local suspension motion at the frequency around 0.2 Hz, however, it is unavoidable to enhance the lower frequency amplitude. In addition, according to the coherence between the X-arm cavity displacement signal and the differential IP-stage motion measured by the inertial sensors, the coherence becomes smaller with the IPsc though still relatively high coherence is observed. This implies that the current IPsc system dose not compensate all of the suspension differential motion at the 0.2 Hz to 0.6 Hz. As another issue, the IPsc does not affect to the peak observed at about 150 mHz, which is the main residual motion of each suspension which IP sensor does not sense. In order to suppress this peak effectively, we need to sense the TM motion and to feedback to IP-stage (or BF-stage), except for the IPsc system. Since the current TM length optical lever is not sensitive enough to sense the TM motion except for the stormy condition, sensitivity improvement or other sensor for this purpose will be necessary in order to realize such system.

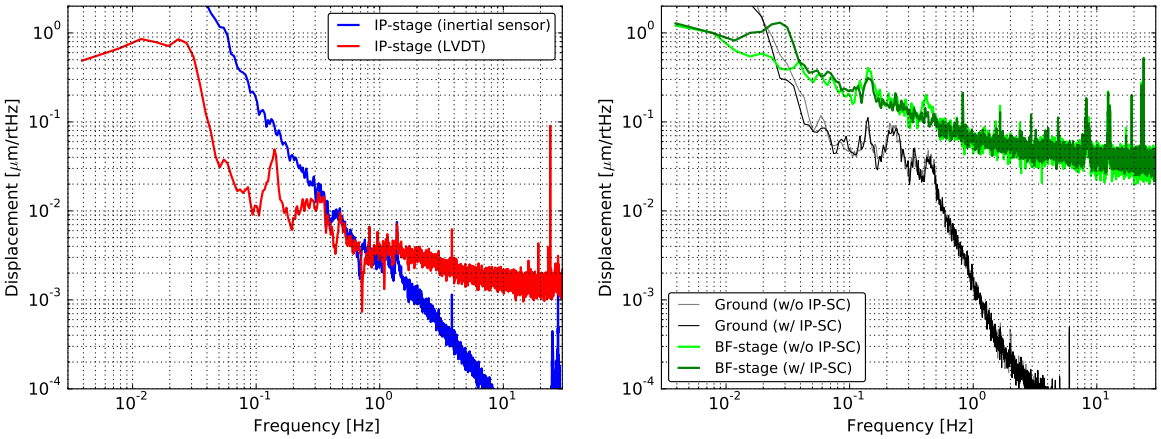

Figure C.2: Comparison between the sensor-corrected IP-LVDT signal and the accelerometer signal when the IPsc is on (*left*) and Comparison of the BF-stage displacement spectrum measured by the LVDT when the IPsc is on and off at ITMX suspension (*right*).

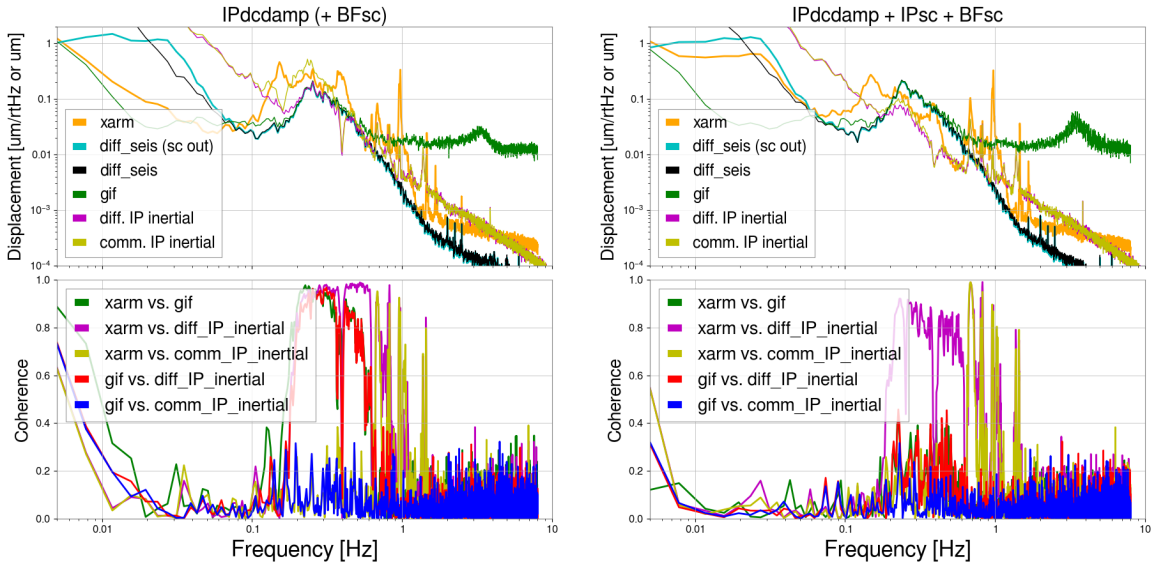

Figure C.3: spectra and the coherence between some signals when the IPsc is off (*left*) and on (*right*).

Bibliography

[1] Cody Messick, Kent Blackburn, Patrick Brady, Patrick Brockill, Kipp Cannon, Romain Cariou, Sarah Caudill, Sydney J. Chamberlin, Jolien D. E. Creighton, Ryan Everett, Chad Hanna, Drew Keppel, Ryan N. Lang, Tjonnie G. F. Li, Duncan Meacher, Alex Nielsen, Chris Pankow, Stephen Privitera, Hong Qi, Surabhi Sachdev, Laleh Sadeghian, Leo Singer, E. Gareth Thomas, Leslie Wade, Madeline Wade, Alan Weinstein, and Karsten Wiesner. Analysis framework for the prompt discovery of compact binary mergers in gravitational-wave data. *Phys. Rev. D*, 95:042001, Feb 2017.

[2] Alexander H. Nitz, Tito Dal Canton, Derek Davis, and Steven Reyes. PyCBC Live: Rapid Detection of Gravitational Waves from Compact Binary Mergers. 2018.

[3] T. Adams et al. Low-latency analysis pipeline for compact binary coalescences in the advanced gravitational wave detector era. *Class. Quant. Grav.*, 33(17):175012, 2016.

[4] L. P. Singer and L. R. Price. Rapid bayesian position reconstruction for gravitational-wave transients. *Phys. Rev. D*, 93:024013, Jan 2016.

[5] A. Einstein. Die grundlage der allgemeinen relativitätstheorie. *Annalen der Physik*, 354(7):769–822, 1916.

[6] B. P. Abbott et al. Observation of gravitational waves from a binary black hole merger. *Phys. Rev. Lett.*, 116:061102, Feb 2016.

[7] B. P. Abbott, R. Abbott, T. D. Abbott, F. Acernese, K. Ackley, C. Adams, T. Adams, P. Addesso, R. X. Adhikari, V. B. Adya, and et al. Multi-messenger observations of a binary neutron star merger. *The Astrophysical Journal Letters*, 848:L12, October 2017.

[8] Michele Maggiore. *Gravitational Waves: Volume 1: Theory and Experiments*. Oxford University Press, 2007.

[9] B. P. Abbott et. al. Multi-messenger observations of a binary neutron star merger. *The Astrophysical Journal*, 848(2):L12, oct 2017.

[10] GraceDB. https://gracedb.ligo.org. Cited April 2019.

[11] Hiroki Takeda, Atsushi Nishizawa, Koji Nagano, Yuta Michimura, Kentaro Komori, Masaki Ando, and Kazuhiro Hayama. Prospects for gravitational-wave polarization tests from compact binary mergers with future ground-based detectors. *Phys. Rev. D*, 100:042001, Aug 2019.

[12] B. P. Abbott et al. A gravitational-wave standard siren measurement of the Hubble constant. *Nature*, 551(7678):85–88, 2017.

[13] Adam G. Riess, Lucas M. Macri, Samantha L. Hoffmann, Dan Scolnic, Stefano Casertano, Alexei V. Filippenko, Brad E. Tucker, Mark J. Reid, David O. Jones, Jeffrey M. Silverman, Ryan Chornock, Peter Challis, Wenlong Yuan, Peter J. Brown, and Ryan J. Foley. A 2.4% DETERMINATION OF THE LOCAL VALUE OF THE HUBBLE CONSTANT. *The Astrophysical Journal*, 826(1):56, jul 2016.

[14] Planck Collaboration and P. A. R. Ade et. al. Planck 2015 results. xiii. cosmological parameters. *A&A*, 594:A13, Sep 2016.

[15] B. D. Metzger and E. Berger. WHAT IS THE MOST PROMISING ELECTROMAGNETIC COUNTERPART OF a NEUTRON STAR BINARY MERGER? *The Astrophysical Journal*, 746(1):48, jan 2012.

[16] C Markakis, J S Read, M Shibata, K Uryū, J D E Creighton, J L Friedman, and B D Lackey. Neutron star equation of state via gravitational wave observations. *Journal of Physics: Conference Series*, 189:012024, oct 2009.

[17] Eemeli Annala, Tyler Gorda, Aleksi Kurkela, and Aleksi Vuorinen. Gravitational-wave constraints on the neutron-star-matter equation of state. *Phys. Rev. Lett.*, 120:172703, Apr 2018.

[18] Christian D Ott. The gravitational-wave signature of core-collapse supernovae. *Classical and Quantum Gravity*, 26(6):063001, feb 2009.

[19] Takami Kuroda, Kei Kotake, and Tomoya Takiwaki. A NEW GRAVITATIONAL-WAVE SIGNATURE FROM STANDING ACCRETION SHOCK INSTABILITY IN SUPERNOVAE. *The Astrophysical Journal*, 829(1):L14, sep 2016.

[20] Thibault Damour and Alexander Vilenkin. Gravitational radiation from cosmic (super)strings: Bursts, stochastic background, and observational windows. *Phys. Rev. D*, 71:063510, Mar 2005.

[21] K. Kawabe. PhD Thesis, University of Tokyo. 1998.

[22] Akito Araya, Akiteru Takamori, Wataru Morii, Kouseki Miyo, Masatake Ohashi, Kazuhiro Hayama, Takashi Uchiyama, Shinji Miyoki, and Yoshio Saito. Design and operation of a 1500-m laser strainmeter installed at an underground site in kamioka, japan. *Earth, Planets and Space*, 69(1):77, 2017.

[23] William J. Startin, Mark A. Beilby, and Peter R. Saulson. Mechanical quality factors of fused silica resonators. *Review of Scientific Instruments*, 69(10):3681–3689, 1998.

[24] S. Rowan, G. Cagnoli, P. Sneddon, J. Hough, R. Route, E.K. Gustafson, M.M. Fejer, and V. Mitrofanov. Investigation of mechanical loss factors of some candidate materials for the test masses of gravitational wave detectors. *Physics Letters A*, 265(1):5 – 11, 2000.

[25] T Tomaru, T Suzuki, T Uchiyama, A Yamamoto, T Shintomi, C.T Taylor, K Yamamoto, S Miyoki, M Ohashi, and K Kuroda. Maximum heat transfer along a sapphire suspension fiber for a cryogenic interferometric gravitational wave detector. *Physics Letters A*, 301(3):215 – 219, 2002.

[26] M. G. Beker. PhD Thesis, Vrije Universiteit. 2013.

[27] Eric D. Black. An introduction to pound–drever–hall laser frequency stabilization. *American Journal of Physics*, 69(1):79–87, 2001.

[28] Adam J. Mullavey, Bram J. J. Slagmolen, John Miller, Matthew Evans, Peter Fritschel, Daniel Sigg, Sam J. Waldman, Daniel A. Shaddock, and David E. McClelland. Arm-length stabilisation for interferometric gravitational-wave detectors using frequency-doubled auxiliary lasers. *Opt. Express*, 20(1):81–89, Jan 2012.

[29] Y. Aso et al. Interferometer design of the kagra gravitational wave detector. *Phys. Rev. D*, 88:043007, Aug 2013.

[30] K. Somiya. Detector configuration of kagra–the japanese cryogenic gravitational-wave detector. *Classical and Quantum Gravity*, 29(12):124007, 2012.

[31] Y Aso, K Somiya, and O Miyakawa. Length sensing and control strategies for the LCGT interferometer. *Classical and Quantum Gravity*, 29(12):124008, jun 2012.

[32] Jon R. Peterson. Observations and modeling of seismic background noise. Technical report, 1993. Report.

[33] Seismic noise at KAGRA. https://gwdoc.icrr.u-tokyo.ac.jp/cgi-bin/private/DocDB/ShowDocument?docid=10436. Cited January 2020.

[34] Trillium120QA user's guide. https://gwdoc.icrr.u-tokyo.ac.jp/cgi-bin/private/DocDB/ShowDocument?docid=7554. Cited December 2019.

[35] Peter M. Shearer. *Introduction to Seismology*. Cambridge University Press, 2 edition, 2009.

[36] M. G. Beker, G. Cella, R. DeSalvo, M. Doets, H. Grote, J. Harms, E. Hennes, V. Mandic, D. S. Rabeling, J. F. J. van den Brand, and C. M. van Leeuwen. Improving the sensitivity of future gw observatories in the 1–10 hz band:

Newtonian and seismic noise. *General Relativity and Gravitation*, 43(2):623–656, Feb 2011.

[37] Bruce Allen, Warren G. Anderson, Patrick R. Brady, Duncan A. Brown, and Jolien D. E. Creighton. Findchirp: An algorithm for detection of gravitational waves from inspiraling compact binaries. *Phys. Rev. D*, 85:122006, Jun 2012.

[38] Stephen Fairhurst. Triangulation of gravitational wave sources with a network of detectors. *New Journal of Physics*, 11(12):123006, dec 2009.

[39] Summary page. https://summary.ligo.org/ detchar/summary/O3a/. Cited January 2020.

[40] Masaomi Tanaka and Kenta Hotokezaka. RADIATIVE TRANSFER SIMULATIONS OF NEUTRON STAR MERGER EJECTA. *The Astrophysical Journal*, 775(2):113, sep 2013.

[41] Shaon Ghosh and Gijs Nelemans. Localizing gravitational wave sources with optical telescopes and combining electromagnetic and gravitational wave data. In Carlos F. Sopuerta, editor, *Gravitational Wave Astrophysics*, pages 51–58, Cham, 2015. Springer International Publishing.

[42] Henry A. Sodano, Jae-Sung Bae, Daniel J. Inman, and W. Keith Belvin. Improved Concept and Model of Eddy Current Damper. *Journal of Vibration and Acoustics*, 128(3):294–302, 11 2005.

[43] A. Takamori. PhD Thesis, University of Tokyo. 2002.

[44] K. Okutomi. PhD Thesis, SOKENDAI. 2019.

[45] G. Cella, V. Sannibale, R. DeSalvo, S. Márka, and A. Takamori. Monolithic geometric anti-spring blades. *Nuclear Instruments and Methods in Physics Research Section A: Accelerators, Spectrometers, Detectors and Associated Equipment*, 540(2):502 – 519, 2005.

[46] Alberto Stochino, Riccardo DeSalvo, Yumei Huang, and Virginio Sannibale. Improvement of the seismic noise attenuation performance of the monolithic geometric anti-spring filters for gravitational wave interferometric detectors. *Nuclear Instruments and Methods in Physics Research Section A: Accelerators, Spectrometers, Detectors and Associated Equipment*, 580(3):1559 – 1564, 2007.

[47] L. Trozzo. PhD Thesis, Universitá di Siena. 2018.

[48] T. Sekiguchi. PhD Thesis, University of Tokyo. 2016.

[49] F Matichard, B Lantz, R Mittleman, K Mason, J Kissel, B Abbott, S Biscans, J McIver, R Abbott, S Abbott, E Allwine, S Barnum, J Birch, C Celerier, D Clark, D Coyne, D DeBra, R DeRosa, M Evans, S Foley, P Fritschel, J A Giaime, C Gray, G Grabeel, J Hanson, C Hardham, M Hillard, W Hua, C Kucharczyk, M Landry, A Le Roux, V Lhuillier, D Macleod, M Macinnis, R Mitchell, B O'Reilly, D Ottaway, H Paris, A Pele, M Puma, H Radkins, C Ramet, M Robinson, L Ruet, P Sarin, D Shoemaker, A Stein, J Thomas, M Vargas, K Venkateswara, J Warner, and S Wen. Seismic isolation of advanced LIGO: Review of strategy, instrumentation and performance. *Classical and Quantum Gravity*, 32(18):185003, aug 2015.

[50] L. P. Singer et al. The first two years of electromagnetic follow-up with advanced ligo and virgo. *The Astrophysical Journal*, 795(2):105, 2014.

[51] Yoshinori Fujii, Thomas Adams, Frédérique Marion, and Raffaele Flaminio. Fast localization of coalescing binaries with a heterogeneous network of advanced gravitational wave detectors. *Astroparticle Physics*, 113:1 – 5, 2019.

[52] B. P. Abbott et al. Implementation and testing of the first prompt search for gravitational wave transients with electromagnetic counterparts. *Astron. Astrophys.*, 539:A124, 2012.

[53] The LIGO Scientific Collaboration, the Virgo Collaboration, the KAGRA Collaboration, and B. P. Abbott et. al. Prospects for observing and localizing gravitational-wave transients with advanced ligo, advanced virgo and kagra, 2013.

[54] Y. Fujii. Master's Thesis, University of Tokyo. 2017.

[55] F. Cordero, F. Corvasce, R. Franco, G. Paparo, E. Maiorana, P. Rapagnani, F. Ricci, S. Braccini, C. Casciano, R. De Salvo, F. Frasconi, R. Passaquieti, M. De Sanctis, A. Solina, and R. Valentini. Elastic and anelastic properties of marval 18 steel. *Journal of Alloys and Compounds*, 310(1):400 – 404, 2000. Intern. Conf. Internal Friction and Ultrasonic Attentuation in Solids (ICIFUAS-12).

[56] Hareem Tariq, Akiteru Takamori, Flavio Vetrano, Chenyang Wang, Alessandro Bertolini, Giovanni Calamai, Riccardo DeSalvo, Alberto Gennai, Lee Holloway, Giovanni Losurdo, Szabolcs Márka, Massimo Mazzoni, Federico Paoletti, Diego Passuello, Virginio Sannibale, and Ruggero Stanga. The linear variable differential transformer (lvdt) position sensor for gravitational wave interferometer low-frequency controls. *Nuclear Instruments and Methods in Physics Research Section A: Accelerators, Spectrometers, Detectors and Associated Equipment*, 489(1):570 – 576, 2002.

[57] Virgo Internal Document. Advanced Virgo Technical Design Report, VIR-0128A-12. 2012.

[58] Riccardo Desalvo. Review: Accelerometer development for use in gravitational wave-detection interferometers. *Bulletin of the Seismological Society of America*, 99, 05 2009.

[59] R. Sleeman. Three-Channel Correlation Analysis: A New Technique to Measure Instrumental Noise of Digitizers and Seismic Sensors. *The Bulletin of the Seismological Society of America*, 96(1):258–271, Feb 2006.

[60] S. Aston. LIGO Internal Document, T050111-04-K. 2009.

[61] S. Zeidler. KAGRA Internal Document, JGW-T1605788. 2016.

[62] M. Fukunaga. Master's Thesis, University of Tokyo. 2019.

[63] Yuta Michimura, Tomofumi Shimoda, Takahiro Miyamoto, Ayaka Shoda, Koki Okutomi, Yoshinori Fujii, Hiroki Tanaka, Mark A Barton, Ryutaro Takahashi, Yoichi Aso, Tomotada Akutsu, Masaki Ando, Yutaro Enomoto, Raffaele Flaminio, Kazuhiro Hayama, Eiichi Hirose, Yuki Inoue, Takaaki Kajita, Masahiro Kamiizumi, Seiji Kawamura, Keiko Kokeyama, Kentaro Komori, Rahul Kumar, Osamu Miyakawa, Koji Nagano, Masayuki Nakano, Naoko Ohishi, Ching Pin Ooi, Fabián Erasmo Peña Arellano, Yoshio Saito, Katsuhiko Shimode, Kentaro Somiya, Hiroki Takeda, Takayuki Tomaru, Takashi Uchiyama, Takafumi Ushiba, Kazuhiro Yamamoto, Takaaki Yokozawa, and Hirotaka Yuzurihara. Mirror actuation design for the interferometer control of the KAGRA gravitational wave telescope. *Classical and Quantum Gravity*, 34(22):225001, oct 2017.

[64] Y. Sakakibara. PhD Thesis, University of Tokyo. 2015.

[65] T. Yamada. Master's Thesis, University of Tokyo. 2018.

[66] T. Ochi. Master's Thesis, University of Tokyo. 2018.

[67] et. al A. Shoda. KAGRA Internal Document, JGW-T1604756. 2016.

[68] et. al M. A. Barton. KAGRA Internal Document, JGW-E1504235. 2017.

[69] KAGRA Logbook. http://klog.icrr.u-tokyo.ac.jp/osl/?c=1. Cited February 2020.

[70] K. Izumi. Master's Thesis, University of Tokyo. 2009.

[71] Y. Michimura Y. Enomoto and K. Izumi. KAGRA Internal Document, JGW-T1808343. 2018.

[72] Y. Michimura. KAGRA Internal Document, JGW-T1202403. 2014.

[73] 3D rigid body suspension modeling tool. https://gwdoc.icrr.u-tokyo.ac.jp/cgi-bin/private/DocDB/ShowDocument?docid=3729. Cited January 2020.

[74] KAGRA wiki page for ETMX. http://gwwiki.icrr.u-tokyo.ac.jp/JGWwiki/KAGRA/Subgroups/VIS/TypeA/ETMX. Cited January 2020.

[75] D. Martynov. PhD Thesis, California Institute of Technology. 2015.

[76] J. Abadie et al. Sensitivity Achieved by the LIGO and Virgo Gravitational Wave Detectors during LIGO's Sixth and Virgo's Second and Third Science Runs. 2012.

[77] M. Barsanti, M. Beghini, F. Frasconi, R. Ishak, B.D. Monelli, and R. Valentini. Experimental study of hydrogen embrittlement in maraging steels. *Procedia Structural Integrity*, 8:501 – 508, 2018. AIAS2017 - 46th Conference on Stress Analysis and Mechanical Engineering Design, 6-9 September 2017, Pisa, Italy.